

*“Studies on some vanadium complexes with
polydentate ligands”*

*THESIS SUBMITTED FOR THE
DEGREE OF DOCTOR OF PHILOSOPHY (SCIENCE)
OF
JADAVPUR UNIVERSITY*

May, 2023



BY

Roumi Patra

INDEX NO. 48/19/Chem./26

*DEPARTMENT OF CHEMISTRY
JADAVPUR UNIVERSITY
KOLKATA- 700 032, INDIA*

যাদবপুর বিশ্ববিদ্যালয়
কলকাতা-৭০০০৩২, ভারত



*JADAVPUR UNIVERSITY
KOLKATA-700 032, INDIA

FACULTY OF SCIENCE: DEPARTMENT OF CHEMISTRY : INORGANIC CHEMISTRY SECTION

CERTIFICATE FROM THE SUPERVISER

This is to certify that the thesis entitled "Studies on some vanadium complexes with polydentate ligands" submitted by Rouni Patra who got her name registered on 29.08.2019 for the award of Ph.D. (Science) degree of Jadavpur University, is absolutely based upon her own work under my supervision and neither this thesis nor any part of it has been submitted for any degree/diploma or any other academic award anywhere before.

Date: 19th May 2023

Kajal Krishna Rajak
(Dr. Kajal Krishna Rajak)

Signature of Supervisor

Date with Official Seal

Dr Kajal Krishna Rajak
Professor of Chemistry
Jadavpur University
Kolkata-700032

* Established on and from 24th December, 1955 vide Notification No.10986-Edn/TU-42/55 dated 6th December, 1955 under Jadavpur University Act, 1955 (West Bengal Act XXXIII of 1955) followed by Jadavpur University Act, 1981 (West Bengal Act XXIV of 1981)

দূরভাষ: ২৪১৪-৬৬৬৬/৬১২৪/৬৬৪০/৬৪৪০/৬৪৪০ প্রসারণ: ২৪৬৬
দূরবার্তা: (৯১)-০০০-২৪১৪-৬৪৪০/৬২১০/২৪১০-৭১২১

Website: www.jadavpur.edu

Phone: 2414-6666/6194/6643/6495/6443 Extn.2469

E-mail : hod@chemistry.jdvu.ac.in

Fax: (91)-033-2414-6414/6210/2413-7121

Dedicated to my
Dedicated to my

Parents

Preface

Preface

The work described in this thesis “**Studies on some vanadium complexes with polydentate ligands**” was commenced in August 2019.

This thesis consists of five chapters. **Chapter-I** contains a summary of the work presented in this thesis along with a brief description of the physical methods and equipments employed.

Chapter-II describes solvent mediated syntheses and characterizations of a four mononuclear and two dinuclear vanadium(V) complexes with hydrazide functionalized Schiff base ligands (H_2L^{1-2}). Electro synthesized type II mixed-valence vanadium (V/IV) complexes were reported. The redox properties were supported by theoretical calculations. Catecholase like activity using 3, 5 DTBC was examined.

Chapter-III deals with syntheses, X-ray structures of two valproic acid hydrazide based Schiff base ligands (H_2L^{3-4}) and their corresponding mono nuclear dioxo vanadium(V) complexes. Constant potential electrolysis (CPE) of the complexes yielded dioxo vanadium (IV) species. The complexes catalytically oxidized pyrogallol to purpurogallin under aerobic condition. The experimental observations including redox properties were well corroborated with the computational results.

Chapter-IV discusses solvent dependent syntheses and characterizations of two different sets of mono and dinuclear vanadium(V) complexes using tautomeric form of two valproic acid hydrazide-based Schiff base ligands (H_2L^{3-4}). Electrochemically synthesized type II vanadium (V/IV) complexes were reported. The catalytic oxidation of 3, 5-DTBC was reported to proceed via semiquinone radical pathway. Peroxidase like activity was monitored following the oxidation of pyrogallol.

Chapter-V consists of syntheses of four vanadium(V) complexes with 3-amino-2-naphthol based Schiff base ligands (H_2L^{5-8}) Detailed characterization with respect to crystal structures and unique redox properties are reported here. Theoretical calculations are also employed to correlate the experimental findings.

(Roumi Patra)

Roumi Patra
Department of Chemistry
Jadavpur University
Kolkata- 700 032, India.

Acknowledgement

It is my pleasure to acknowledge the roles of the people whose love, care, affection, inspiration and staunching support have made this thesis work possible.

First of all, I would like to express my deep regards and gratitude to my guide **Prof. Kajal Krishna Rajak** for giving me the opportunity for this work. I am lucky to have such a wonderful teacher. Thank you, Sir, for your love, guidance, and advice to me in every aspect of my research work. I shall cherish it forever.

I would like to mention the role of my parents, *Bapi and Maa*, in shaping me as an individual. They are the primary source of energy and encouragement for me for taking this journey of a researcher. They always try to enlighten me through their teaching and inspiration so that I can maintain my focus

My sincere thanks to my past seniors and the present members of my lab for their help and cooperations. My thanks also go to the research group of Prof. Kaushikisankar Pramanik and Prof. Subratanath Koner. My special regards to Dr. Prasanta Ghosh, *Ramakrishna Mission Residential College, Narendrapur* for his support and help.

I would also like to express my regards to Prof. Samaresh Bhattacharya, Prof. Sujoy Baitalik and his fellow for their help in several ways. I am grateful indeed to all the faculty members of Department of Chemistry for their support.

I humbly acknowledge CSIR for my fellowship and Jadavpur University for infrastructure facilities.

(Roumi Patra)

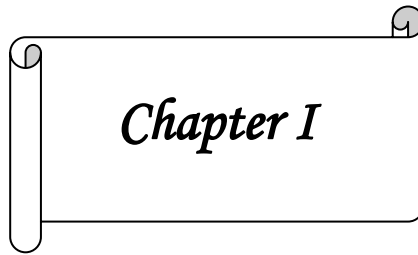


15/5/23

Department of Chemistry
Jadavpur University
Kolkata-700032

CONTENTS

	Page
Preface	i
Acknowledgement	ii
Chapter I Introduction	1-19
Chapter II Di and Mono nuclear Vanadium (V) complexes: Solvent dependent structural versatility, electro syntheses of mixed-valence oxovanadium (IV/V) entities in solution and catecholase activity	20-66
Chapter III Synthesis and characterization of dioxovanadium (V) complexes and its catalytic activity towards pyrogallol oxidation	67-97
Chapter IV Influence of solvent in Vanadium (V) complex structures: Electro-generated type II mixed-valent $V^{V}V^{IV}$ entities in solution, peroxidase activity and catecholase activity via semiquinone pathway	98-137
Chapter V Synthesis, crystal structure and redox studies of vanadium (V) complexes with Schiff base ligands derived from 3 -amino -2 -naphthol	138-171
List of Publications	iv



Introduction

Introduction

Abstract

The systems of chemical compounds comprising this thesis are briefly introduced in this chapter following a preamble on chemistry of vanadium. Here we also describe general introduction of the thesis. The equipment and instruments used in the work and methods of synthesis of this thesis are summarized comprehensively.

I.1 PREAMBLE

For the author, her first exposure to the metal vanadium probably came from her biology textbook, which discussed its function as a trace element in relation to nutrition. The Scandinavian legendary goddess *Vanadis* inspired the name of the element vanadium. A mentionable issue in the matriculation chemistry syllabus has always been the function of vanadium pentoxide, V_2O_5 , as an oxidation catalyst in the conversion of sulphur dioxide to sulphur trioxide in the well-known Contact Process. Due to its capacity to absorb light¹, smaller bandgap (2.3 eV) than TiO_2 and ZnO , chemical stability, and surface catalytic characteristics, vanadium oxide has enormous potential for use in the treatment of water. The V_2O_5 catalyst also showed substantial photocatalytic activity against different organic contaminants.^{2,3,4}

Vanadium has always been occupying a position of biological importance in the form of versatile cellular activities and physiological functions⁵. Research on specific aspects of the biological activity⁶ of vanadium has shown that this element is crucial for the metabolism of lipids, phospholipids, cholesterol, and carbohydrates for its influence on the pathways of glycolysis, glycogenolysis, gluconeogenesis, and other enzymatic reactions⁷. It is also known that vanadium has an impact on the metabolism of thyroid and erythrocytes⁸, the storage and transit of calcium in cells, and the production of secondary transmitters that facilitate the transduction of intracellular impulses. In addition, it controls the activity of crucial enzymes involved in the phosphorylation as well as dephosphorylation of proteins, kinases, and phosphatases⁹, contributing to cell growth.^{10, 11} Vanadium's ability to mimic insulin, which can stimulate the uptake and metabolism of glucose in living organisms, is another significant biological action.¹² This has led to research exploring the potential use of vanadium compounds in the treatment of diabetes and metabolic disorders.¹³ Again, as a component of a catalyst, vanadium is used in a variety of chemical reactions, including those produce maleic anhydride, convert propane and propylene into acrylonitrile and toluene into benzonitrile, as well as those oxidise alkanes and

alcohols and reduce emissions of sulphur and nitrogen oxides brought on by human activity.^{14, 15}

Vanadium has electronic configuration as $[\text{Ar}]3d^34s^2$. It assumes versatile role with respect to redox state. The states +2 to +5 are sustainable in aqueous solution. Significantly, the most stable oxidation states +3, +4 and +5 both in vivo and in vitro.¹⁶ Two categories of vanadium containing enzymes¹⁷ nitrogenase (V-Nase)¹⁷ and haloperoxidase (VHPO)¹⁸ have been isolated and characterized. The first one is of oxidative in nature and later one is reductive. These two enzymes particularly signify the importance of +5 and +4 oxidation state of vanadium.

Currently, vanadium's chemistry is being examined for usage as photographic developer, a reducing agent, a drying agent in a variety of paints and varnishes, a drying agent in the manufacture of insecticides, and a component of the black dyes, inks, and pigments used by the textile, printing, and ceramics industries.^{19, 20, 21} Additionally, versatile redox states of vanadium have been explored in making Vanadium redox flow batteries (VRFB) are a type of rechargeable flow battery that uses vanadium ions in different oxidation states to store and release electrical energy. VRFBs are known for their long cycle life and high energy efficiency, making them suitable for large-scale energy storage applications^{22, 23}. This is still a very nascent yet promising area of research.

I.2. INTRODUCTION AND SUMMARY OF PRESENT WORK

A. Introduction

It is not surprising that natural evolution has incorporated some metal ions into performing a wide range of functions and playing essential roles in organisms, because many metal ions have a general inclination to interact with biomolecules²⁴. Vanadium is a transition metal that is prevalent in soil, crude oil, water, and air. Naturally, it found roles in biological systems²⁵, specifically as a

necessary component for many living organisms, given that it is omnipresent in the crust of our globe. A newfound interest in the coordination chemistry of vanadium has been sparked by the identification of cofactors containing vanadium in nitrogenases²⁶ and bromoperoxidases.²⁷ Vanadium's coordination chemistry has given a boost to a number of catalytic processes²⁸⁻³², biochemical processes such as peroxidase mimicking activity³³, insulin mimicking activities,³⁴ cytotoxic activities,³⁵ nitrogen fixation,³⁶ haloperoxidation,³⁷ epoxidation³⁸, inhibition of phosphate-metabolizing enzymes³⁹, alleviation of diabetes mellitus symptoms⁴⁰ and more. So, vanadium chemistry has undoubtedly garnered medical interest.

On the other hand, Schiff base ligands, particularly those based on hydrazones, have drawn attention, primarily due to their facile synthesis, easily tunable electronic properties, conformational diversity⁴¹, and potential use in pharmacotherapy⁴²⁻⁴³ widespread biological applicability⁴⁴. Depending on variables such as the oxidation state of the metal ions, reaction conditions, nature of substituents on the hydrazone skeleton, and tautomerization, these types of ligands are crucial in defining the overall charge of the metal complexes and, consequently, their stability.⁴⁵⁻⁴⁶ This increases the variety of complexes that can be formed depending on the parameters of synthetic processes, such as solvent, co-ligands with various numbers of donor atoms (mostly O, N), stoichiometry, substrate (in the case of vanadium, $\text{VO}(\text{SO}_4)(\text{aq})$, $[\text{VO}(\text{acac})_2]$, $[\text{V}(\text{acac})_3]$, and others), atmosphere (aerobic/anaerobic), as well as flexibility during coordination and protonation/deprotonation responding to metal oxidation state etc.⁴⁷ In addition, the literature discloses oxidovanadium complexes of salicylaldehyde and salicylaldehyde-hydrazones as prospective anti-cancer drugs⁴⁸ for treating brain cancer.

Furthermore, it is worthwhile to consider the significance of monooxido-bridged binuclear vanadium(V/V) species of the type $(\text{V}^{\text{V}}\text{OL})_2\text{O}$, which are likely to serve as predecessors of mixed-valence V(IV,V) species.^{49, 50} An important component of the applicability of mixed-valence complex in molecular

electronics and molecular computing is the function of the electronic environment of the ligand towards electron localization or delocalization across the metal centre⁵¹. In the context of odd electron behaviour in solid and solution in various biological processes, the rich coordination chemistry of mixed-valence vanadium integrating acyl hydrazone⁵² ligands is obvious. Compared to the well-known oxidovanadium complexes⁵³ having $V^{IV}O^{2+}$ or V^{VO}^{3+} moieties, comparatively few mixed-valence divanadium (IV/V) complexes have been chemically synthesized and studied. Traditionally, Robin–Day mixed valency scheme for complexes refers, in type I (valence-trapped), the odd electron is not delocalised.⁵⁴ In type III (delocalised), the odd electron is shared equally over both redox sites^{52b}. Between these two extremes, type II (hopping)^{55, 56} are found, where some delocalization takes place over both redox centres.

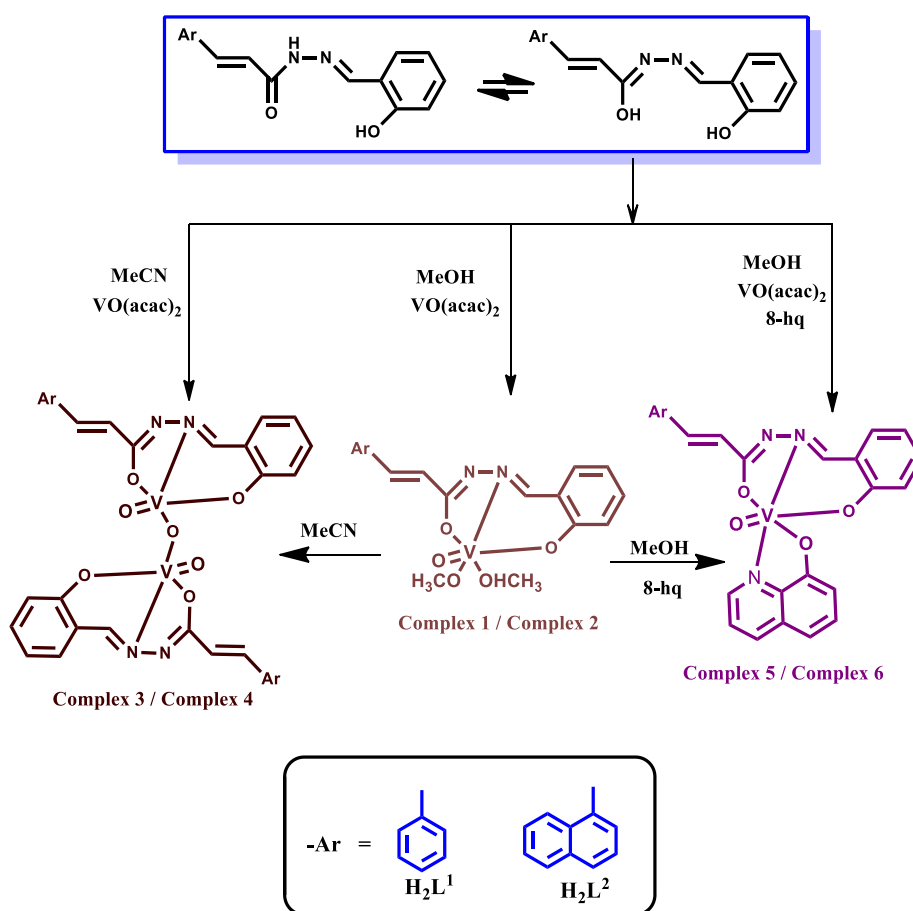
The chemistry of vanadium has also been found to be relevant for catecholase mimics.^{57, 58} The intricate details of the reaction pathways are always a welcome to the scientific community for further improvement of the knowledge. There is also little information available regarding the peroxidase-mimicking activity that uses vanadium catalyzed oxygenations of pyrogallol.⁵⁹ In addition, Metal complexes of Schiff base ligands, particularly those containing vanadium, have caught the interest of researchers due to potential biological and catalytic applications⁶⁰. This adaptability of different oxidation states followed by one electron redox process enables the creation of a variety of organic reactions by manipulating the redox potential of the vanadium molecule⁶¹.

In this dissertation, we focus mainly in the synthesis and characterization of various vanadium(V) complexes in with *O*, *O*, *N* coordinating ligands. We have reported type II mixed-oxidation state species which were electrogenerated from their respective divanadium (V/V) predecessors. Following the oxidation of 3, 5-di-tert-butylcatechol and pyrogallol catalytic potential of the complexes were assessed. Cyclic voltammetry and spectroelectrochemical measurements were used to explain redox behaviour which is further supported by density functional theory (DFT) calculations.

B. Summary of Present work

The present work has been emphasized on searching new vanadium complexes using different polydentate Schiff base ligands having functionalized hydrazone and amino naphthyl moieties and exploring their important properties like solvent dependent structural diversity, electrochemical properties and redox behavior.

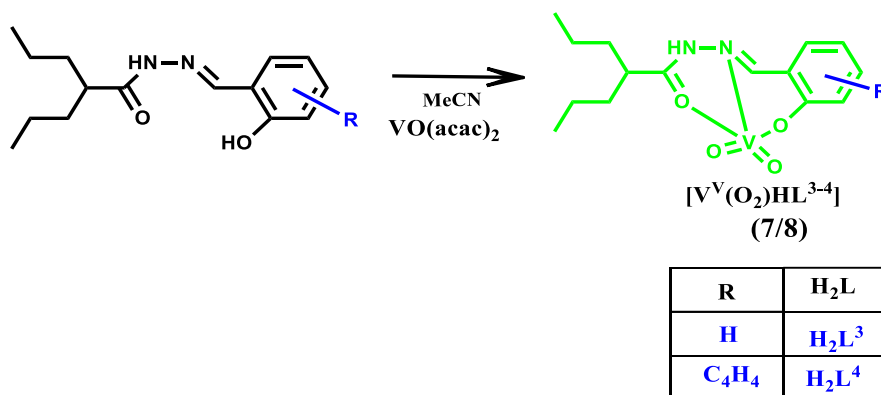
Chapter-II we describe the syntheses and characterisation of two mononuclear $[VVO(L^{1-2})(OMe)(MeOH)]$ (**1**, **2**) and two binuclear $[(L^{1-2})(O)V^V-O-V^V(O)(L^{1-2})]$ (**3**, **4**) vanadium complexes with the ligands H_2L^1 and H_2L^2 . The ligands were prepared by condensation of salicylaldehyde with cinnamic acid hydrazide (H_2L^1) or 3-(1-naphthyl)acrylic acid hydrazide (H_2L^2) Both monomeric and dimeric complexes can be synthesised upon switching the solvent from



methanol to acetonitrile respectively. Another two complexes $[VVO(L^{1-2})(8-Hq)]$ (**5**, **6**) and incorporating 8-hydroxyquinoline (8-hq) as co-ligand have also

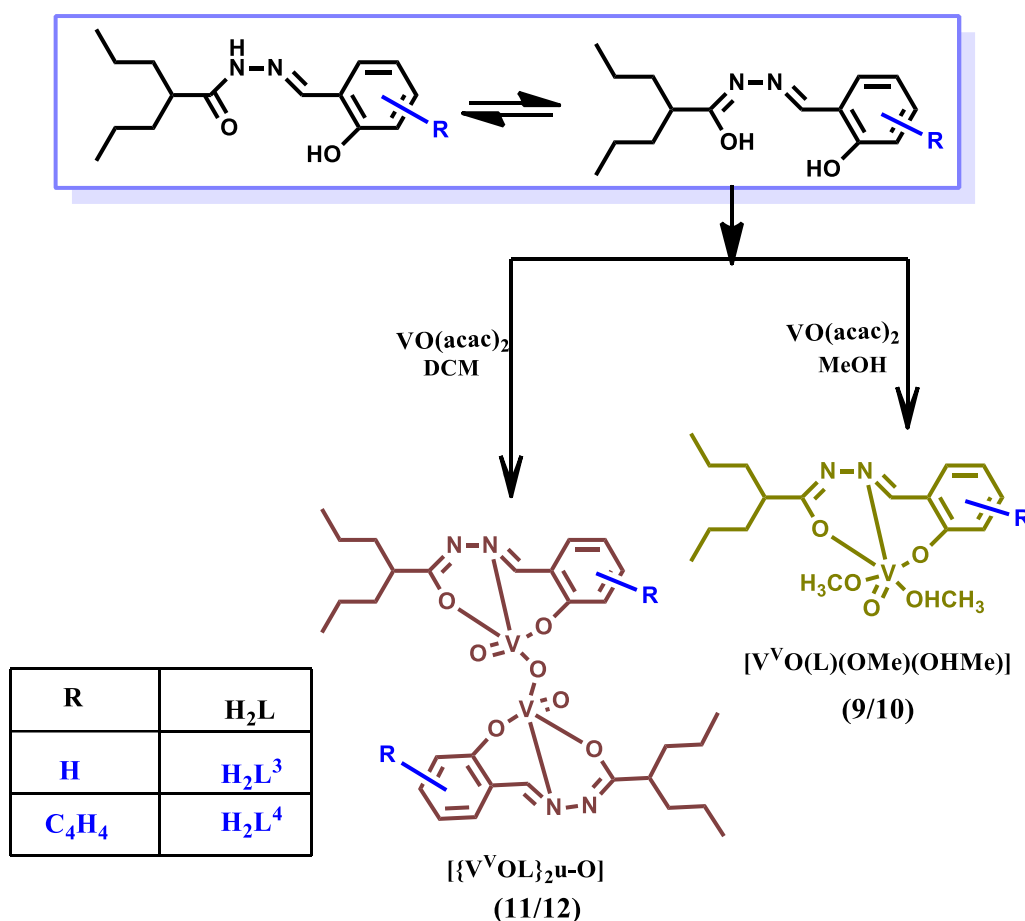
reported. The redox activities were investigated by cyclic voltammetry along with spectroelectrochemistry experiments. Type II mixed-oxidation vanadium (V/IV) complexes **3a** and **4a**, were generated through coulometric reduction of **3** and **4**. For ligand H_2L^1 and complexes **1** - **5** geometrical analysis were done by X-ray analysis. Complex **1** and **2** were selected to act as functional templates for catechol oxidase.

Chapter III Having succeeded with O, N, O coordinating hydrazone ligands, we were interested to work with another type of hydrazone ligands. The selected ligands H_2L^{3-4} were synthesized by the condensation of valproic acid hydrazide with their respective aldehydes (for H_2L^3 = salicylaldehyde, H_2L^4 = 2-hydroxy naphthaldehyde). The ligands crystallised in the most stable trans keto-amine tautomeric form in the solid state as elucidate by single crystal X-ray



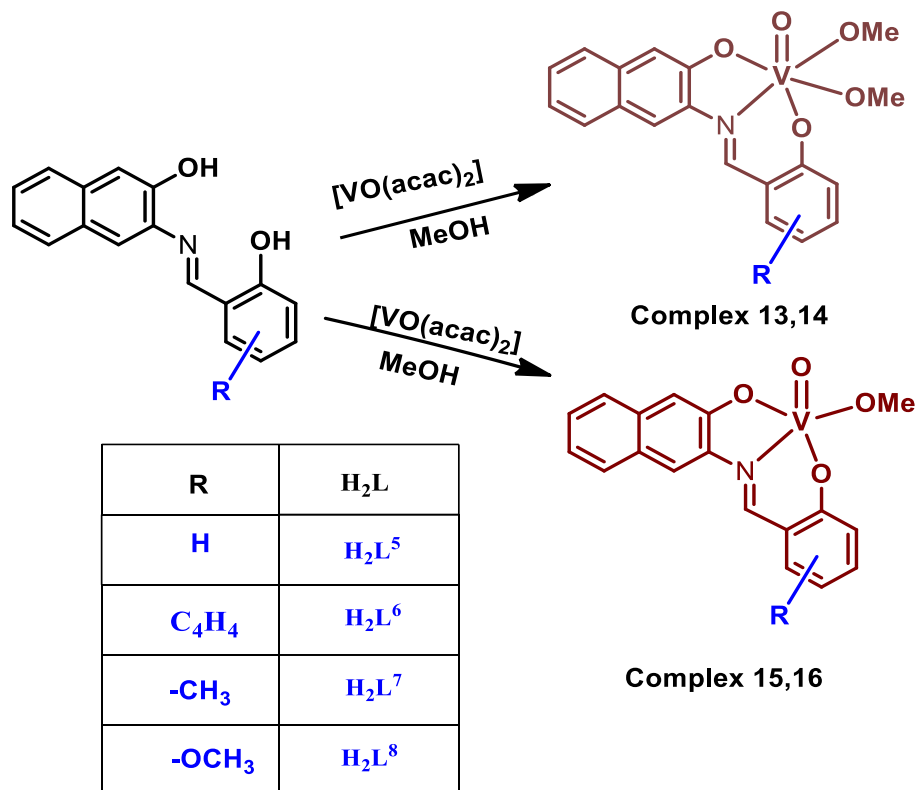
diffraction. In acetonitrile solution the ligands retain this tautomeric form and subsequently bind to vanadium center through O, N, O coordinating neutral amide form generating two dioxo vanadium (V) complexes $[V^V(O)_2HL^{3-4}]$ (**7**, **8**). Constant potential electrolysis (CPE) of **7**, **8** yielded dioxo vanadium (IV) species identified by unusual EPR signal. Complexes **7** and **8** were also successfully applied in the oxidation of pyrogallol to purpurogallin under aerobic condition.

Chapter-IV deals with the same ligands as described in Chapter III, but with different tautomeric forms as well as the solvent dependent structural diversity in the synthesis of complexes. Here the ligands bind via O, N, O coordinating dianionic iminoato form producing oxidomethoxido complexes $[V^VO(L^{3-4})(OMe)(OHMe)]$ (**9**, **10**) in methanol and the corresponding monooxobridged dinuclear μ -oxidodioxido divanadium complexes $[{V^VOL^{3-4}}]_2 \mu -O]$ (**11**, **12**) in dichloromethane. We have reported mixed-oxidation state species **11a** and **12a**,



electrogenerated from its divanadium (V/V) precursors **11** and **12** respectively. The efficacy to catalyse the oxidation of catechol to quinone by **9** and **10** were evaluated by utilizing 3, 5-di-tert-butylcatechol, the reaction of which proceeds via semiquinone radical pathway. Peroxidase like activity was also for monitored.

Chapter-V describe the preparation of four mononuclear vanadium(V) complexes (**13 - 16**) with four different Schiff base ligands (H_2L^{5-8}). The Schiff base compounds, were synthesized by the condensation of of 3-amino-2-naphthol with respective aldehydes [with salicylaldehyde (H_2L^5), naphthaldehyde (H_2L^6), 4-methylsalicylaldehyde (H_2L^7) and 4-methoxysalicylaldehyde (H_2L^8)] in methanol.



Crystal structure the ligand H_2L^8 was determined by single crystal XRD analysis which indicate that the ligand favours the keto-amine tautomeric form. X-ray analysis showed octahedral geometry for **13**, **14** having general formula $VO(L^{5-6})(OMe)(MeOH)$ whereas penta-coordinated square-pyramidal geometry for **15**, **16** of general formula $VO(L^{7-8})(OMe)$ where there is no coordinated solvent molecule. The compounds have been characterized by different spectroscopic methods. Redox analysis was performed by cyclic voltammetry.

I.3. PHYSICAL MEASUREMENT

Various physical methods have been employed for the characterization and elucidation of the properties of the synthesized compounds and these are described in the subsequent chapters. A brief description is given below.

A. *Elemental Analysis*

The C, H, N content of the samples were determined with the help of Perkin-Elmer 2400 series II elemental analyzer which utilizes thermal conductivity data for gas (CO₂, H₂O, N₂) analysis. 1.5-2.5 mg of sample was introduced into the combustion cell usually at a temperature in the range of 900-980 °C. Pure oxygen was used for combustion, and pure helium was used as the driving gas.

B. *Infrared Spectra*

IR spectra were recorded in KBr disk with the help of Perkin-Elmer L-0100 spectrophotometer.

C. *Electronic Spectra*

Electronic spectra of samples were recorded on a Perkin-Elmer LAMBDA 25 UV- Vis spectrophotometer (200-1100 nm). A pair of quartz cells of path length 1 cm was used in this purpose.

D. *Mass Spectra*

Electrospray ionization mass spectrometry (ESI-MS) spectra of the samples were recorded on a Micromass Qtof YA 263 mass spectrometer and on Shimadzu LCMS 2020 mass spectrometers equipped with electrospray ionization (ESI) ion source. Only characteristic fragments are given with intensities. The spectra were normalized against the most intense peak having intensity 100.

E. *NMR Spectra*

¹H spectra were recorded in mainly CDCl₃, and DMSO-d₆ with the help of Bruker FT 300 MHz spectrometer using tetramethyl silane (TMS) as an internal standard depending upon the solubility of the products. Signals are assigned to individual protons based on chemical shifts, spin-spin coupling and substituent

effects. The atom-numbering scheme used for ^1H and was same as that used in the crystallography.

F. *Crystallographic Studies*

The X-ray intensity data were collected on Bruker AXS SMART APEX CCD diffractometer (Mo K_{α} , $\lambda = 0.71073 \text{ \AA}$) at 293 K. The detector was placed at a distance 6.01 cm from the crystal. Total 606 frames were collected with a scan width of 0.5° in different settings of φ . The data were reduced in SAINTPLUS⁶² and empirical absorption correction was applied using the SADABS package.⁶² Metal atom was located by Patterson Method and the rest of the non-hydrogen atoms were emerged from successive Fourier synthesis. The structures were refined by full matrix least-square procedure on F^2 . All non-hydrogen atoms were refined anisotropically. All calculations were performed using the SHELXTL V 6.14 program package.⁶³ Molecular structure plots were drawn using the Oak Ridge thermal ellipsoid plot (ORTEP).⁶⁴

R1, wR2 and goodness-of-fit (GOF) are given by the following equations 1, 2 and 3 respectively.

$$R1 = \Sigma | |F_o| - |F_c| | / \Sigma | F_o | \quad \dots\dots (1)$$

$$wR2 = [\Sigma[w(F_o^2 - F_c^2)^2] / \Sigma[w(F_o^2)^2]]^{1/2} \quad \dots\dots (2)$$

$$GOF = S = [\Sigma[w(F_o^2 - F_c^2)^2] / (\mathbf{n}_o - \mathbf{n}_p)]^{1/2} \quad \dots\dots (3)$$

\mathbf{n}_o = number of reflections

\mathbf{n}_p = total number of parameters refined

Specific details for each compound will be given in the concerned chapter.

G. *EPR Studies*

The X-band electron paramagnetic resonance (EPR) spectra were measured on a Magnettech GmbH MiniScope MS400 EPR spectrometer, equipped with temperature controller TC H03, where the microwave frequency was measured with a frequency counter FC400. Simulated EPR Spectra and Line width values

were obtained from the simulation of the experimental spectra using the Easy Spin EPR⁶⁵ spectrum simulation program.

***H.* Electrochemical Studies and Spectroelectrochemistry**

The electro analytical instrument, BASi Epsilon-EC for cyclic voltammetry experiments in CH₂Cl₂ (some cases CH₃CN and DMF) solutions containing 0.20 M tetrabutylammonium hexafluorophosphate as supporting electrolyte was used. The BASi platinum working electrode, platinum auxiliary electrode, Ag/AgCl reference electrode were used for the measurements. Measurements were made under an inert atmosphere (N₂ or Ar). The redox potential data are referenced vs. ferrocenium/ferrocene, Fc⁺/Fc, couple. In all cases, the experiments were performed with the multiple scan rates to analyse the reversibility of the electron transfer waves. BASi SEC-C thin layer quartz glass spectroelectrochemical cell 13 kit (light path length of 1 mm) with platinum gauze working electrode and SEC-C platinum counter electrode were used for spectroelectrochemistry measurements.

I.4. DFT STUDY AND COMPUTATIONAL DETAILS

All the quantum mechanical calculations were performed with the Gaussian 09W software package.⁶⁶ Figures showing MOs, and the difference density plots were prepared by using the GaussView 5.1 software. All the calculations were carried out in Supermicro Superserver work station. The geometrical structures of the singlet ground state (S₀) were optimized by the DFT⁶⁷ method with B3LYP exchange correlation functional⁶⁸ approach. The geometry of the complexes were fully optimized in solution phase without any symmetry constraints.

In the calculation, Vanadium's core electron (1s²2s²2p⁶) was described using calculation approach associated with effective core potential (ECP) approximation of Hay and Wadt⁶⁹, while the valence shell was described using the corresponding "double-zeta" quality basis set LANL2DZ. For H we used 6-

31(g) basis set and the 6-311+G⁷⁰ basis set for C, N, and O atoms for the optimization of the ground state geometries.

The vibrational frequency calculations were also performed for all the complexes to ensure that the optimized geometries represent the local minima and there were only positive Eigen values. There was a good agreement between the theoretical and experimental structures.

I.5. CHEMICALS AND SOLVENTS

All commercially available chemicals and solvents utilized in this work were of analytical grade and in the most cases the chemicals and solvents were used without further purification in the synthesis.

All references in this thesis are given in the following format: Name of the author(s), *Journal*, **year**, *volume*, page.

References

1. Armaković, S. J.; Jovanoski-Kostić, A.; Bilić, A.; Savanović, M. M.; Tomić, N.; Kremenović, A.; Šćepanović, M.; Grujić-Brojčin, M.; Ćirković, J.; Armaković, S. *Molecules*. **2023**, *28*, 655.
2. Sajid, M. M.; Shad, N. A.; Javed, Y.; Khan, S. B.; Zhang, Z.; Amin, N.; Zhai, H. *Surf. Interfaces* **2020**, *19*, 100502.
3. Sun, J.; Li, X.; Zhao, Q.; Ke, J.; Zhang, D. *Novel. J. Phys. Chem. C* **2014**, *118*, 10113-10121
4. Karthik, K.; Nikolova, M.; P.; Phuruangrat, A.; Pushpa, S.; Revathi, V.; Subbulakshmi, M. *Mater. Res. Innov.* **2020**, *24*, 229-234.
5. Selvaraj, S.; Krishnan, U. M. *J. Med. Chem.* **2021**, *64*, 12435-12452.
6. Rehder, D. *Inorganica Chim. Acta* **2023**, *549*, 121387
7. Zeng, X.; Wang, H.; Ma, Y.; Xu, X.; Lu, X.; Hu, Y.; Xie, J.; Wang, X.; Wang, Y.; Guo, X.; Zhao, L. *ACS Appl. Mater. Interfaces* **2023**, *15*, 13941-13955
8. Zaporowska, H.; Wasilewski, W. *Camp. Biochem. Physiol.* **1992**, *102*, 223-231.
9. Pessoa, J. C.; Garribba, E.; Santos, M. F.; Santos-Silva, T. *Coord. Chem. Rev.*, **2015**, *301*, 49-86.
10. Tracey, A. S.; Willsky, G. R.; Takeuchi, E. S. 1st Edition; CRC Press, Taylor and Francis Group, 2007. DOI: <https://doi.org/10.1201/9781420046144>
11. Hendriks, W. J.; Elson, A.; Harroch, S.; Stoker, A. W. *FEBS J.* **2008**, *275*, 816-380
12. Ścibior, A.; Pietrzyk, Ł.; Plewa, Z.; Skiba, A. *J. Trace Elem. Med. Biol.* **2020**, *61*, 126508.
13. Treviño, S.; Díaz, A.; Sánchez-Lara, E.; Sanchez-Gaytan, B. L.; Perez-Aguilar, J. M.; González-Vergara, E. *Biol. Trace Elem. Res.* **2019**, *188*, 68-98.
14. Sutradhar, M.; Pombeiro, A. J. L.; da Silva, J. A. L. *Vanadium Catalysis*, Vol. 41; Royal Society of Chemistry, 2020. DOI: <https://doi.org/10.1039/9781839160882>

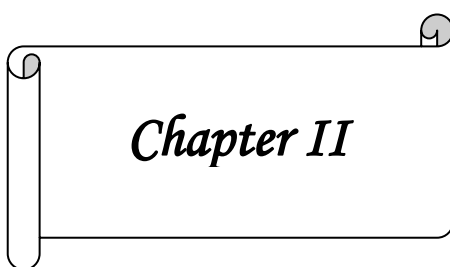
15. Zhao, L.; Yang, P.; Shi, S.; Zhu, G.; Feng, X.; Zheng, W.; Vlachos, D. G.; Xu, J. *ACS Catal.* **2022**, *12*, 15249-15258
16. (a) Cotton, F.A.; Wilkinson, G.; Murillo, C.A.; Bochmann, N.; *Advanced Inorganic Chemistry*, 6th Ed, A Wiley-Interscience Publication, **1999**, p714, (b) Fraston da silva, J.J.R.; Williams, R.J.P., *The Biological Chemistry of the Elements. The Inorganic Chemistry of Life*, **1991**, p 427. (c) Boas, L.V.; Pessoa, J.C. in *Comprehensive Coordination Chemistry: The Synthesis, Reaction, Properties and Application of Coordination Compounds*; Ed. Sir G.Willkinson, **1987**, vol.3; p 454.
17. (a) Crans, D.C., Smee, J.J.; Gaidamuskas, E.; Yang, L., *Chem. Rev.*, **2004**, *104*, 849. (b) Rehder, D. J. *Inorg. Biochem.*, **2000**, *80*, 133. (c) Chen, J.; Christiansen, J.; Tiltsworth, R.C.; Hales, B.J.; George, S.J.; Coucouvanis, D.; Cramer, S.P. *J. Am. Chem. Soc.*, **1993**, *115*, 5509. (d) Vitter, H. in *Metal ions in Biological Systems*; Sigel, H.; Sigel, A.; Eds. Marcel Dekker: New York, **1995**, vol.31, Chapter 10.
18. Butler, A.; Baldwin, A.H.; *Metal Sites in Protein and Model, Phosphatases, Lewis Acids and Vanadium*; Hill, H.A.O.; Salder, P.J. Thompson, A.J.; Eds.; Spingler-Verleg, Heidelberg, **1999**, 108.
19. Gao, F.; Olayiwola, A. U.; Liu, B.; Wang, S.; Du, H.; Li, J.; Wang, X.; Chen, D.; Zhang, Y. *Miner. Process. Extr. Metall. Rev.* **2022**, *43*, 466-488.
20. Perron, L. Minerals & Resources Sector, Canada Minerals Yearbook. 2001, Vol. 59, pp. 59.1-59.7.
21. Moskalyk, R. R.; Alfantazi, A. M. *Miner. Eng.* **2003**, *16*, 793-805.
22. He, Z.; Lv, Y.; Zhang, T.; Zhu, Y.; Dai, L.; Yao, S.; Zhu, W.; Wang, L. *J. Chem. Eng.* **2022**, *427*, 131680.
23. Lourenssen, K.; Williams, J.; Ahmadpour, F.; Clemmer, R.; Tasnim, S. *J. Chem. Eng.* **2019**, *25*, 100844.
24. Awan, R.S.; Liu, C.; Yang, S.; Wu, Y.; Zang, Q.; Khan, A.; Li, G. *Acta Geochim.* **2021**, *40*, 973-997.
25. Chasteen, N. D. Springer Dordrecht, 1990. DOI: <https://doi.org/10.1007/978-94-009-2023-1>

26. Robson, R. L.; Eady, R. R.; Richardson, T. H.; Miller, R. W.; Hawkins, M.; Postgate, J. R. *Nature*. **1986**, 322, 388-390.
27. Chen, Z. *Coord. Chem. Rev.* **2022**, 457, 214404.
28. Huang, W.; Peng, L. Y.; Zhang, J.; Liu, C.; Song, G.; Su, J. H.; Fang, W. H.; Cui, G.; Hu, S. *J. Am. Chem. Soc.* **2023**, 145, 811-821
29. Schober, L.; Sako, M.; Takizawa, S.; Gröger, H.; Sasai, H. *Chem. Commun.* **2020**, 56, 10151-10154.
30. Sako, M.; Takizawa, S.; Sasai, H. *Tetrahedron*, **2020**, 76, 131645.
31. Griffin, S. E.; Schafer, L. L. *Inorg. Chem.* **2020**, 59(8), 5256-5260.
32. (a) Sutradhar, M.; Martins, L.M.D.R.S.; Silva, M.F.C.G.; Pombeiro, A.J.L. *Coord. Chem. Rev.* **2015**, 301-302, 200-239. (b) Ta, S.; Ghosh, M.; Ghosh, K.; Brandão, P.; Félix, V.; Hira, S. K.; Manna, P. P.; Das, D. *ACS Appl. Bio Mater.* **2019**, 2, 2802-2811.
33. Maurya, M. R.; Tomar, R.; Avecilla, F.; Ribeiro, N.; Carvalho, M. F. N. N.; Kuznetsov, M. L.; Correia, I.; Pessoa, J. C. *Dalton Trans.*, **2020**, 49(8), 2589-2609.
34. Pessoa, J. C.; Etcheverry, S.; Gambino, D. *Coord. Chem. Rev.* **2015**, 301-302, 24-48.
35. (a) Reytman, L.; Braitbard, O.; Hochman, J.; Tshuva, E. Y. *Inorg. Chem.*, **2016**, 55, 610-618. (b) Pessoa, J.C.; Correia, I. *Inorganics* **2021**, 9, 17. c) Ribeiro, N.; Bulut, I.; Cevatemre, B.; Teixeira, C.; Yildizhan Y.; André V.; Adão, P.; Pessoa, J. C.; Acilan, C.; Correia, I. *Dalton Trans.*, **2021**, 50, 157.
36. Eady, R. R. *Coord. Chem. Rev.* **2003**, 237, 23-30.
37. Butler, A.; Walker, J. V. *Chem. Rev.* **1993**, 93, 1937-1944.
38. (a) Hoshino Y.; Yamamoto, H. *J. Am. Chem. Soc.* **2000**, 122(42), 10452-10453. (b) Pesiri, D. R.; Morita, D. K.; Walker, T.; Tumas, W. *Organometallics* **1999**, 18, 4916-4924.
39. Chasteen, N. D. **1983**, 53, 105-138.
40. Thompson, K. H.; Orvig, C. J. *Inorg. Biochem.* **2006**, 100(12), 1925-1935.
41. Su, X.; Aprahamian, I. *Chem. Soc. Rev.* **2014**, 43, 1963-1981.
42. Kalinowski, D. S., Sharpe, P. C.; Bernhardt, P. V.; Richardson, D. R. *J. Med.*

- Chem.* **2008**, *51*, *2*, 331–344.
43. (a) Bouzayani, N.; Marque, S.; Djelassi, B.; Kacem, Y.; Marrot, J.; Ben Hassine, B. *New J.Chem.* **2018**, *42*(8), 6389–6398. (b) De, P.; Baltas, M.; Bedos-Belval, F. *Curr Med Chem.* **2011**, *18*(11), 1672–1703.
44. (a) Kalinowski, D. S., Sharpe, P. C.; Bernhardt, P. V.; Richardson, D. R. *J. Med. Chem.* **2008**, *51*, *2*, 331–344. (b) Bouzayani, N.; Marque, S.; Djelassi, B.; Kacem, Y.; Marrot, J.; Ben Hassine, B. *New J.Chem.* **2018**, *42*(8), 6389–6398. (c) De, P.; Baltas, M.; Bedos-Belval, F. *Curr Med Chem.* **2011**, *18*(11), 1672–1703.
45. Mukiza, J.; Habarurema, G.; Gerber, T. I. A.; Hosten, E.; Betz, R.; Umumararungu, T. *Polyhedron.* **2020**, *175*, 114192.
46. Joseph, B.; Kurup, M. R. P. **2014**, <http://dyuthi.cusat.ac.in/purl/4944>.
47. Szklarzewicz, J.; Jurowska, A.; Hodorowicz, M.; Gryboś, R.; Kruczała, K.; Głuch-Lutwin, M.; Kazek, G. *J Coord Chem.* **2020**, *73*, 986–1008.
48. Levina, A.; Pires Vieira, A.; Wijetunga, A.; Kaur, R.; Koehn, J. T.; Crans, D. C.; Lay, P. A. *Angew. Chem.* **2020**, *59*(37), 15834–15838.
49. (a) Mondal, A.; Sarkar S.; Chopra, D.; Guru Row, T. N.; Pramanik, K.; Rajak, K. K. *Inorg. Chem.* **2005**, *44*, 703–708.
50. Dinda, R.; Sengupta, P.; Sutradhar, M.; Mak, T. C. W.; Ghosh, S. *Inorg. Chem.* **2008**, *47*(13), 5634–5640. (c) Mondal, S.; Ghosh, P.; Chakravorty, A. *Inorg. Chem.* **1997**, *36*(1), 59–63.
51. Albino, A.; Benci, S.; Tesi, L.; Atzori, M.; Torre, R.; Sanvito, S., Sessoli, R.; Lunghi, A. *Bits. Inorg. Chem.* **2019**, *58*(15), 10260–10268.
52. (a) Maurya, M. R. *Coord. Chem. Rev.* **2019**, *383*, 43–81. (b) Dutta, S. K.; Samanta, S.; Kumar, S. B.; Han, O. H.; Burckel, P.; Pinkerton A. A.; and Chaudhury, M. *Inorg. Chem.* **1999**, *38*, 1982–1988. (c) Mondal, B.; Ghosh, T.; Sutradhar, M.; Mukherjee, G.; Drew, M. G. B.; Ghosh, T. *Polyhedron* **2008**, *27*(9-10), 2193–2201.
53. (a) Majumder, M.; Rajak, K. K. *Polyhedron* **2019**, *176*, 114241. (b) Chakravarty, J.; Dutta, S.; Chandra, S. K.; Basu, P.; Chakravorty, A. *Inorg. Chem.* **1993**, *32*(20), 4249–4255.

54. Dutta, S. K.; Kumar, S. B.; Bhattacharyya, S.; Tiekink, E. R. T.; Chaudhury, M. *Inorg. Chem.* **1997**, *36*, 4954-4960
55. Patra, R.; Mondal, S.; Sinha, D.; Rajak, K. K. *ACS Omega* **2022**, *7*, 14 11710-11721.
56. Mahroof-Tahir, M.; Keramidas, A. D.; Goldfarb, R. B.; Anderson, O. P.; Miller, M. M.; Crans, D. C. *Inorg. Chem.* **1997**, *36*, 1657-1668.
57. (a) Salonen, P.; Peuronen, A.; Lehtonen, A. *Inorg. Chem. Commun.* **2017**, *86*, 165-167. (b) Banu, K. S.; Chattopadhyay, T.; Banerjee, A.; Bhattacharya, S.; Suresh, E.; Nethaji, M.; Zangrando, E., Das, D. *Inorg. Chem.* **2008**, *47*, 16, 7083-7093. (c) Dey, S. K.; Mukherjee A. *Coord. Chem. Rev.* **2016**, *310*, 80-115.
58. (a) Rath, S. P.; Rajak, K. K.; Chakravorty, A. *Inorg. Chem.* **1999**, *38*, 4376-4377. (b) Salonen, P.; Savela, R.; Peuronen, A.; Lehtonen, A. *Dalton Trans.* **2021**, *50*, 6088.
59. Maurya, M. R.; Sarkar, B.; Avecilla, F.; Correia, I. *Eur. J. Inorg. Chem.* **2016**, 2016, 4028-4044.
60. Bendia, S.; Benabid, W.; Bourzami, R.; Ouari, K. *J. Mol. Struct.* **2023**, *1281*, 135131
61. Hirao, T. *Chem. Rev.* **1997**, *97*, 2707 -2724.
62. SMART; SAINT; SADABS; XPREP; SHELXTL, Bruker AXS Inc., Madison, WI, **1998**.
63. Sheldrick, G. M. *SHELXTL, v. 6.14*, Bruker AXS Inc., Madison, WI, **2003**.
64. Johnson, C. K. ORTEP Report ORNL-5138, Oak Ridge National Laboratory, Oak Ridge, TN, **1976**.
65. Stoll, S.; Schweiger, A.; *J. Magn. Reson.* **2006**, *178(1)*, 42-55.
66. Frisch, M. J.; Trucks, G. W.; Schlegel, H. B.; Scuseria, G. E.; Robb, M. A.; Cheeseman, J. R.; Scalmani, G.; Barone, V.; Mennucci, B.; Petersson, G. A.; Nakatsuji, H.; Caricato, M.; Li, X.; Hratchian, H. P.; Izmaylov, A. F.; Bloino, J.; Zheng, G.; Sonnenberg, J. L.; Hada, M.; Ehara, M.; Toyota, K.; Fukuda, R.; Hasegawa, J.; Ishida, M.; Nakajima, T.; Honda, Y.; Kitao, O.; Nakai, H.; Vreven, T.; Montgomery Jr., J. A.; Peralta, J. E.; Ogliaro, F.;

- Bearpark, M.; Heyd, J. J.; Brothers, E.; Kudin, K. N.; Staroverov, V. N.; Kobayashi, R.; Normand, J.; Raghavachari, K.; Rendell, A.; Burant, J. C.; Iyengar, S. S.; Tomasi, J.; Cossi, M.; Rega, N.; Millam, J. M.; Klene, M.; Knox, J. E.; Cross, J. B.; Bakken, V.; Adamo, C.; Jaramillo, J.; Gomperts, R.; Stratmann, R. E.; Yazyev, O.; Austin, A. J.; Cammi, R.; Pomelli, C.; Ochterski, J. W.; Martin, R. L.; Morokuma, K.; Zakrzewski, V. G.; Voth, G. A.; Salvador, P.; Dannenberg, J. J.; Dapprich, S.; Daniels, A. D.; Farkas, Ö.; Foresman, J. B.; Ortiz, J. V.; Cioslowski, J.; Fox, D. J. *Gaussian 09, (Revision A.1)*, Gaussian, Inc., Wallingford, CT, **2009**.
67. Runge, E.; Gross, E. K. U. *Phys. Rev. Lett.* **1984**, *52*, 997-1000.
68. (a) Becke, A. D. *J. Chem. Phys.*, **1993**, *98*, 5648-5652.
(b) Lee, C.; Yang, W.; Parr, R. G. *Phys. Rev. B.*, **1988**, *37*, 785-789.
69. (a) Hay, P. J.; W. R. Wadt, *J. Chem. Phys.*, **1985**, *82*, 270-283.
(b) Hay, P. J.; Wadt, W. R. *J. Chem. Phys.*, **1985**, *82*, 299-310.
70. Gao, X.; Wang, Y.; Wang, Y.; Jia, J.; Su, X. *Sci. Sin. Chim.* **2011**, *41*, 1145-1155.



Chapter II

Di and Mono nuclear Vanadium (V) complexes: Solvent dependent structural versatility, electro syntheses of mixed-valence oxovanadium (IV/V) entities in solution and catecholase activity

*Di and Mono nuclear Vanadium(V) complexes: Solvent dependent structural versatility, electro syntheses of mixed-valence oxovanadium(IV/V) entities in solution and catecholase activity**

Abstract

Two mononuclear oxovanadium(V) complexes of the form $[V^VO(L^1)(OMe)(MeOH)]$ (**1**), $[V^VO(L^2)(OMe)(MeOH)]$ (**2**), two $[V_2O_3]^{4+}$ core of μ -

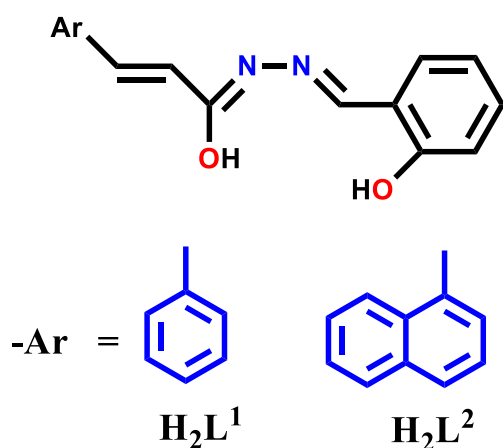


Chart II.1

oxidodioxidovanadium(V)

complexes $(L^1)(O)V^V-O-V^V(O)(L^1)$ (**3**)

and $(L^2)(O)V^V-O-V^V(O)(L^2)$ (**4**) and

two complexes $[V^VO(L^1)(8-Hq)]$ (**5**) and

$[V^VO(L^2)(8-Hq)]$ (**6**) incorporating 8-

hydroxyquinoline (8-hq) as co-ligand

have been synthesised with Schiff base

ligands H₂L¹ or H₂L² with $VO(acac)_2$.

The transition from methanol to

acetonitrile as the solvent results in the

formation of the μ -

oxidodioxidovanadium complexes. The X-ray study revealed octahedral

geometry for the mononuclear complexes **1**, **2**, and **5**, but penta-coordinated

square-pyramidal geometry around metal atoms for the oxido-bridged dinuclear

complexes **3** and **4**. Two mixed-valence species ($V^{IV}OV^V$) of type II, **3a** and **4a**, as

indicated by the 13 line Frozen solution EPR spectra and are being generated

upon constant potential electrolysis (CPE) of **3** and **4** respectively. Various

physio-chemical approaches were used to characterise every component.

Following the oxidation of 3, 5-di-tert-butyl catechol (3, 5-DTBC) to 3, 5-di-tert-

butyl benzoquinone (3, 5-DTBQ), the oxidomethoxido complexes **1** and **2** were

used to examine the catechol oxidase mimicking activity.

*This has been published *ACS Omega* **2022**, 7, 14, 11710–11721

Introduction

Researchers frequently choose nitrogen-oxygen donor ligands with hydrazone moieties due to their simple production, easily tunable electrical characteristics, conformational variety¹, and broad biological applicability². Depending on variables such as the oxidation state of the metal ions, reaction circumstances, the nature of the substituents on the hydrazone skeleton, and tautomerization, these types of ligands are crucial in defining the overall charge of the metal complexes and, consequently, their stability³. In addition, the literature discloses oxidovanadium complexes of salicylaldehyde and salicylaldehyde-hydrazone as prospective anti-cancer drugs⁴ for treating brain cancer as well as 8-hydroxyquinoline vanadium complexes as anti-tuberculosis and anti-proliferative metallodrugs⁵. Furthermore, it is worthwhile⁶ to consider the significance of monooxido-bridged binuclear vanadium (V/V) species of the type $(V^V OL)_2 O$, which are likely to serve as precursors of mixed-valence V(IV, V) species. The rich coordination chemistry of mixed-valence vanadium⁷ integrating acyl hydrazone^{7c} ligands is evident in the context of odd electron behaviour in solid and solution in different biological processes. The chemistry of type II mixed-valence oxidovanadium (IV/V) species and their precursors is being addressed here. Six vanadium complexes, $[VO(L^{1-2})(OMe)(MeOH)]$ (**1**, **2**), $[V^V_2O_3(L^{1-2})_2]$ (**3**, **4**), $[V^VO(L^{1-2})(8-Hq)]$ (**5**, **6**), illustrated in **Chart II.1**. With the aid of several physio-chemical procedures, all substances were identified. Solid-state structures of the complexes **1** – **5** verified using a single crystal X-ray diffraction method. Cyclic voltammetry was used to analyse the complexes redox sites. Electro-generation of the reduced species was monitored by spectro-electrochemical measurements and theoretically supported by density functional theory (DFT) calculations. Many model first transition metal complexes, including vanadium, have been the subject of extensive studies on catecholase activity.⁸ It is noteworthy that the synthesised small molecules mimic enzyme like cores and their mode of binding with the substrate is extremely significant. In this regard, we studied the ability of these complexes to catalyse the oxidation of catechol to quinone using a well-known model substrate, 3,5-di-tert-

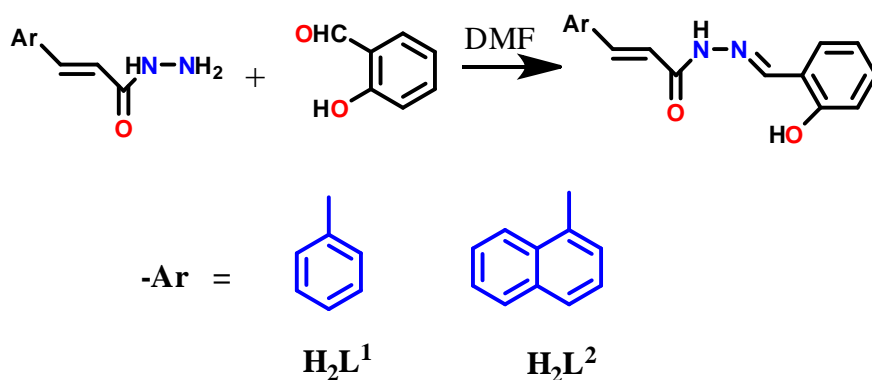
butylcatechol, in order to identify them as functional templates for catechol oxidase. Surprisingly not, the complexes **5** and **6** were inactive, whilst complexes **1** and **2** were active oxidant and their reactivities are similar to their corresponding dimer **3** and **4**.

II.1 RESULTS AND DISCUSSION

A. SYNTHESIS

i) LIGAND

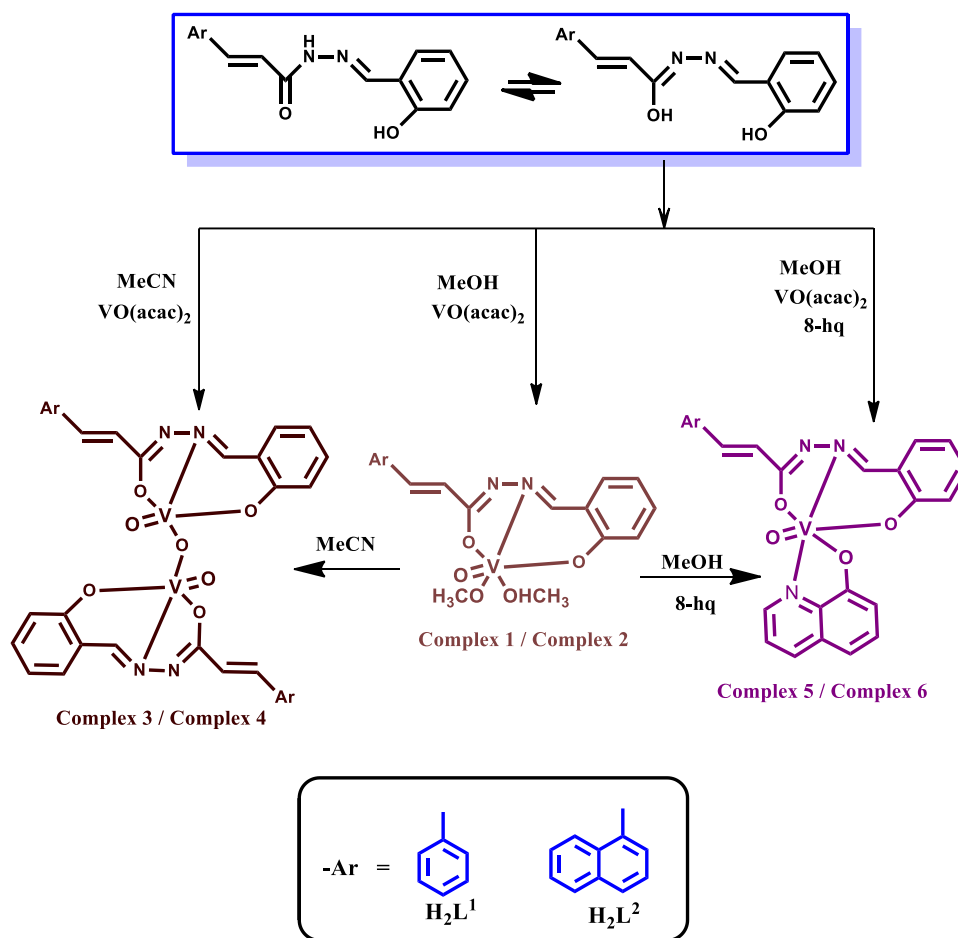
The tridentate hydrazone ligand H_2L^{1-2} has been used in the present work (**Scheme II.1.**) and it was synthesized by reacting salicylaldehyde and aroyl hydrazine in a ratio of 1:1 in *N,N*-dimethyl formamide.



Scheme II.1. Schematic representation for the synthesis of the ligands

ii) COMPLEX

At room temperature, stoichiometric reactions between a methanolic solution of H_2L^{1-2} and $\text{VO}(\text{acac})_2$ produced complexes **1** and **2** in good yields. In acetonitrile medium, we obtained dinuclear species **3** and **4**. A noteworthy finding is that complexes **1** and **2** slowly evaporated in acetonitrile solvent, forming solitary crystals of the same dinuclear complexes. In the presence of 8-hydroxyquinoline as a co-ligand in methanol, complexes **5** and **6** were produced. In **Scheme II.2.** the specifics of the synthetic methods are depicted. Constant potential electrolysis (CPE) of complexes **3** and **4** at 298 K resulted in the synthesis of dinuclear type II mixed-valence ($V^{IV}V^V$) species, i.e. complexes **3a** and **4a**.



Scheme II.2. Schematic representation for the synthesis of the complexes

B. CRYSTAL STRUCTURES

H₂L¹: Single-crystal X-ray diffractometric experiment was used to identify the molecular structure of H₂L¹. The ligand crystallized in the non-centrosymmetric orthorhombic space group Pna21. The geometry was nearly planar based on the dihedral angles O1–C1–C2–C3, C1–N1–N2–C10, O1–C1–N1–N2 as 3.1(4)°, 179.5(2)°, 2.8(4)° respectively. **Table II.1** lists the chosen bond lengths and angles for the crystal, and **Figure II.1.** displays the molecular perspective. The closed packed crystal structure of two separate units were stabilized by a number of non-covalent interactions. Inter-molecular hydrogen bonding interactions [O1···H–C10 (2.515 Å), O1···H–C16 (2.513 Å)] between acyl oxygen with imine hydrogen and aromatic hydrogen respectively and hydrogen bonding interaction [O2···H–N1 (2.126 Å)] due to the presence of the hydrazine

functionality maintain the supramolecular arrangement. The core structure was again strengthened by $\text{CH}\cdots\pi$ (3.823 Å) and pseudo $\pi\cdots\pi$ interactions (5.200 Å). Additionally, intra-molecular hydrogen bonding interaction [$\text{O2-H}\cdots\text{N2}$ (1.890Å)] between phenolic hydrogen and imine nitrogen determine the structure to be in the most stable E configuration around $\text{C}=\text{N}$ in the solid-state. (Figure II.2. (a) and Figure II.2. (b))

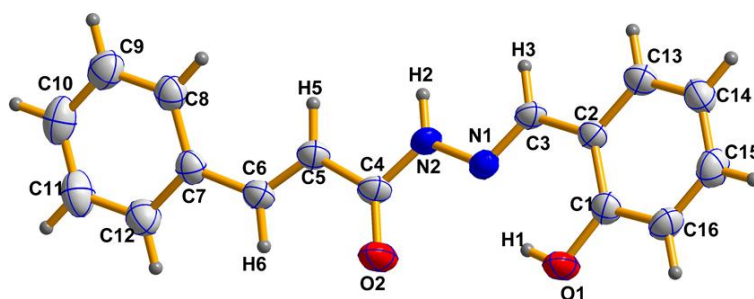


Figure II.1. Perspective view of H_2L^1

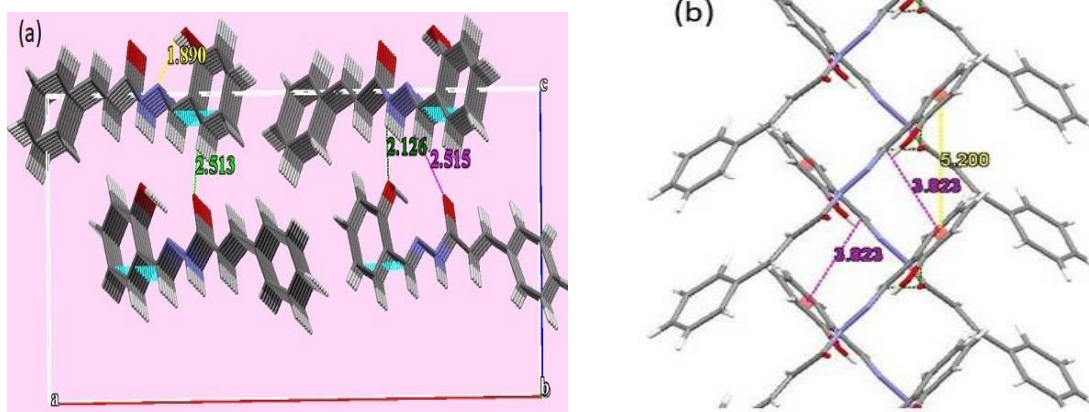


Figure II.2. (a) Depth que view of H_2L^1 along b -axis showed H bonding interaction only. (b) Illustration of supramolecular interactions stabilizing the 2D framework

Table II.1. Selected bond lengths (Å) and bond angles (°) for H₂L¹

Bond lengths (Å)		Bond Angles(°)	
O1-C1	1.228(4)	C10-N2-N1	116.6(3)
O2-C12	1.373(4)	C1-N1-N2	120.3(3)
N2-C10	1.271(4)	O1-C1-N1	122.6(3)
N2-N1	1.375(3)	O1-C1-C2	124.1(3)
N1-C1	1.356(4)	N1-C1-C2	113.3(3)
C1-C2	1.464(4)	C3-C2-C1	121.3(3)
C2-C3	1.320(4)	C2-C3-C4	127.7(3)
C3-C4	1.462(4)	O2-C12-C11	122.0(3)
		C9-C4-C3	122.4(3)
		C12-C11-C10	122.3(3)

Complex 1 and 2: The complexes **1** and **2** both crystallised in the triclinic crystal system, according to single crystal X-ray diffractometric data, with the P-1 space group adopting a deformed octahedral geometry. (**Figure II.3.**) Charge balance in these complexes depends on the coordination of the solvent molecule (methanol) and the binding of the metal centre via the iminolate anion by giving up the N-H proton (ONO²⁻). Selected bond parameters are given in **Table II.2** and **Table II.3**. This is evident from the bond lengths N2-C4 (1.313(2) Å) and C4 - O2 (1.299 (2) Å). The methoxy group and three donors from the ligand define the equatorial coordination plane of the octahedron. The oxo group and methanol molecule reside in the axial positions with O3-V1-O4 bond angle of 174.5 (7) for complex **1** and 175.37 (6) for complex **2**, forming distorted octahedron. The coordinated methanol and methoxy groups are cis to each other and they exhibit typical short V1-O5 (V1-methoxy) bond distances of 1.771 (15) Å and elongated V1-O4 (V1-methanol) bond of 2.364 (16) Å. The elongation may also occur due to axial placement of methanol with respect to V=O moiety forming the shortest V1-O3 bond 1.583 (17) Å. The other bonds are within their normal ranges⁹⁻¹⁰. The solid state structure of **1** is naturally stabilized through several hydrogen bonding (HB) interactions (V=O/ imine H, phenolic O/Ar-H,

amine N/ OHMe). For complex **2**, in addition to HB interaction (amine N/ OHMe), two $\text{CH}\cdots\pi$ interactions are also present forming a 2D network. (Figure II.4.)

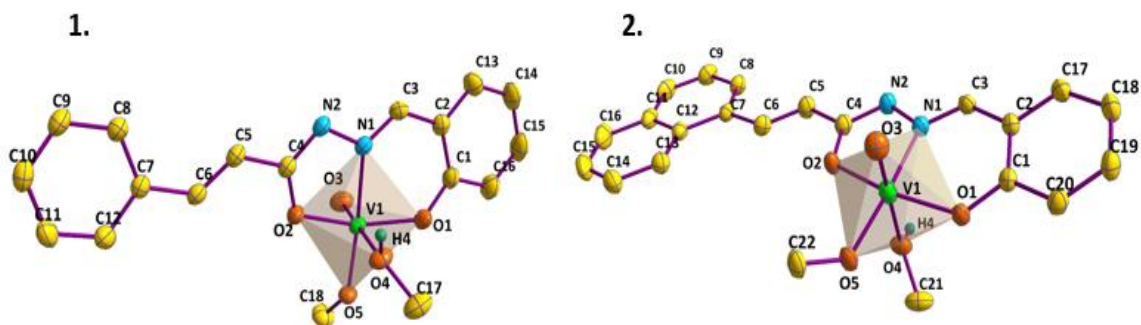


Figure II.3. Perspective view of Complex 1 and 2.

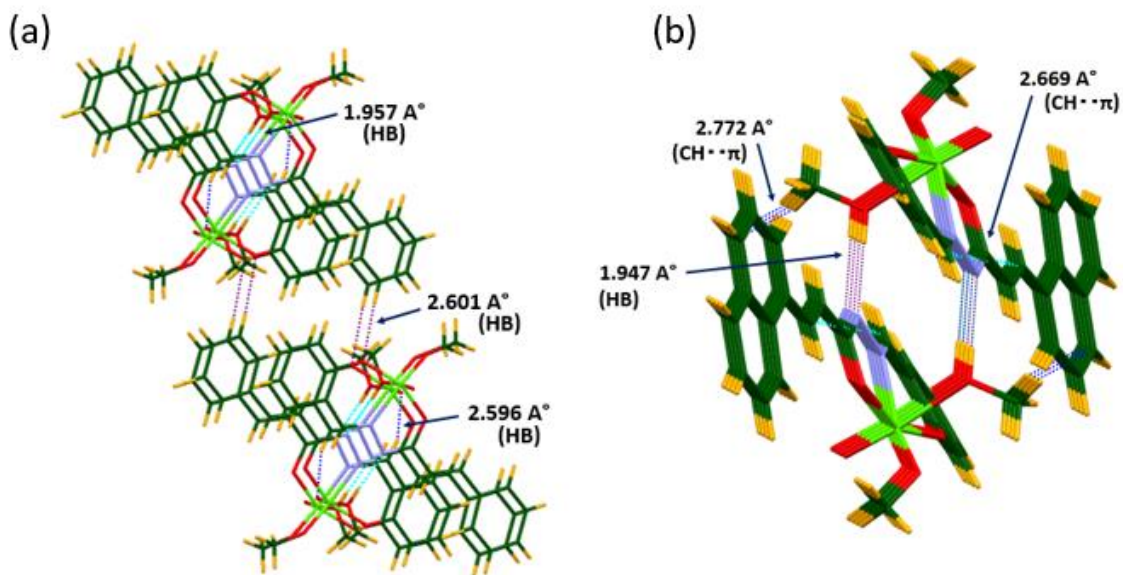


Figure II.4. Supramolecular architecture of complex 1(a), 2(b).

Table II.2. Selected bond lengths (Å) and bond angles (°) for complex 1

Bond Length (Å)		Bond Angle (°)	
V1-O1	1.8536(18)	O1-V1-O2	152.11(8)
V1-O2	1.9546(16)	O1-V1-O3	100.60(10)
V1-O3	1.5826(17)	O1-V1-O4	81.69(8)
V1-O4	2.3642(17)	O1-V1-O5	102.66(7)
V1-O5	1.7715(15)	O1-V1-N1	83.66(7)
V1-N1	2.1275(18)	O2-V1-O3	97.75(8)
O1-C1	1.336(3)	O2-V1-O4	78.36(6)
O2-C4	1.299(2)	O2-V1-O5	93.62(7)
N2-C4	1.306(3)	O2-V1-N1	74.33(7)
N1-C3	1.288(3)	O3-V1-O4	174.50(7)
N1-N2	1.396(2)	O3-V1-O5	102.42(9)
		O3-V1-N1	93.68(8)
		O4-V1-O5	81.83(7)
		O4-V1-N1	81.55(6)
		O5-V1-N1	161.15(7)

Table II.3. Selected bond lengths (Å) and bond angles (°) for complex 2

Bond Length (Å)			Bond angle (°)			
V1	-O1	1.8470(15)	O1	-V1	-O2	152.52(6)
V1	-O2	1.9573(14)	O1	-V1	-O3	100.80(7)
V1	-O3	1.5835(17)	O1	-V1	-O4	81.42(6)
V1	-O4	2.3637(15)	O1	-V1	-O5	105.04(7)
V1	-O5	1.7737(14)	O1	-V1	-N1	84.15(6)
V1	-N1	2.1223(14)	O2	-V1	-O3	97.49(8)
O1	-C1	1.341(2)	O2	-V1	-O4	79.03(6)
O2	-C4	1.299(2)	O2	-V1	-O5	90.67(6)
N1	-N2	1.392(2)	O2	-V1	-N1	74.02(6)
N1	-C3	1.288(2)	O3	-V1	-O4	175.37(6)
N2	-C4	1.312(2)	O3	-V1	-O5	102.52(7)
			O3	-V1	-N1	94.73(7)
			O4	-V1	-O5	80.69(6)
			O4	-V1	-N1	81.41(6)
			O5	-V1	-N1	158.35(6)

Complex 3 and 4: Complex 3 was crystallized in the monoclinic crystal system with the $C2/c$ space group. The asymmetric unit consists of one vanadium atom, V1, one oxo group O3 and one tridentate (ONO^{2-}) Schiff base ligand binding to the vanadium (V) centre. (**Figure II.5.**) The numbering scheme of the symmetry related atoms are n and n_a in complex 3, e.g. V1–O1 and V1_a–O1_a. The basal plane around each vanadium centre is defined with three donors from the

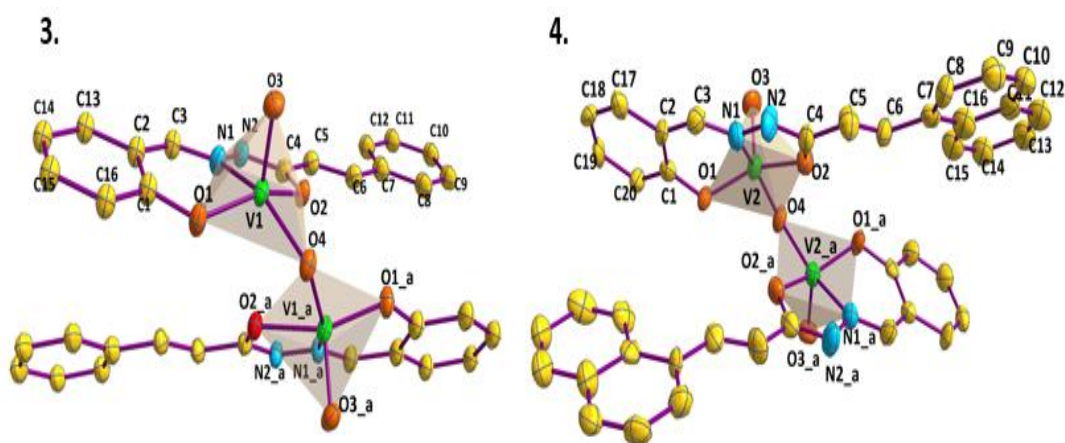


Figure II.5. Perspective view of Complex 3 and 4.

ligand, i.e. phenolic oxygen atom, O1, imine nitrogen atom, N1, and an iminolate oxygen atom, O2 along with the bridging oxygen atom, O4 for both the complexes 3 and 4. The remaining apical position of the square pyramid is occupied by the oxo oxygen O4. The short V1=O3 bond distance in the range $\sim 1.6 \text{ \AA}$ is comparable with other structurally characterized oxidovanadium complexes.⁹ The relative disposition of the two V=O groups in 3 is almost trans with the O3=V1 \cdots V1_a=O3_a torsion angle of 107.733° and V1 \cdots V1_a separation of 2.9728 \AA . However, such a type of symmetry is not observed in the case of 4. Complex 4 crystallized in the orthorhombic crystal system with the $Pbcn$ space group. The asymmetric unit of 4 consists of one vanadium atom, V2, one oxo group O3 along with corresponding tridentate Schiff base ligand. Other molecular arrangements around the vanadium centres and the numbering

scheme are same as that of complex **3**. The relative disposition of the two V=O groups in **4** is almost trans with the O3=V2...V2_a=O3_a torsion angle of 97.21° and V2...V2_a separation 3.077 Å. The τ value is found to be ~0.01 for complex **3** and ~0.07 for **4**, indicating almost ideal square pyramidal geometry around the vanadium (V) centres. In **3**, no such significant supramolecular interactions are present except weak CH... π interaction. (**Figure II.6.**) In contrast, a supramolecular 2D chain is formed in **4** due to the participation of the two V=O groups in HB and CH... π interactions (**Figure II.7.**). Selected bond parameters are given in **Table II.4** and **Table II.5**.

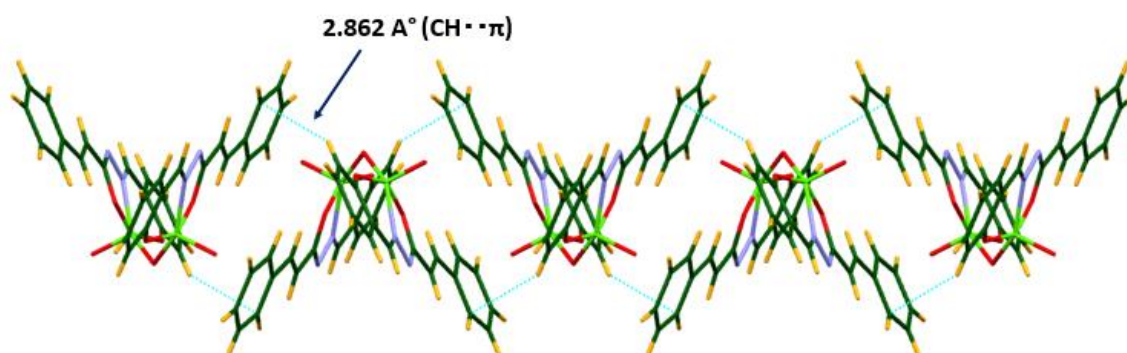


Figure II.6. Supramolecular architecture of complex 3

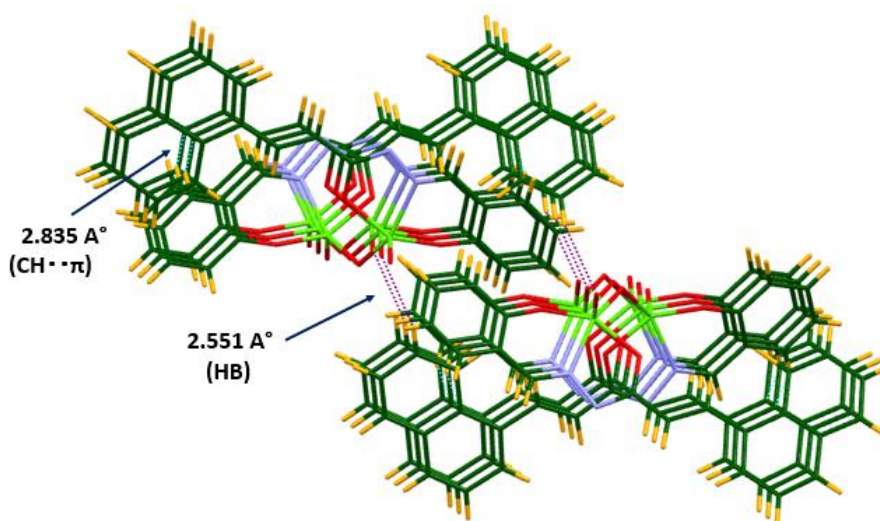


Figure II.7. Supramolecular architecture of complex 4.

Table II.4. Selected bond lengths (Å) and bond angles (°) for complex 3

Bond Length (Å)			Bond angle (°)			
V1	-O1	1.820(4)	O1	-V1	-O2	149.20(16)
V1	-O2	1.949(3)	O1	-V1	-O3	103.43(19)
V1	-O3	1.572(5)	O1	-V1	-O4	104.34(14)
V1	-O4	1.802(3)	O1	-V1	-N1	83.63(15)
V1	-N1	2.094(5)	O2	-V1	-O3	101.31(17)
O1	-C1	1.343(6)	O2	-V1	-O4	84.93(14)
O2	-C4	1.317(6)	O2	-V1	-N1	74.39(14)
N1	-N2	1.389(6)	O3	-V1	-O4	108.00(19)
N1	-C3	1.293(6)	O3	-V1	-N1	99.5(2)
N2	-C4	1.307(6)	O4	-V1	-N1	148.32(17)
			V1	-O1	-C1	135.3(4)
			V1	-O2	-C4	118.1(3)
			V1	-O4	-V1_a	111.2(2)

Table II.5. Selected bond lengths (Å) and bond angles (°) for complex 4

Bond length (Å)			Bond Angle (°)			
V2	-O1	1.806(7)	O1	-V2	-O2	145.8(3)
V2	-O2	1.929(6)	O1	-V2	-O3	104.3(3)
V2	-O3	1.587(6)	O1	-V2	-O4	100.8(2)
V2	-O4	1.800(4)	O1	-V2	-N1	83.0(3)
V2	-N1	2.073(8)	O2	-V2	-O3	104.2(3)
O2	-C4	1.313(11)	O2	-V2	-O4	88.1(3)
N2	-C4	1.314(11)	O2	-V2	-N1	74.6(3)
O1	-C1	1.361(9)	O3	-V2	-O4	107.8(3)
N1	-N2	1.406(9)	O3	-V2	-N1	98.1(3)
N1	-C3	1.306(10)	O4	-V2	-N1	151.7(3)
			V2	-O4	-V2_a	117.5(4)
			V2	-O1	-C1	130.0(5)
			V2	-O2	-C4	118.5(6)

Complex 5: Complex 5 also crystallized in the triclinic crystal system with the P-1 space group. The four coordination sites of the metal, three from the ligand and one from the oxo group, are similar to complex 1 (ONO^{2-}). The remaining two sites are occupied by the oxygen and nitrogen atom from co-ligand (NO^-) 8-hq moiety forming an overall (ONO^{2-} - NO^-) arrangement. The equatorial coordination plane of the octahedron is defined by three donors from the ligand (ONO), and oxygen atom from 8-hq. The oxo group and nitrogen atom of 8-hq lie in the axial positions with O3-V1-N3 bond angle of $175.14(1)^\circ$ and V1-N3 bond length ($2.3521(2) \text{ \AA}$) being the largest. The other bonds are within normal ranges. Self-assembly by three types of HB interactions ($\text{V=O}/ \text{Ar-H}$, $\text{V=O}/ \text{imine H}$, phenolic $\text{O}/ \text{Ar-H}$) links the molecule into a two-dimensional network (**Figure II.8.b**). Considering all the compounds 1, 2, 3, 4, and 5 the overall V-O bond lengths follow the order $\text{V-O (oxido)} < \text{V-O (alkoxido)} < \text{V-O (quinolato)} < \text{V-O (enolato)}$. These data indicate stronger binding of the alkoxido moiety compared to those of quinolato and enolato O atoms. The ortep diagram of the complexes 5 are shown in **Figure II.8a** and crystallographic parameters are given in **Table II.6**.

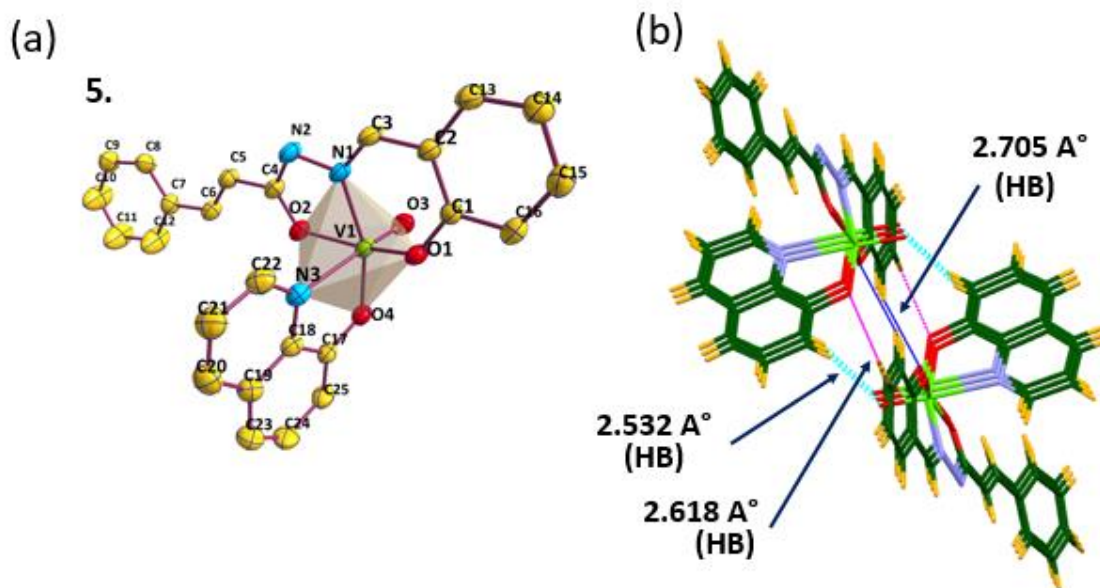


Figure II.8. (a) Perspective view of Complex 5. (b) Supramolecular architecture of complex 5

Table II.6. Selected bond lengths (Å) and bond angles (°) for complex 5

Bond Length (Å)			Bond Angle (°)			
V1	-O1	1.8669(1)	O1	-V1	-O2	152.22(1)
V1	-O2	1.9377(1)	O1	-V1	-O3	100.16(1)
V1	-O3	1.5850(1)	O1	-V1	-O4	102.87(1)
V1	-O4	1.8421(1)	O1	-V1	-N1	84.02(1)
V1	-N1	2.0793(2)	O1	-V1	-N3	82.72(1)
V1	-N3	2.3521(2)	O2	-V1	-O3	100.15(1)
O1	-C1	1.3313(1)	O2	-V1	-O4	92.31(1)
O2	-C4	1.3039(1)	O2	-V1	-N1	74.68(1)
N1	-N2	1.3968(1)	O2	-V1	-N3	78.47(1)
N1	-C3	1.2838(1)	O3	-V1	-O4	99.32(1)
N2	-C4	1.2991(1)	O3	-V1	-N1	97.60(1)
			O3	-V1	-N3	175.14(1)
			O4	-V1	-N1	160.25(1)
			O4	-V1	-N3	76.15(1)
			N1	-V1	-N3	86.57(1)

C. ELECTRONIC SPECTRA

The ligand HL² exhibited two peaks at 336 nm and 308 nm. The absorption bands of shortest wavelength appearing at 308 nm might be attributed to intra-

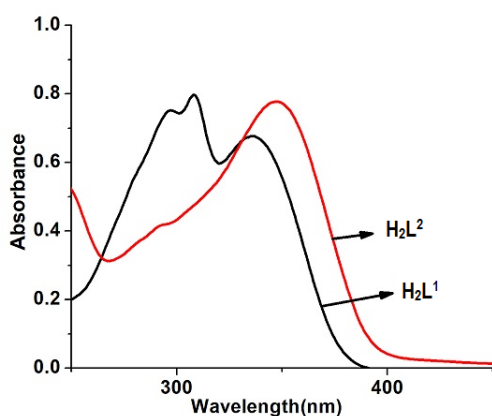


Figure II.9. Absorption spectra of the ligands in methanol

ligand $\pi \rightarrow \pi^*$ transition and the band at 336 nm were most probably due to $n \rightarrow \pi^*$ electronic transitions of imine and carbonyl groups. HL² showed only one peak at 348 nm. (**Figure II.9.**)

The UV-vis absorption spectra of complexes (1-6) were recorded in CH₂Cl₂ at 298 K by employing concentrations in the range ~20 μ M and they are being illustrated in **Figure II.10**. In the UV-vis spectra, the complexes followed a particular pattern with respect to their structural motif. Here observed three distinct sets of absorption spectra in general. The monoxido mononuclear vanadium (V) complexes **1**, **2** and monoxido bridged-di-vanadium (V, V)

complexes **3**, **4** were nearly identical in appearance. The first set, complexes **1** and **3**, showed closely spaced twin humps ~ 305 nm and 335 nm. For the oxidovanadium (V) complexes no d-d bands are expected. These low energy twin humps can be attributed to ligand-centred charge transfer (LCT) bands. With the second set of complexes **2** and **4**, the presence of naphthyllic conjugation induces a significant red shift of twin humps (LCT band) to single bands at around 344 nm and 351 nm respectively.

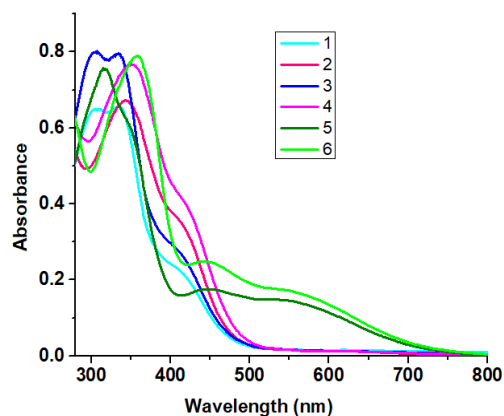


Figure II.10. Absorption spectra of all the complexes in CH_2Cl_2 at 298K

Moreover, for all the complexes **1** - **4**, a broad shoulder in the range 405 - 416 nm was observed in the spectra. This region can be assigned to set of common LMCT bands. The third set of spectra, in the case of intense violet complexes **5** and **6**, is distinctly different in peak pattern and position. The additional π -conjugated NO^- donor unit of 8-hq (8-hq as co-ligand) induces a significant bathochromic shift of the LMCT absorption band at ~ 445 nm and 546 nm respectively along with a relatively intense peak at 316 nm and 359 nm. A careful look into the spectra of **5** and **6** reveals the presence of three distinct

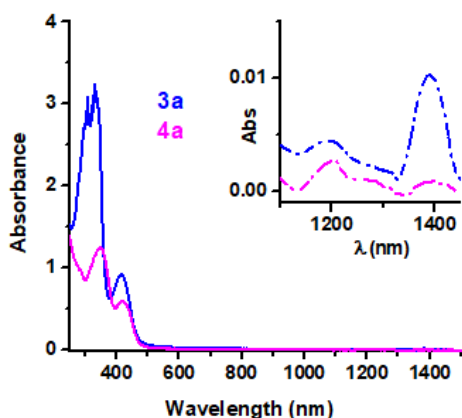


Figure II.11. Absorption spectra of **3a** and **4a** in CH_2Cl_2

absorption channels in the molecules which is aptly supported by its coordination environment. Relevant absorption parameters are given in **Table II.7.**

For Complexes, **3a** and **4a** a characteristic feature of the $[\text{V}_2\text{O}_3]^{3+}$ is also observed in the near-IR region between 1200 - 1500 nm.

It is indicative of intra-valence charge transition (IVCT) between mixed valence vanadium nuclei.⁶ (**Figure II.11.**)

Table II.7. Absorption parameters of all the compounds.

Compound	$\lambda_{\max}(\text{nm})[\epsilon(\text{M}^{-1}\text{cm}^{-1})]$
H₂L¹	335 (33500), 308 (39000)
H₂L²	348 (38881)
1	305 (32500), 336 (33000)
2	344 (33650), 410 (17450)
3	306 (4000), 334 (39500), 408 (13850)
4	351 (38400), 423 (19250)
5	316 (37750), 546 (7300), 446 (8800)
6	342 (39000), 550 (8400), 448 (12450)

D. REDOX PROPERTIES

The redox activities of **1** - **6** were investigated by cyclic voltammetry in CH₂Cl₂ using [N(n-Bu)₄]PF₆ as supporting electrolyte at 298 K. The cyclic voltammograms with the redox potential data referenced to ferrocinium/ferrocene (Fc⁺/Fc) redox couple is illustrated in **Figure II.12**. All the experiments were performed in the nitrogen atmosphere. The cyclic voltammograms of all the mononuclear vanadium complexes (**1**, **2**, **5** and **6**) displayed reversible cathodic waves in the range -0.08 to -0.56 V assigned to V^V/V^{IV} reduction couple. The nature of the graph authenticated the redox non-innocent role of the ligand framework towards the coordination of the metal centre. Complex **1** and **2** exhibits reversible cathodic waves at -0.082 and -0.15 V respectively due to the V^{VO}/V^{IVO} redox couple as shown in **Figures II.12 (a)** and **(b)**. The redox activity of **5** and **6** are quite similar to those of **1** and **2** as depicted in **Figures II.12 (e)** and **(f)** respectively. The cyclic voltammograms of **5** and **6** displayed the cathodic waves at - 0.55 and - 0.56 V respectively due to

V^{VO}/V^{IVO} redox couple. The introduction of NO⁻ donor aromatic co-ligand, for complexes **5** and **6**, causes vanadium (V) centre less susceptible to reduction in comparison to complexes **1** and **2**. Hence, a higher potential is utilized to reduce the metal centre. The redox activities of **3** and **4** are notably different from those of **1**, **2**, **5** and **6**. Complex **3** exhibits two reversible cathodic waves [Figure II.12 (c)] due to the presence of V^{VOVV}/V^{IVOVV} and V^{IVOVV}/V^{IVOVIV} redox couples at -0.20 and -1.25 V respectively. Similarly, **4** also shows the similar redox properties as **3** depicted in Figure II.12 (d), two reversible cathodic waves arises at -0.25 and -1.30 V. The very slight increment of the reduction potential values in complex **4** over complex **3** can be rationalised by the presence of extra π conjugation of naphthalene ring in otherwise similar structural motifs.

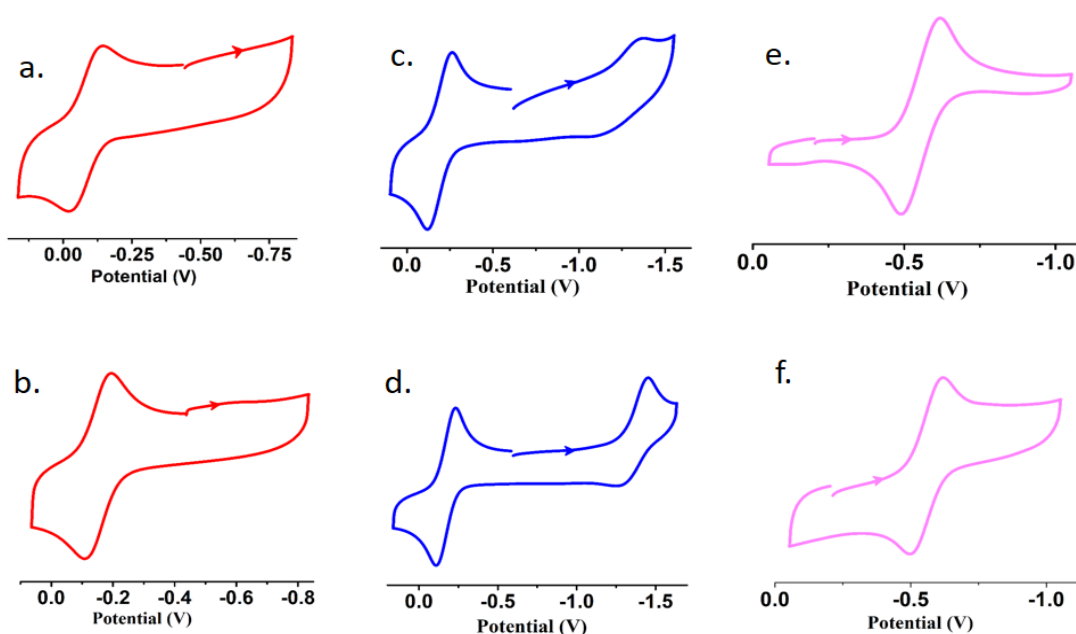


Figure II.12. Cyclic voltammograms of (a) **1**, (b) **2**, (c) **3**, (d) **4**, (e) **5** and (f) **6** in CH₂Cl₂ at 298 K. Conditions: scan rate, 100 mV s⁻¹; 0.20 M [N(n-Bu)₄]PF₆ supporting electrolyte; platinum working electrode.

E. SPECTROELECTROCHEMISTRY

To evaluate spectroscopic signatures of the reduced species in monomeric complexes **1**, **2**, **5**, **6** we have conducted spectro-electrochemical experiments in the CH₂Cl₂/0.3 M [N(n-Bu)₄]PF₆ system. In the case of the monomeric

monooxido (ONO^{2-}) complex **1**, the reduction under constant potential conditions resulted in an intensity decrease of the high-energy twin humps at 305 and 336 nm and the formation of a distinct peak with increased intensity at 406 nm. Isobestic crossover points at 386 nm and 450 nm further proved the transformation of reduced species through a common intermediate [Figure II.13 (a)]. For complex **2**, the UV-vis spectral transformations during reduction look similar to those observed in complex **1**. The intensity of the higher energy band at 344 nm decreased gradually and that at 410 nm increased gradually to form a distinct peak [Figure II.13 (b)]. Moreover, two almost similar isobestic points at 390 nm and 450 nm confirmed the structural and electrochemical uniformity of complexes **1** and **2**.

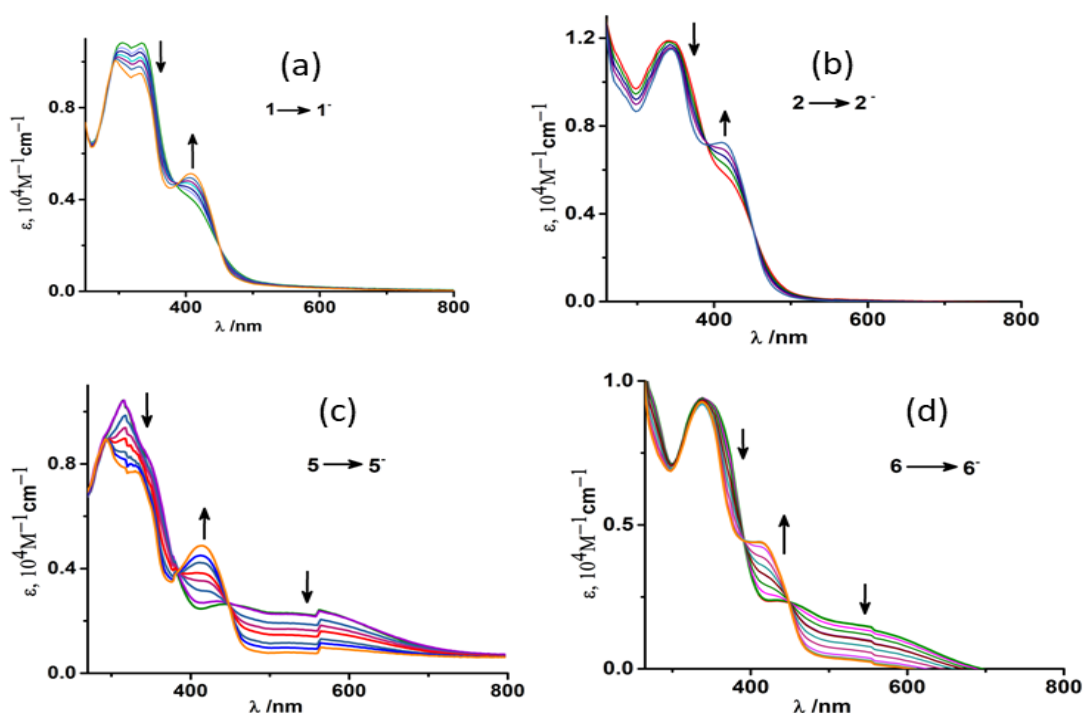


Figure II.13. Change of absorption spectra during (a) $1 \rightarrow 1^-$ and (b) $2 \rightarrow 2^-$ (c) $5 \rightarrow 5^-$ (d) $6 \rightarrow 6^-$ conversions in CH_2Cl_2 achieved by constant potential spectroelectrochemical measurements at 298 K

The single-electron reduction for complex **5** resulted in a decrease in the intensities of 316 and 546 nm bands and the formation of a new band at 414 nm [Figure II.13 (c)] with the appearance of two isobestic points at 384 nm and 446

nm respectively. As expected, the electrochemical reduction of complex 6 resulted in a decrease in the intensity of two bands at 342 and 550 nm [Figure II.13 (d)]. A closer look at the spectral features of all the reduced species unveils that all the complexes undergo a reduction process through common pathways (isobestic points ~385 and ~450 nm). Thus, spectroscopic signatures of all reduced species are characterized by spectroelectrochemical experiments.

F. EPR STUDY

All the six complexes were found to be EPR silent hence diamagnetic in nature.

The electro-reduced species were found to be paramagnetic. The EPR spectra of all the species were recorded in CH₂Cl₂ solution at ambient temperature. The EPR spectrum of all the electro-generated mononuclear anionic complexes exhibited eight line spectrum due to $S = 1/2$ and hyperfine coupling of ⁵¹V ($I=7/2$).

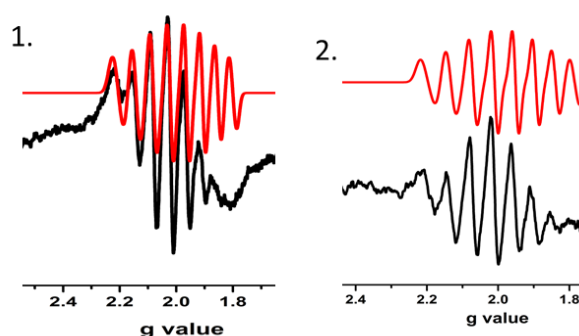


Figure II.14. X-band EPR spectra of $[V_2O_3L^{1-2}]^{3+}$, (1) **3a**, (2) **4a** in CH₂Cl₂ at 298 K (black, experimental; red, simulated)

Spectra were compatible with octahedral coordination sphere of vanadium (IV) complexes. This change of diamagnetic $[V^VO]^{2+}$ to paramagnetic $[V^{IV}O]^{2+}$ is also supported by spin density data from DFT calculations.

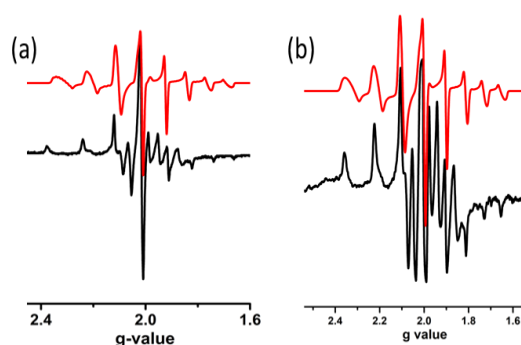


Figure II.15. X-band EPR spectra of $[V_2O_3L^{1-2}]^{3+}$, (a) **3a**, (b) **4a** in frozen solution at 77 K (black-experimental; red-simulated)

Electrochemically generated mixed-valence $[V^V V^{IV}O_2(L)_2]^{-\mu-O}$ species (**3a** and **4a**) were paramagnetic. For divanadium (IV,V) complexes, 15-hyperfine profile on the EPR time scale suggest a type II or III character according to Robin and Day

classification. Type III, when the unpaired electron is uniformly delocalized over both of the vanadium centers and type II when the electron is partially delocalized, i.e. weakly interacting. An 8-line pattern, suggests a valence-trapped situation for the odd electron (type I). The EPR spectra of solid solution of **3a** and **4a** consist of eight lines pattern at room temperature (**Figure II.14, Table II.8**). In contrast, the frozen glass solution of the same showed 13 lines at 77K (**Figure II.15, Table II.9**). The absence of 15 line patterns in case of **3a** and **4a** indicate that the complexes are not exactly mixed valance of type III as it requires complete delocalization of electronic spin between the two vanadium nuclei. In this case, from the EPR pattern it can be concluded that the unpaired electron spin is mostly localized above one of the vanadium (IV) center and partially mixed with adjacent vanadium nuclei, thus defined by the $[\{V^{VO}(L)\}\{V^{IV}O(L)\}-\mu-O] \leftrightarrow [\{V^{IV}O(L)\}\{V^{VO}(L)\}-\mu-O]$. This type of anisotropic distribution of unpaired electron spin in the EPR spectra reveals that **3a** and **4a** are type II mixed valance complexes.

*Table II.8. X-band EPR Spectral parameter of complexes **3a** and **4a** at room temperature*

Complex	Matrix	g_{\parallel}	g_{\perp}	g_{av}	A_{\parallel} (G)	A_{\perp} (G)	A_{av} (G)	lw (mT)
3a	CH ₂ Cl ₂ , 77 K	1.978	1.947	1.957	141.78	75.87	97.84	1.35
4a	CH ₂ Cl ₂ , 77 K	1.965	1.925	1.938	153.85	64.23	94.10	1.8

*Table II.9. X-band EPR Spectral parameter of complexes **3a** and **4a** at 77 K.*

Complex	Matrix	g_{\parallel}	g_{\perp}	g_{av}	A_{\parallel} (G)	A_{\perp} (G)	A_{av} (G)	lw (mT)
3a	CH ₂ Cl ₂ , 77 K	1.978	1.947	1.957	141.78	75.87	97.84	1.35
4a	CH ₂ Cl ₂ , 77 K	1.965	1.925	1.938	153.85	64.23	94.10	1.8

G. DFT STUDY

To elucidate spectroscopic and redox properties of the monomeric complexes **1**, **2**, **5**, and **6** as well as dimers **3** and **4**, we have conducted DFT calculations of all the target complexes. First, occupied frontier orbitals are indicative of the spin free d^0 configuration of the vanadium centres. In particular, in the case of monomeric complexes **1**, **2**, **5**, and **6**, the HOMO is largely ligand centric whereas the LUMO is admixture of metal and ligand contribution (**Figure II.16**). Again, for these monomeric complexes, on reduction spin polarization was observed from mainly oxido ligand to vanadium centre (**Figure II.18**). It confirms that the first reduction is metal-centered with no significant participation of ligand moiety supported by EPR spectra of electro-reduced mononuclear complexes.

Second, the lowest unoccupied molecular orbital (LUMO) of the dinuclear compounds $[\{V^{VO}(L^1)\}_2-\mu-O]$ (**3**) and $[\{V^{VO}(L^2)\}_2-\mu-O]$ (**4**) is centred at the V atoms, oxido ligands, and bridging O atom whereas the highest occupied molecular orbital (HOMO) mainly ligand centric (**Figure II.17**). In the singly reduced complex $[V^{VO}(L^1)-O-V^{VO}(L^1)]^-$ **3a**, with the ground state optimized geometries, the spin density is mostly localized at one of the V centre [1.09 e ; **Figure II.18(c)**]. The negative spin density values at the bridging O atom, carbonyl O atom, hydrazine N atom and one of the dioxo ligand (-0.01 to -0.14 e) indicate some spin polarization and delocalization between the metal centre with O and N atoms.

All of these data clearly indicate that reduction affect largely one metal centre which weakly interacts with another vanadium centre and thus lead to the formation of a mixed-valence complex of type II. Overall, the spin density data indicate that the electronic spin is anisotropically distributed over two vanadium centre which is well supported by EPR data showing 8 line in solid solution at room temperature (**Figure II.14**) and 13 line (**Figure II.15**) in frozen glass solution at 77K. (It would be perfect 15 line spectra in case of complete delocalization). Similar phenomena regarding electron spin density is being observed for complex **4a** too.

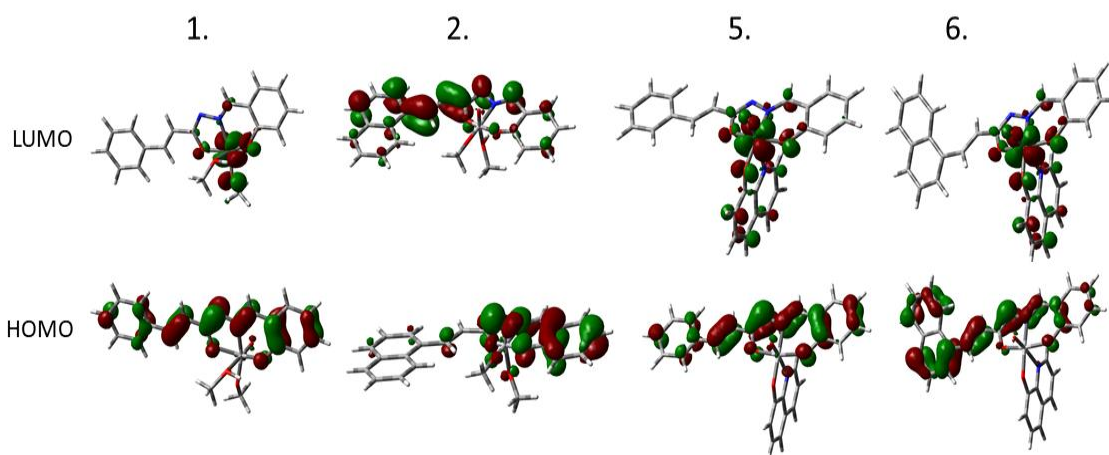


Figure II.16. Isodensity plot of selected frontier orbitals of mononuclear complexes 1, 2, 5 and 6

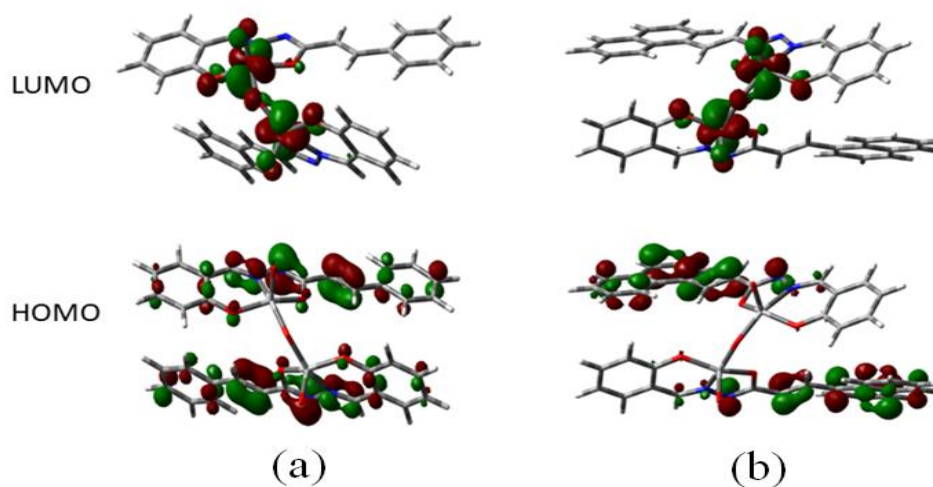


Figure II.17. Isodensity plot of selected frontier orbitals of (a) 3 and (b) 4

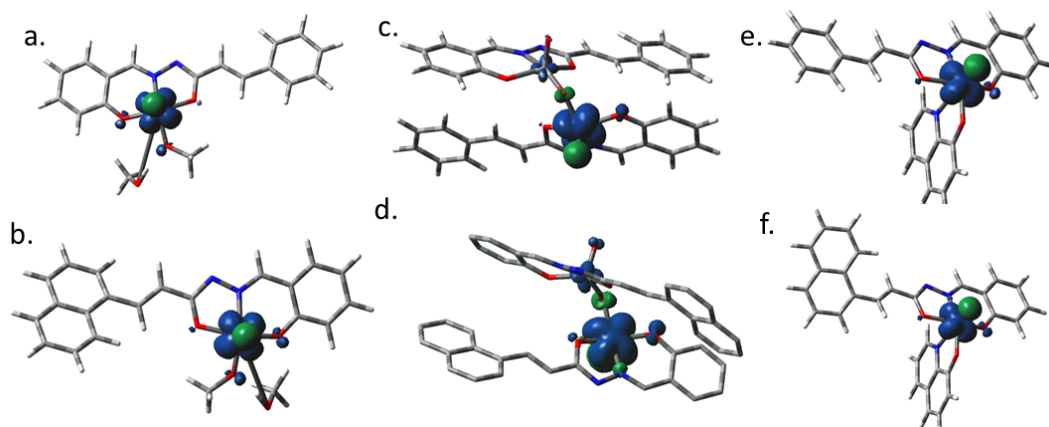


Figure II.18. Spin density plot of (a) 1⁻ (b) 2⁻, (c) 3a, (d) 4a, (e) 5⁻ and (f) 6⁻

H. CATECHOL OXIDATION

Employing 3, 5-di-tert-butyl catechol as the substrate, catecholase activity of all the six complexes has been checked. Complexes **1**, **2** found to be catalytically active with respect to catechol oxidation reaction. Complexes **3** and **4** behaved similarly to their respective monomers i.e. **3** with **1** and **2** with **4**. As expected, the complexes **5** and **6** turned out to be inactive towards the above reaction due to strong ligating environment. The rate of catechol oxidation reaction for **1** and **2** was investigated using time dependent UV-vis absorption spectra in 1:1 CH₃OH and CH₂Cl₂ under atmospheric air. To check the ability of the complexes to oxidize 3,5-DTBC, the reaction was initiated by adding 2×10^{-4} M solutions of **1** and **2** with 0.01 M of 3,5-DTBC at 25 °C. The immediate spectral run exhibited two peaks around ~596 nm and ~415 nm. The low energy broad band appearing at 596 nm (for **1**) and 598 nm (for **2**) may be assigned to charge transfer (CT) bands from phenolate to vanadium (dπ), diminished gradually with the advancement of reaction time (5 minutes interval) [Figure II.19., Figure 20.]. Meanwhile, the growing quinone band resulted blue shifting of the spectra at around 414 nm (for **1**) and 417 nm (for **2**). It finally saturated to ~ 400 nm

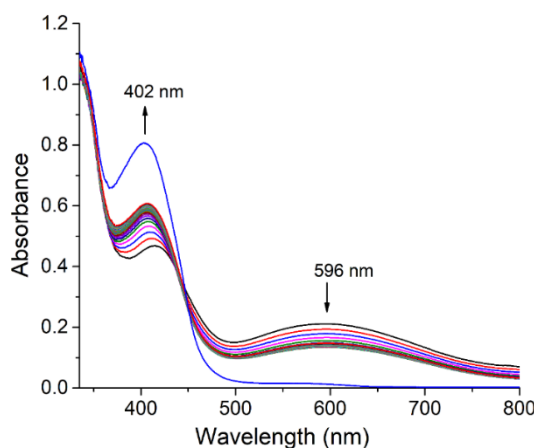


Figure II.19. Absorption spectra of a solution containing 2×10^{-4} M of complex **1** and 0.01 M of 3,5-DTBC, recorded at the interval of 5 min

indicating the formation of 3, 5-di-tert-butyl quinone (3,5-DTBQ). These changes were accompanied by the formation of isosbestic point at 440 nm (for **1**) and 428 nm (for **2**) with a colorimetric transformation of the reaction mixture from bluish green to deep brown. The brown solution so obtained after completion of the reaction

was purified by column chromatography to get the yield of 3, 5-DTBC. The yield for complex **2** was higher (~ 62 %) than that of the complex **1** (~ 54 %). To obtain the kinetic parameters, 2×10^{-4} M solution of complexes were treated with 0.001 M - 0.01 M solution of the substrate and considering the absorption at quinone band ~ 400 nm, the rates of the reactions were determined. The rate of the reaction was found to depend on substrate - catalyst ratio as depicted in **Figure II.20**. The Michaelis-Menten and Lineweaver-Burk equations were applied to determine the kinetic parameters for complexes as follows. [Complex **1**: K_2 (Turnover no) = 11.3 min^{-1} , $K_M = 2.57 \times 10^{-3}$ and $V_{\max} = 2.22 \times 10^{-3} \text{ M min}^{-1}$ [**Figure II.19-20**]. Complex **2**: K_2 (Turnover no) = 9.8 min^{-1} , $K_M = 2.25 \times 10^{-3}$ and $V_{\max} = 2.0 \times 10^{-3} \text{ M min}^{-1}$ and [**Figure II.21-22**].

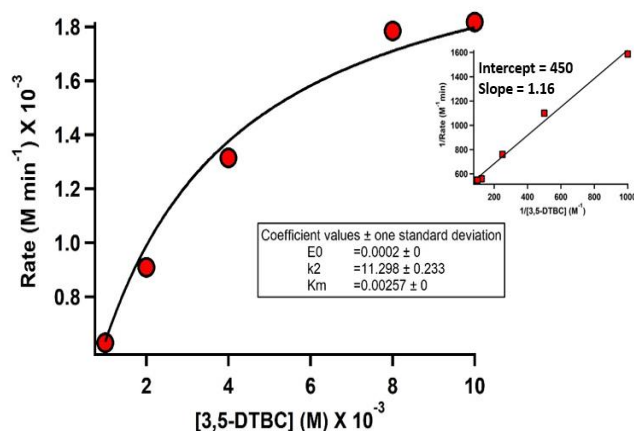


Figure II.20. Plot of rate versus concentration of 3,5-DTBC for the oxidation reaction catalyzed by complex **1** (Inset: Lineweaver–Burk plot).

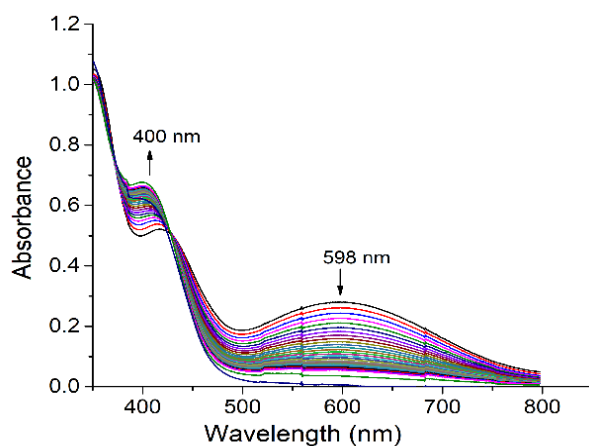


Figure II.21. Absorption spectra of a solution containing 2×10^{-4} M of complex **2** and 0.01 M of 3,5-DTBC, recorded at the interval of 5 min

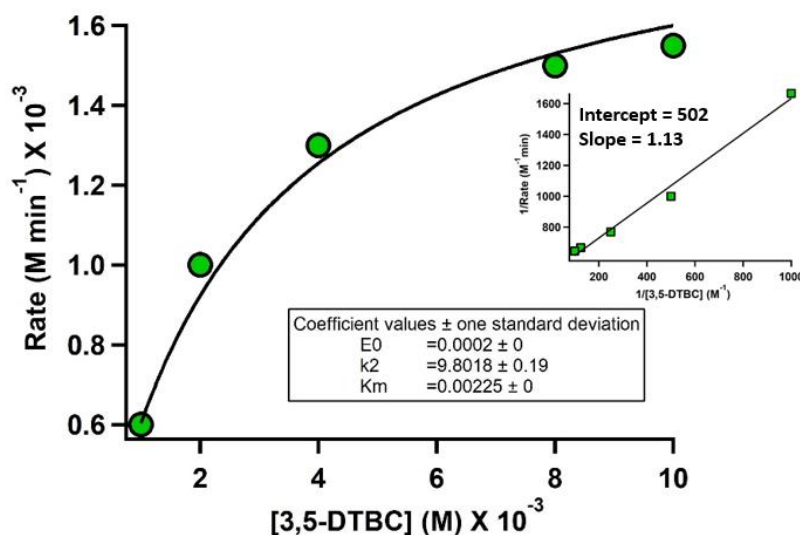
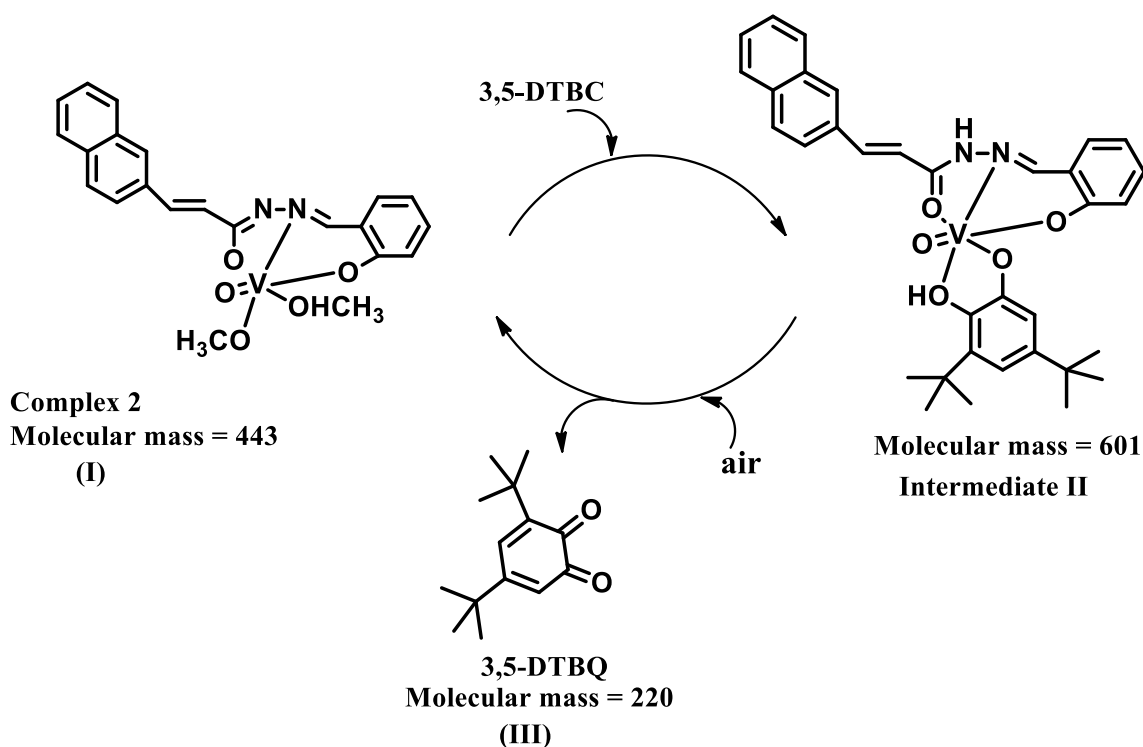


Figure II.22. Plot of rate versus concentration of 3,5-DTBC for the oxidation reaction catalyzed by complex 2 (Inset: Lineweaver–Burk plot).

Reaction pathway monitoring through mass spectrometry

To elucidate the reaction pathway, we have chosen complex $[V^{\text{VO}}(L^2)(\text{OMe})(\text{MeOH})]$ (**2**) as a model (**Scheme II.3**). The presence of two weak V-O bonds, one from the attached methoxy group and the other from the solvent moiety, makes it labile and susceptible to attack by catechol derivatives. The progress of the reaction was monitored by ESI-Mass spectrometry. Free complex **2** has a peak at $m/z = 443$. After initial reaction the base peaks was detected at $m/z = 601$, corresponding to intermediate II. After completion of reaction, the reaction mixture exhibited two characteristics peaks at m/z 221 and 443 corresponding to 3, 5-DTBQ and complex **2** (**Figures II.35-37**). This means after completion of the reaction compound **2** is regenerated. For complex **1** we have observed similar kind of observation, the corresponding mass spectra are given in the experimental section (**Figures II.38-39**).



Scheme II.3. Proposed reaction pathway for Catecholase oxidation for complex 2.

II.2. CONCLUSION

This article deals with the syntheses and characterisation of four mononuclear and two binuclear vanadium complexes with the ligands H_2L^1 [(E)-N'-(2-hydroxybenzylidene)cinnamohydrazide] and H_2L^2 [(2E,N'E)-N'-(2-hydroxybenzylidene)-3-(naphthalen-1-yl)acrylohydrazide]. Both monomeric and dimeric complexes can be synthesised by suitable tuning of solvents. Furthermore, mononuclear (ONO_2^-) complexes **1** and **2** directly combined with NO^- donor (as 8hq) to form a mixed ligand (ONO_2^- - NO^-) complexes **5** and **6**. Dimeric complexes (V/V) **3** and **4** have been treated as precursor to mixed-valence vanadium (V/IV) complexes **3a** and **4a**, generated through coulometric reduction of **3** and **4**. The compounds are characterised in solution state through UV-vis and EPR spectroscopy. Frozen solution EPR results demonstrate the electron is partly localized on one of the two vanadium centres in the electro reduced complexes. Theoretically, electronic spin density calculation of these complexes also supports this fact. Thus, they can be best described as mixed

valance of type II on the EPR time scale. These types of mixed-valence complexes have high degree of importance in exploring the redox and electronic behaviour of vanadium compounds. Complex **1** and **2** appear to be an active catalyst for catechol oxidation.

II.3 EXPERIMENTAL SECTION

A. MATERIALS

All Reagents or analytical grade materials were purchased from commercial sources and used without further purification.

B. PREPARATION OF COMPOUNDS

LIGAND

H₂L¹: The H₂L¹ ligand used in this work was prepared by the following method. Cinnamic acid hydrazide (10 mmol) was added to a DMF solution (20 mL) of salicylaldehyde (10 mmol) and refluxed for 30 min. After cooling, the solution was poured into 50 mL water containing few drops of concentrated H₂SO₄. The white solid so obtained was filtered, washed several times with distilled water, dried and recrystallized from methanol. Yield: 18 g (75%). Anal. Calc. for C₁₆H₁₄N₂O₂: C 72.16%; H 5.30%; N 10.52%; Found: C 72.04%; H, 5.22%; N, 10.26%. ¹H NMR {400 MHz, DMSO-d₆, δ (ppm), J (Hz)}: 11.94 (NH, s), 11.19 (OH, s), 8.395 (1H, s), 7.832 (1H, d, J=6), 7.684–7.545 (5H, m), 7.456 (1H, d, J=7.6), 7.308 (1H, t), 7.252 (1H, d, J=5.6), 6.930 (2H, t), 6.714 (1H, d, J=12.4). ESI-MS (positive) in MeOH: The base peak was detected at *m/z* = 289.1052, corresponding to [HL+23]⁺. IR (cm⁻¹): ν (O-H) 3375; ν (N-H) 3224; ν(C=O) 1661; ν (C=N) 1622.

H₂L²: The ligand H₂L² was synthesized using the same procedure as for H₂L¹, except that 3-(1-naphthyl)acrylic acid hydrazide was used instead of cinnamic acid hydrazide. Yield: 22 g (72%). Anal. Calc. for C₂₀H₁₅N₂O₂: C 75.93%; H 5.10%; N 8.86%; Found: C 75.82%; H, 5.08%; N, 8.68%. ¹H NMR {500 MHz, DMSO-D₆, δ (ppm), J (Hz)}: 12.032 (NH, s), 11.222 (OH,s), 8.430 (1H, s), 8.277–8.260 (1H, d),

8.041–7.997 (2H, m), 7.894–7.879 (1H, d), 7.681–7.574 (6H, m), 7.337–7.306 (1H, t), 6.971–6.929 (1H, m), 6.917–6.890 (1H, d), ESI-MS (positive) in MeOH: The base peak was detected at $m/z = 339.1004$, corresponding to $[HL2+23]^+$. IR (cm^{-1}): $\nu(O-H)$ 3188; $\nu(N-H)$ 3008; $\nu(C=O)$ 1655, 1621; $\nu(C=N)$ 1604.

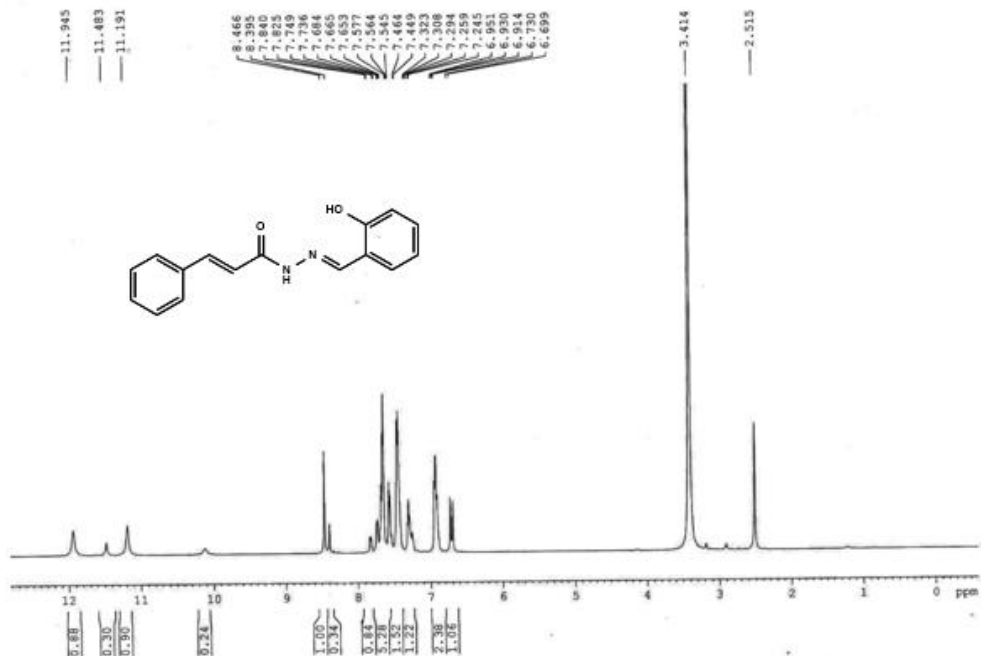


Figure II.23. 1H NMR spectra of H_2L^1 in $DMSO-D_6$.

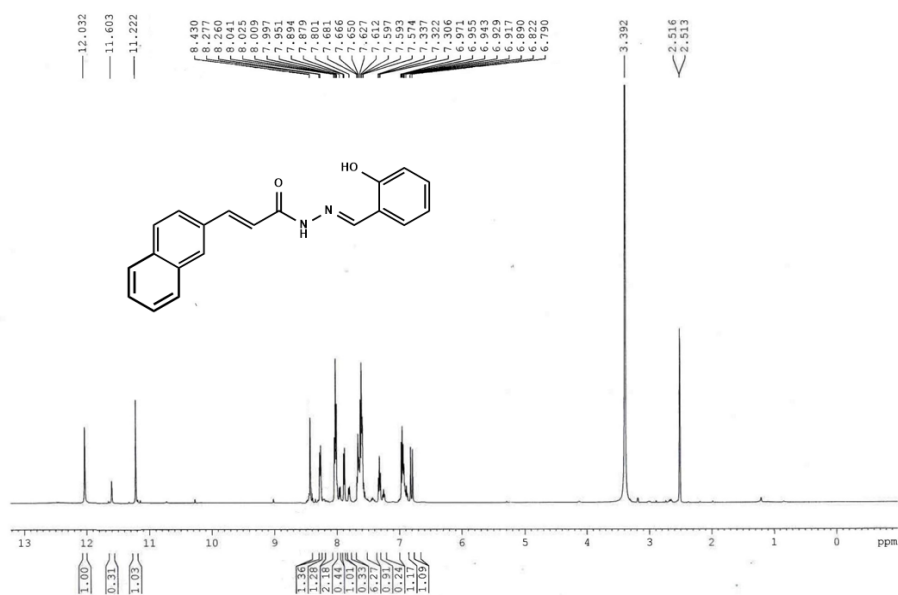


Figure II.24. 1H NMR spectra of H_2L^2 in $DMSO-D_6$.

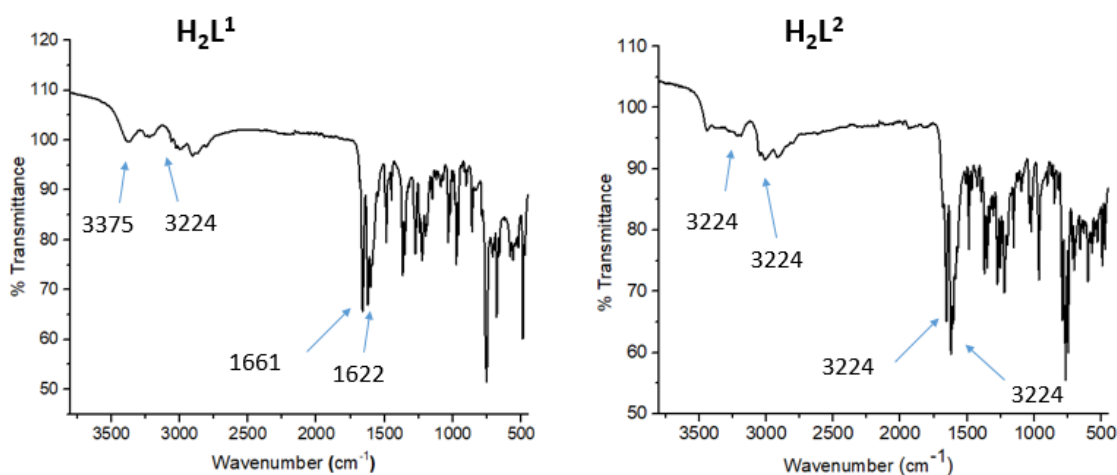


Figure II.25. IR Spectra of ligand H_2L^1 and H_2L^2

COMPLEXES

(a) Oxidomethoxido vanadium(V) complexes $[VVO(L^{1-2})(OMe)(MeOH)]$, (1 and 2).

A 2 mL methanolic solution of $[VO(acac)_2]$ (5 mmol) was added to a 20 mL methanolic solution of ligand (H_2L^1 or H_2L^2) (5 mmol) and stirred for 15 minutes. The colour immediately changed to deep brown. After few days brown coloured crystals suitable for X-ray diffraction analysis were obtained after slow evaporation of the solvent.

$VVO(L^1)(OMe)(MeOH)$ (1) : Yield: 81%. Anal. Calc. for $C_{18}H_{19}N_2O_5V$: C 54.83%; H 4.86%; N 7.10%; Found: C 55.05%; H, 4.94%; N, 7.18%. 1H NMR {300 MHz, $CDCl_3$, δ (ppm), 8.551 (1H, s, $-N=CH$), 7.843–7.763 (2H, m, Ar-H), 7.740–7.642 (1H, m, Ar-H), 7.620–7.122 (5H, m), 6.899–6.876 (1H, d, Ph- $\underline{CH=CH}$), 6.770–6.718 (1H, d, Ph- $\underline{CH=CH}$), 6.634–6.585 (1H, t, Ar-H). IR (KBr, ν_{max} / cm^{-1}): 1638 (imine C=N), 1211 ($C-O$)_{enolic}, 2323 (broad from bound MeOH moiety), 956 (V=O).

$VVO(L^2)(OMe)(MeOH)$ (2) : Yield: 75%. Anal. Calc. for $C_{22}H_{21}N_2O_5V$: C 59.47%; H 4.76%; N 6.30%; Found: C 59.62%; H, 4.88%; N, 6.42%. 1H NMR {300 MHz, DMSO- D_6 , δ (ppm), 8.447 (1H, s, $-N=CH$), 7.835–7.736 (3H, m, Ar-H),

7.637–7.614 (1H, d, Ar-H), 7.546–7.518 (1H, d, Ar-H), 7.463–7.348 (3H, m, Ar-H), 7.169–7.119 (1H, t, Ar-H), 6.898–6.872 (1H, d, Ph-CH=CH), 6.763–6.713 (1H, d, Ph-CH=CH), 6.627–6.579 (1H, t, Ar-H). IR (KBr, ν_{\max} / cm^{-1}): 1634 (imine C=N), 1227 (C-O)_{enolic}, 2284 (broad from bound MeOH moiety), 951 (V=O), 760 (V-O), 559 (V-N).

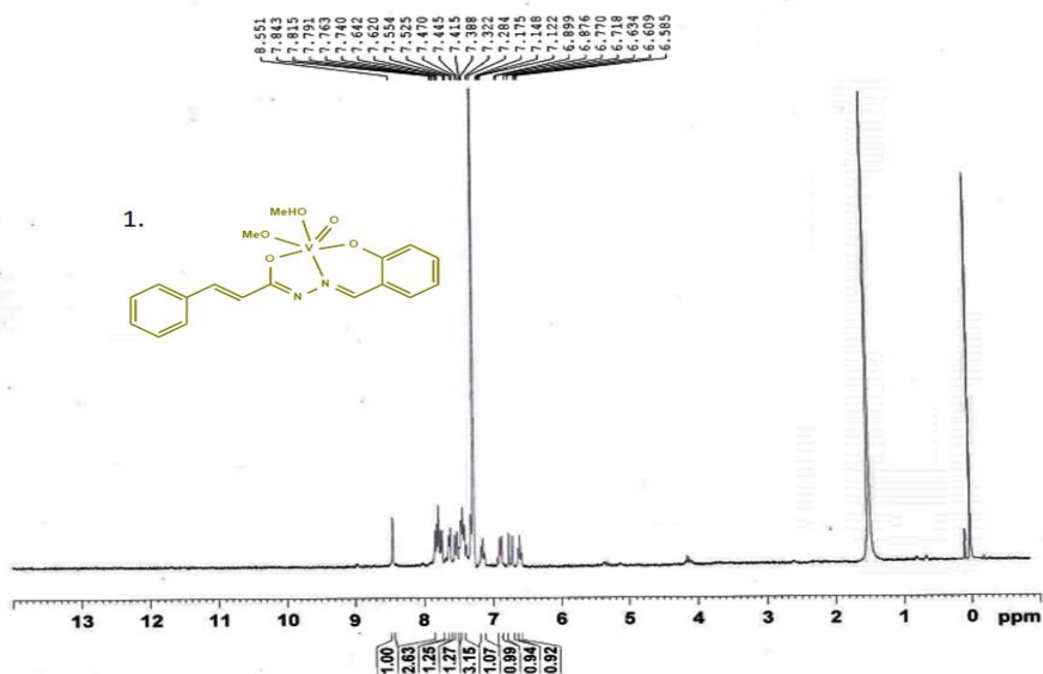


Figure II.26. ¹H NMR spectra of complex 1 in CDCl₃.

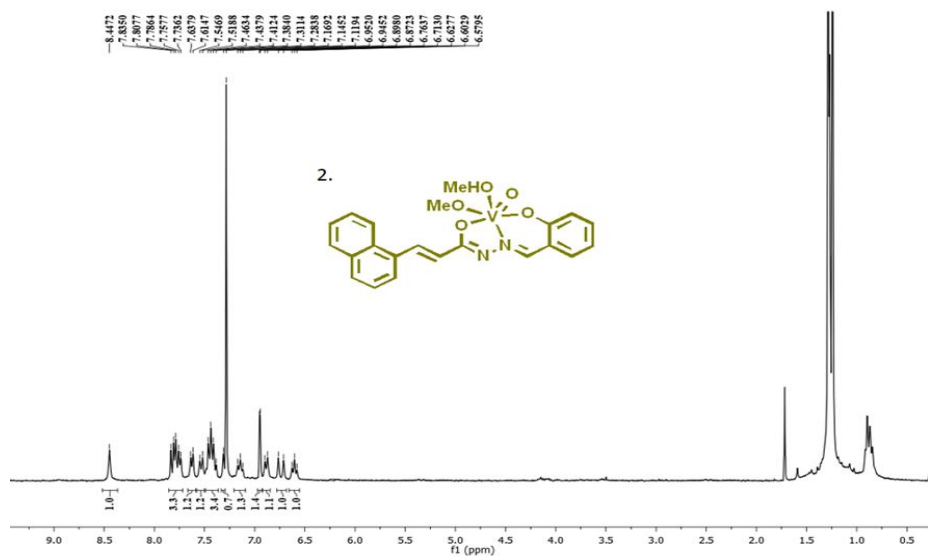


Figure II.27. ¹H NMR spectra of complex 2 in CDCl₃

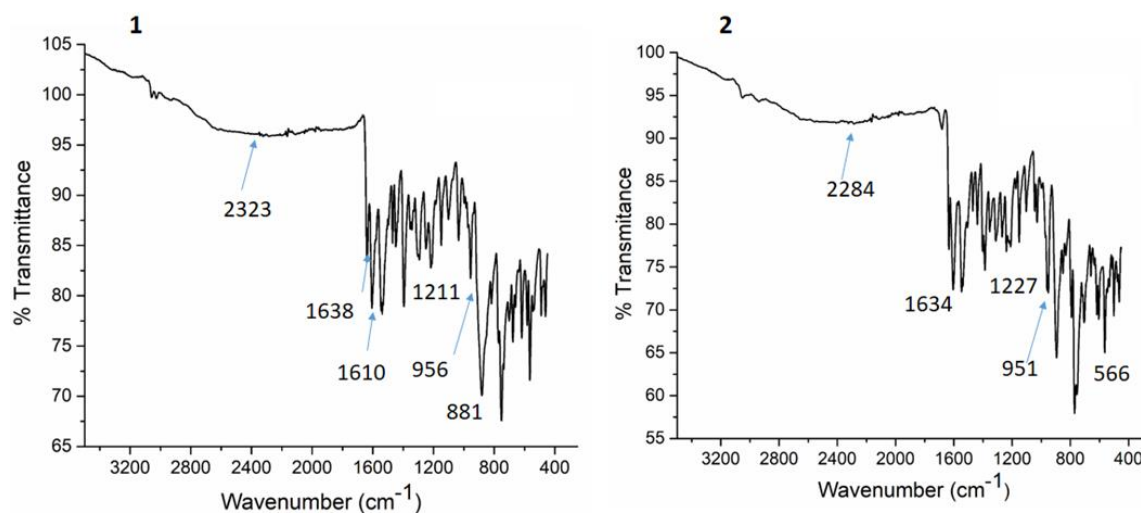


Figure II.28. IR Spectra of Complex 1, 2

(b) μ -Oxidodioxidovanadium(V) complexes $[\text{V}^{\text{V}}_2\text{O}_3(\text{L}^{1-2})_2]$ (3 and 4).

When $[\text{VO}(\text{acac})_2]$ was allowed to react with CH_3CN solution of ligand (H_2L^1 or H_2L^2) and other reaction conditions were kept the same as that of methanol solution, we have got brown coloured crystals of binuclear μ -Oxidovanadium(V) complexes **3** and **4** from H_2L^1 and H_2L^2 respectively. Moreover, the same binuclear complexes were formed when the corresponding mononuclear complexes were dissolved in acetonitrile and kept for slow evaporation.

$\text{V}^{\text{V}}_2\text{O}_3(\text{L}^1)_2$ (3). Yield: 64%. Anal. Calc. for $\text{C}_{32}\text{H}_{24}\text{N}_4\text{O}_7\text{V}_2$: C 56.65%; H 3.57%; N 8.26%; Found: C 56.82%; H, 3.66%; N, 8.34%. ^1H NMR {300 MHz, CDCl_3 , δ (ppm), 8.451 (1H, s, $-\text{N}=\text{CH}$), 7.842–7.740 (2H, m, Ar-H), 7.642–7.620 (1H, d, Ar-H), 7.554–7.524 (1H, d, Ar-H), 7.469–7.387 (3H, m, Ar-H), 7.174–7.121 (1H, t, Ar-H), 6.899–6.875 (1H, d, $\text{Ph}-\underline{\text{C}}\text{H}=\text{CH}$), 6.770–6.617 (2H, d, $\text{Ph}-\text{CH}=\underline{\text{C}}\text{H}$), 6.633–6.584 (1H, t, Ar-H), IR (KBr, ν_{max} / cm^{-1}): 1596 (imine $\text{C}=\text{N}$), 1256 ($\text{C}-\text{O}$)_{enolic}, 984 ($\text{V}=\text{O}$), 752 ($\text{V}-\text{O}-\text{V}$), 664 ($\text{V}-\text{O}$), 464 ($\text{V}-\text{N}$).

$\text{V}^{\text{V}}_2\text{O}_3(\text{L}^2)_2$ (4). Yield: 64%. Anal. Calc. for $\text{C}_{40}\text{H}_{28}\text{N}_4\text{O}_7\text{V}_2$: C 61.71%; H 3.62%; N 7.30%; Found: C 61.82%; H, 3.72%; N, 7.41%. ^1H NMR {300 MHz, CDCl_3 , δ (ppm), 8.451 (1H, s, $-\text{N}=\text{CH}$), 7.954–7.442 (10H, m, Ar-H), 7.204–7.149 (1H, t,

Ar-H), 6.770–6.717 (1H, d, Ph-CH=CH), 6.585–6.545 (1H, d, Ph-CH=CH), IR (KBr, ν_{\max} / cm^{-1}): 1619 (imine C=N), 1265 (C-O)_{enolic}, 995 (V=O), 762 (V-O), 695 (V-O-V), 483 (V-N).

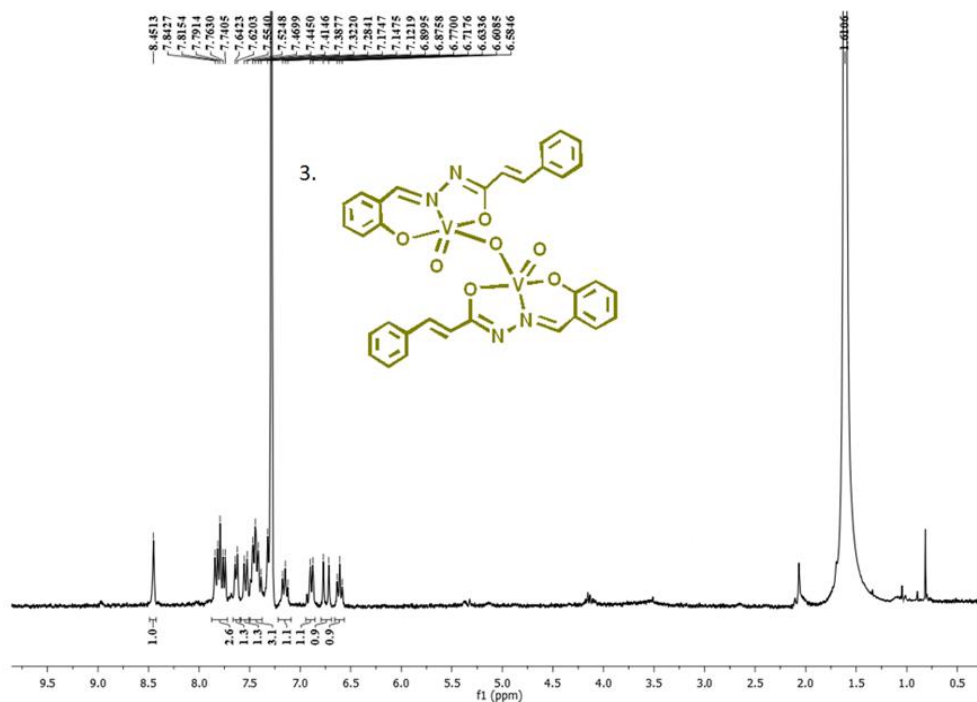


Figure II.29. ^1H NMR spectra of complex 3 in CDCl_3

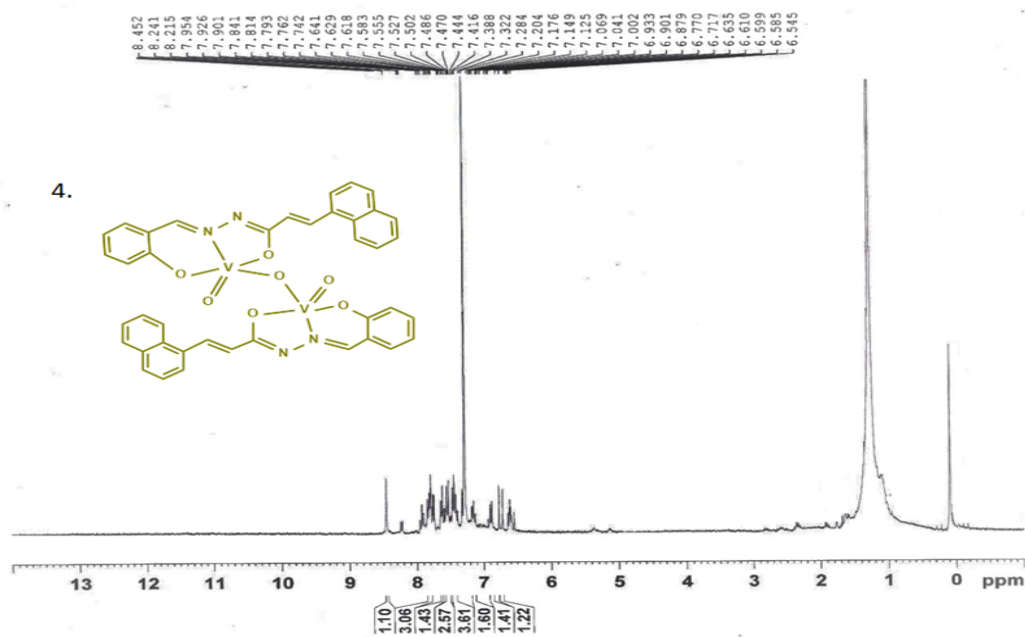


Figure II.30. ^1H NMR spectra of complex 4 in CDCl_3

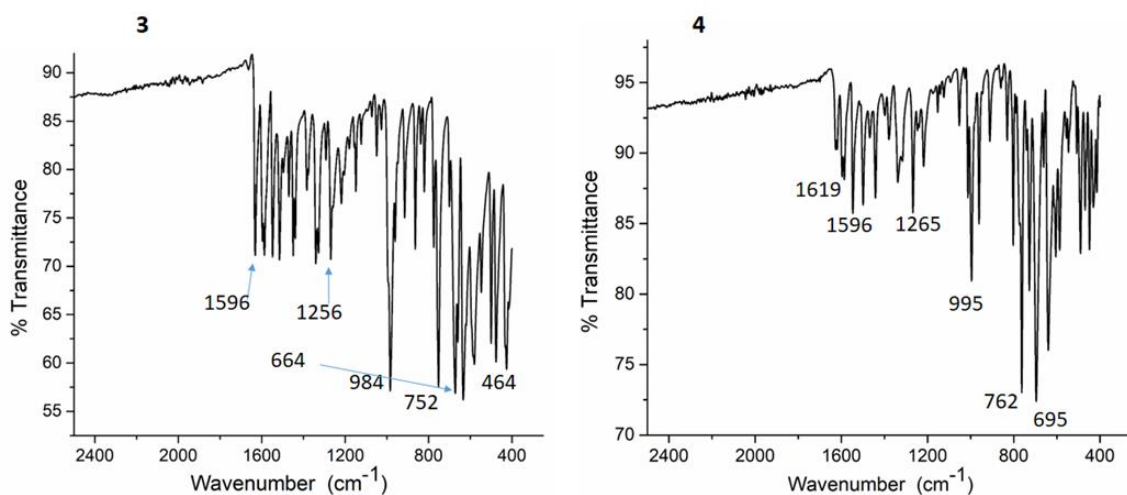


Figure II.31. IR Spectra of Complex 3, 4

(c) 8-hydroxyquinolato vanadium(V) complexes [V^VO(L¹⁻²)(8-hq)], (5 and 6).

[VO(acac)₂] (5 mmol) was added to a 20 mL methanolic solution of ligand (H₂L¹ or H₂L¹) (5 mmol) and stirred for 15 minutes. Then 8-hydroxyquinoline was added in-situ and the colour changed immediately from brown to blackish. The solution was filtered off and kept for slow evaporation. After few days black crystals of complex 5 were obtained used directly for SCXRD structure determination. Moreover, one observation was that same complexes 5 and 6 were also obtained from complex 1 and 2 respectively on addition of 8-hydroxyquinoline in methanol solvent.

[V^VO(L¹)(8-hq)], (5). Yield: 85%. Anal. Calc. for C₂₅H₁₈N₃O₄V: C 63.17%; H 3.82%; N 8.84%; Found: C 63.22%; H, 3.94%; N, 8.96%. ¹H NMR {300 MHz, CDCl₃, δ (ppm), 8.870 (1H, s, -N=CH), 8.212–8.209 (1H, d, Ar-H), 8.185–8.181 (1H, d, Ar-H), 8.075–7.013 (12H, m, Ar-H), 6.989–6.963 (1H, t, Ar-H), 6.835–6.807 (1H, d, Ph-CH=CH), 6.628–6.577 (1H, d, Ph-CH=CH). IR (KBr, ν_{max} / cm⁻¹): 1606 (imine C=N), 1276 (C-O)_{enolic}, 966 (V=O), 756 (V-O), 498 (V-N).

[V^VO(L²)(8-hq)], (6). Yield: 76%. Anal. Calc. for C₂₉H₂₀N₃O₄V: C 66.29%; H 3.84%; N 8.00%; Found: C 66.35%; H, 3.95%; N, 8.14%. ¹H NMR {300 MHz, CDCl₃, δ (ppm), 8.907 (1H, s, -N=CH), 8.219 – 8.192 (1H, t, Ar-H), 8.115 – 8.105

(1H, d, Ar-H), 8.070–7.304 (14H, m, Ar-H), 7.283–7.000 (1H, t, Ar-H), 6.974–6.855 (1H, d, Ph-CH=CH), 6.827–6.721 (1H, d, Ph-CH=CH). IR (KBr, ν_{max} / cm^{-1}): 1629 (imine C=N), 1257 (C-O)_{enolic}, 968 (V=O), 772 (V-O), 497 (V-N).

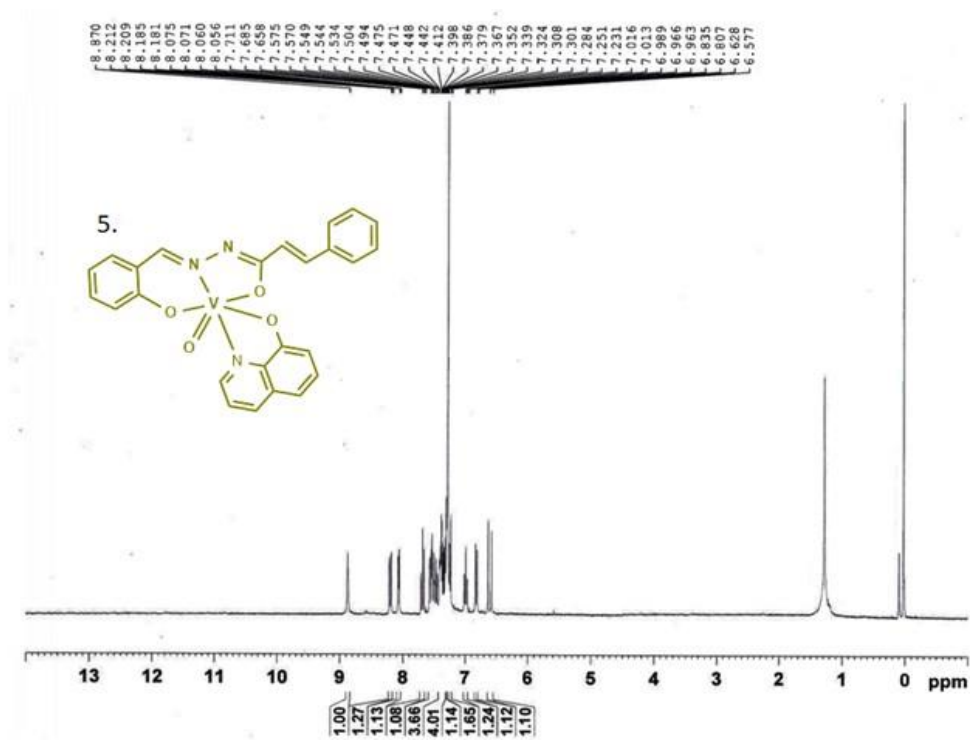


Figure II.32. ¹H NMR spectra of complex 5 in CDCl₃.

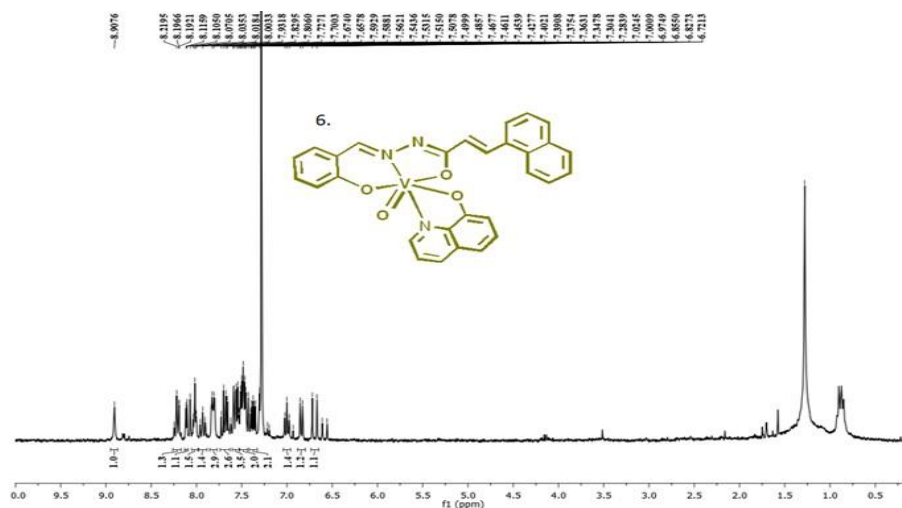


Figure II.33. ¹H NMR spectra of complex 6 in CDCl₃.

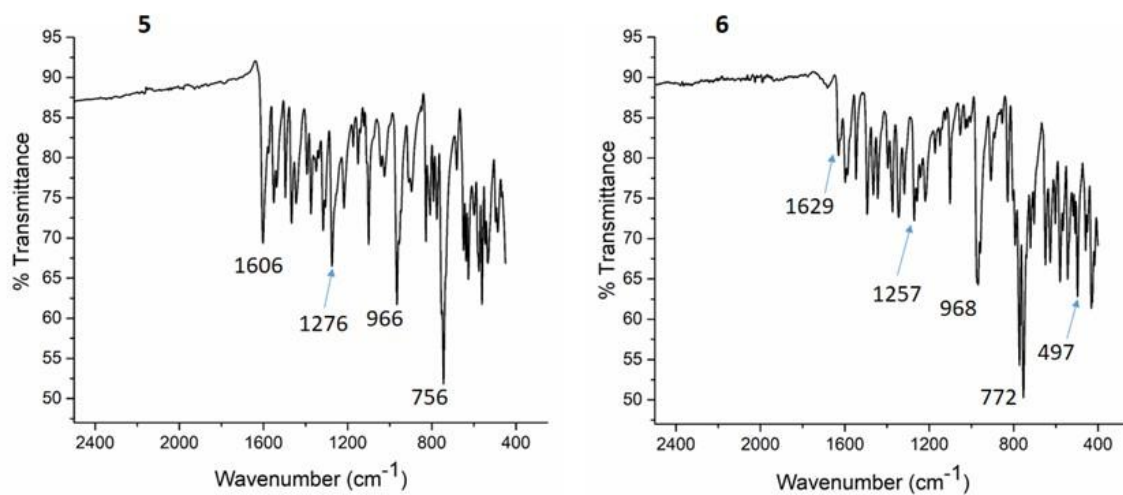


Figure II.34. IR Spectra of complex 5 and 6

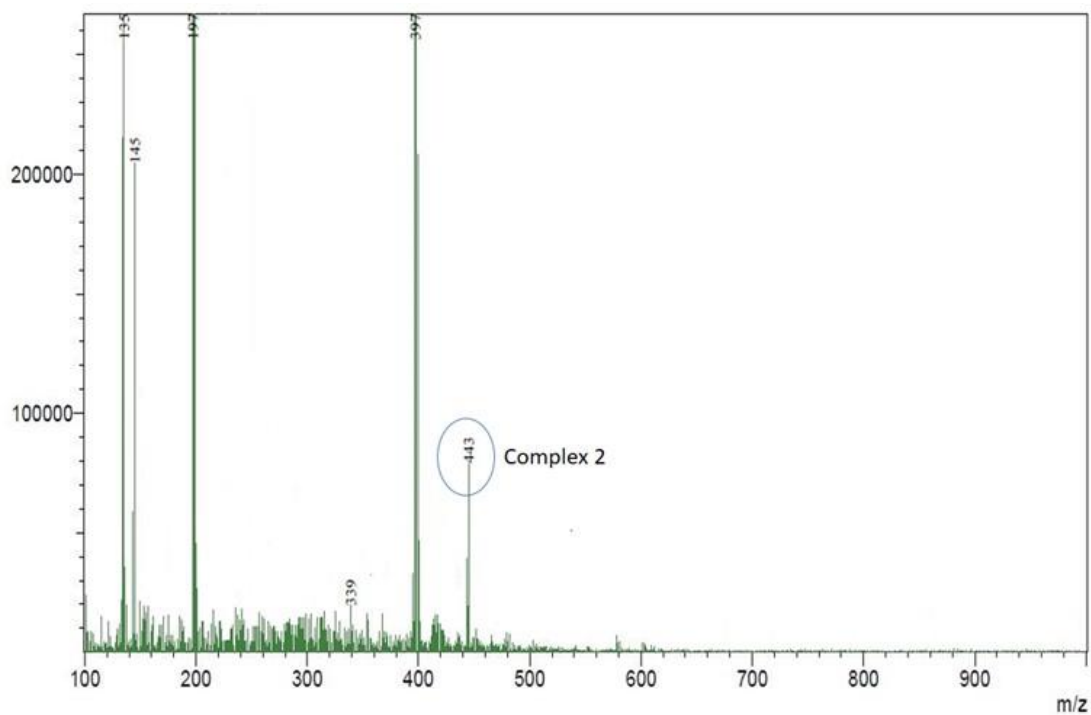


Figure II.35. Mass spectrum of complex 2.

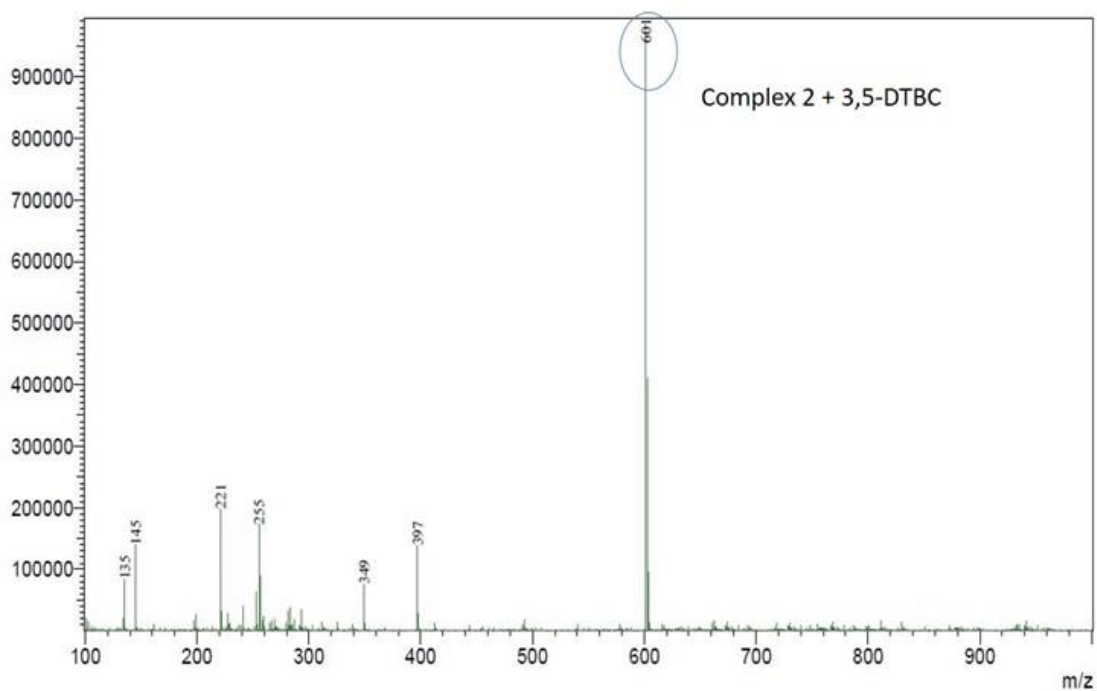


Figure II.36. Mass spectrum of [Complex 2 + catechol]

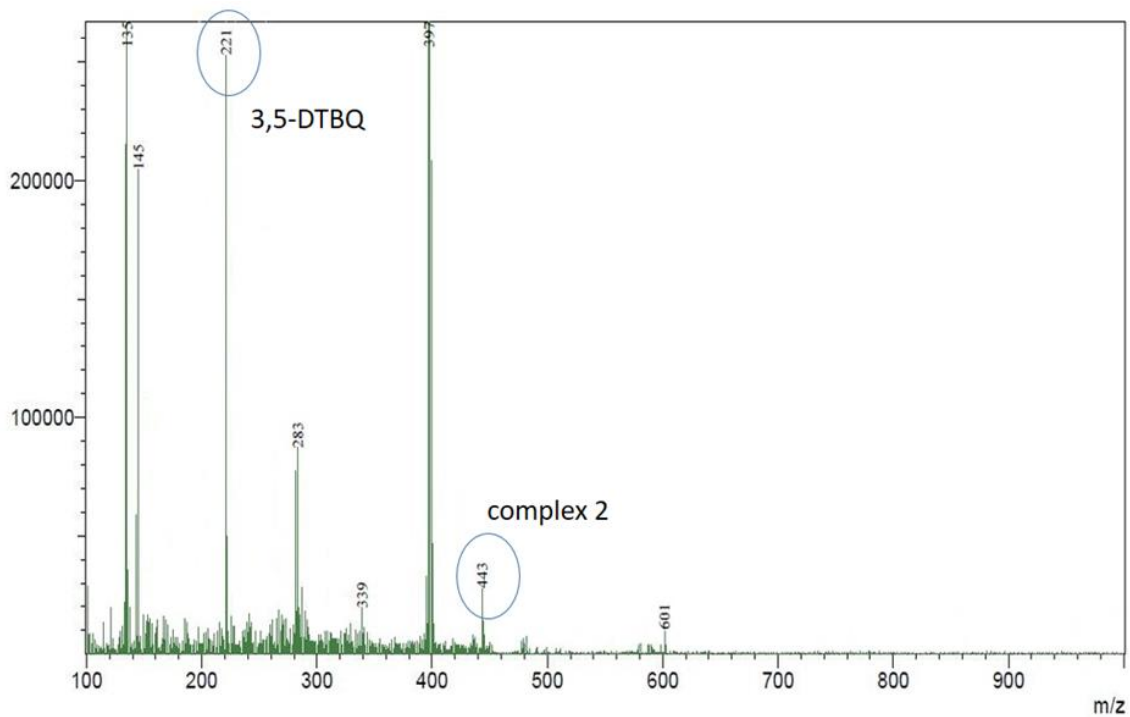


Figure II.37. Mass spectrum of [Complex 2 + catechol] system after infinite time

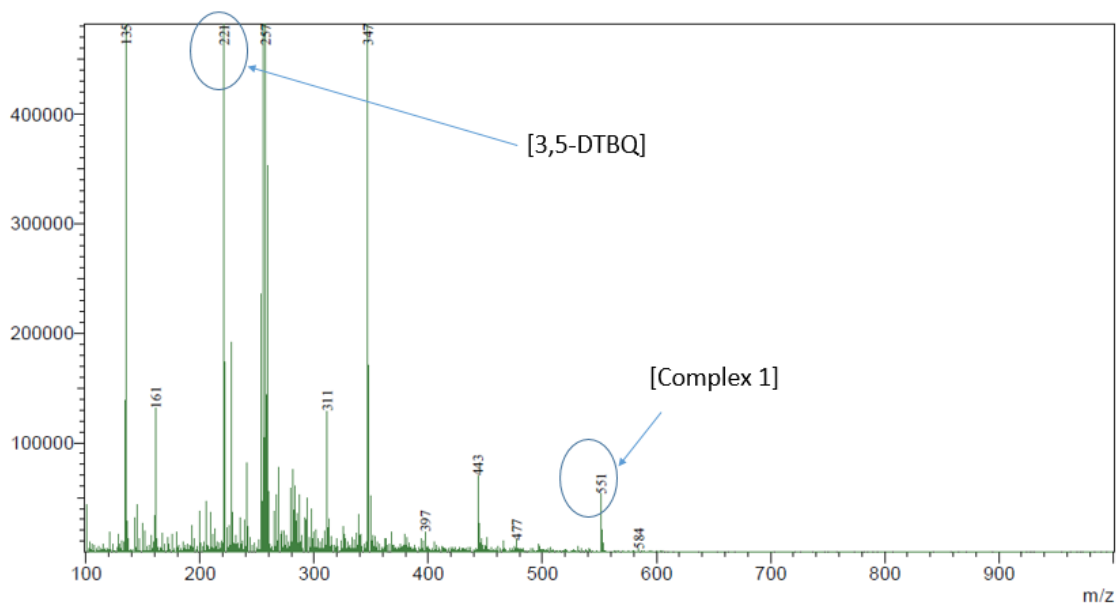


Figure II.38 Mass spectrum of [Complex 1 + catechol] system after infinite time

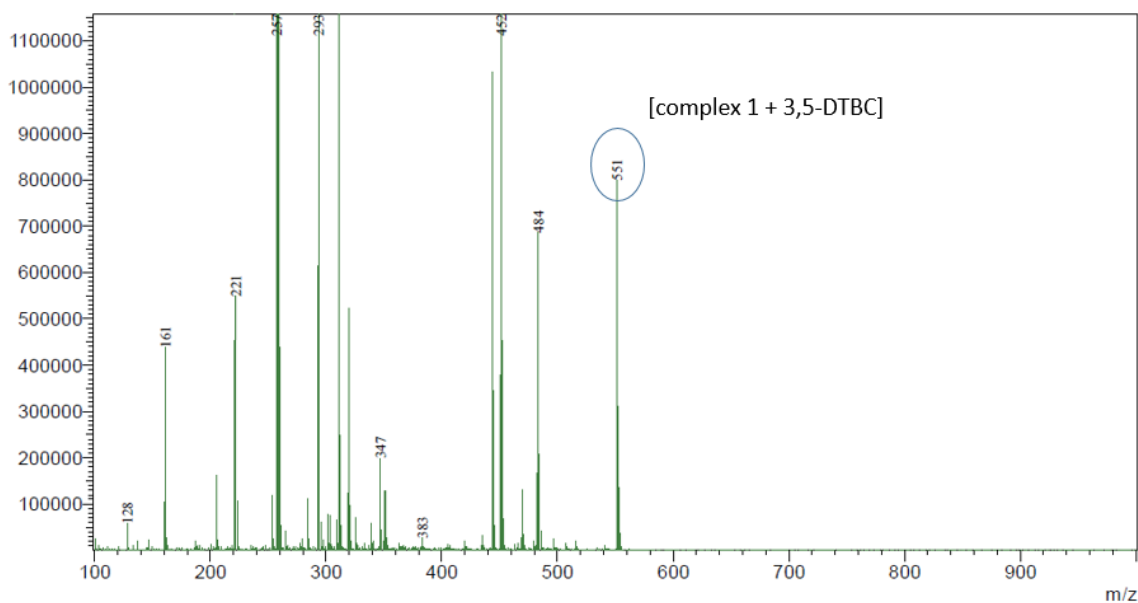


Figure II.39. Mass spectrum of [Complex 1 + catechol] system after infinite time

C. X-RAY STRUCTURE DETERMINATION

The single crystal suitable for X-ray crystallographic analysis of ligands and complexes were grown by slow diffusion of methanol or acetonitrile solution. Details of the X-ray work are given in tabular form in **Table II.9.** and **Table II.10** (see also Chapter I).

D. PHYSICAL MEASUREMENTS

All physical measurements that included elemental analyses, IR, absorption spectra, ¹H NMR and spectra, ESI mass spectra, emission spectra measurement were performed as described in **Chapter I.**

Table II.9. Crystallographic data for ligand and complexes

Crystal Data

	H₂L¹	Complex 1	Complex 2	Complex 3	Complex 4	Complex 5
Chemical Formula	C ₁₆ H ₁₄ N ₂ O ₂	C ₁₈ H ₁₉ N ₂ O ₅ V	C ₂₂ H ₂₁ N ₂ O ₅ V	C ₃₂ H ₂₄ N ₄ O ₇ V ₂	C ₄₀ H ₂₈ N ₄ O ₇ V ₂	C ₂₅ H ₁₈ N ₃ O ₄ V
Formula weight	266.30	394.29	444.35	678.43	778.54	475.38
Crystal system	orthorhombic	Triclinic	Triclinic	Monoclinic	orthorhombic	Triclinic
Space group	Pna2 ₁	P-1	P-1	C 1 2/c 1	P b c n	P-1
<i>a</i> /Å	24.330(11)	7.4370(5)	9.8458(7)	14.8867(14)	17.4194(16)	9.1778(6)
<i>b</i> /Å	5.196(2)	11.4179(8)	11.1247(8)	11.7486(11)	26.1120(18)	9.4230(7)
<i>c</i> /Å	10.710(5)	12.4578(9)	11.2027(8)	17.3655(16)	7.6982(5)	13.4652(9)
α /°	90	64.765(2)	117.555(2)	90	90	76.493(2)
β /°	90	78.163(2)	106.626(2)	101.175(3)	90	87.816(2)
γ /°	90	73.881(2)	92.192(2)	90	90	74.545(2)
<i>V</i> /Å ³	1353.8(10)	914.69	1021.14(13)	2979.6(5)	3501.6(5)	1090.99(13)
<i>Z</i>	4	2	2	4	4	2
<i>D</i> _{calcd} /mg m ⁻³	1.3064	1.432	1.445	1.389	1.477	1.4470
μ /mm ⁻¹	0.088	0.073	0.523	0.683	0.526	0.493
θ /°	26.95	27.08	27.08	26.90	27.36	27.12
<i>T</i> /K	296.15	273.15	293.15	273.15	273.15	273.15

Data collection

	H₂L¹	Complex 1	Complex 2	Complex 3	Complex 4	Complex 5
Total refl. collected	10721	30874	33688	49511	9916	37118
Unique refl. (R _{int})	2500	4038	4496	3287	3909	4828
Used refl.	1635	3649	4057	2724	1207	4040
<i>h k l</i> range	-21 ≤ <i>h</i> ≤ 29 -6 ≤ <i>k</i> ≤ 6 -13 ≤ <i>l</i> ≤ 12	-9 ≤ <i>h</i> ≤ 9 -14 ≤ <i>k</i> ≤ 14 -15 ≤ <i>l</i> ≤ 15	-12 ≤ <i>h</i> ≤ 12 -14 ≤ <i>k</i> ≤ 14 -14 ≤ <i>l</i> ≤ 14	-19 ≤ <i>h</i> ≤ 19 -15 ≤ <i>k</i> ≤ 15 -22 ≤ <i>l</i> ≤ 22	-8 ≤ <i>h</i> ≤ 8 -18 ≤ <i>k</i> ≤ 18 -44 ≤ <i>l</i> ≤ 44	-11 ≤ <i>h</i> ≤ 11 -11 ≤ <i>k</i> ≤ 12 -11 ≤ <i>l</i> ≤ 17

Structure Solution and Refinement

	H ₂ L ¹	Complex 1	Complex 2	Complex 3	Complex 4	Complex 5
Solution	Patterson	Patterson	Patterson	Patterson	Patterson	Patterson
Refinement	Full- matrix least- squares on F ²	Full- matrix least- squares on F ²	Full- matrix least- squares on F ²	Full- matrix least- squares on F ²	Full- matrix least- squares on F ²	Full- matrix least- squares on F ²
GOF on F ²	1.540	1.135	1.021	1.076	1.072	1.0619
R1, ^a [I > 2σ(I)]	0.0547	0.0422	0.0353	0.0803	0.1126	0.0525
wR2 ^b [I > 2σ(I)]	0.0772	0.1009	0.0907	0.1917	0.1722	0.1320
R1 [all data]	0.1081	0.0406	0.04	0.0961	0.3250	0.0647
wR2 [all data]	0.0842	0.1049	0.0943	0.2029	0.2697	0.1424

$$^a R1 = \frac{\sum ||F_o| - |F_c||}{\sum |F_o|} \cdot ^b wR2 = [\frac{\sum [w(F_o^2 - F_c^2)^2]}{\sum [w(F_o^2)^2]}]^{1/2}$$

Table II.10. Fractional Atomic Coordinates ($\times 10^4$) and Equivalent Isotropic Displacement Parameters ($\text{\AA}^2 \times 10^3$) for H_2L^1 . U_{eq} is defined as 1/3 of the trace of the orthogonalized U_{ij} tensor.

Atom	x	y	z	U(eq)
V1	7820.6(5)	2796.6(4)	7179.5(3)	35.32(12)
O1	7380(2)	2378.2(15)	5901.4(12)	40.6(3)
O4	7395(2)	1277.0(14)	8313.6(12)	40.2(3)
O3	4499(2)	3329.9(16)	7288.2(13)	45.2(4)
N2	7170(2)	4551.4(17)	4624.8(14)	35.0(4)
O2	7364(3)	3886.1(16)	8005.7(13)	50.8(4)
N1	7485(2)	4621.0(17)	5660.5(14)	32.8(4)
C1	7156(3)	3326(2)	4854.2(17)	34.2(4)
C2	6867(3)	3021(2)	3883.7(18)	37.8(5)
C10	7676(3)	5746(2)	5573.9(18)	36.5(4)
C3	6858(3)	1814(2)	4005.3(18)	38.8(5)
C5	6179(3)	203(2)	3389(2)	46.1(5)
C11	7967(3)	5976(2)	6567(2)	37.7(5)
C4	6588(3)	1434(2)	3073.7(18)	37.0(4)
C16	8359(3)	7191(2)	6364(2)	48.6(6)
C18	8678(4)	42(3)	8716(3)	60.0(7)
C9	6686(4)	2271(2)	1871(2)	45.9(5)
C17	3267(4)	3184(3)	8336(2)	60.7(7)
C8	6352(4)	1894(3)	1024(2)	51.2(6)
C6	5814(4)	-161(3)	2541(2)	52.5(6)
C12	7820(3)	5036(2)	7746(2)	40.5(5)
C7	5895(4)	687(3)	1365(2)	53.0(6)
C13	8079(4)	5335(3)	8674(2)	56.0(6)
C15	8605(4)	7471(3)	7286(3)	58.1(7)
C14	8462(4)	6540(3)	8437(3)	60.8(7)
O5	10044(2)	2513.4(18)	6972.4(15)	54.6(4)

Table II.11. Fractional Atomic Coordinates ($\times 10^4$) and Equivalent Isotropic Displacement Parameters ($\text{\AA}^2 \times 10^3$) for **Complex 1**. U_{eq} is defined as 1/3 of the trace of the orthogonalized U_{ij} tensor.

Atom	<i>x</i>	<i>y</i>	<i>z</i>	U(eq)
V1	7820.6(5)	2796.6(4)	7179.5(3)	35.32(12)
O1	7380(2)	2378.2(15)	5901.4(12)	40.6(3)
O4	7395(2)	1277.0(14)	8313.6(12)	40.2(3)
O3	4499(2)	3329.9(16)	7288.2(13)	45.2(4)
N2	7170(2)	4551.4(17)	4624.8(14)	35.0(4)
O2	7364(3)	3886.1(16)	8005.7(13)	50.8(4)
N1	7485(2)	4621.0(17)	5660.5(14)	32.8(4)
C1	7156(3)	3326(2)	4854.2(17)	34.2(4)
C2	6867(3)	3021(2)	3883.7(18)	37.8(5)
C10	7676(3)	5746(2)	5573.9(18)	36.5(4)
C3	6858(3)	1814(2)	4005.3(18)	38.8(5)
C5	6179(3)	203(2)	3389(2)	46.1(5)
C11	7967(3)	5976(2)	6567(2)	37.7(5)
C4	6588(3)	1434(2)	3073.7(18)	37.0(4)
C16	8359(3)	7191(2)	6364(2)	48.6(6)
C18	8678(4)	42(3)	8716(3)	60.0(7)
C9	6686(4)	2271(2)	1871(2)	45.9(5)
C17	3267(4)	3184(3)	8336(2)	60.7(7)
C8	6352(4)	1894(3)	1024(2)	51.2(6)
C6	5814(4)	-161(3)	2541(2)	52.5(6)
C12	7820(3)	5036(2)	7746(2)	40.5(5)
C7	5895(4)	687(3)	1365(2)	53.0(6)
C13	8079(4)	5335(3)	8674(2)	56.0(6)
C15	8605(4)	7471(3)	7286(3)	58.1(7)
C14	8462(4)	6540(3)	8437(3)	60.8(7)
O5	10044(2)	2513.4(18)	6972.4(15)	54.6(4)

Table II.12. Fractional Atomic Coordinates ($\times 10^4$) and Equivalent Isotropic Displacement Parameters ($\text{\AA}^2 \times 10^3$) for **Complex 2**. U_{eq} is defined as $1/3$ of the trace of the orthogonalized U_{ij} tensor.

Atom	<i>x</i>	<i>y</i>	<i>z</i>	U(eq)
V ₁	3570.5(3)	3737.4(3)	1366.7(3)	37.88(10)
N ₂	4510.3(15)	6084.7(14)	4405.2(14)	37.7(3)
O ₁	5384.2(13)	5104.2(13)	2553.6(13)	43.0(3)
O ₂	2013.2(13)	2547.8(12)	1101.9(13)	45.3(3)
C ₂₁	4901(3)	2966(3)	-772(3)	62.7(6)
O ₃	2772.2(15)	4545.1(15)	615.8(14)	54.2(3)
O ₄	4832.9(15)	2705.2(13)	2661.7(13)	49.4(3)
N ₁	3328.6(14)	5032.5(13)	3368.5(14)	33.9(3)
C ₁	5528.5(18)	6038.0(17)	3851.3(17)	36.4(3)
C ₂	6871.4(19)	7064.8(19)	4734.0(19)	41.6(4)
C ₃	7932.1(18)	7097.6(18)	4232.7(19)	38.4(4)
C ₄	9343.1(17)	8040.2(17)	5005.9(18)	37.3(3)
C ₅	10304.6(19)	8021.9(18)	4249(2)	41.0(4)
C ₆	9966(2)	7144(2)	2752(2)	51.8(5)
C ₇	10942(3)	7161(3)	2107(3)	70.4(7)
C ₈	12286(3)	8058(4)	2900(4)	85.1(9)
C ₉	12641(3)	8929(3)	4318(4)	75.2(7)
C ₁₀	11678(2)	8948(2)	5051(3)	52.3(5)
C ₁₁	12029(2)	9852(2)	6529(3)	59.4(6)
C ₁₂	11108(2)	9856(2)	7228(2)	55.0(5)
C ₁₃	9766(2)	8943.9(19)	6459(2)	45.2(4)
C ₁₄	2163.9(18)	5015.5(18)	3671.9(18)	37.3(3)
C ₁₅	860.4(17)	3992.5(17)	2706.1(18)	36.4(3)
C ₁₆	818.6(18)	2800.0(18)	1447.4(18)	37.5(4)
C ₁₇	-475(2)	1843(2)	570(2)	47.1(4)
C ₁₈	-1711(2)	2073(2)	922(2)	56.1(5)
C ₁₉	-1692(2)	3244(2)	2150(3)	55.7(5)
C ₂₀	-418(2)	4181(2)	3032(2)	45.8(4)
O ₅	4400.3(14)	2681.8(13)	144.9(13)	46.9(3)
C ₂₂	4700(4)	1265(3)	2062(4)	79.4(8)

Table II.13. Fractional Atomic Coordinates ($\times 10^4$) and Equivalent Isotropic Displacement Parameters ($\text{\AA}^2 \times 10^3$) for Complex 3. U_{eq} is defined as 1/3 of the trace of the orthogonalized U_{ij} tensor.

Atom	<i>x</i>	<i>y</i>	<i>z</i>	U(eq)
V1	4472.1(6)	8274.5(7)	3144.1(4)	33.7(3)
O2	4074(2)	7326(3)	2220.2(18)	37.4(7)
O4	5000	9141(4)	2500	37.0(10)
O1	5197(3)	8467(3)	4106.7(19)	41.2(8)
O3	3547(3)	8858(4)	3231(2)	51.2(10)
N1	4258(3)	6653(4)	3575(2)	40.5(7)
N2	3900(3)	5830(4)	3027(2)	40.5(7)
C4	3814(3)	6276(4)	2327(3)	37.6(10)
C2	4785(4)	7043(5)	4947(3)	43.1(5)
C7	2824(4)	5465(5)	197(3)	50.2(6)
C1	5182(4)	8099(5)	4836(3)	43.1(5)
C6	3267(3)	6033(4)	923(3)	40.1(8)
C3	4380(4)	6341(5)	4302(3)	43.1(5)
C8	2754(4)	6056(5)	-504(3)	50.2(6)
C16	5594(4)	8753(5)	5472(3)	43.1(5)
C5	3397(3)	5595(4)	1652(3)	40.1(8)
C12	2462(4)	4371(5)	175(3)	50.2(6)
C13	4845(4)	6648(5)	5722(3)	43.1(5)
C11	2024(4)	3907(5)	-530(3)	50.2(6)
C14	5263(4)	7289(5)	6346(3)	43.1(5)
C15	5630(4)	8346(5)	6231(3)	43.1(5)
C9	2322(4)	5598(5)	-1209(3)	50.2(6)
C10	1949(4)	4512(5)	-1215(3)	50.2(6)
C15	5630(4)	8346(5)	6231(3)	43.1(5)
C9	2322(4)	5598(5)	-1209(3)	50.2(6)
C10	1949(4)	4512(5)	-1215(3)	50.2(6)
C15	5630(4)	8346(5)	6231(3)	43.1(5)
C9	2322(4)	5598(5)	-1209(3)	50.2(6)
C10	1949(4)	4512(5)	-1215(3)	50.2(6)

Table II.14. Fractional Atomic Coordinates ($\times 10^4$) and Equivalent Isotropic Displacement Parameters ($\text{\AA}^2 \times 10^3$) for Complex 4. U_{eq} is defined as 1/3 of the trace of the orthogonalized U_{ij} tensor.

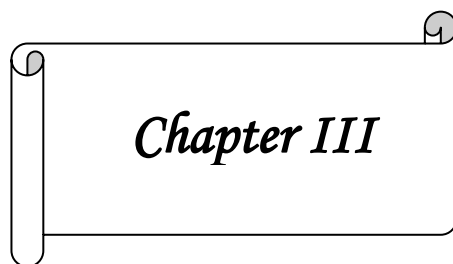
Atom	<i>x</i>	<i>y</i>	<i>z</i>	U(eq)
C1	2794(5)	2980(4)	4040(11)	55(2)
N1	3970(4)	3703(3)	4960(10)	66(2)
O1	3485(3)	2921(2)	3238(8)	66.7(18)
C2	2666(5)	3402(4)	5104(12)	63(3)
N2	4469(5)	4115(3)	5295(11)	77(3)
O2	5290(3)	3501(2)	4217(8)	64.7(18)
V2	4444.2(8)	3026.1(6)	4053(2)	60.3(5)
C17	1926(5)	3463(4)	5844(13)	69(3)
O4	5000	2668(3)	2500	62(2)
C18	1368(5)	3103(4)	5601(12)	72(3)
O3	4465(4)	2724(2)	5842(8)	82(2)
C19	1508(5)	2685(4)	4534(13)	75(3)
C20	2219(5)	2621(4)	3754(12)	69(3)
C3	3255(5)	3778(4)	5402(12)	68(3)
C4	5161(6)	3955(4)	4888(14)	75(3)
C5	5813(6)	4282(4)	5230(14)	82(3)
C6	6540(5)	4140(4)	5008(12)	67(3)
C7	7231(5)	4434(4)	5387(12)	67(2)
C8	7188(5)	4929(4)	5960(13)	77(3)
C9	7856(6)	5216(4)	6307(13)	84.4(12)
C10	8553(6)	5002(4)	6144(13)	84.4(12)
C11	8642(6)	4495(4)	5582(14)	84.4(12)
C12	9383(6)	4266(4)	5360(13)	84.4(12)
C13	9448(6)	3792(4)	4742(13)	84.4(12)
C14	8815(6)	3493(4)	4342(13)	84.4(12)
C15	8078(6)	3691(4)	4569(13)	84.4(12)
C16	7968(6)	4204(4)	5153(14)	84.4(12)

Table II.14. Fractional Atomic Coordinates ($\times 10^4$) and Equivalent Isotropic Displacement Parameters ($\text{\AA}^2 \times 10^3$) for Complex 5. U_{eq} is defined as 1/3 of the trace of the orthogonalized U_{ij} tensor.

Atom	<i>x</i>	<i>y</i>	<i>z</i>	U(eq)
V1	2580.2(5)	631.0(5)	6840.7(3)	46.60(16)
O1	688(2)	667(2)	6357.5(12)	55.5(5)
O2	3867(2)	1243(2)	7674.8(13)	53.0(4)
O4	3529(2)	1298(2)	5661.8(13)	51.2(4)
N1	1510(2)	610(3)	8231.3(15)	47.8(5)
N2	2207(3)	1045(3)	8972.2(16)	58.2(6)
N3	1564(2)	3273(3)	6455.3(16)	50.5(5)
O3	3383(3)	-1126(2)	7042.5(16)	67.3(6)
C1	-428(3)	89(3)	6775.3(18)	44.5(5)
C16	-1492(3)	-121(3)	6154(2)	50.0(6)
V1	2580.2(5)	631.0(5)	6840.7(3)	46.60(16)
O1	688(2)	667(2)	6357.5(12)	55.5(5)
C15	-2682(3)	-661(3)	6577(2)	55.3(6)
C14	-2826(3)	-1044(4)	7627(2)	63.9(8)
C13	-1811(3)	-818(4)	8245(2)	64.6(8)
C2	-606(3)	-237(3)	7839.4(19)	51.1(6)
C3	329(3)	146(4)	8501.2(19)	58.4(7)
C4	3436(3)	1362(3)	8592.6(19)	50.5(6)
C5	4343(3)	1902(3)	9214(2)	56.1(7)
C6	5520(3)	2402(3)	8865(2)	59.0(7)
C7	6427(3)	3052(3)	9415(2)	58.0(7)
C8	6296(4)	3019(4)	10442(2)	67.6(8)
C9	7134(4)	3688(4)	10923(3)	76.3(9)
C10	8109(5)	4398(7)	10387(4)	123.2(11)
C11	8205(5)	4527(7)	9357(4)	123.2(11)
C12	7409(5)	3801(7)	8877(4)	123.2(11)
C17	3390(3)	2768(3)	5228.9(19)	50.1(6)
C18	2322(3)	3848(3)	5639.4(19)	50.1(6)
C19	2078(4)	5409(4)	5214(2)	63.4(7)
C20	986(4)	6381(4)	5690(3)	80.7(10)
C21	255(4)	5792(4)	6514(3)	79.4(10)
C22	564(3)	4229(4)	6867(2)	62.8(7)
C23	2931(5)	5867(4)	4359(3)	78.2(9)
C24	3962(5)	4813(4)	3990(3)	78.2(10)
C25	4219(4)	3245(4)	4412(2)	64.9(8)

References

1. Su, X.; Aprahamian, I. *Chem. Soc. Rev.* **2014**, *43*, 1963-1981.
2. (a) Kalinowski, D. S., Sharpe, P. C.; Bernhardt, P. V.; Richardson, D. R. *J. Med. Chem.* **2008**, *51*, 2, 331-344. (b) Bouzayani, N.; Marque, S.; Djelassi, B.; Kacem, Y.; Marrot, J.; Ben Hassine, B. *New J.Chem.* **2018**, *42(8)*, 6389-6398. (c) De, P.; Baltas, M.; Bedos-Belval, F. *Curr Med Chem.* **2011**, *18(11)*, 1672-1703.
3. (a) Mukiza, J.; Habarurema, G.; Gerber, T. I. A.; Hosten, E.; Betz, R.; Umumararungu, T. *Polyhedron.* **2020**, *175*, 114192. (b) Joseph, B.; Kurup, M. R. P. **2014**, <http://dyuthi.cusat.ac.in/purl/4944>.
4. Levina, A.; Pires Vieira, A.; Wijetunga, A.; Kaur, R.; Koehn, J. T.; Crans, D. C.; Lay, P. A. *Angew. Chem.* **2020**, *59(37)*, 15834-15838.
5. Correia, I.; Adão, P.; Roy, S.; Wahba, M.; Matos, C.; Maurya, M. R.; Marques, F.; Pavan F. R.; Leite, C. Q.F.; Avecilla, F.; Pessoa, J. C. *J. Inorg. Biochem.* **2014**, *141*, 83-93.
6. (a) Mondal, A.; Sarkar S.; Chopra, D.; Guru Row, T. N.; Pramanik, K.; Rajak, K. K. *Inorg. Chem.* **2005**, *44*, 703-708. (b) Dinda, R.; Sengupta, P.; Sutradhar, M.; Mak, T. C. W.; Ghosh, S. *Inorg. Chem.* **2008**, *47(13)*, 5634-5640. (c) Mondal, S.; Ghosh, P.; Chakravorty, A. *Inorg. Chem.* **1997**, *36(1)*, 59-63.
7. (a) Maurya, M. R. *Coord. Chem. Rev.* **2019**, *383*, 43-81. (b) Dutta, S. K.; Samanta, S.; Kumar, S. B.; Han, O. H.; Burckel, P.; Pinkerton A. A.; and Chaudhury, M.. *Inorg. Chem.* **1999**, *38*, 1982-1988. (c) Mondal, B.; Ghosh, T.; Sutradhar, M.; Mukherjee, G.; Drew, M. G. B.; Ghosh, T. *Polyhedron* **2008**, *27(9-10)*, 2193-2201.
8. Chen, C. Y.; Zhou, Z. H.; Chen, H. B.; Huang, P. Q.; Tsai, K. R.; Chow, Y. L. *Inorg. Chem.* **2008**, *47*, 19, 8714-8720.



Chapter III

Synthesis and characterization of dioxovanadium (V) complexes and its catalytic activity towards pyrogallol oxidation.

*Synthesis and characterization of dioxovanadium (V) complexes and its catalytic activity towards pyrogallol oxidation. **

Abstract

Reaction between vanadyl acetyl acetonate and valproic acid hydrazone ligands, H_2L^3 and H_2L^4 leads to the formation of two mononuclear dioxo complexes $[V^V(O)_2HL^{3-4}]$ (**7**, **8**) in acetonitrile. Here H_2L^3 is valproic acid hydrazone of salicylaldehyde and H_2L^4 is that of

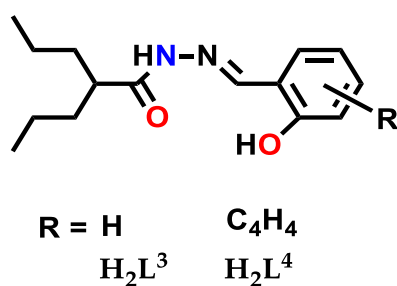


Chart III.1

2-hydroxy naphthaldehyde. X-ray crystallographic studies revealed the ligands bind through O, N, O coordinating neutral amide form. Partial reduction of **7**, **8** by constant potential electrolysis (CPE) successfully yielded corresponding dioxidovanadium (IV) complexes which was confirmed by EPR study. Solid state structures of all the complexes were established by single crystal X-ray diffraction technique. In the solution state all the ligands and complexes were characterized by 1H NMR, IR, absorption studies. Redox behaviors of the complexes were examined by cyclic voltametric and Spectroelectrochemical studies. The redox states were further explained with the help of theoretical spin density calculation using DFT. The complexes were found to be catalytically active towards oxidation of pyrogallol in aerobic condition.

*Manuscript is under review.

Introduction

Valproic acid¹ is a key building block for many medicinally important molecules for the treatment of cancer and various neurological diseases. Right now, the bio-potency of its hydrazone derivatives² is of special interest. This is because of its simple synthesis³, intrinsic conformational flexibility⁴ and medicinal uses.⁵

On the other hand, the coordination chemistry of vanadium with hydrazones is one of the most fascinating topics owing to their various applications⁶ including anticancer therapeutic potential⁷. Vanadium compound had been found wide spread bio-mimetic and catalytic application⁸ viz. insulin mimicking⁹, haloperoxidase activity,¹⁰ epoxidation.¹¹ Furthermore, vanadium dioxo compounds have always generated a great degree of interest for the chemist due to its potential catalytic¹² activity. Additionally, little is known about peroxidase mimicking activity employing oxygenations of pyrogallol¹³ catalysed by vanadium metal.

Herein, we presented two vanadium complexes $[V^V(O_2)HL^{3-4}]$ (**7**, **8**) depicted in **Chart III.2**. Two Schiff base ligands H_2L^3 and H_2L^4 were synthesised from condensation of valproic acid hydrazide and salicylaldehyde or 2-hydroxy naphthaldehyde. In order to characterise the compounds, various physio-chemical techniques were used. Solid-state structures of all the compounds were confirmed using single crystal X-ray diffraction technique. Cyclic voltammetry and Spectroelectrochemical techniques were employed to explore the redox behaviour of the complexes that was further supported by density functional theory (DFT) calculations.

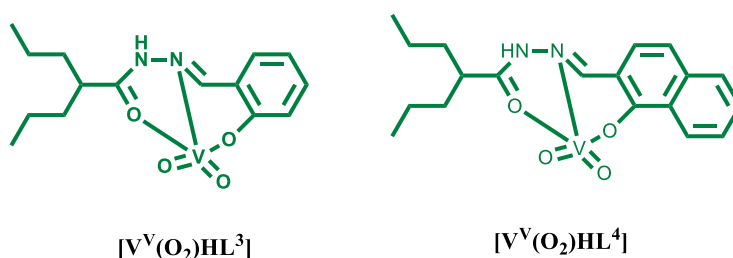


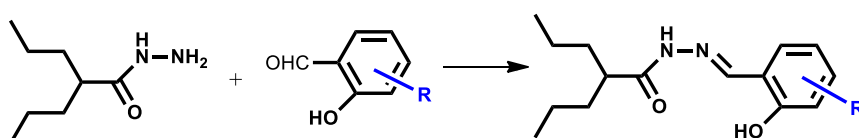
Chart III.2

III.1 RESULTS AND DISCUSSION

A. SYNTHESIS

i) LIGAND

The tridentate hydrazide based Schiff base ligands H_2L^2 and H_2L^4 used in this work are given in **Scheme III.1**. In this case, both acted as a mono-anionic neutral amido O, N, O donor for the preparation of the vanadium dioxo complex. Structure of the both the ligands were confirmed by X-ray crystallography.

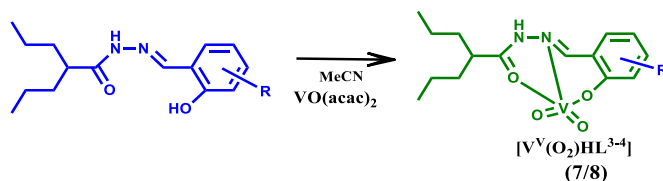


R	H_2L
H	H_2L^3
C_4H_4	H_2L^4

Scheme III.1. Schematic representation for the synthesis of the ligands

ii) COMPLEX

The reactions of $[VO(acac)_2]$ with an equimolar amount of the ligands in acetonitrile producing the green coloured monomeric dioxo complexes (**7** and **8**) in excellent yields. (**Scheme III.2.**) Structures were confirmed by X-ray crystallography.



R	H_2L
H	H_2L^3
C_4H_4	H_2L^4

Scheme III.2. Schematic representation for the synthesis of the complexes.

B. CRYSTAL STRUCTURE

Ligand H₂L³: The ligand H₂L³ was crystallized in the non-centrosymmetric monoclinic space group P21/c while H₂L⁴ was crystallized in orthorhombic system having space group P 21 21 21. The dihedral angles C2–C3–N1–N2 [-176.6°(2) in H₂L³ & 175.3°(3) in H₂L⁴], C3–N1–N2–C4 [(177.1°(2) in H₂L³ & 165.7°(4) in H₂L⁴], O2–C4–N2–N1 as [(2.9°(4) in H₂L³ & -6.9°(6) in H₂L⁴] indicated that the moiety containing hydrazone part in conjugation with aromatic ring was more close to planarity for H₂L³ than in H₂L⁴. The selected bond parameters for the crystal are listed in **Table III.1** and **Table III.2**, and the structures is shown in **Figure III.1**. Hydrazones generally exist in the amido form in the solid state, which is also confirmed from the HN2–C4 [1.353(3) Å in H₂L³ & 1.347(5) Å in H₂L⁴] and C4=O2 [1.221(3) Å in H₂L³ & 1.227(5) Å in H₂L⁴] bond lengths. Intermolecular hydrogen bonding interaction (**Figure III.2**), between acyl oxygen with imine hydrogen, O2 ⋯ H–N2 [2.033 Å in H₂L³ & 1.973 Å in H₂L⁴] due to the presence of the hydrazine functionality further determine the stability of the anti-isomer over the syn one.

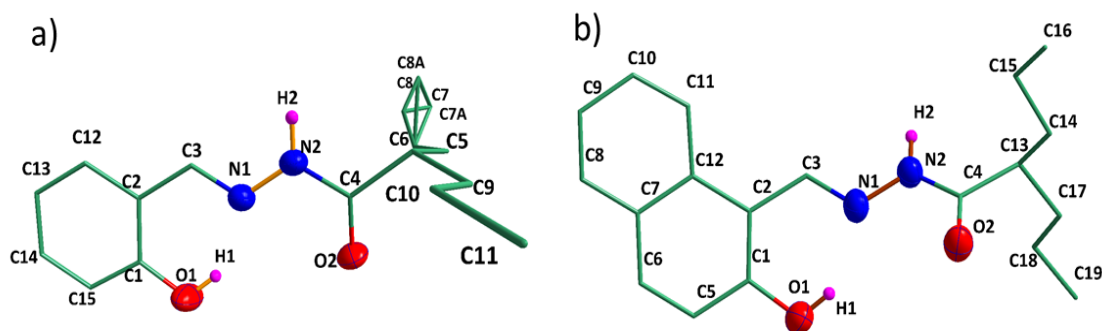


Figure III.1. ORTEP diagram (35% probability) ellipsoid and atom-numbering scheme for ligand a) H₂L³ and b) H₂L⁴

Table III.1. Selected Bond Distances (Å) and Angles (°) for H₂L³

Bond Length (Å)			Bond Angle (°)			
O1	-C1	1.342(3)	O1	-C1	-C2	122.5(3)
O2	-C4	1.220(4)	O1	-C1	-C15	117.8(3)
N1	-N2	1.368(3)	O2	-C4	-C5	123.1(2)
N1	-C3	1.275(3)	O2	-C4	-N2	121.8(3)
N2	-C4	1.353(3)	N1	-N2	-C4	119.8(2)
			N2	-N1	-C3	117.5(2)

Table III.2. Selected Bond Distances (Å) and Angles (°) for H₂L⁴

Bond Length (Å)			Bond Angle (°)			
O1	-C1	1.353(5)	O1	-C1	-C2	123.0(4)
O2	-C4	1.227(5)	O1	-C1	-C15	115.4(4)
N1	-N2	1.379(4)	O2	-C4	-C13	122.1(4)
N1	-C3	1.292(5)	O2	-C4	-N2	121.7(4)
N2	-C4	1.347(5)	N1	-N2	-C4	118.7(4)
			N2	-N1	-C3	118.1(4)

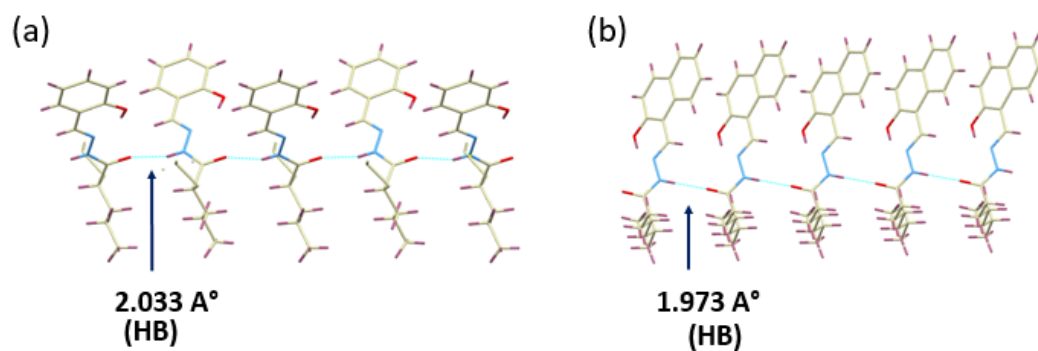


Figure III.2. Intramolecular Hydrogen bonding interaction of ligand a) H₂L³ b) H₂L⁴

Complex 7 and 8: Complex 7 crystallises in monoclinic system with space group P21/n 1 while complex 8 in triclinic system with P-1 space group. In the all the complexes V atom assumed five-coordinated distorted square pyramidal geometry, in which the basal plane is defined by the phenolate O, azomethine N, and acyl O atoms of the hydrazone ligand along with one of the oxo O atoms. The other terminal oxo O atom occupies apical position. The acyl oxygen-carbon bond distances i.e., C4=O2 bond distances are in the range 1.26-1.29 Å and HN2-C4 distances are around 1.32 Å which is consistent with binding through neutral amido form of the concerned hydrazones. The shortest V=O distances were ~1.6Å which is commonly found for typical V=O double bonds. The τ values of 0.37 for 7 and 0.36 for 8 suggest the geometries are very close to distorted square pyramid for both the complexes. The angles in the basal planes ranges from 73°-154° and that with the apical oxo O atom and the basal donor atoms falls in the range 96°-119°. The relevant crystallographic bond parameters are presented in **Table III.3.** and **Table III.4.** The crystal structure is shown in **Figure III.3.**

In complex 7, the N-H...O and C-H...O hydrogen bonds between the oxygen atoms of the two oxo groups with NNH functional group and aliphatic H, lead to the formation of 1D molecular chain. (**Figure III.4.**) Although the coordination environment in complex 8 around the metal centre in same as that of 7, but it contains water molecule as solvent of crystallization. Various hydrogen bonding interactions are present in 8 as the water molecule acts as both hydrogen bond donor and acceptor. As acceptor form N-H...O hydrogen bond and as donor, O-H...N and O-H...O hydrogen bonds between the oxygen atom of water with NNH functional group and one of the oxo oxygen leads to the formation of 1D molecular chain. In addition, presence of $\pi \cdots \pi$ interactions between phenyl rings of adjacent molecules (intermolecular) and phenyl ring of one with C=N group of other connect the chains into a two-dimensional double layer form. (**Figure III.5**)

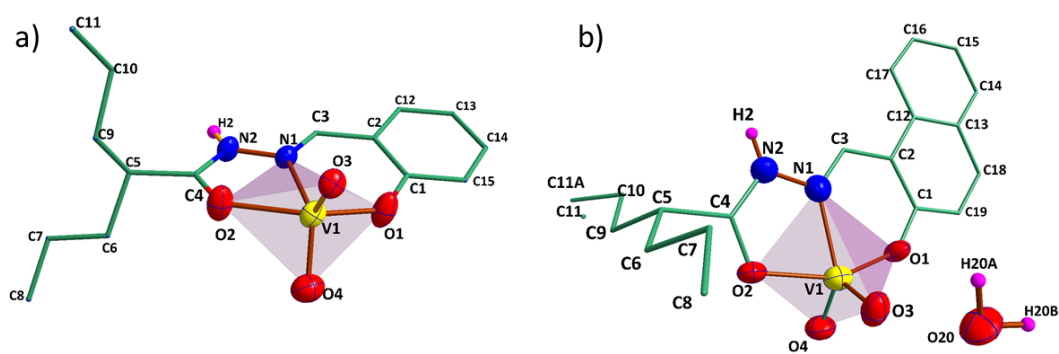


Figure III.3. ORTEP diagram (35% probability) ellipsoid and atom-numbering scheme for ligand a) Complex 7 and b) Complex 8

Table III.3. Selected Bond Distances (Å) and Angles (°) for Complex 7

Bond Length (Å)			Bond Angle (°)			
V1	-O1	1.8933(18)	O1	-V1	-O2	153.10(6)
V1	-O2	2.0391(18)	O1	-V1	-O3	103.08(8)
V1	-O3	1.6317(16)	O1	-V1	-O4	98.95(9)
V1	-O4	1.6068(19)	O1	-V1	-N1	80.90(7)
V1	-N1	2.1664(16)	O2	-V1	-O3	96.23(7)
O1	-C1	1.320(3)	O2	-V1	-O4	92.17(9)
O2	-C4	1.260(2)	O2	-V1	-N1	73.36(6)
N1	-N2	1.389(3)	O3	-V1	-O4	108.92(9)
N1	-C3	1.299(3)	O3	-V1	-N1	119.05(7)
N2	-C4	1.322(3)	O4	-V1	-N1	130.84(8)

Table III.4. Selected Bond Distances (Å) and Angles (°) for Complex 8

Bond Length (Å)			Bond angle (°)			
V1	-O1	1.888(8)	O1	-V1	-O2	154.1(4)
V1	-O2	2.022(8)	O1	-V1	-O3	100.7(4)
V1	-O3	1.629(10)	O1	-V1	-O4	98.2(5)
V1	-O4	1.605(10)	O1	-V1	-N1	80.7(4)
V1	-N1	2.117(11)	O2	-V1	-O3	97.6(4)
O1	-C1	1.295(16)	O2	-V1	-O4	92.6(5)
O2	-C4	1.290(17)	O2	-V1	-N1	74.6(4)
N1	-C3	1.294(16)	O3	-V1	-O4	109.6(5)
N1	-N2	1.393(15)	O3	-V1	-N1	117.5(4)
N2	-C4	1.320(18)	O4	-V1	-N1	132.3(4)

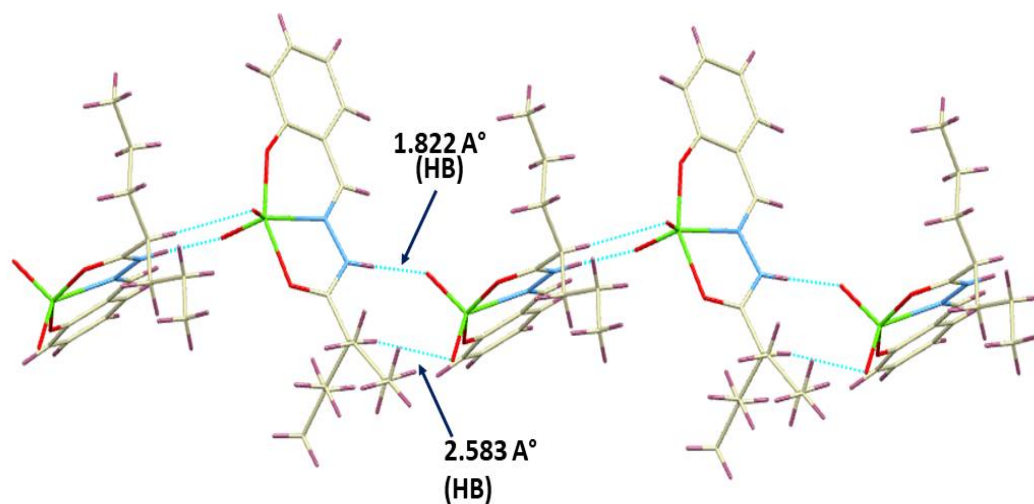


Figure III.4. Supramolecular architect of Complex 7

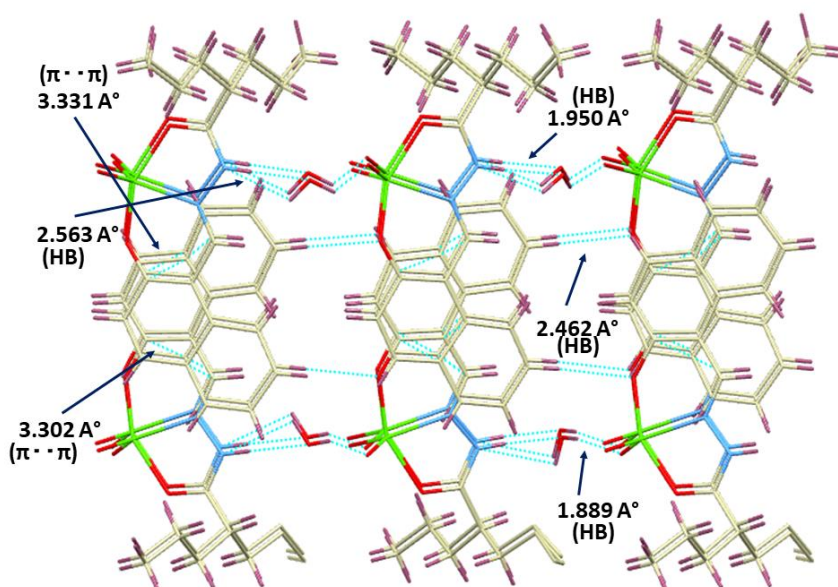


Figure III. 5. Supramolecular architect of Complex 8

C. ELECTRONIC ABSORPTION SPECTRA

The UV-vis absorption spectra of the ligands and complexes were recorded in

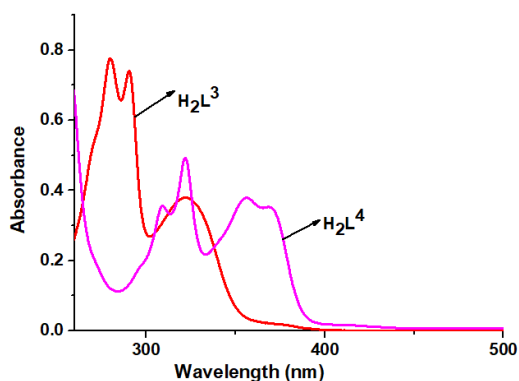


Figure III.6. Absorption spectra of HL^3 and HL^4 in methanol- CH_2Cl_2

methanol- CH_2Cl_2 (2: 8 ratio) at 298 K by employing concentrations in the range ~ 20 μM . The electronic spectrum of H_2L^3 exhibits three absorption bands. The band at 322 nm corresponds to intra-ligand $n \rightarrow \pi^*$ transition. The band with a shoulder at 290 nm and 280 nm may be assigned for the $\pi \rightarrow \pi^*$ transition of the aromatic rings and azomethine moiety. Ligand H_2L^4 showed similar type of band at around 355

nm with a weak shoulder at 368 nm and 321 nm with little hump at 308 nm. The red shift of λ_{max} value for H_2L^4 resulted from the extended conjugation. The spectra are illustrated in Figure III.6.

The electronic spectra of complexes are depicted in **Figure III.7**. As for the dioxovanadium (V) complexes no d-d bands are expected, the low energy bands in the region 263-268 nm and 320-336 nm can be attributed to ligand-centered charge transfer (LCT) bands. A broad shoulder in the range 396 - 412 nm for all the complexes can be assigned to LMCT bands. The presence of naphthalic conjugation induces a slight red shift for complex of H_2L^4 in comparison to complex of H_2L^3 . Absorption parameters of all the compounds are listed in **Table III.5**.

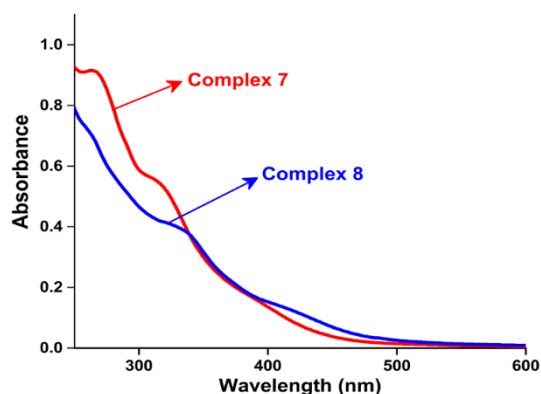


Figure III.7. Absorption spectra of complexes in methanol- CH_2Cl_2 (2:8) at 298K

Table III.5. Absorption parameters of the ligands and complexes -

Compounds	$\lambda_{\text{max}}(\text{nm})[\epsilon(\text{M}^{-1}\text{cm}^{-1})]$
Ligand H_2L^1	280 (38700), 290 (37000), 322 (18900)
Ligand H_2L^2	308 (17800), 321 (24500), 356 (19000), 368 (17700)
Complex 7	265 (45500), 320 (26800), 396 (7500)
Complex 8	263 (35000), 336 (19500), 412 (6700)

D. CYCLIC VOLTAMMETRY

The redox activities of **7** and **8** (referenced to the ferrocenium/ferrocene couple) were investigated by cyclic voltammetry in CH_2Cl_2 at 295 K containing $[\text{N}(\text{n-Bu})_4]\text{PF}_6$ as a supporting electrolyte. The cyclic voltammograms are illustrated in **Figure III.8**. The one electron reversible cathodic process in **7** and **8** at -0.168 and -0.174 V respectively are attributed to $\text{V}^{\text{V}}/\text{V}^{\text{IV}}$ reduction couple.

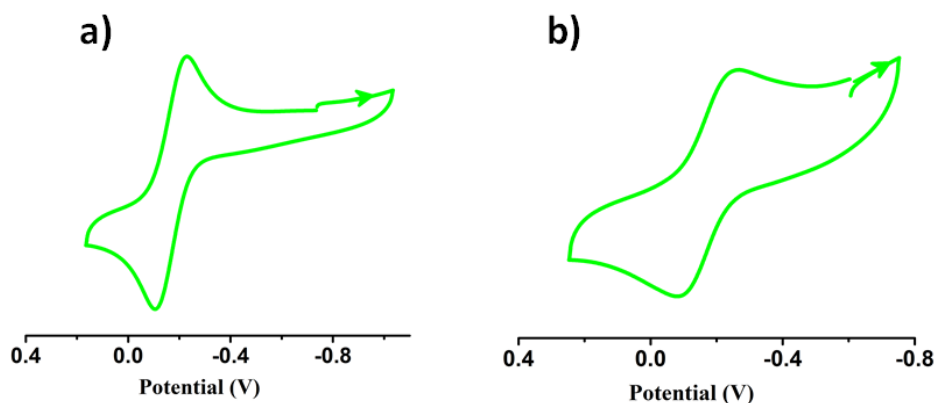


Figure III.8. Cyclic voltammograms of (a) **7**, (b) **8** in CH_2Cl_2 at 298 K. Conditions: scan rate, 100 mV s^{-1} ; 0.20 M $[\text{N}(\text{n-Bu})_4]\text{PF}_6$ supporting electrolyte; platinum working electrode.

E. SPECTROELECTROCHEMISTRY

Spectro-electrochemical measurements of the complexes were conducted to evaluate spectroscopic signatures of the reduced species in $\text{CH}_2\text{Cl}_2/0.3 \text{ M}$ $[\text{N}(\text{n-Bu})_4]\text{PF}_6$ system. The electron transfer process in complex **7** resulted in decrease of intensity at 280 nm, 370 nm, and very lower intensity band at 445 nm with generation of a new band around 383 nm. Whereas, in case of dioxo complex **8**, the changes in the existing peaks 338 nm (decreasing), lower intensity broad band 460 nm (decreasing), 270 nm (increasing) resulted along with shifting of the peaks from 407 nm to 414 nm. Isosbestic crossover points $\sim 406 \text{ nm}$ and $\sim 448 \text{ nm}$ respectively proved the transformation of reduced species through a common intermediate for both. (**Figure III.9.**)

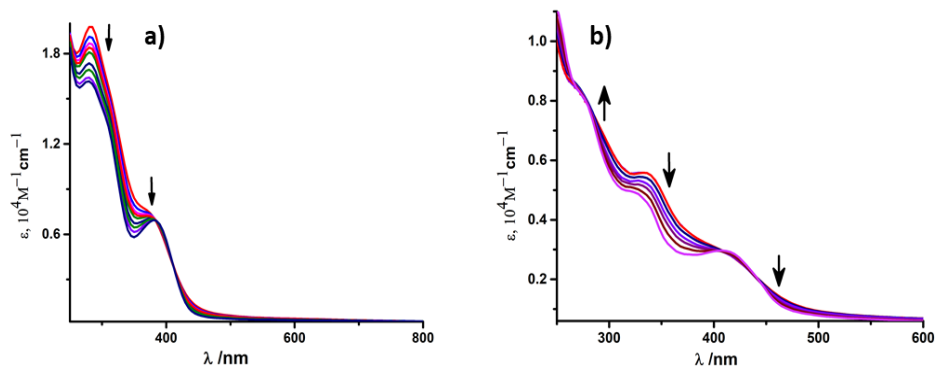


Figure III.9. Change of absorption spectra during (a) **7** \rightarrow **7⁻** and (b) **8** \rightarrow **8⁻** conversions in CH_2Cl_2 achieved by constant potential Spectro electrochemical

F. EPR STUDY

The complexes were diamagnetic in nature hence EPR silent whereas, the electrochemically reduced species were found to be paramagnetic. The EPR spectra of all the species were recorded in CH_2Cl_2 solution at ambient temperature. The EPR spectrum of all the electro-generated mononuclear anionic complexes exhibited characteristic eight-line spectrum (**Figure III.10**, **Table III.6**) due to presence of one extra unpaired electron spin ($S = 1/2$) and hyperfine coupling of ^{51}V ($I=7/2$). Spectra resembled octahedral coordination sphere of vanadium (IV) complexes. This shifting of diamagnetic $[\text{V}^{\text{VO}}]^{2+}$ to paramagnetic $[\text{V}^{\text{IVO}}]^{2+}$ is also supported by spin density data from DFT calculations.

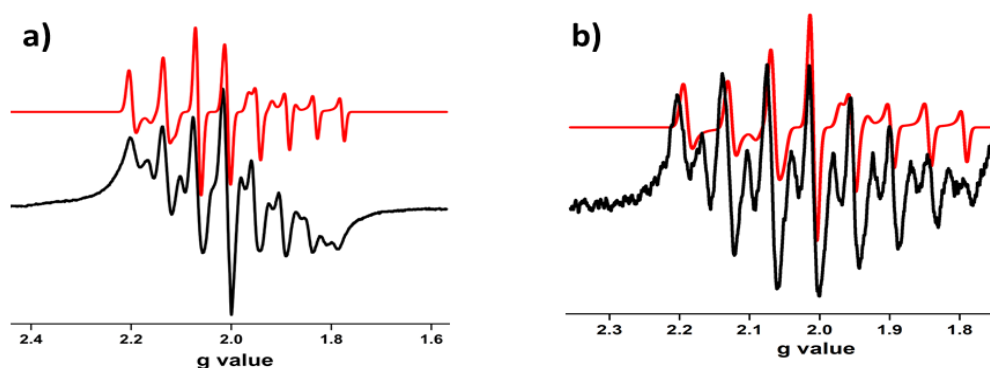


Figure III.10. X-band EPR spectra of a) complex **7**⁻ b) complex **8**⁻ at RT (black-experimental; red-simulated)

Table III.6. X-band EPR Spectral parameter of complex **7**⁻ and **8**⁻

Complex	Matrix	g_{\parallel}	g_{\perp}	g_{av}	A_{\parallel} (G)	A_{\perp} (G)	A_{av} (G)	lw (mT)
7 ⁻	CH_2Cl_2 , 300 K	1.9525	1.9643	1.9564	262.05	204.73	223.84	1.6
8 ⁻	CH_2Cl_2 , 300 K	1.9525	1.9643	1.9564	270.00	186.647	223.84	1.6

G. THEORETICAL CALCULATIONS

In all the cases, the highest occupied molecular orbital (HOMO) is localized mostly on the ligand framework. (**Figure III.11.**) This is an obvious sign of metal-centred reduction. However, in contrast, the LUMO of **7** & **8** is localized predominantly on the ligand moiety and very little on vanadium. The spin density obtained (**Figure III.12**) from the Mulliken spin population analysis of 7^- and 8^- scatters mainly on the ligand moiety, most on the imine nitrogen and very little on vanadium core, inferring the electron density transfer from vanadium to ligand or electron density reconstruction. But from cyclic voltammetry study one electron vanadium centre reduction was observed. CV study and spin density pattern infers that the V^V to V^{IV} and subsequently the spin delocalization for imine reduction process. (**Figure III.10, Table III.6.**)

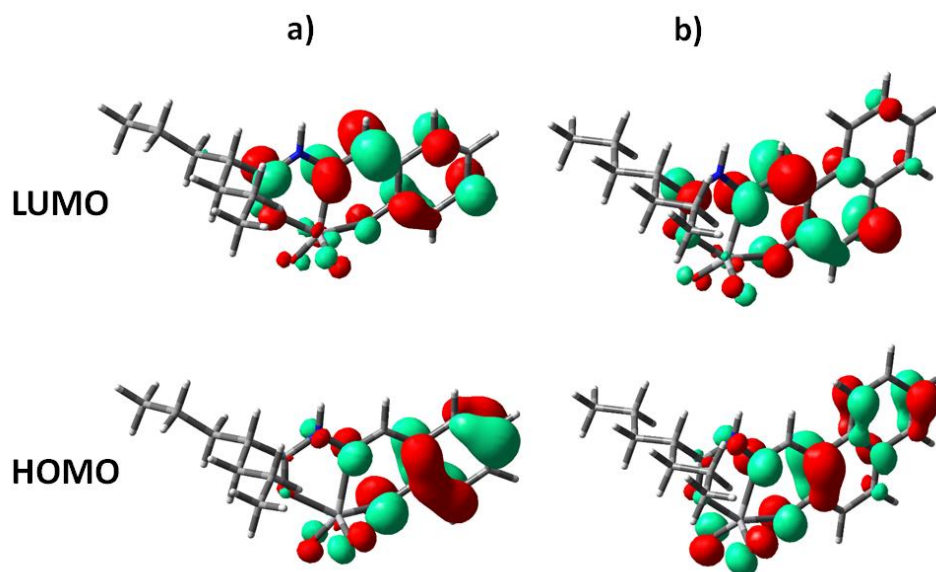


Figure III.11. Isodensity plot of selected frontier orbitals of complexes 7 and 8

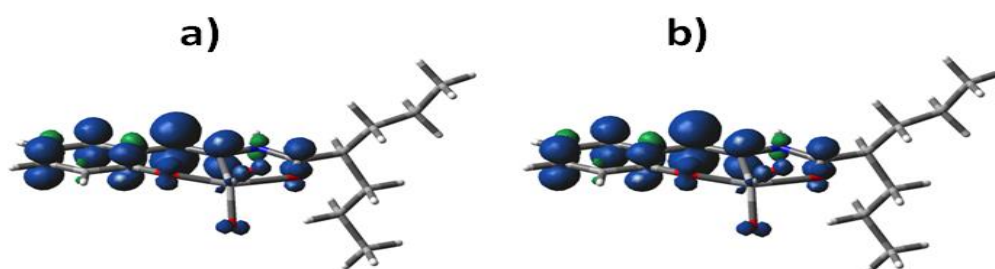


Figure III.12. Spin density plot of (a) 7^- (b) 8^-

H. CATALYTIC OXIDATION OF PYROGALLOL

Active oxygen molecules, such as hydrogen peroxide, peroxy compounds, or molecular oxygen, are frequently used as primary oxidants in transition metal catalysed oxidations. We were interested in examining pyrogallol's oxidation by the vanadium complexes since it shares structural similarities with catechol. In this case the dioxo complexes (7, 8) catalyzed the reaction mere aerobic condition in absence of H₂O₂. To check the catalytic potential of complexes 7-8 towards oxidation of pyrogallol, 6 × 10⁻⁴ M solution of complexes was treated with a 10-fold concentrated solution of pyrogallol in aerobic condition and the course of the reaction was followed by recording UV-vis spectra up to 20 min. The first spectral run of the dark blue solution showed a nearly identical pattern to that of catechol due to the similarity in substrate structure. The band near 580 nm gradually decreases while the band near 412 nm (for 8) or 388 nm (for 7) gradually increases, indicating formation of purpurogallin. The kinetics of the pyrogallol oxidation was determined by the initial rates method by monitoring the increase of the product purpurogallin. For this purpose, a 6 × 10⁻⁴ M solution of complexes were treated with 0.001 M - 0.01 M solution of pyrogallol. Following are the conclusions drawn from the Michaelis-Menten and Lineweaver-Burk equations. [Complex 7: $k_2 = 10.2 \text{ min}^{-1}$, $K_M = 1.2 \times 10^{-3}$ and $V_{\text{max}} = 6.1 \times 10^{-3} \text{ M min}^{-1}$ (**Figure III.13**) and Complex 8: $k_2 = 8.5 \text{ min}^{-1}$, $K_M = 1.12 \times 10^{-3}$ and $V_{\text{max}} = 5.1 \times 10^{-3} \text{ M min}^{-1}$] (**Figure III.14**)

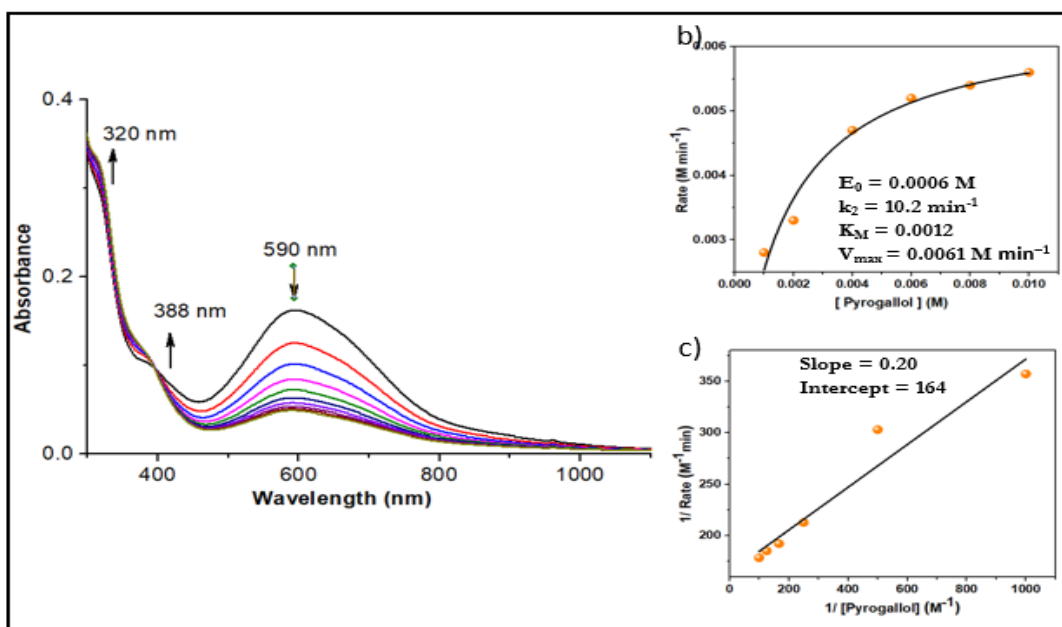


Figure III.13. (a) Absorption spectra of a solution containing 6×10^{-4} M of complex 7 and 0.01 M of Pyrogallol, recorded at the interval of 1 min. (b) Plot of rate versus concentration of Pyrogallol for the oxidation reaction catalysed by complex. (c) Lineweaver–Burk plot

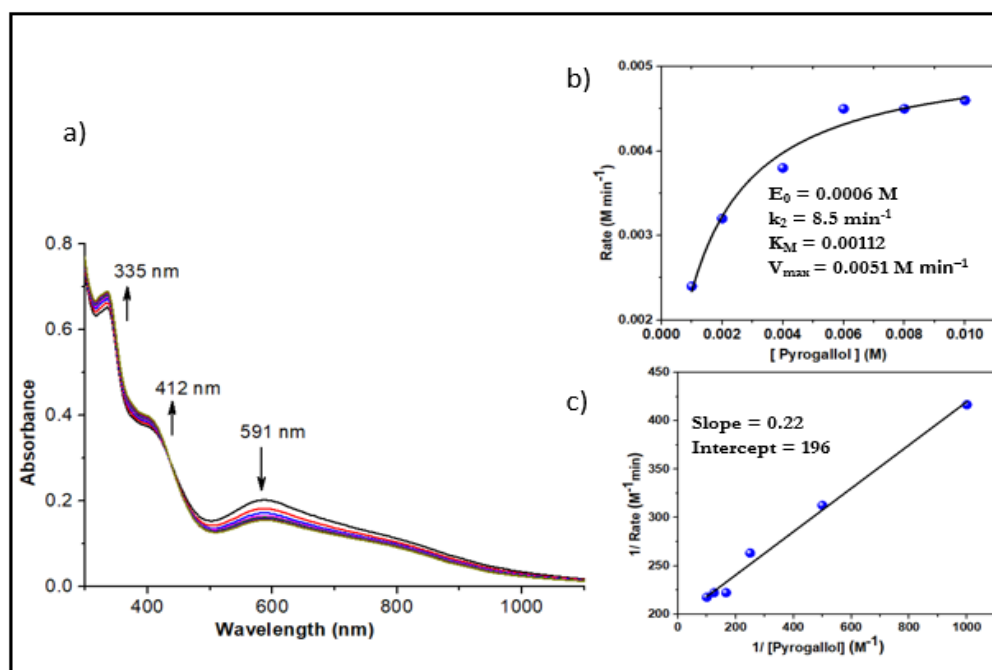
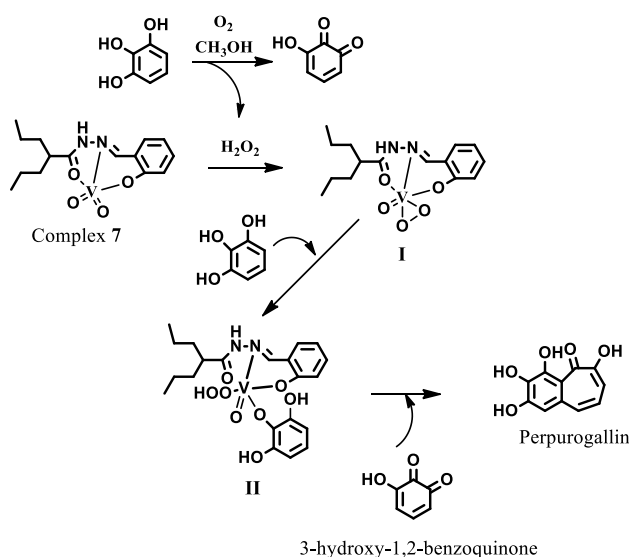


Figure III.14(a) Absorption spectra of a solution containing 6×10^{-4} M of complex 8 and 0.01 M of Pyrogallol, recorded at the interval of 1 min. (b) Plot of rate versus concentration of Pyrogallol for the oxidation reaction catalyzed by complex. (c) Lineweaver–Burk plot

Probable reaction pathway

Complexes **7** and **8** were found to be catalytically active merely in aerobic condition using molecular oxygen. even in the absence of oxidant H_2O_2 although in general, according to literature¹³ the process requires H_2O_2 as a source of oxidant. To comprehend the reaction mechanism, we have performed mass spectrometry analysis in addition to UV/VIS spectra. We discovered the production oxo-peroxo intermediate from mass spectra of reaction mixtures of pyrogallol with dioxo complexes **7** in air. It's possible that the initial autooxidation¹⁴ of pyrogallol results in the production of 3-hydroxy-1,2-benzoquinone and H_2O_2 . This H_2O_2 combines with complex **7** to create intermediate **I** of peroxovanadium ($m/z = 359$), which then joins with pyrogallol to create intermediate **II** ($m/z = 485$) (**Figure III.20.**). Following that, intermediate **II** and 3-hydroxy-1,2-benzoquinone aid in the production of purpurogallin. Once more, comparable kinds of pyrogallol association intermediates ($m/z = 535$) and peroxo vanadium intermediates ($m/z = 409$) were generated for the complexes **8** (**Figure III.21.**). This suggested chemical mechanism is based on mass spectrometry and UV-vis spectra is given for complex **7**. (**Scheme III.3.**) Presence of peak at $m/z = 220$, in both the cases confirmed the formation of purpurogalline.



Scheme III.3. Schematic representation for pyrogallol oxidation by 7

III.2. CONCLUSION

In this chapter, it is shown that use of acetonitrile as a solvent generate two dioxo $[V^V(O_2)HL^{3-4}]$ (7, 8) starting from $VO(acac)_2$ and two valproic acid hydrazine ligands. In comparison to previous chapter, substitution of aromatic fragment with aliphatic group leads to formation of oxidodioxo vanadium (V) complexes instead of mono oxo bridge dimeric complex in the identical reaction condition. Single-crystal X-ray diffraction study revealed that the ligands crystallised in keto-amine tautomeric form, which was retained in complexes too. Redox state of the complexes was characterised by cyclic voltammogram, Spectroelectrochemical study, and EPR spectra. Dioxo Complexes were electrochemically reduced to generate oxidodioxo vanadium (IV) complexes which further confirm their electronic state. Theoretical spin density calculation of the reduced species further supported the electronic distribution of the complex. Lastly, the compounds were found to catalyse the oxidation of pyrogallol in aerobic condition in the absence of any external oxidant like H_2O_2 . In a keyword, the reaction was supposed to be proceeding with in situ generated oxidant.

III.3 EXPERIMENTAL SECTION

A. MATERIALS

$[VO(acac)_2]$ used was prepared according to the literature.¹⁵ are used throughout the study. All the reactions with metal salts are carried out under open air atmosphere. All analytically pure solvents were purchased from reputed commercial sources and used without further purification.

B. PREPARATION OF COMPOUNDS

LIGAND

Schiff base ligands (H_2L^{3-4}), were prepared by condensation of equimolar amount of valprohydrazide (10 mmol) with salicylaldehyde (H_2L^3) or 2-hydroxy naphthaldehyde (H_2L^4) in methanol.

H₂L³: Anal. Calc. for C₁₅H₂₂N₂O₂: C 68.67%; H 8.45%; N 10.68%; Found: C 68.59%; H, 8.38%; N, 10.60%. ¹H NMR {300 MHz, CDCl₃, δ (ppm), J (Hz)}: 10.86 (NH, s), 9.01 (OH, s), 8.06 (-CH=N, s) 7.36–6.94 (4H, ArH), 3.18–3.15 (1H, m, -CH). 1.79–1.33 (8H, m, 4CH₂), 0.95–0.92 (6H, m, 2CH₃). (ESI -MS (positive) in MeOH: The base peak was detected at *m/z* = 285, corresponding to [M + Na]⁺. IR (KBr, ν_{max} / cm⁻¹): 3061(O-H); 2919(N-H); 1659(C=O), 1618(C=N).

H₂L⁴: Anal. Calc. for C₁₉H₂₄N₂O₂: C 73.05%; H 7.74%; N 8.97%; Found: C 72.92%; H, 7.69%; N, 8.91%. ¹H NMR {300 MHz, CDCl₃, δ (ppm), J (Hz)}: 11.52 (NH, s), 9.49 (OH, s), 8.91 (-CH=N, s) 8.03–7.23 (6H, ArH), 2.22–2.19 (1H, m, -CH). 1.66–1.28 (8H, m, 4CH₂), 0.98–0.86 (6H, m, 2CH₃). (ESI -MS (positive) in MeOH: The base peak was detected at *m/z* = 313, corresponding to [M + H]⁺. IR (KBr, ν_{max} / cm⁻¹): 3190(O-H); 2940(N-H); 1725(C=O); 1646(C=N)

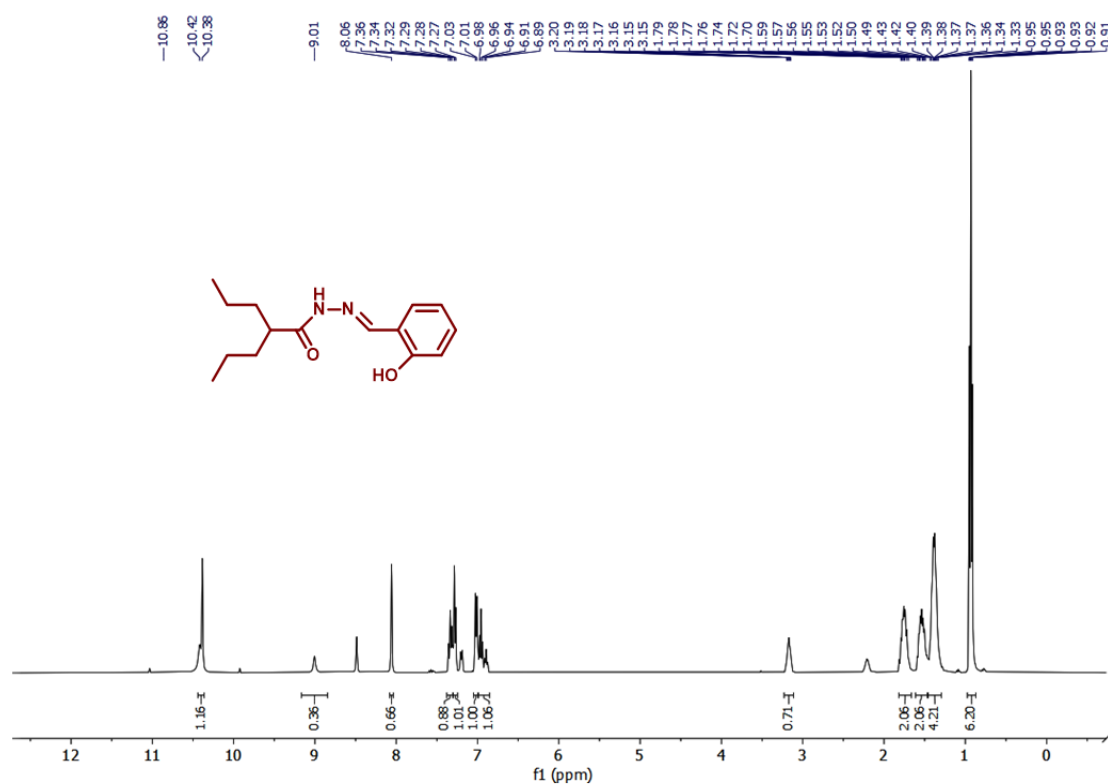


Figure III.15. ¹H NMR spectra of H₂L³ in CDCl₃

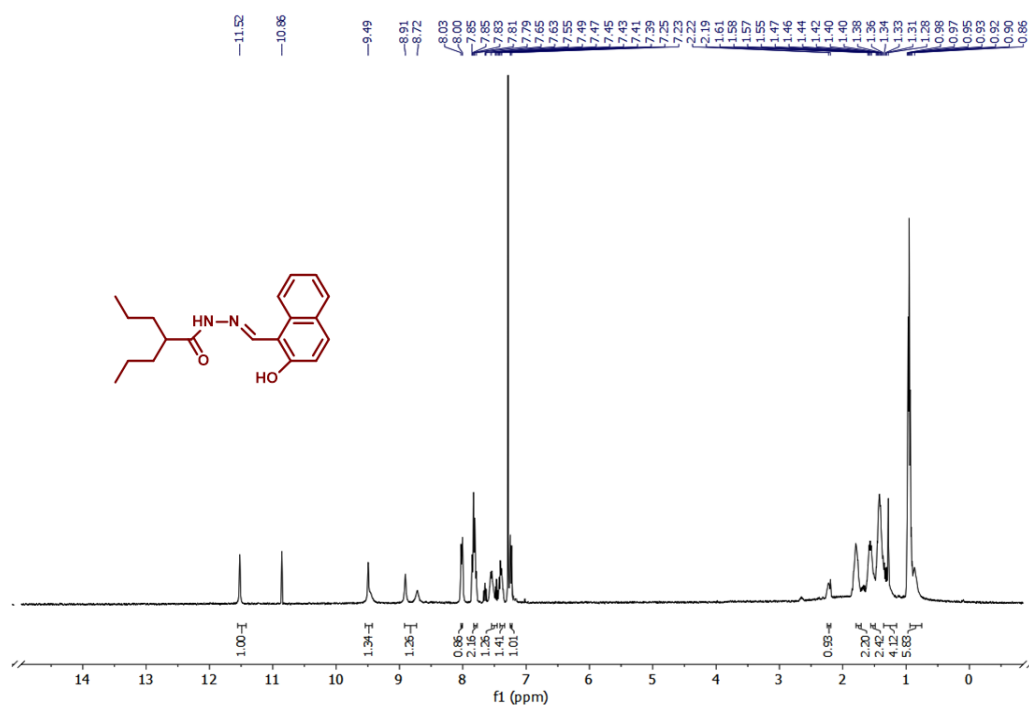


Figure III.15. ¹H NMR spectra of H₂L⁴ in CDCl₃

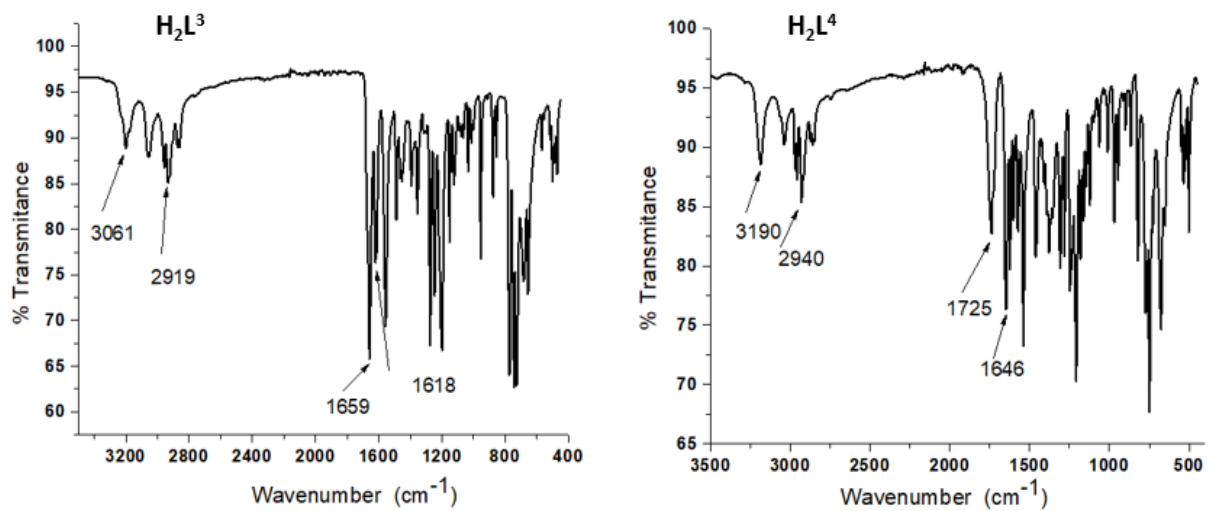


Figure III.16. IR Spectra of ligand H₂L³ and H₂L⁴

COMPLEX

Synthesis of dioxovanadium(V) complexes [V^VO₂(HL³⁻⁴)], (7 and 8).

A 10 ml acetonitrile solution of VO(acac)₂ (5 mmol) was added to an acetonitrile solution of ligand (H₂L³ or H₂L⁴) (5 mmol) and the resultant reaction mixture was stirred at room temperature for 6 h. The solution was then filtered. Light green-coloured crystals resulted from the slow evaporation of acetonitrile solution of the complexes.

[V^VO₂(HL³)] (7): Yield: 76%. Anal. Calc. for C₁₅H₂₁VN₂O₄: C 52.33%; H 6.15 %; N 8.14%. Found: C 52.28%; H 6.02%; N 8.06%. ¹H NMR {300 MHz, CDCl₃, δ (ppm), 11.605 (1H, s, -NH), 8.717 (1H, s, -N=CH), 7.708–6.799 (4H, m, Ar-H), 2.066–2.048 (1H, m, -CH), 1.543–1.249 (8H, m, 4CH₂), 0.843 (6H, m, 2CH₃). (ESI -MS (positive) in MeOH: The base peak was detected at *m/z* = 343, corresponding to [M]⁺. IR (KBr, *v*_{max} / cm⁻¹): 2980 (N-H); 1615 (C=O); 1547 C=N), 1264 (C-O)_{enolic}; 976 (V=O); 748 (V-O).

[V^VO₂(HL⁴)] (8): Yield: 72%. Anal. Calc. for C₁₉H₂₃VN₂O₄: C 57.87%; H 5.88%; N 7.10%; Found: C 57.77%; H, 5.72%; N, 7.03%. ¹H NMR {300 MHz, DMSO-D₆, δ (ppm), 9.635 (1H, s, -NH), 8.525 (1H, s, -N=CH), 8.278–7.073 (6H, m, Ar-H), 2.309–2.284 (1H, m, -CH), 1.603–1.287 (8H, m, 4CH₂), 0.904–0.882 (6H, m, 2CH₃). (ESI -MS (positive) in MeOH: The base peak was detected at *m/z* = 395, corresponding to [M]⁺. IR (KBr, *v*_{max} / cm⁻¹): 2966 (N-H); 1607 (C=O); 1548 C=N), 1291 (C-O)_{enolic}; 964 (V=O); 753 (V-O).

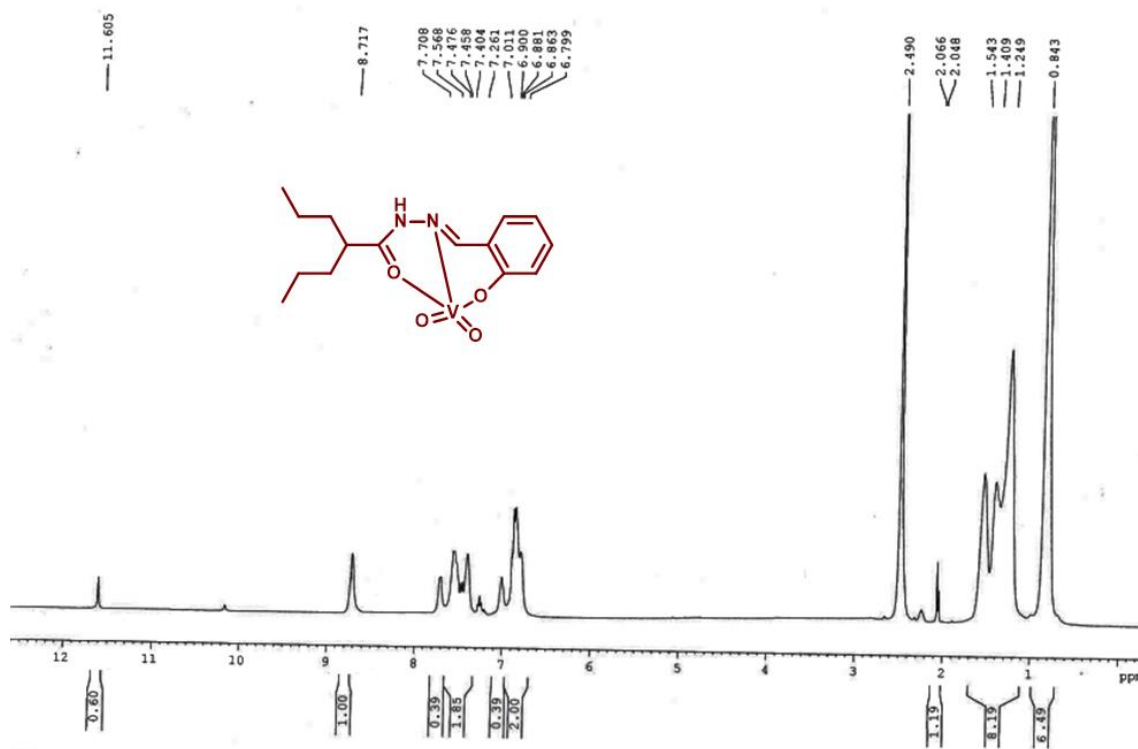


Figure III.17. ¹H NMR spectra of Complex 7 in DMSO-d₆

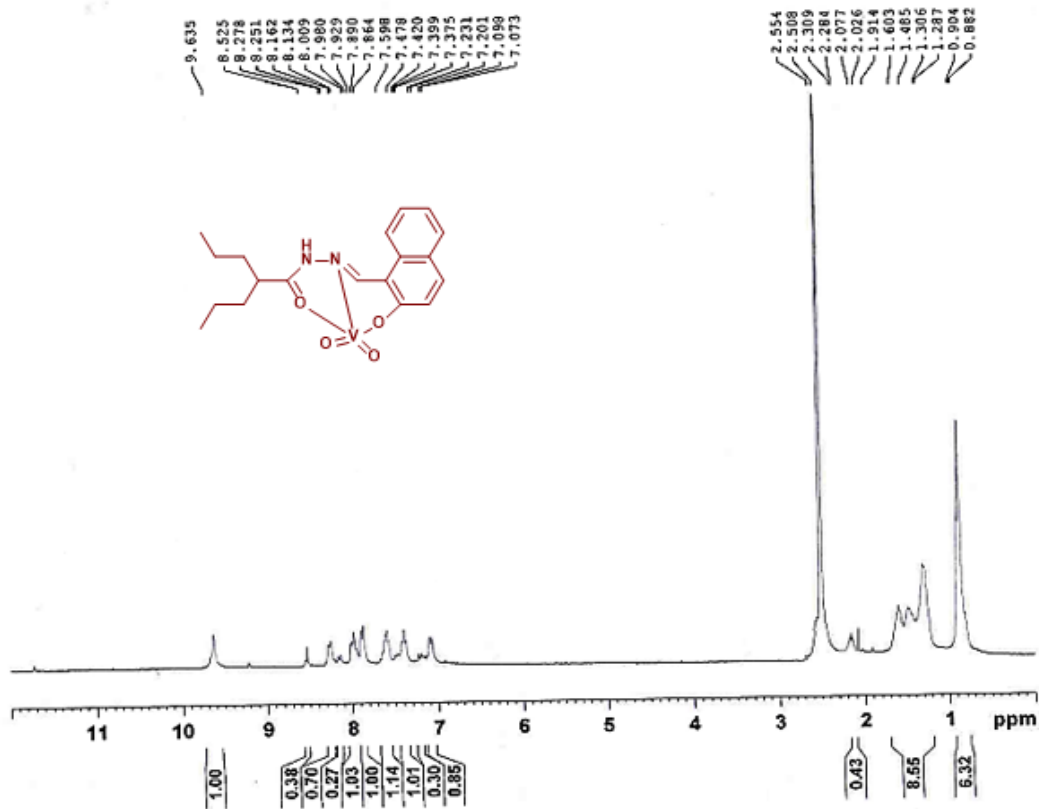


Figure III.18. ¹H NMR spectra of Complex 8 in DMSO-d₆

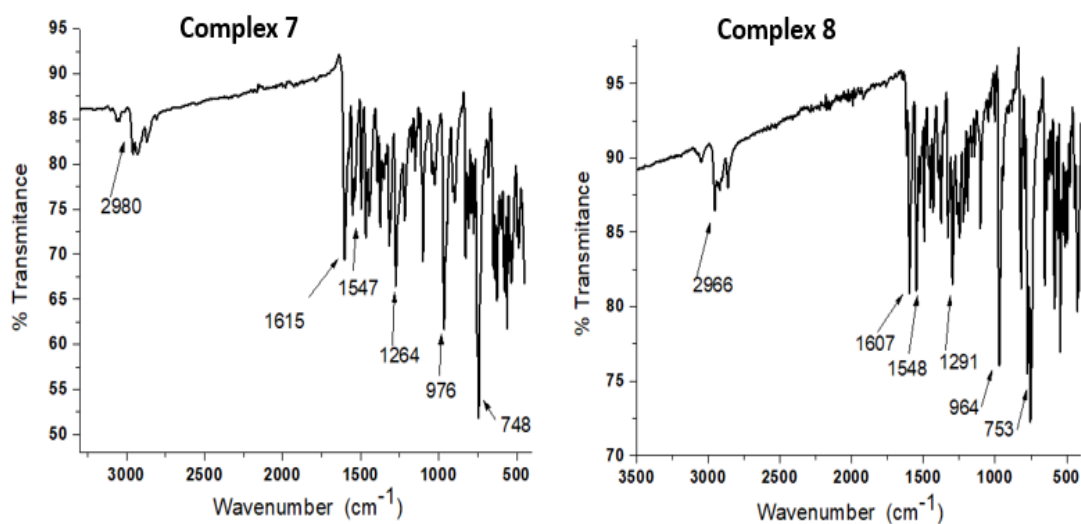


Figure III.19. IR spectra of Complex 7 and Complex 8.

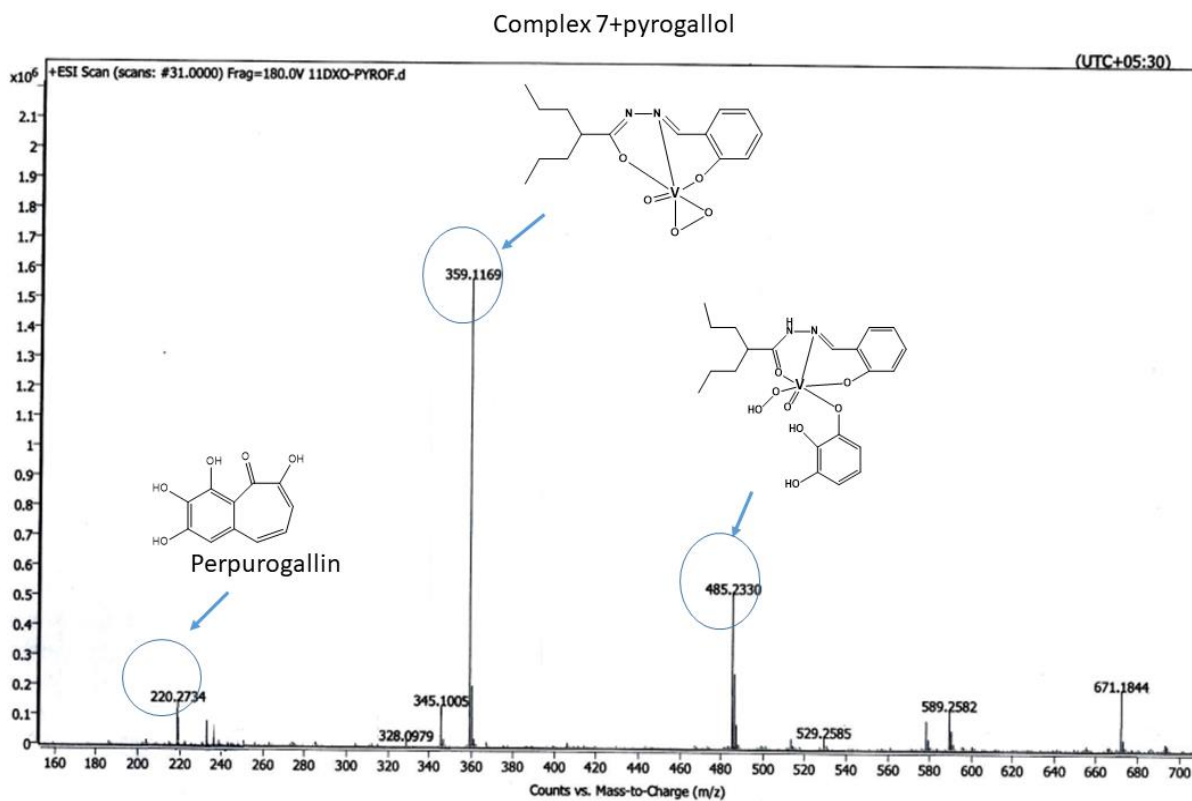


Figure III.20. Mass spectrum of [Complex 7 + pyrogallol] system

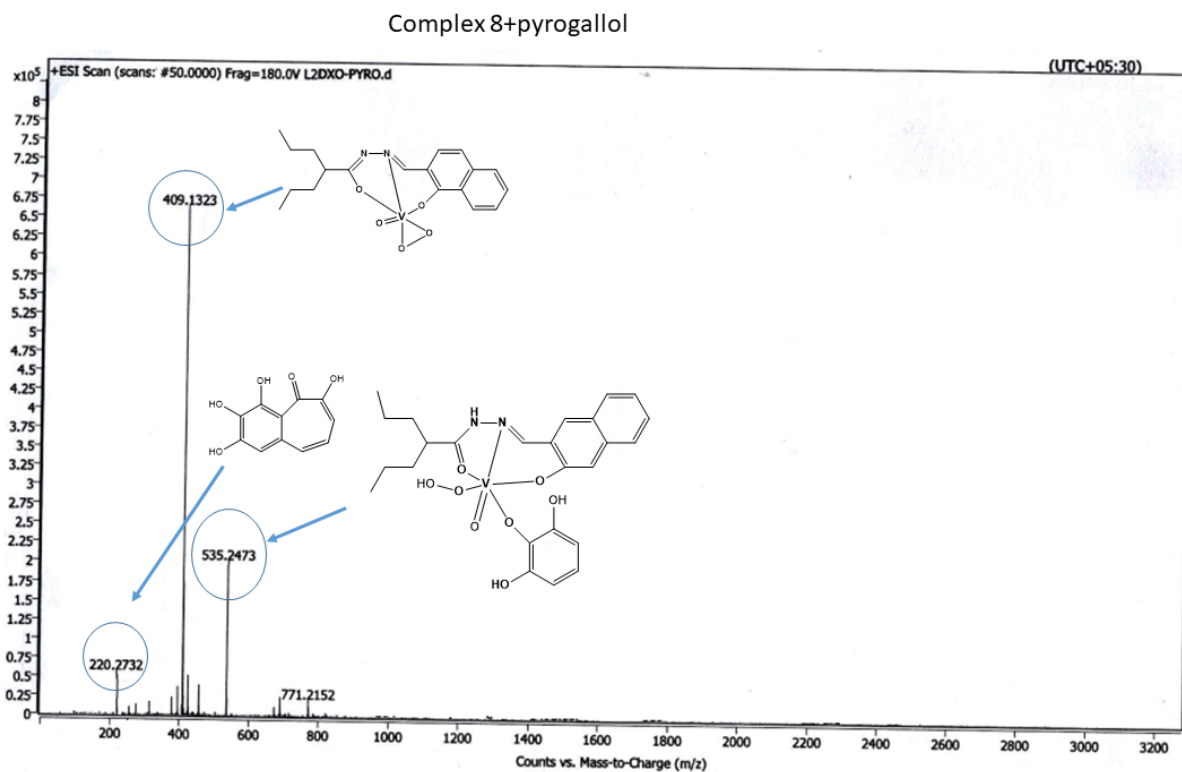


Figure III.21. Mass spectrum of [Complex 8 + pyrogallol] system

C. X-RAY STRUCTURE DETERMINATION

The single crystal suitable for X-ray crystallographic analysis of the ligand H₂L³, H₂L⁴ was obtained by slow evaporation of methanolic solution and for complex 7, 8 it was obtained by slow evaporation from acetonitrile solution at 25°C. Details of the X-ray work are given in tabular form in **Table III.6.** (See also **Chapter I.**). Atomic coordinates and isotropic thermal parameters are collected in **Table III.7., Table III.8., Table III.9.** and **Table III.10.** respectively

D. PHYSICAL MEASUREMENTS AND COMPUTATIONAL STUDIES

All physical measurements that included elemental analyses, IR, ESI-MS studies, absorption spectra, ¹H NMR spectra, Cyclic Voltammetry studies, EPR Spectra, Constant Potential Electrolysis (CPE), Spectroelectrochemistry measurements and computational studies were performed as described in **Chapter I**

Table III.6. Crystallographic data for ligand and complexes

Crystal Data

	H₂L³	H₂L⁴	Complex 7	Complex 8
Chemical Formula	C ₁₅ H ₂₂ N ₂ O ₂	C ₁₉ H ₂₄ N ₂ O ₂	C ₁₅ H ₂₁ N ₂ O ₄ V	C ₁₉ H ₂₃ N ₂ O ₅ V
Formula weight	262.17	312.40	344.283	409.83
Crystal system	Monoclinic	orthorhombic	Monoclinic	Triclinic
Space group	P21/c	P21 21 21	P21/n	P-1
<i>a</i> /Å	9.0199(16)	4.9108(7)	9.75988(12)	6.960(3)
<i>b</i> /Å	19.834(3)	11.4224(14)	13.8657(17)	15.399(7)
<i>c</i> /Å	9.7259(15)	30.400(4)	13.1083(14)	37.316(16)
<i>α</i> /°	90	90	90	89.977(11)
<i>β</i> /°	115.716(5)	90	111.860	90.2300
<i>γ</i> /°	90	90	90	90.4500
<i>V</i> /Å ³	1567.6(4)	1705.2(4)	1646.4(3)	3999(3)
<i>Z</i>	4	4	4	8
<i>D</i> _{calcd} /mg m ⁻³	1.082	1.217	1.389	1.361
<i>μ</i> /mm ⁻¹	0.073	0.079	0.621	0.526
<i>θ</i> /°	26.4	27.07	27.534	25.242
<i>T</i> /K	273.15	293	273.15	293.15

Data collection

	H₂L³	H₂L⁴	Complex 7	Complex 8
Total refl. collected	23220	7437	13959	84225
Unique refl. (<i>R</i> _{int})	3564	3748	3759	14538
Used refl.	3492	1859	3077	4538
<i>h k l</i> range	12 ≤ <i>h</i> ≤ 12 -18 ≤ <i>k</i> ≤ 15 -17 ≤ <i>l</i> ≤ 16	-6 ≤ <i>h</i> ≤ 6 -14 ≤ <i>k</i> ≤ 14 -39 ≤ <i>l</i> ≤ 38	-12 ≤ <i>h</i> ≤ 12 -18 ≤ <i>k</i> ≤ 15 -17 ≤ <i>l</i> ≤ 16	-8 ≤ <i>h</i> ≤ 8 -18 ≤ <i>k</i> ≤ 18 -44 ≤ <i>l</i> ≤ 44

Structure Solution and Refinement

	H ₂ L ³	H ₂ L ⁴	Complex 7	Complex 8
Solution	Patterson	Patterson	Patterson	Patterson
Refinement	Full-matrix least-squares on F ²	Full-matrix least-squares on F ²	Full-matrix least-squares on F ²	Full-matrix least-squares on F ²
GOF on F ²	1.03	1.021	1.05	1.02
R1, ^a [I > 2σ(I)]	0.0828	0.0529	0.0414	0.4250
wR2 ^b [I > 2σ(I)]	0.2836	0.1634	0.1004	0.1300
R1 [all data]	0.0664	0.035	0.084	0.124
wR2 [all data]	0.0976	0.092	0.095	0.28

$$^a R1 = \frac{\sum ||F_o| - |F_c||}{\sum |F_o|} \quad ^b wR2 = [\frac{\sum [w(F_o^2 - F_c^2)^2]}{\sum [w(F_o^2)^2]}]^{1/2}$$

Table III.7 Fractional Atomic Coordinates ($\times 10^4$) and Equivalent Isotropic Displacement Parameters ($\text{\AA}^2 \times 10^3$) for H_2L^3 . \mathbf{U}_{eq} is defined as 1/3 of the trace of the orthogonalized U_{ij} tensor.

Atom	<i>x</i>	<i>y</i>	<i>z</i>	$\mathbf{U}(eq)$
N1	5603(2)	3318.4(9)	5742(2)	56.6(5)
N2	6815(3)	2868.3(10)	5897(2)	59.0(5)
O1	3693(3)	3965.8(13)	6701(2)	90.7(7)
O2	7085(3)	2526.9(10)	8200.0(19)	77.7(6)
C3	5014(3)	3678.6(12)	4537(3)	58.6(6)
C14	1551(4)	5224.0(17)	3883(5)	99.4(11)
C15	2075(4)	4845.3(17)	5160(5)	88.6(10)
C1	3212(3)	4324.1(14)	5408(3)	69.4(7)
C2	3792(3)	4193.5(12)	4322(3)	61.9(6)
C4	7532(3)	2494.8(12)	7184(3)	58.4(6)
C5	8945(3)	2059.5(13)	7281(3)	68.0(7)
C6	8550(5)	1312.1(16)	7401(6)	114.2(14)
C7	7099(8)	1103(4)	5677(8)	103.1(17)
C8	6761(11)	358(5)	5608(10)	127(2)
C9	10523(4)	2273.0(18)	8637(4)	88.0(9)
C10	11010(5)	3002(2)	8561(6)	118.6(14)
C11	12562(8)	3211(3)	9839(9)	192(3)
C13	2096(5)	5107.6(17)	2804(5)	100.0(11)
C12	3215(4)	4591.7(15)	3016(4)	82.2(8)
C7A	6968(12)	1011(5)	6511(12)	87(2)
C8A	7389(19)	802(8)	5139(17)	141(4)

Table III.8 Fractional Atomic Coordinates ($\times 10^4$) and Equivalent Isotropic Displacement Parameters ($\text{\AA}^2 \times 10^3$) for H_2L^4 . U_{eq} is defined as $1/3$ of the trace of the orthogonalized U_{ij} tensor.

Atom	<i>x</i>	<i>y</i>	<i>z</i>	<i>U</i> (eq)
O2	1266(7)	4656(3)	4120.5(9)	69.3(10)
O1	2401(7)	1502(3)	3536.5(10)	67.3(10)
N1	4944(8)	3452(3)	3663.0(11)	54.5(10)
N2	5662(7)	4312(3)	3959.4(11)	52.1(10)
C9	10319(11)	1648(5)	1875.2(15)	67.7(14)
C10	10991(11)	2591(4)	2142.9(16)	65.6(14)
C11	9697(11)	2763(4)	2535.7(15)	58.4(12)
C12	7638(9)	1995(4)	2680.5(13)	49.7(11)
C2	6122(9)	2166(4)	3084.4(13)	47.7(11)
C3	6736(10)	3126(4)	3377.3(13)	52.1(11)
C4	3684(10)	4841(4)	4193.5(13)	51.8(11)
C13	4613(9)	5643(4)	4557.7(13)	54.9(12)
C14	3575(10)	6888(4)	4476.0(14)	62.3(12)
C15	4808(12)	7469(4)	4075.6(16)	74.5(16)
C16	3706(15)	8687(5)	3989.6(19)	103(2)
C17	3577(11)	5163(4)	4996.6(13)	65.9(13)
C18	4548(13)	3956(5)	5109.6(16)	82.6(17)
C19	3516(15)	3508(5)	5550.0(17)	106(2)
C1	4051(9)	1382(4)	3182.7(13)	53.1(11)
C5	3550(10)	393(4)	2919.7(14)	59.0(12)
C6	4977(10)	226(4)	2546.6(14)	58.9(12)
C7	7025(10)	1018(4)	2409.9(14)	53.9(12)
C8	8391(11)	871(4)	2006.5(14)	62.2(13)

Table III.9 Fractional Atomic Coordinates ($\times 10^4$) and Equivalent Isotropic Displacement Parameters ($\text{\AA}^2 \times 10^3$) for Complex 7. U_{eq} is defined as $1/3$ of the trace of the orthogonalized U_{ij} tensor.

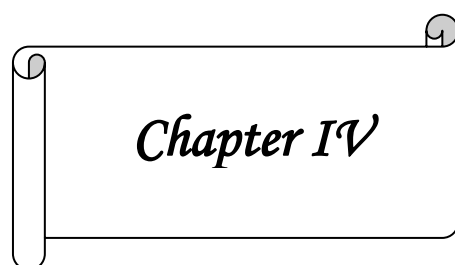
Atom	<i>x</i>	<i>y</i>	<i>z</i>	U(eq)
V1	5843.0(4)	1539.4(3)	7463.1(3)	32.50(13)
O1	6762.2(19)	502.3(12)	7025.6(12)	49.4(4)
O2	4301.4(18)	2603.6(12)	7168.9(11)	45.0(4)
O3	7239.3(16)	2181.7(11)	8246.4(12)	41.2(4)
N1	4975.1(18)	1790.8(12)	5705.6(13)	29.3(4)
N2	3844.3(19)	2467.8(13)	5381.3(13)	31.3(4)
O4	5167(2)	954.6(13)	8225.3(14)	51.4(4)
C1	7132(2)	267.3(15)	6186.7(17)	36.6(5)
C2	6465(2)	700.7(15)	5138.6(17)	33.9(4)
C3	5349(2)	1418.1(15)	4937.7(16)	32.0(4)
C4	3538(2)	2848.7(15)	6196.4(16)	32.9(4)
C5	2266(2)	3535.1(16)	5945.6(17)	35.0(5)
C6	1135(3)	3082.9(19)	6365(2)	43.0(5)
C7	-366(3)	3555(2)	5914(3)	59.0(7)
C8	-1459(3)	3104(3)	6341(3)	76.9(10)
C9	2821(3)	4527.8(17)	6450(2)	42.0(5)
C10	3793(3)	5041(2)	5951(3)	57.5(7)
C11	4264(4)	6036(2)	6441(3)	82.7(11)
C12	6865(3)	380.5(18)	4263(2)	45.2(6)
C13	7917(3)	-321.7(19)	4417(2)	52.1(6)
C14	8567(3)	-740.0(19)	5448(2)	50.0(6)
C15	8173(3)	-466.1(18)	6310(2)	45.6(6)

Table III.10 Fractional Atomic Coordinates ($\times 10^4$) and Equivalent Isotropic Displacement Parameters ($\text{\AA}^2 \times 10^3$) for Complex 8. U_{eq} is defined as $1/3$ of the trace of the orthogonalized U_{ij} tensor.

Atom	<i>x</i>	<i>y</i>	<i>z</i>	<i>U</i> (eq)
V1	-1462(3)	-1006.6(14)	8562.9(6)	60.6(7)
O1	-1831(13)	-1153(5)	8065(2)	71(3)
O20	3642(14)	-2550(7)	8592(3)	87(3)
O2	-1099(13)	-296(6)	9014(2)	76(3)
N2	-32(14)	801(6)	8661(3)	57(3)
N1	-595(14)	242(7)	8386(3)	62(3)
C3	-467(17)	584(8)	8070(3)	54(3)
C2	-919(16)	129(8)	7750(4)	55(3)
C4	-266(19)	451(9)	8981(4)	64(4)
C1	-1546(18)	-754(9)	7764(4)	61(4)
C5	410(20)	869(9)	9320(4)	75(4)
C13	-890(17)	56(8)	7080(3)	53(3)
C14	-670(17)	412(9)	6739(4)	63(4)
C15	-81(19)	1278(10)	6711(3)	72(4)
C17	-149(18)	1453(9)	7349(4)	71(4)
C16	66(19)	1779(9)	7021(4)	72(4)
C6	1620(20)	272(10)	9536(3)	78(4)
C7	3370(20)	-116(10)	9335(4)	87(5)
C8	4400(30)	-786(11)	9547(4)	108(6)
C10	-2480(20)	1929(10)	9335(4)	91(5)
O3	217(14)	-1715(6)	8639(2)	85(3)
O4	-3492(13)	-1388(6)	8695(3)	86(3)
C9	-1320(20)	1239(9)	9532(3)	77(4)
C11	-4450(60)	2290(30)	9550(11)	96(14)
C11A	-3680(60)	2460(20)	9574(10)	83(12)
C19	-1855(18)	-1207(9)	7456(4)	65(4)
C18	-1538(18)	-851(10)	7117(4)	72(4)

References

1. Mishra, M. K.; Kukal, S.; Paul, P. R.; Bora, S.; Singh, A.; Kukreti, S.; Saso, L.; Muthusamy, K.; Hasija, Y.; Kukreti, *Molecules* **2022**, *27*, 104.
2. Dong, L.; Fang, L.; Dai, X.; Zhang, J.; Wang, J.; Xu, P. *Drug Dev Res.* **2022**, *83*, 131-141.
3. El-Faham, A.; Farooq, M.; Khattab, S. N.; Elkayal, A. M.; Ibrahim, M. F.; Abutaha, N.; Wadaan, M. A.; Hamed, E. A. *Chem. Pharm. Bull.* **2014**, *62*, 591-599.
4. Su, X.; Aprahamian, I. *Chem. Soc. Rev.* **2014**, *43*, 1963-1981.
5. Popiołek, Ł.; Tuszyńska, K.; Biernasiuk, A. *Biomed. pharmacother.* **2022**, *153*, 113302
6. Szklarzewicz, J.; Jurowska, A.; Matoga, D.; Kruczała, K.; Kazek, G.; Mordyl, B.; Sapa, J.; Papież, M. *Polyhedron* **2020**, *185*, 114589.
7. Levina, A.; Pires Vieira, A.; Wijetunga, A.; Kaur, R.; Koehn, J. T.; Crans, D. C.; Lay, P. A. *Angew. Chem.* **2020**, *59*, 15834-15838.
8. (a) Sako, M.; Takizawa, S.; Sasai, H. *Tetrahedron*, **2020**, *76*, 131645. (b) Griffin, S. E.; Schafer, L. L. *Inorg. Chem.* **2020**, *59*, 5256-5260.
9. Pessoa, J. C.; Etcheverry, S.; Gambino, D. *Coord. Chem. Rev.* **2015**, *301-302*, 24-48.
10. Butler, A.; Walker, J. V. *Chem. Rev.* **1993**, *93*, 1937-1944.
11. (a) Hoshino, Y.; Yamamoto, H. *J. Am. Chem. Soc.* **2000**, *122*, 10452-10453.
12. Maurya, M. R.; Khurana, S.; Zhang, W.; Rehder, D. J. *Chem. Soc., Dalton Trans.* **2002**, 3015-3023.
13. Maurya, M. R.; Sarkar, B.; AVECILLA, F.; Correia, I. *Eur. J. Inorg. Chem.* **2016**, *25*, 4028-4044.
14. Siegel, S. M.; Siegel, B. Z. *Nature* **1958**, *181(4616)*, 1153-1154.
15. Patra, R.; Mondal, S.; Sinha, D.; Rajak, K. K. *ACS Omega* **2022**, *7*, 11710-11721.



Chapter IV

*Influence of solvent in Vanadium (V) complex structures:
Electro-generated type II mixed-valent $V^V V^{IV}$ entities in
solution, peroxidase activity and catecholase activity via
semiquinone pathway.*

*Influence of solvent in Vanadium (V) complex structures: Electro-generated type II mixed-valent $V^V V^{IV}$ entities in solution, peroxidase activity and catecholase activity via semiquinone pathway **

Abstract

Two valproic acid hydrazide based Schiff base ligands, H_2L^3 and H_2L^4 , reacted with vanadyl acetylacetonate to form two oxidomethoxido complexes $[V^V O(L^{3-4})(OMe)(OHMe)]$ (**9**, **10**) in methanol and the corresponding dinuclear μ -oxidodioxidodivanadium

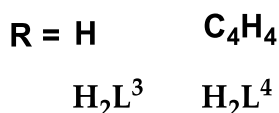
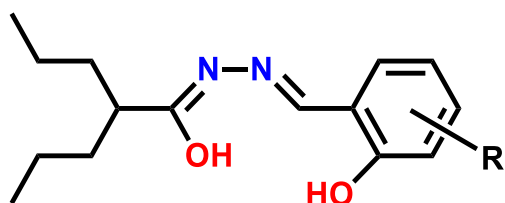


Chart IV.1

complexes $[V^V O(L^{3-4})_2 \mu -O]$ (**11**, **12**) in dichloromethane. Here the ligands used are of same as chapter III. However, binding mode of the ligands was dianionic iminoato form in the oxidomethoxido (**9**, **10**) and dinuclear complexes (**11**, **12**) contrary to the earlier case. Partial reduction of **11**, **12** by constant potential electrolysis (CPE)

conforming to a Robin–Day type II mixed-valence species **11a** and **12a** of general formula $(L)(O)V^{IV}-O-V^V(O)(L)$. Catecholase activity in the oxidation of 3, 5-di-tert-butylcatechol and peroxidase mimetic activity in the oxidation of pyragallol were used to examine the reactivity of the complexes and their catalytic potential. Absorption, EPR and mass Spectrometry have revealed a very intriguing radical mechanism underlying the catecholase-like activity observed by **9** and **10**. Moreover, the complexes' capacity to detect H_2O_2 was also examined spectrophotometrically. Calculations using density functional theory were in good agreement with most of our experimental findings

*Manuscript is under review.

Introduction

A key building block for many pharmaceutically important molecules, especially for the treatment of epilepsy, bipolar disorder, migraine, neurological diseases, cancer, and other conditions, is valproic acid, a fatty acid.¹ A growing body of evidence also supports its pharmacological action in treating neurodevelopmental disorders including ADHD (attention deficit hyperactivity disorder) and cardio protection by inhibiting the activity of histone deacetylases (HDACs).² Right now, the bio-potency of its hydrazone derivatives³ is of special interest. This is because of its simple synthesis⁴, intrinsic conformational flexibility⁵ and medicinal uses.⁶ The coordination chemistry of vanadium with hydrazones is one of the most fascinating as discussed earlier chapters.topics.^{7, 8}

The synthesis of μ -oxidodioxidovanadium (IV,V) complex⁹ from its binuclear vanadium(V/V) analogue of the type $(V^V OL)_2O$ has garnered considerable interest. The application of valence isomers in molecular electronics and molecular computing is made possible by the diversity of the ligand's electronic environment across the metal core.¹⁰ Traditionally, Robin–Day mixed valency scheme for complexes refer type I (valence-trapped) i.e. the odd electron is not delocalised¹¹ and type III (delocalised) where the odd electron is shared equally over both redox sites^{12, 9a}. Between these two extremes, type II (hopping)¹³ are found, where some delocalization takes place over both redox centers. Herein, we are trying to explore the extent of electronic communication of the odd electron within type II mixed-valence oxidovanadium (IV/V) species and their predecessors.

A pertinent area of vanadium chemistry has also been identified for catecholase imitators.¹⁴ However, catecholase-like activity via semiquinone radical mechanism¹⁵ for vanadium compounds are scarcely known. Additionally, little is known about peroxidase mimicking activity employing oxygenations of pyrogallol¹⁶ catalysed by vanadium metal.

In the current contribution, we envisage to extend our previous research^{13a} about solvent mediated coordination chemistry of vanadium. For this purpose we presented four vanadium complexes $[V^V O(L^{3-4})(OMe)(OHMe)]$ (**9**, **10**), $[V^V_2O_3(L^{3-4})_2]$ (**11**, **12**) (**Chart I**.) with Schiff base ligands H_2L^3 and H_2L^4 . In order to characterise the complexes, various physio-chemical techniques were used. Solid-state structures of the complexes **9**, **12** were confirmed using single crystal X-ray diffraction technique. Cyclic voltammetry and spectro-electrochemical techniques were employed to explore the redox behaviour that was further supported by density functional theory (DFT) calculations. We have reported

type II mixed-oxidation state species **11a** and **12a**, electrogenerated from their respective divanadium (V/V) predecessors **11** and **12**.

Catalytic efficacy towards the oxidation of catechol to quinone was assessed by using the model substrate 3,5-di-tert-butylcatechol. The reaction proceeds via semiquinone radical route established together with mass spectrometry, UV-Vis and EPR spectroscopy. Following the oxidation of pyrogallol by H₂O₂, peroxidase-like activity was observed. Our continued interest on the involvement of H₂O₂ in peroxidases catalysis directed us to check the sensing ability¹⁷ of the complexes towards H₂O₂.

IV.1 RESULTS AND DISCUSSION

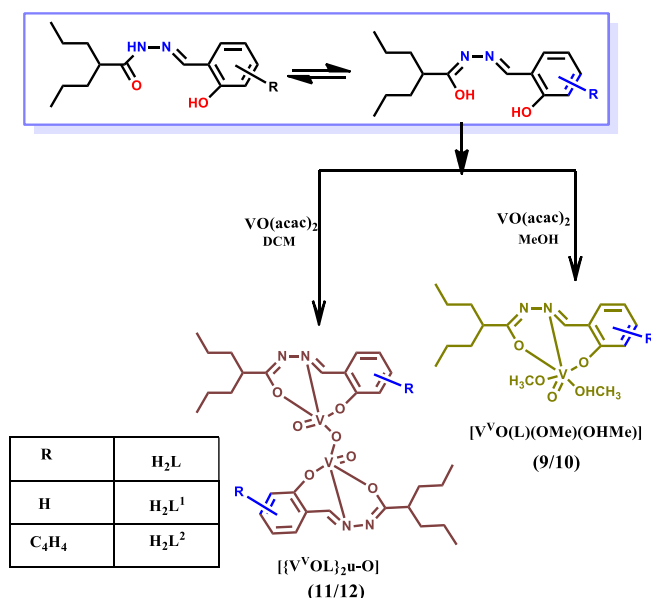
A. SYNTHESIS

i) Ligand

The tridentate ligands H_2L^3 and H_2L^4 were prepared in manner described in Chapter III. The tautomeric form which coordinates with metal is given in **Chart IV.1**. The ligands bind as bi-anionic N, O, O donor on the reaction condition for the preparation of the complexes.

ii) Complexes

The reactions of $[VO(acac)_2]$ with an equimolar amount of the ligands in methanol yielded monomeric oxidomethoxido complexes (**9, 10**). Further reaction in dichloromethane led to the formation of dinuclear oxovanadium complexes (**11, 12**). The ligand binds via iminolate form in methanol and dichloromethane. **Scheme IV.1**. provides an overview of the synthesis of complexes. Constant potential electrolysis (CPE) of **11** & **12** generated type II mixed oxidation state species **11a** & **12a**.



Scheme IV.1. Schematic representation for the synthesis of the complexes

B. CRYSTAL STRUCTURES

Complex 9: The coordination geometry of the oxo-methoxo complex **9** can be described as distorted octahedral with the doubly bonded oxo group and methanol in the axial position. The N₂O donor from ligand and methoxide oxygen atom define the equatorial plane. (**Figure IV.1.**) The molecule crystallises in monoclinic system with P21/c space group. The bond parameters are given in **Table**

IV.1. The overall charge balance and respective bond lengths of the C=O (1.29 Å) and HN-C (1.28 Å) suggest coordination through iminolate form. The O=V-O_(methanol) axis is almost linear with bond angle 175.1(3). The *trans* effect of the oxo group causes elongation of V-O_(methanol) bond length (2.354(6)Å), making methanol weakly coordinated.

The V=O bond at 1.594(7)Å is the shortest. Other bond lengths, and the bond angles are in normal ranges. Hydrogen bonding interactions O-H⋯N established between the coordinated methanolic O-H with uncoordinated N atom and the other C-H⋯O between imine hydrogen with phenolato oxygen connect the molecules to form one dimensional chain structure. (**Figure IV.2.**)

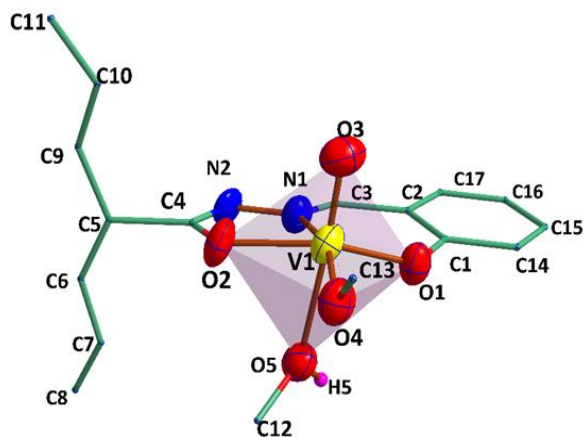


Figure IV.1. ORTEP diagram (35% probability) ellipsoid and atom-numbering scheme for complex **9**

Table IV.1. Selected Bond Distances (Å) and Angles (°) for **Complex 9**

Bond Length (Å)			Bond Angle (°)			
V1	-O1	1.850(5)	O1	-V1	-O2	152.1(2)
V1	-O2	1.949(6)	O1	-V1	-O3	100.1(3)
V1	-O3	1.594(7)	O1	-V1	-O4	100.7(2)
V1	-O4	1.766(5)	O1	-V1	-O5	81.6(2)
V1	-O5	2.354(6)	O1	-V1	-N1	83.6(2)
V1	-N1	2.114(6)	O2	-V1	-O3	98.9(3)
O1	-C1	1.324(10)	O2	-V1	-O4	95.1(2)
O2	-C4	1.288(11)	O2	-V1	-O5	78.0(2)
N1	-N2	1.377(9)	O2	-V1	-N1	74.1(2)
N1	-C3	1.265(12)	O3	-V1	-O4	102.1(3)
N2	-C4	1.293(14)	O3	-V1	-O5	175.1(3)
			O3	-V1	-N1	96.4(3)
			O4	-V1	-O5	82.1(2)
			O4	-V1	-N1	159.9(3)
			O5	-V1	-N1	79.2(2)

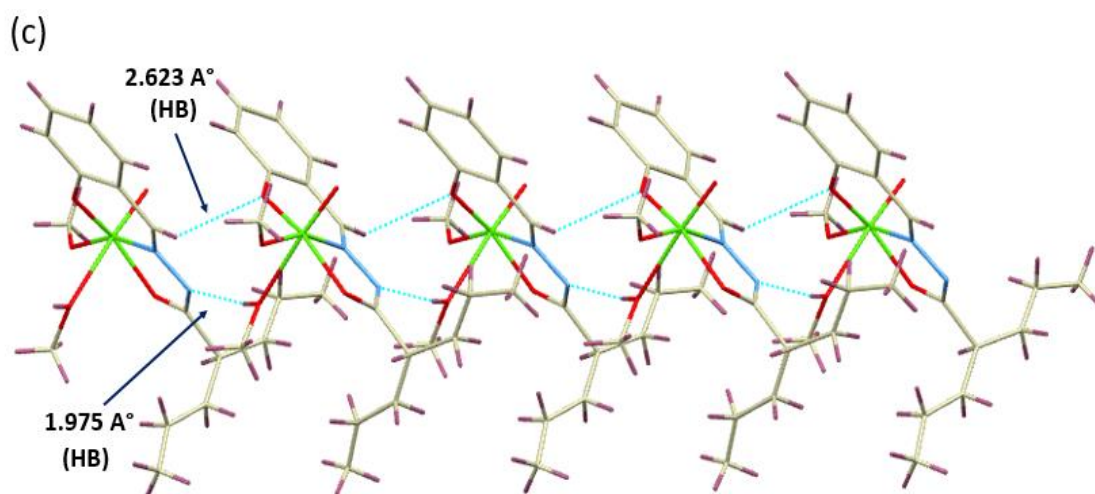


Figure IV.2. Supramolecular architect of **Complex 9**

Complex 12: It is a μ_2 -oxo bridge dinuclear complex which possesses triclinic crystal system having space group P-1. Crystallography data (**Figure IV.3, Table IV.2.**) indicates that in the asymmetric complex $[\{VOL\}_2\mu-O]$, the two vanadium centres are penta coordinated with the basal plane composed of imine nitrogen atom, acyl oxygen, phenolate oxygen atom from the Schiff base ligand and the μ_2 -oxo O atom in each case. The apical positions are occupied by the oxo group. The distance of the μ_2 -bridging oxo group from two vanadium centers are 1.769(8) Å and 1.795(8) Å for V1 and V2 respectively indicating slightly asymmetric bridge. The V...V intramolecular distance, 3.164 Å. The relatively long C12–O2 and C31–O6 bond lengths of

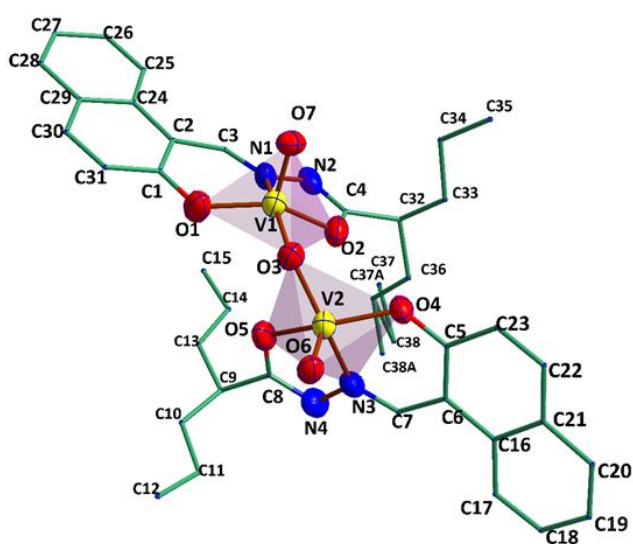


Figure IV.3. ORTEP diagram (35% probability) ellipsoid and atom-numbering scheme for complex **12**

C31–O6 bond lengths of 1.295(14) Å and 1.289(16) Å, and relatively short C12–N1 and C31–N4 bond lengths of 1.313(14) Å and 1.312(16) Å, indicate that there are tautomeric effects along the backbones of the hydrazone ligands and the ligand binds through dianionic iminolate form. The $\tau=0.25$ for V1 and $\tau=0.18$ for V2 suggests the geometry around each

vanadium is very close to distorted square pyramid. The V1–O3–V2 bond angle is only 125.0(6)° and the torsion angle O7–V1...V2–O6 being 79.88°, the $[V_2O_3]^{4+}$ core have twisted angular configuration, where the relative disposition of the two V=O group is intermediate between the syn and anti-forms. In the crystal hydrogen bonds between aromatic H atoms and the oxo-oxygen atoms, C–H... π interactions between methyne hydrogen and naphthyl ring, π ... π interactions between naphthyl rings of adjacent molecules lead to the formation of two-dimensional molecular chains. (**Figure IV.4**)

Table IV.2. Selected Bond Distances (Å) and Angles (°) for **Complex 12**

Bond Length (Å)			Bond angle (°)			
V1	-O1	1.818(8)	O1	-V1	-O2	139.1(4)
V1	-O2	1.907(9)	O1	-V1	-O3	102.2(4)
V1	-O3	1.767(8)	O1	-V1	-O7	107.0(5)
V1	-O7	1.564(10)	O1	-V1	-N1	83.1(4)
V1	-N1	2.058(12)	O2	-V1	-O3	87.3(4)
V2	-O3	1.802(9)	O2	-V1	-O7	107.7(4)
V2	-O4	1.826(8)	O2	-V1	-N1	73.4(4)
V2	-O5	1.925(11)	O3	-V1	-O7	107.8(5)
V2	-O6	1.578(9)	O3	-V1	-N1	154.5(5)
V2	-N3	2.050(12)	O7	-V1	-N1	94.2(5)
O1	-C1	1.353(18)	O3	-V2	-O4	103.0(4)
O2	-C4	1.29(2)	O3	-V2	-O5	88.0(4)
N1	-N2	1.379(15)	O3	-V2	-O6	107.1(4)
N2	-C4	1.30(3)	O3	-V2	-N3	153.7(5)
N1	-C3	1.318(19)	O4	-V2	-O5	142.8(4)
N3	-N4	1.411(17)	O4	-V2	-O6	105.2(4)
			O4	-V2	-N3	82.0(4)
			O5	-V2	-O6	105.2(4)
			O5	-V2	-N3	73.9(5)
			O6	-V2	-N3	96.2(5)
			V1	-O3	-V2	125.0(6)

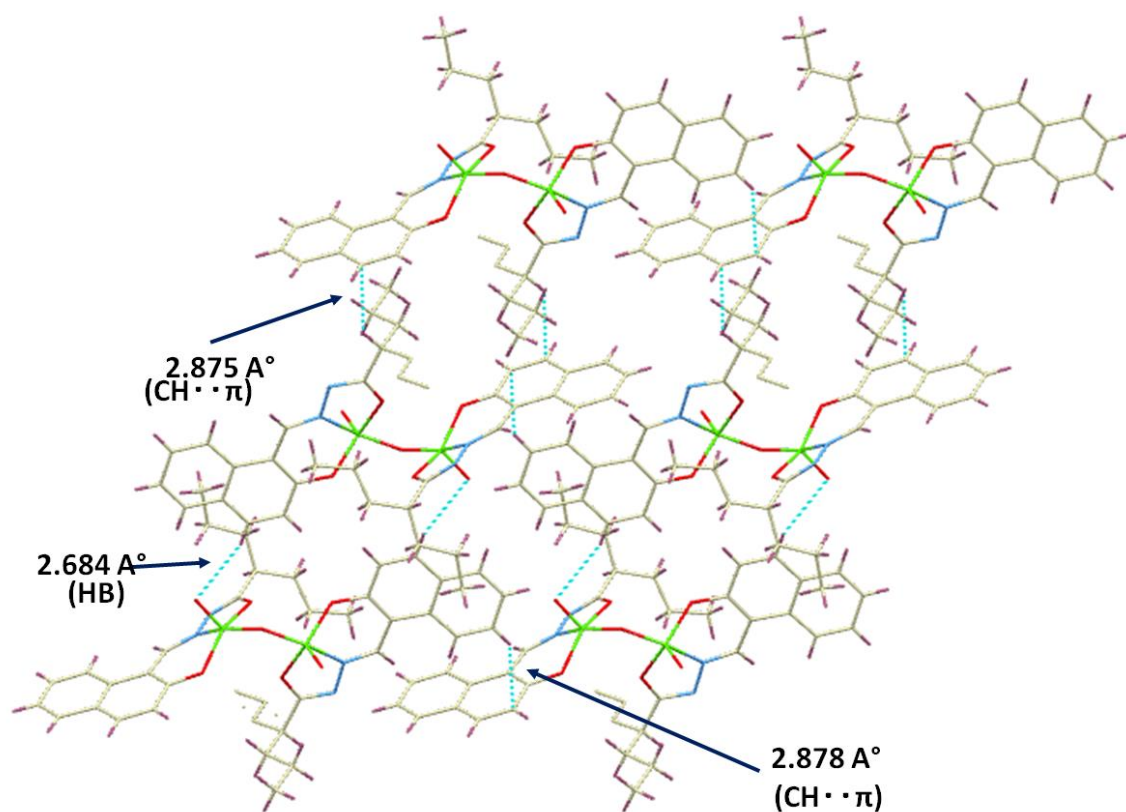


Figure IV.4. supramolecular architecture for complex 12

C. ELECTRONIC ABSORPTION SPECTRA

The UV-vis absorption spectra of the complexes 9 – 12 (Figure IV.5.) were recorded in methanol-CH₂Cl₂ (2: 8 ratio) at 298 K by employing concentrations in the range ~20 μM. The electronic spectra of the ligand H₂L³ and H₂L⁴ were already being discussed in Chapter III.

Complexes of each set of the ligand possess a particular pattern with respect to their structural motif. For the methoxido complexes of H₂L³ and H₂L⁴ i.e., 9 and 10 a broad shoulder in the range 396 - 412 nm was observed. It can be assigned to LMCT bands. In the case of monoxido bridged-di-vanadium (V, V) complexes 11, 12 spectral appearances are quite similar, but a careful look into the spectra reveals that both the lower energy bands around 270 nm, in the range 321-339 nm and the higher energy bands in the range 390-406 nm are well-developed in comparison to its monomeric oxido-methoxido complexes which is aptly supported by its co-ordination environment. For all the cases the presence of

naphthalic conjugation induces a slight red shift for complexes of H_2L^4 in comparison to complexes of H_2L^3 . Absorption parameters are given in Table IV.

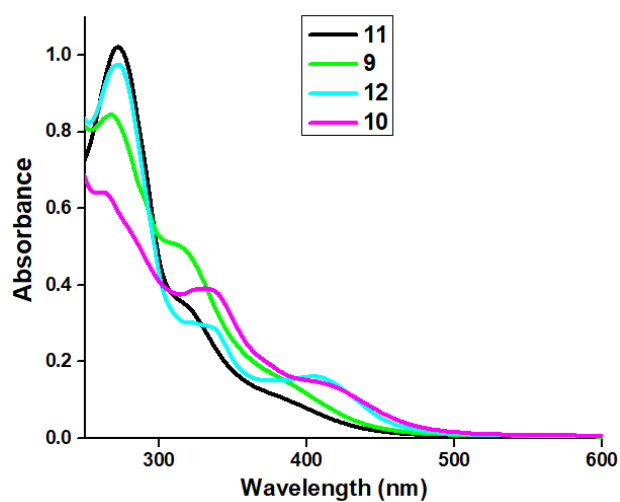


Figure IV.5. Absorption spectra of complexes in methanol- CH_2Cl_2 (2:8) at 298K

Table IV.3. Absorption parameter of complexes at RT

Complexes	$\lambda_{\text{max}}(\text{nm})[\epsilon(\text{M}^{-1}\text{cm}^{-1})]$
9	268 (42000), 320 (22450), 396 (7350)
10	266 (31750), 333 (19700), 411 (6850)
11	272 (51000), 321 (16100), 390 (4600)
12	271 (48500), 339 (14400), 406 (8150)

D. CYCLIC VOLTAMMETRY

The redox activities of **9–12** (referenced to the ferrocinium/ferrocene couple) were investigated by cyclic voltammetry in CH_2Cl_2 at 295 K containing $[\text{N}(\text{n-Bu})_4]\text{PF}_6$ as a supporting electrolyte. The cyclic voltammograms are illustrated in **Figure IV.6**. The cyclic voltammograms of the mononuclear complexes (**9** and **10**) displayed reversible cathodic waves in the range -0.168 to -0.226 V assigned to $\text{V}^{\text{V}}/\text{V}^{\text{IV}}$ reduction couple. The cathodic processes occur at considerably lower potentials for the methoxido complexes i.e., for **9** and **10** as reversible waves at -0.244 and -0.226 V respectively. Such a trend may be attributed to the net increase of electron density on the metal centre causing vanadium(V) centre less susceptible to reduction than that of dioxo complexes. (complex **7**, **8** of **Chapter III**.) The redox activities of the dinuclear **11** and **12** are notably different from the rest. **11** exhibits two peaks, reversible and quasi-reversible; cathodic waves (**Figure IV.6**.) due to $\text{V}^{\text{V}}\text{O}^{\text{V}}/\text{V}^{\text{IV}}\text{O}^{\text{V}}$ and $\text{V}^{\text{IV}}\text{O}^{\text{V}}/\text{V}^{\text{IV}}\text{O}^{\text{IV}}$ redox couples at -0.252 and -0.709 V respectively. **12** also shows the similar redox properties as **11** depicted in **Figure IV.6**, two reversible cathodic waves at -0.204 and -1.57 V.

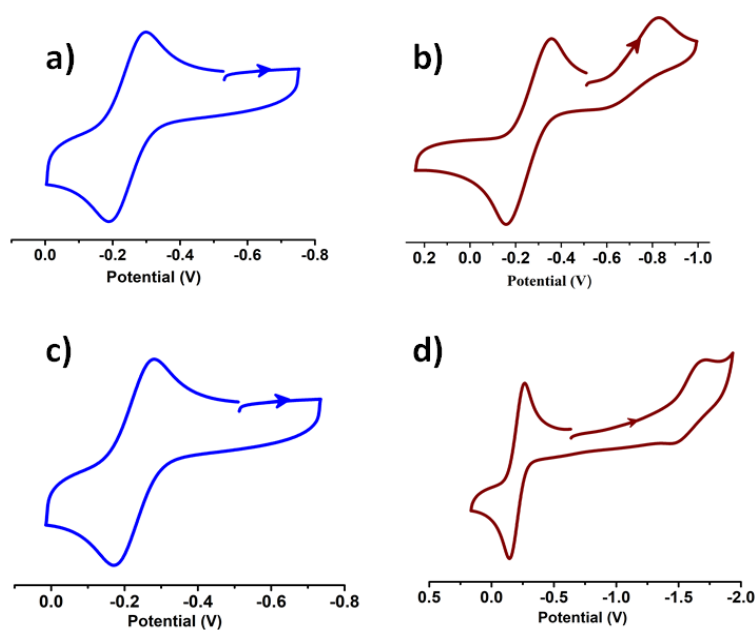
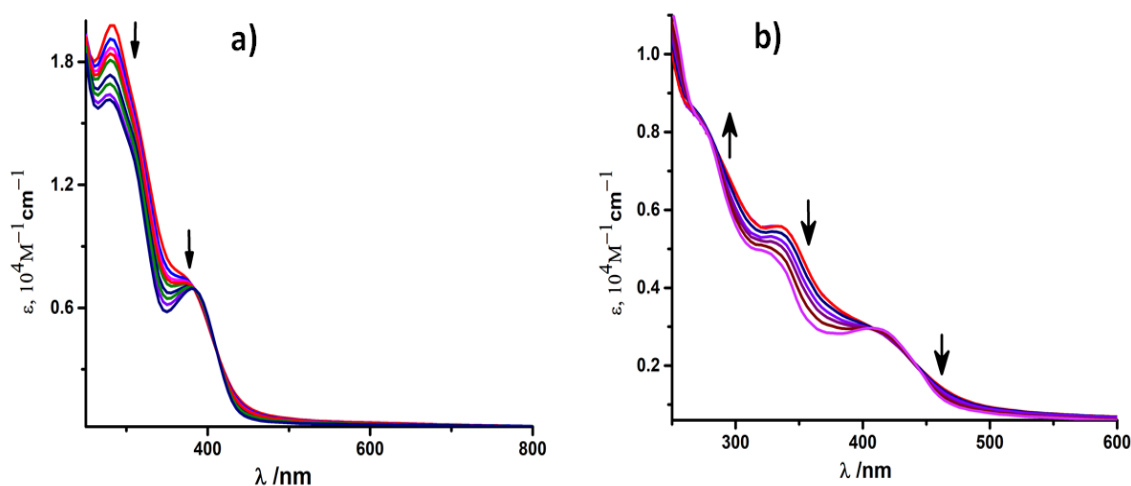


Figure IV.6. Cyclic voltammograms of (a) **9**, (b) **11**, (c) **10**, (d) **12** in CH_2Cl_2 at 298 K. Conditions: scan rate, 100 mV s^{-1} ; $0.20 \text{ M } [\text{N}(\text{n-Bu})_4]\text{PF}_6$ supporting electrolyte; platinum working electrode.

E. SPECTROELECTROCHEMISTRY

Spectro-electrochemical measurements of the complexes were conducted to evaluate spectroscopic signatures of the reduced species in $\text{CH}_2\text{Cl}_2/0.3 \text{ M } [\text{N}(\text{n-Bu})_4]\text{PF}_6$ system. In the case of the monomeric methoxido complexes **9**, the reduction under constant potential conditions resulted in an intensity decrease of bands $\sim 370 \text{ nm}$ and $\sim 280 \text{ nm}$ with the formation of distinct peak at $\sim 380 \text{ nm}$. For **10**, the intensity of the higher energy band $\sim 335 \text{ nm}$ decreased gradually and that of $\sim 410 \text{ nm}$ increased with the generation of new peak at 419 nm . The spectra look almost similar with their comparative analogues complexes **7**, **8** respectively (of **Chapter III**.) Isosbestic crossover points proved the transformation of reduced species. (**Figure IV.7**.)



*Figure IV.7. Change of absorption spectra during (a) **9** \rightarrow **9**⁻ and (b) **10** \rightarrow **10**⁻ conversions in CH_2Cl_2 achieved by constant potential Spectro electrochemical measurements at 298 K.*

F. EPR STUDY

All the four complexes were diamagnetic in nature hence EPR silent whereas, the electrochemically reduced species were found to be paramagnetic. The EPR spectra of all the species were recorded in CH_2Cl_2 solution at ambient temperature. The EPR spectrum of all the electro-generated mononuclear anionic complexes exhibited characteristic eight-line spectrum due to presence of one

extra unpaired electron spin ($S = 1/2$) and hyperfine coupling of ^{51}V ($I=7/2$). Spectra resembled octahedral coordination sphere of vanadium (IV) complexes. This shifting of diamagnetic $[\text{V}^{\text{VO}}]^{3+}$ to paramagnetic $[\text{V}^{\text{IV}}\text{O}]^{2+}$ is also supported by spin density data from DFT calculations.

Electrochemically synthesized mixed-valence $[\{\text{V}^{\text{V}}\text{V}^{\text{IV}}\text{O}_2(\text{L})_2\}-\mu\text{-O}]$ species (**11a** and **12a**) were paramagnetic. The EPR spectra of solid solution of **11a** and **12a** consist of eight lines pattern at room temperature (**Figure IV.8., Table IV.4**). In contrast, the frozen glass solution of the same showed 13 lines at 77K (**Figure IV.9., Table IV.5**). The missing 15-line patterns in case of **11a** and **12a** indicate that the complexes are not exactly mixed valence of type III as it requires complete delocalization of electronic spin between the two vanadium nuclei. In this case, EPR pattern justified that the unpaired electron spin is mostly localized

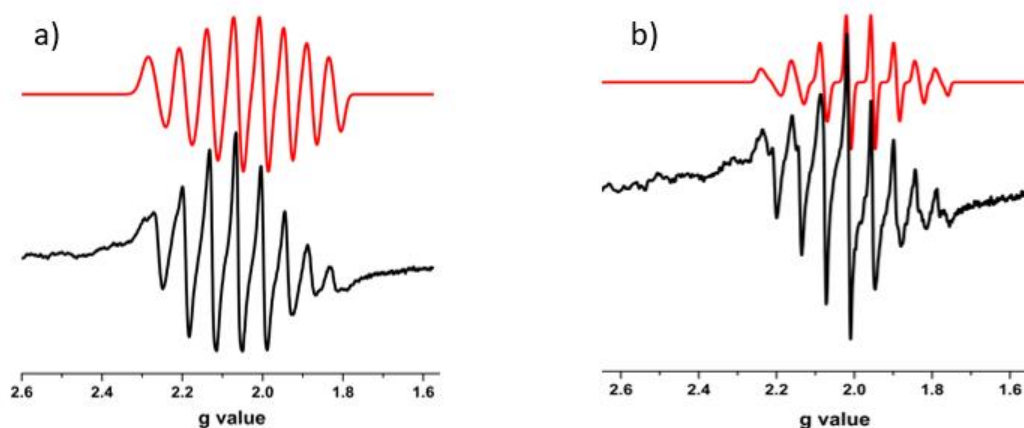


Figure IV.8. X-band EPR spectra of $[\text{V}_2\text{O}_3\text{L}^{3-4}_2]^{3+}$, (a) **11a**, (b) **12a** at RT (black-experimental; red-simulated)

on one of the vanadium (IV) center and partially mixed with adjacent vanadium nuclei, thus defined by the $[\{\text{V}^{\text{VO}}(\text{L})\}\{\text{V}^{\text{IV}}\text{O}(\text{L})\}-\mu\text{-O}] \leftrightarrow [\{\text{V}^{\text{IV}}\text{O}(\text{L})\}\{\text{V}^{\text{VO}}(\text{L})\}-\mu\text{-O}]$. This type of anisotropic distribution of unpaired electron spin in the EPR spectra confirms that **11a** and **12a** are type II mixed valence complexes.

Table IV.4. X-band EPR Spectral parameter of complex **11a** and **12a** at RT

Complex	Matrix	g	A (G)	Iw (mT)
11a	CH ₂ Cl ₂ ,	1.96775	284.98	3.8
12a	CH ₂ Cl ₂ ,	1.9678	294.40	2.0

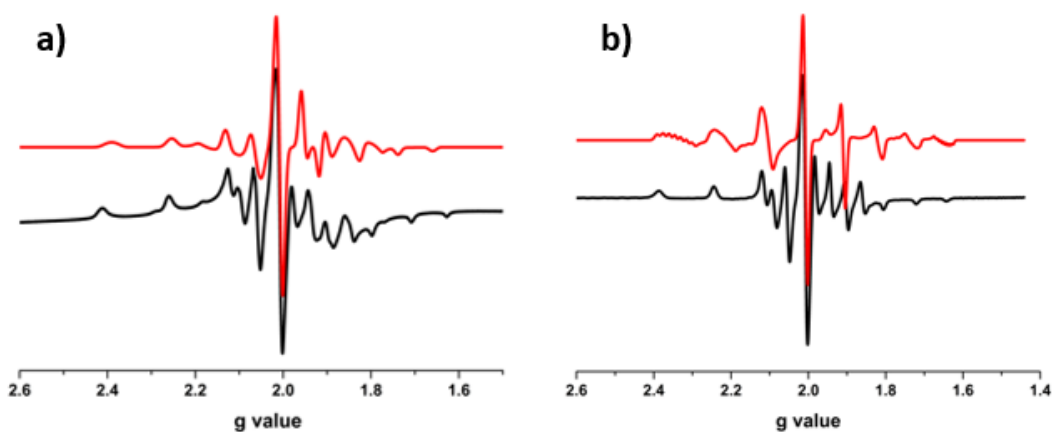


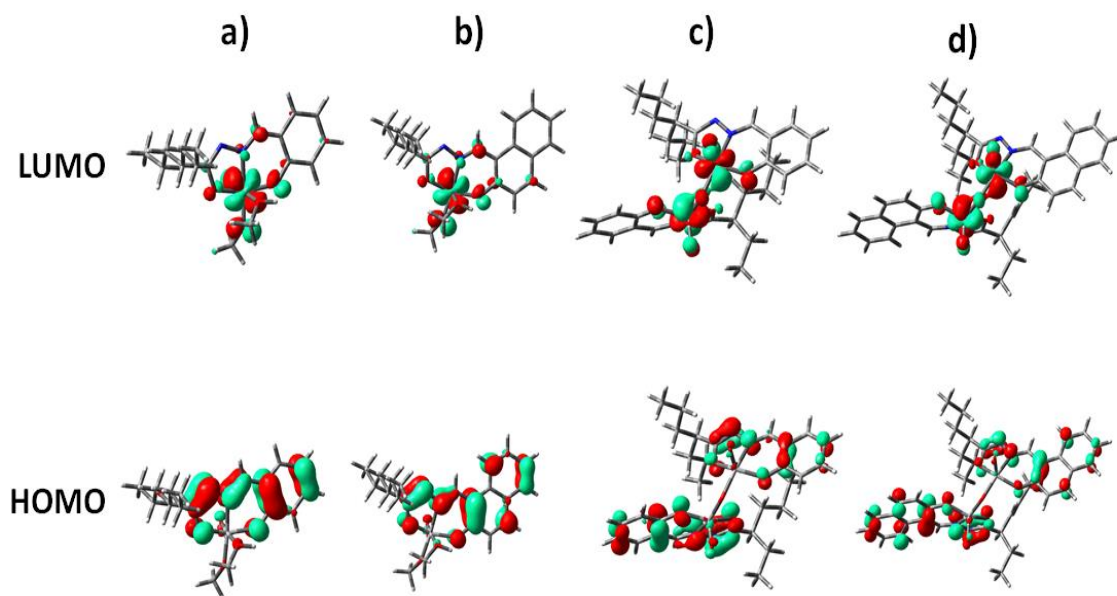
Figure IV.9. X-band EPR spectra of $[V_2O_3L^{3-4}_2]^{3+}$, (a) **11a**, (b) **12a** in frozen solution at 77 K (black-experimental; red-simulated)

Table IV.5. X-band EPR Spectral parameter of complex **11a** and **12a** at 77K

Complex	Matrix	g_{\parallel}	g_{\perp}	g_{av}	A_{\parallel} (G)	A_{\perp} (G)	A_{av} (G)	Iw (mT)
11a	CH ₂ Cl ₂ , 77 K	1.9576	1.9587	1.9583	468.25	230.57	309.79	2.0
12a	CH ₂ Cl ₂ , 77 K	1.9526	1.9336	1.9399	450.05	269.97	329.99	1.25

G. THEORETICAL CALCULATIONS

In all the cases, **9** – **12**, the highest occupied molecular orbital (HOMO) is localized mostly on the ligand framework. For methoxido complexes, **9** & **10**, and dimeric complexes **11** & **12**, the lowest unoccupied molecular orbital (LUMO) localized predominantly on the vanadium atom and very little on oxo ligands and bridging oxygen for the dimers. (**Figure IV.10.**). This is an obvious sign of metal-centred reduction. Spin density calculated for the monocharged **9**⁻ and **10**⁻ is located mainly on central vanadium atom indicating usual metal centred reduction. In **11**⁻ (**11a**) and **12**⁻ (**12a**) spin density localised mostly on one vanadium(V) atom with a very small fraction on the second vanadium atom. (**Figure IV.11.**). The EPR data also corroborated the DFT calculations, which predict formation of type II mixed-valence complexes. An 8-line spectra in solid solution taken at room temperature and 13-line spectra in frozen glass solution at 77K clearly indicates anisotropic distribution of electron density over the two vanadium



*Figure IV.10. Isodensity plot of selected frontier orbitals of complexes a) **9**, b) **10**, c), **11**, d) **12***

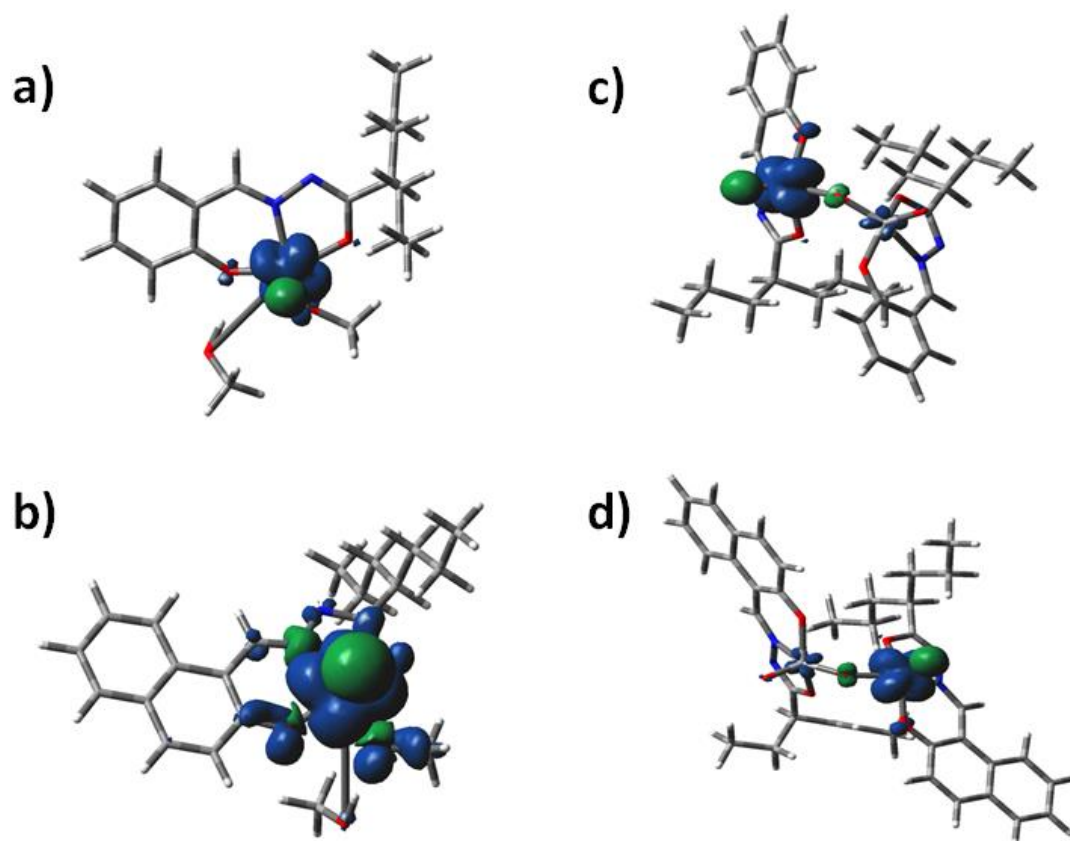


Figure IV.11. Spin density plot of (a) **9**, (b) **10**, (c) **11a** and (d) **12a**

H. CATECHOL OXIDATION

To study catecholase activity of all the complexes, we have considered 3,5-di-tert-butyl catechol (DTBC) as a model substrate. During the investigation of catecholase activity, it was found that mononuclear oxidomethoxido complexes **9**, **10** were catalytically active. The course of the reaction was monitored by time dependent UV-Vis spectroscopy saturated 2:8 CH₃OH and CH₂Cl₂ solvent at 25 °C. The reaction was initiated by adding 2×10^{-4} M solutions of **9** and **10** with 0.004 M solution of 3,5-DTBC in aerobic condition. The immediate spectral run exhibited three peaks around ~860 nm and ~580 nm ~410 nm. These bands ~860 nm along with the broad band appearing at 580 nm (for **9**) and 573 nm (for **10**) may be assigned to charge transfer (CT) bands. With the progress of catalytic oxidation these bands gradually declined, the bands around 410 nm shifts and grows passing through a single isosbestic point and finally saturated ~400 nm due to formation of quinone over the time. Colorimetric shift of the reaction mixture

from greenish blue to deep brown and formation of single isobestic point suggested that one intermediate is involved in the conversion of 3, 5-DTBC to 3, 5-DTBQ. The yield of 3, 5-DTBQ was obtained from purification of the brown solution so obtained after completion of the reaction was by column chromatography. The yield for complex **9** was $\sim 52\%$ and that of the complex **10** $\sim 40\%$. To obtain the kinetic parameters, 2×10^{-4} M solution of complexes were treated with varying the concentration from 0.001 M - 0.01 M solution of the substrate and. Considering the growing absorption at quinone band, the rates of the reactions were determined and the kinetic parameters estimated using Michaelis-Menten and Lineweaver-Burk equations are as follows. [Complex **9**: $k_2 = 25.7 \text{ min}^{-1}$, $K_M = 2.9 \times 10^{-3}$ and $V_{\max} = 5.1 \times 10^{-3} \text{ M min}^{-1}$ (Figure IV.12.) Complex **10**: $k_2 = 22.6 \text{ min}^{-1}$, $K_M = 2.03 \times 10^{-3}$ and $V_{\max} = 4.5 \times 10^{-3} \text{ M min}^{-1}$ (Figure IV.13.)

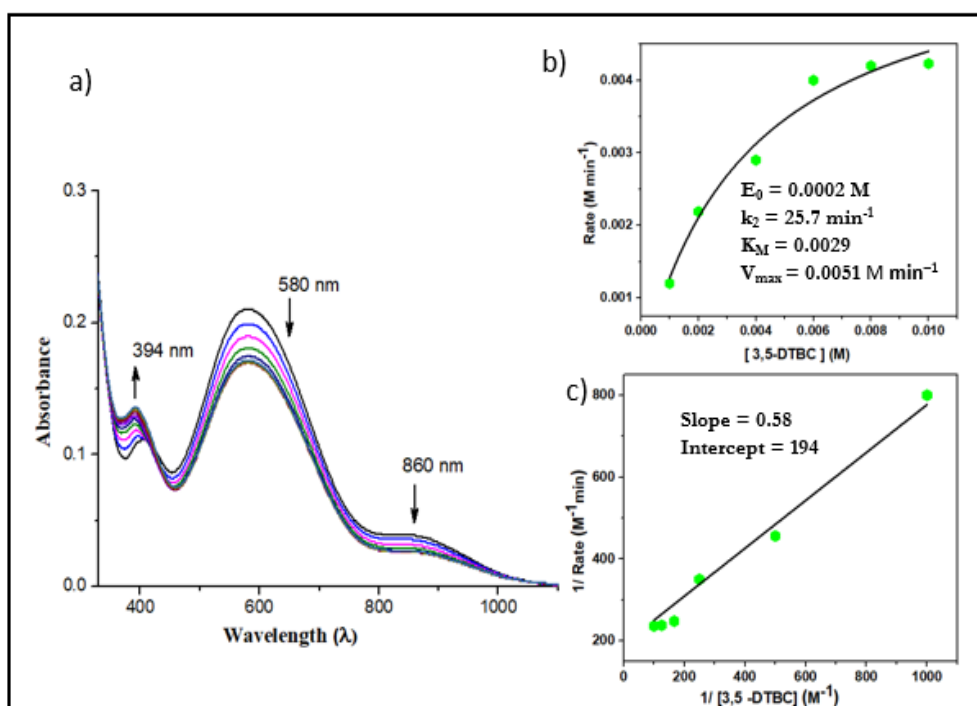


Figure IV.12. (a) Absorption spectra of a solution containing 2×10^{-4} M of complex **9** and 0.01 M of 3,5-DTBC, recorded at the interval of 5 min. (b) Plot of rate versus concentration of 3, 5-DTBC for the oxidation reaction catalysed by complex. (c)

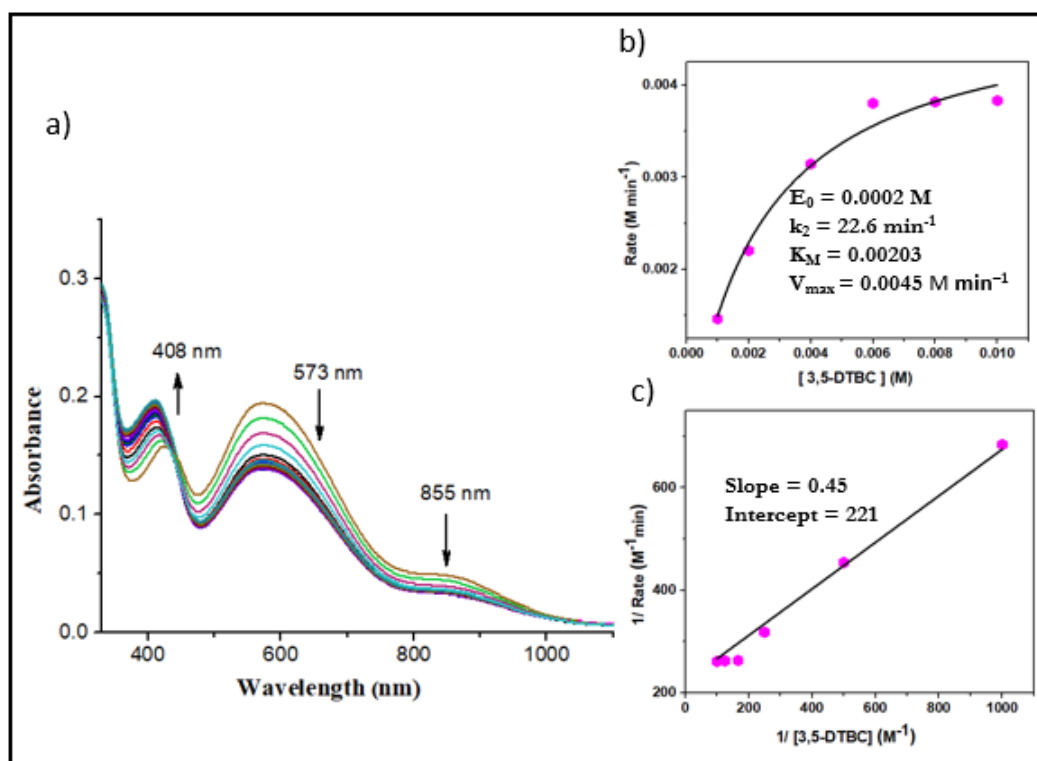
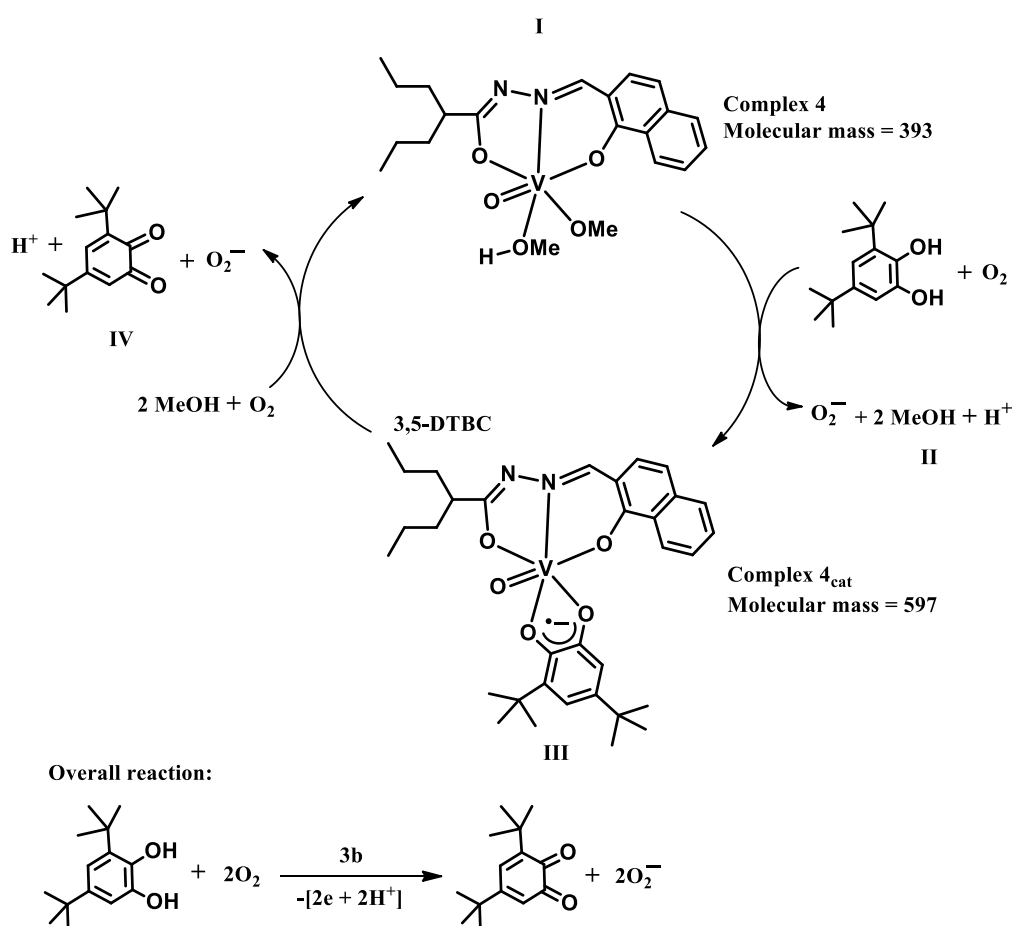


Figure IV.13. (a) Absorption spectra of a solution containing 2×10^{-4} M of complex **10** and 0.01 M of 3,5-DTBC, recorded at the interval of 5 min. (b) Plot of rate versus concentration of 3, 5-DTBC for the oxidation reaction catalysed by complex. (c) Lineweaver–Burk plot

Probable reaction pathway: Catechol binds to metal either the semiquinone or the more nucleophilic catecholate form. The bands appearing at the low energy region 860 nm (for **9**) and 855 nm (for **10**) gave a hint towards the formation of radical intermediate $[V^{VO}(L^{3-4})(3,5\text{-DTBSQ}\cdot)]$. X-band EPR measurements were done in order to ascertain the presence of any paramagnetic species that might have formed in the reaction mixture as indicated by the absorption spectra. Complexes **9**, **10** were observed to be EPR quiet as expected for V^V species. Immediately after the addition of 3,5-DTBC to respective complexes (complex: 3,5-DTBC = 1: 10), one line EPR spectrum ($g_{\text{avg}} = 1.9949$) characteristic of $[V^{VO}(L^{3-4})(3,5\text{-DTBSQ}\cdot)]$ was observed. (**Figure IV.14.**, **Table IV.7.**) This result conclusively establishes that the reaction predominantly follows a radical intermediate. LCMS techniques were used to track the development of the complex-substrate adducts. Free complex **10** has a peak $m/z = 441$, corresponding to complex **2**. After adding 3,5-

DTBC to complexes the base peak was detected at $m/z = 597$, corresponding to intermediate III. After completion, the reaction mixture exhibited two characteristics peaks at m/z 221 and 441 corresponding to 3,5-DTBQ and complex 10 (Figure IV.25). This means after completion of the reaction complex 10 was regenerated. The detailed reactions occurring are depicted in Scheme IV.2. All the data corresponding to complex 9 are given in Figure IV.14., Figure IV.26. and Table IV.6.



Scheme IV.2. Schematic representation for catechol oxidation of complex 10.

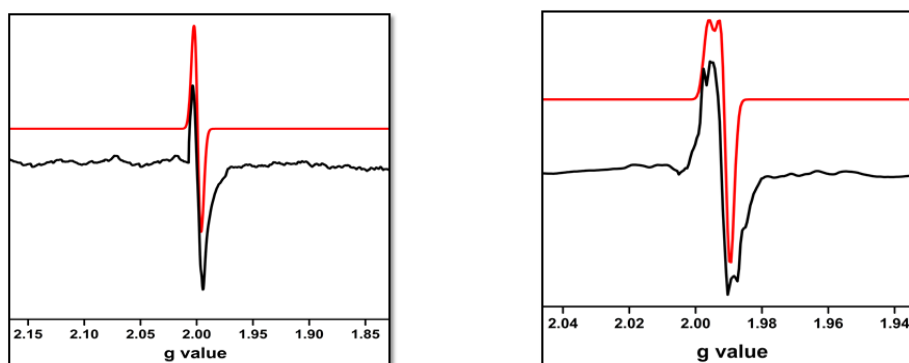


Figure IV.13. X band EPR spectra of the intermediate **III** a) Complex **9_{cat}**,
b) Complex **10_{cat}** (black-experimental; red-simulated)

Table IV.6. X-band EPR Spectral parameter of complex **9_{cat}**

Complex	Matrix	g	A (G)	lw (mT)
9_{cat}	CH ₂ Cl ₂ , 300 K	1.9998	20.0071	1.0

Table IV.7. X-band EPR Spectral parameter of complex **10_{cat}**

Complex	Matrix	g	g _⊥	g _{av}	A (G)	A _⊥ (G)	A _{av} (G)	lw (mT)
10_{cat}	CH ₂ Cl ₂ , 300 K	1.9932	1.9984	1.9949	5.007	0.4937	1.9981	0.8

I. CATALYTIC OXIDATION OF PYROGALLOL

Active oxygen molecules, such as hydrogen peroxide, peroxy compounds, or molecular oxygen, are frequently used as primary oxidants in transition metal catalysed oxidations. The oxidomethoxido complexes **9**, **10** require H₂O₂ for the oxidation process of pyrogallol contrary to the corresponding dioxo complexes **7** and **8** (See **Chapter III**). To check the catalytic potential of complexes **9-10** towards oxidation of pyrogallol, 6×10^{-4} M solution of complexes was treated with a 10-fold concentrated solution of pyrogallol in presence of one drop portion

of 10^{-2} M H_2O_2 and the course of the reaction was followed by recording UV-vis spectra up to 15 min. The first spectral run of the dark blue solution showed a nearly identical pattern to that of catechol due to the similarity in substrate structure. Spectral changes of complex **9** in methanol_dichloromethane is shown in **Figure IV.14**. The band near 580 nm gradually decreases while the band near 415 nm (for **10**) or 388 nm (for **9**) gradually increases, indicating formation of purpurogallin. The initial rates were slightly higher in presence of H_2O_2 . The kinetic parameters were evaluated by the initial rates method by monitoring the increase of the product purpurogallin. For this purpose, a 6×10^{-4} M solution of complexes were treated with 0.001 M – 0.01 M solution of pyrogallol. The results obtained from the conventional Michaelis-Menten and Lineweaver-Burk equations are as follows. [Complex **9**: $k_2 = 13.4 \text{ min}^{-1}$, $K_M = 1.4 \times 10^{-3}$ and $V_{\text{max}} = 8.03 \times 10^{-3} \text{ M min}^{-1}$ (**Figure IV.14**.) Complex **10**: $k_2 = 10.6 \text{ min}^{-1}$, $K_M = 1.08 \times 10^{-3}$ and $V_{\text{max}} = 6.4 \times 10^{-3} \text{ M min}^{-1}$ and] [**Figure IV.15**]. From this result, we were interested to learn the effect of H_2O_2 on each of the complexes **9** and **10**.

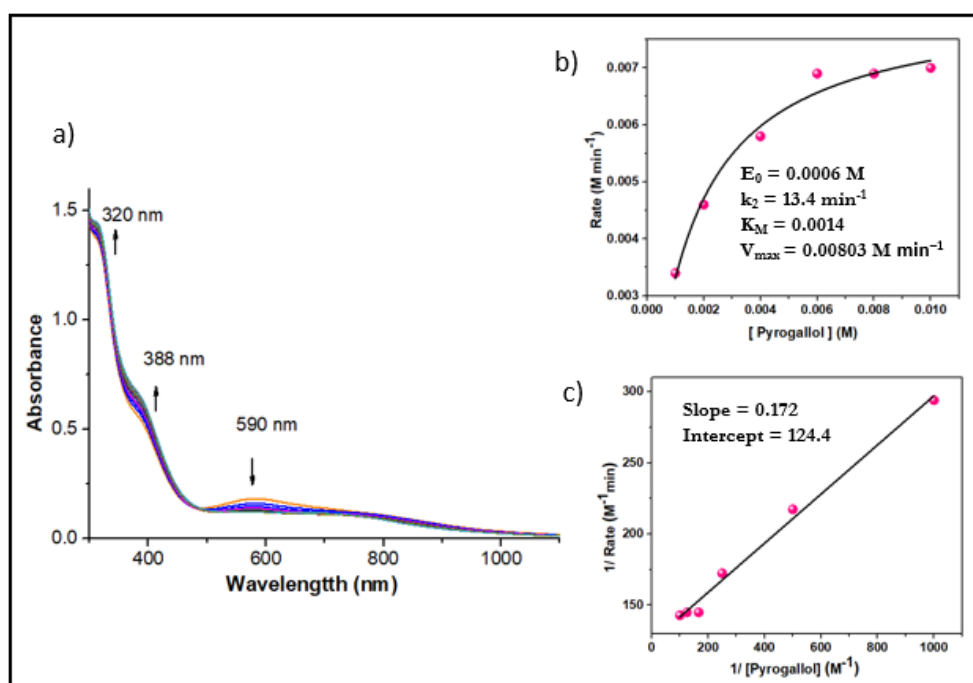


Figure IV.14. (a) Time dependent absorption spectra of a solution containing 6×10^{-4} M of complex **9** and 0.01 M of Pyrogallol in presence of one drop portion of 10^{-2} M H_2O_2 , recorded in the time intervals of 1 min. (b) Plot of rate versus concentration of Pyrogallol for the oxidation reaction catalysed by complex. (c) Lineweaver–Burk plot

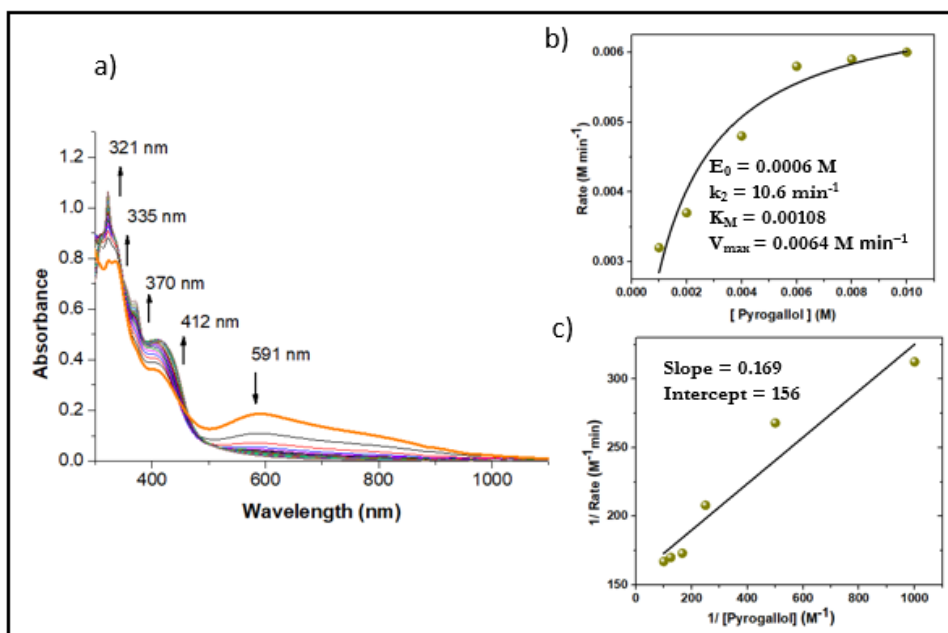
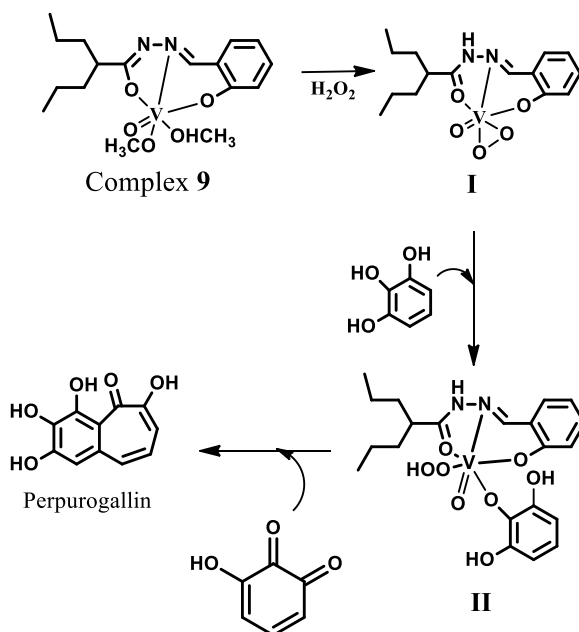


Figure IV.15. (a) Absorption spectra of a solution containing 6×10^{-4} M of complex **10** and 0.01 M of Pyrogallol in presence of one drop portion of 10^{-2} M H_2O_2 recorded at the interval of 1 min. (b) Plot of rate versus concentration of Pyrogallol for the oxidation reaction catalyzed by complex. (c) Lineweaver–Burk plot

Probable reaction pathway: To comprehend the reaction mechanism, we have performed mass spectrometry analysis in addition to UV/VIS spectra. First H_2O_2 combines with complex **9** to create intermediate **I** of peroxovanadium ($m/z = 359$), which then joins with pyrogallol to create intermediate **II** ($m/z = 485$). Following that, intermediate **II** and 3-hydroxy-1:2-benzoquinone aid in the production of perpyrogallin. The aforementioned intermediates were generated in the case of similar methoxido complex **10**. Similar kinds of pyrogallol association intermediates ($m/z = 535$) and peroxo vanadium intermediates ($m/z = 409$) were generated for the complexes **10**. (**Figure IV.25.**) For complex **9**, the intermediate mass spectra is obtained at $m/z = 547$ (**Figure IV.26.**). This suggested chemical mechanism is based on mass spectrometry and UV-vis spectra. Here mechanism for complex **9** is displayed in **Scheme III.3**. We discovered the production of the identical oxo-peroxo intermediate with the reaction mixtures of pyrogallol and dioxo complex **7** in air. On this basis it is concluded that whereas the mono oxo

methoxido complexes **9**, **10** used H_2O_2 as an oxidant, the dioxo complexes **1**, **2** (See **Chapter III**) utilised aerobic oxygen for oxidation of pyrogallol to perpurogallin.



Scheme III.3. Schematic representation for pyrogallol oxidation by 9

J. REACTIVITY WITH H_2O_2

The behaviour of complex **9**, **10** towards H_2O_2 was studied with absorption spectroscopy in dichloromethane: methanol (8:2) solvent. **Figure IV.16.** shows time dependent spectral changes for a solution of **9** (2×10^{-4} M) after addition of one drop portion of H_2O_2 (10^{-2} M) in time intervals of 1 min. With the advancement of the reaction (for complex **9**) the immediately generated peak around 400 nm gradually disappeared with generation of new peaks at around 332 nm, 290 nm, and 280 nm. Complex **10** (**Figure IV.17.**) also showed similar kind of spectra where immediately formed band around 421 nm gradually decreases with formation of new peaks around 370, 355 and 321 nm. Presence of several isosbestic points, confirming the formation of new species, bands around 328-355 nm may be assigned to a LMCT band related to the formation of a $\text{VO}(\text{O}_2)$ moiety.

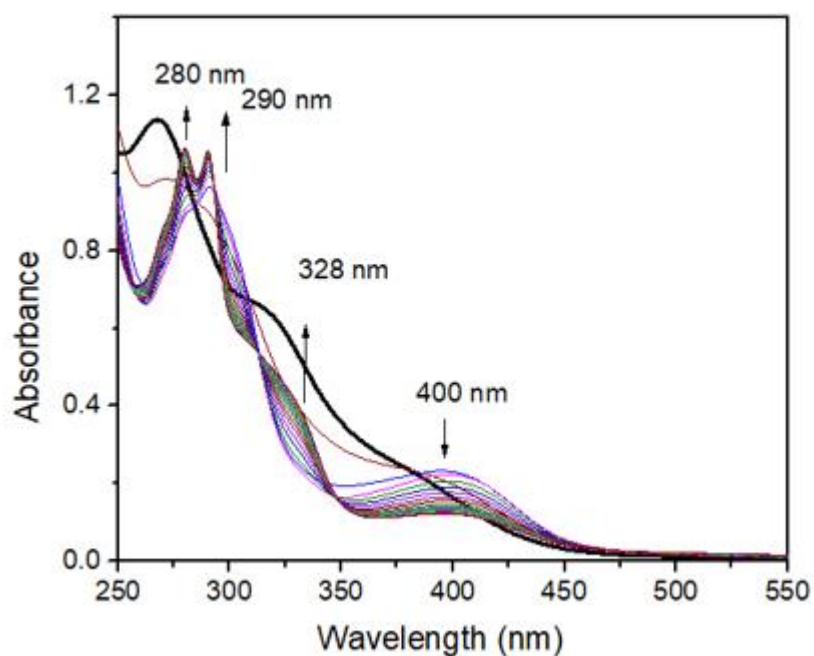


Figure IV.16. Time dependent absorption spectra (1 min interval) of a solution containing 2×10^{-2} M of complex 9 and one drop portion of H_2O_2 (10^{-2} M).

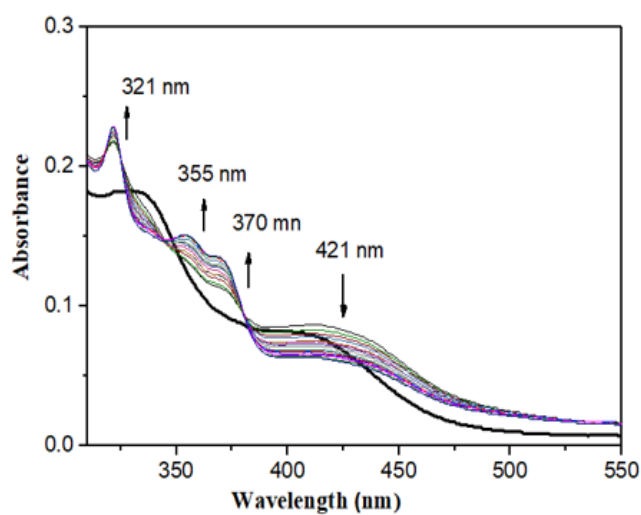


Figure IV.17. Time dependent absorption spectra (1 min interval) of a solution containing 2×10^{-4} M of complex 10 and one drop portion of H_2O_2 (10^{-2} M).

IV.2. CONCLUSION

In the study, it is shown how the choice of solvent influences structural variety in vanadium complexes generating two oxido-methoxido [$V^{VO}(L^1)(OMe)(OHMe)$] (**9**, **10**) and two dinuclear [$V^V(O_2)HL^{1-2}$] (**11**, **12**) starting from $VO(acac)_2$ and two valproic acid hydrazine ligands. Single-crystal X-ray diffraction study was employed to structurally analyse two of the four complexes. It was observed that the ligand systems had various binding modes towards vanadium metal core via amide-iminol tautomeric interconversion. Our present approach is a successful procedure to prepare electro generated mixed-valence vanadium (V/IV) complexes **11a** and **12a**. Frozen solution EPR data and electronic spin density calculations points to a type II complex in solution. The catecholase-like activity of complexes **9** and **10**, which follows the semiquinone radical intermediate pathway as demonstrated by UV-Vis and EPR investigations, was assessed. Additionally, conversion of pyrogallol to purpurogallin by **9** and **10** in the presence of H_2O_2 was examined. The current research made a case for the significance of solvent choice in the creation of mixed oxidation dimers and the subsequent investigation of redox characteristics.

IV.3 EXPERIMENTAL SECTION

A. MATERIALS

$[VO(acac)_2]$ used was prepared according to the literature.^{13a} are used throughout the study. All the reactions with metal salts are carried out under open air atmosphere. All analytically pure solvents were purchased from reputed commercial sources and used without further purification.

B. PREPARATION OF COMPOUNDS

Ligand

Schiff base ligands (H_2L^{3-4}), were prepared by method as described in Chapter III.

Complexes

Synthesis of oxidomethoxido vanadium(V) complexes [V^VO(L¹⁻²)(OMe)(MeOH)], (9 and 10).

When [VO(acac)₂] was allowed to react with methanolic solution of ligand (H₂L³ or H₂L⁴) and other reaction conditions were kept the same as that of acetonitrile solution, we have got light brown coloured crystals of oxidomethoxido vanadium(V) complex **9** of H₂L³ and for complex **10** of H₂L⁴ we have got crystalline product. respectively.

[V^VO(L¹)(OMe)(MeOH)] (9): Yield: 68%. Anal. Calc. for C₁₇H₂₇VN₂O₅: C 52.31%; H 6.97%; N 7.18%. Found: C 52.25%; H 6.89%; N 7.09%. ¹H NMR {300 MHz, CDCl₃, δ (ppm), 8.900 (1H, s, -N=CH), 7.712–7.608 (2H, m, Ar-H), 7.283–7.128 (2H, m, Ar-H), 2.586–2.238 (1H, m, -CH), 1.606–1.171 (8H, m, 4CH₂), 0.907–0.863 (6H, m, 2CH₃). (ESI -MS (positive) in MeOH: The base peak was detected at *m/z* = 391, corresponding to [M + H]⁺. IR (KBr, *v*_{max} / cm⁻¹): 2402 (broad from bound MeOH moiety), 1600 (imine C=N), 1304 (C-O)_{enolic}, 950 (V=O), 766 (V-O).

[V^VO(L²)(OMe)(MeOH)] (10): Yield: 70%. Anal. Calc. for C₂₁H₂₉VN₂O₅: C 57.27%; H 6.64%; N 6.36%; Found: C 57.19%; H, 6.52%; N, 6.24%. ¹H NMR {300 MHz, DMSO-D₆, δ (ppm), 9.78 (1H, s, -N=CH), 8.29–7.44 (6H, m, Ar-H), 2.55–2.52 (1H, m, -CH), 1.659–1.18 (8H, m, 4CH₂), 0.93–0.78 (6H, m, 2CH₃). (ESI -MS (positive) in MeOH: The base peak was detected at *m/z* = 441, corresponding to [M + H]⁺. IR (KBr, *v*_{max} / cm⁻¹): 1596 (imine C=N), 1215 (C-O)_{enolic}, 2595 (broad from bound MeOH moiety), 926 (V=O), 750 (V-O).

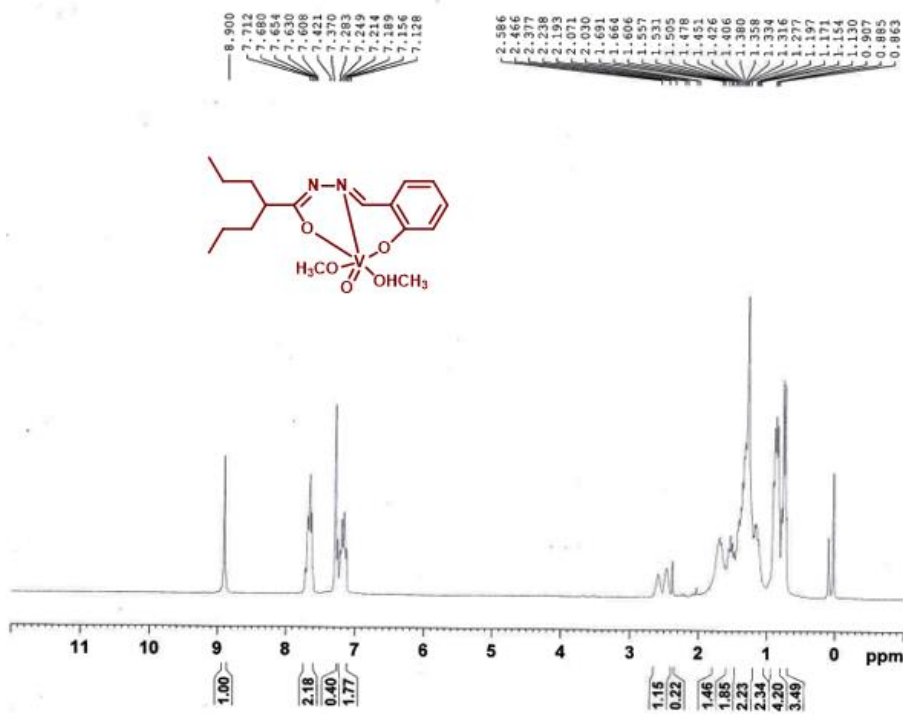


Figure IV.18. ¹H NMR spectra of complex 9 in CDCl₃

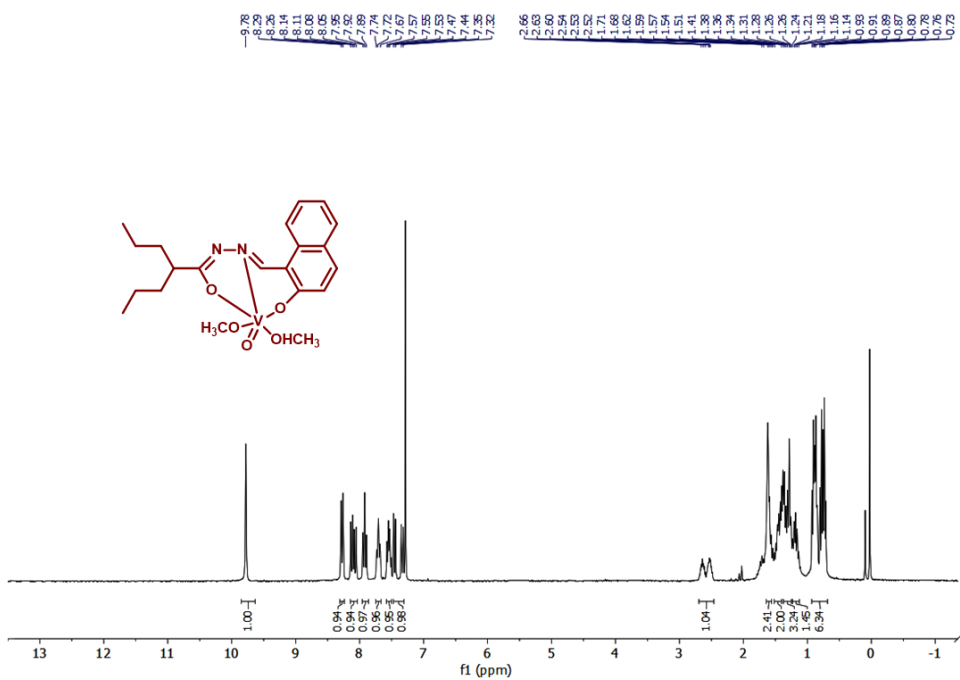


Figure IV.21. ¹H NMR spectra of complex 10 in CDCl₃

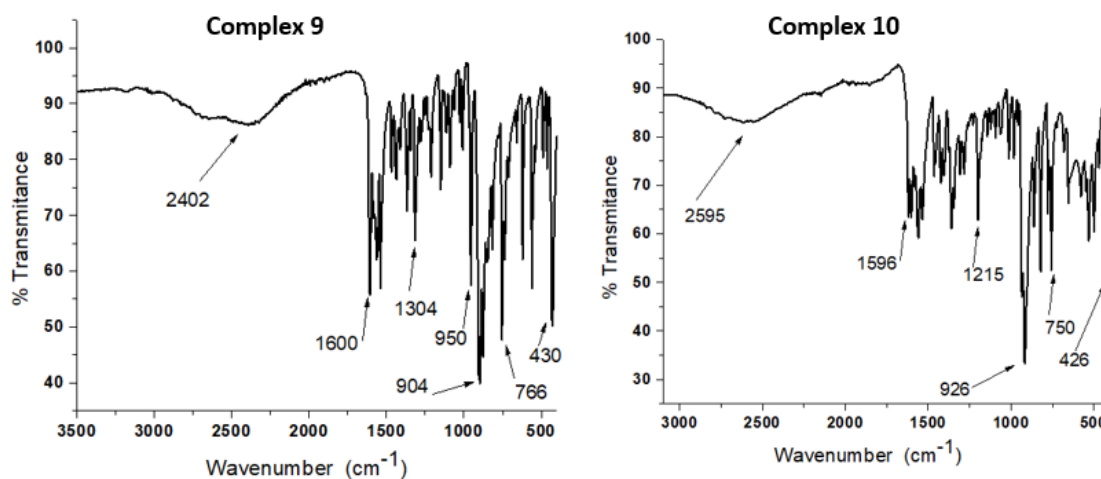


Figure IV.20. IR Spectra of Complex 9, 10

Synthesis of μ -Oxidodioxidovanadium(V) complexes $[\text{V}^{\text{V}}_2\text{O}_3(\text{L}^{1-2})_2]$ (**11** and **12**).

$[\text{VO}(\text{acac})_2]$ was allowed to react with dichloromethane solution of ligand (H_2L^3 or H_2L^4) and other reaction conditions were kept the same as that of the previous two cases. The solution was filtered off and kept for crystallization in dichloromethane-hexane system. After few days deep brown coloured crystalline products were obtained for **11** and for **12** we got tiny needle like crystals.

$[\text{V}^{\text{V}}_2\text{O}_3(\text{L}^1)_2]$ (**11**): Yield: 62%. Anal. Calc. for $\text{C}_{30}\text{H}_{40}\text{V}_2\text{N}_4\text{O}_7$: C 53.74%; H 6.01%; N 8.36%. Found: C 53.63%; H 5.89%; N 8.29%. ^1H NMR {300 MHz, CDCl_3 , δ (ppm), 8.810 (1H, s, $-\text{N}=\text{CH}$), 7.657–6.973 (4H, m, Ar-H), 2.300–2.168 (1H, m, $-\text{CH}$), 1.484–1.101 (8H, m, 4 CH_2), 0.995–0.767 (6H, m, 2 CH_3): (ESI -MS (positive) in MeOH: The base peak was detected at $m/z = 671$, corresponding to $[\text{M} + \text{H}]^+$. IR (KBr, ν_{max} / cm^{-1}): 1595 (imine $\text{C}=\text{N}$), 1275 ($\text{C}-\text{O}$)_{enolic}, 986 ($\text{V}=\text{O}$), 779 ($\text{V}-\text{O}$).

$[\text{V}^{\text{V}}_2\text{O}_3(\text{L}^2)_2]$ (**12**): Yield: 60%. Anal. Calc. for $\text{C}_{38}\text{H}_{44}\text{V}_2\text{N}_4\text{O}_7$: C 59.22%; H 5.75%; N 7.27%; Found: C 59.08%; H, 5.61%; N, 7.18%. ^1H NMR {300 MHz, $\text{DMSO}-\text{D}_6$, δ (ppm), 9.70 (1H, s, $-\text{N}=\text{CH}$), 8.21–7.073 (6H, m, Ar-H), 2.309–2.284 (1H, m, $-\text{CH}$), 1.603–1.287 (8H, m, 4 CH_2), 0.904–0.882 (6H, m, 2 CH_3). (ESI -MS (positive) in MeOH: The base peak was detected at $m/z = 771$, corresponding to $[\text{M} + \text{H}]^+$. IR (KBr, ν_{max} / cm^{-1}): 1590 (imine $\text{C}=\text{N}$), 1261 ($\text{C}-\text{O}$)_{enolic}, 966 ($\text{V}=\text{O}$), 770 ($\text{V}-\text{O}$).

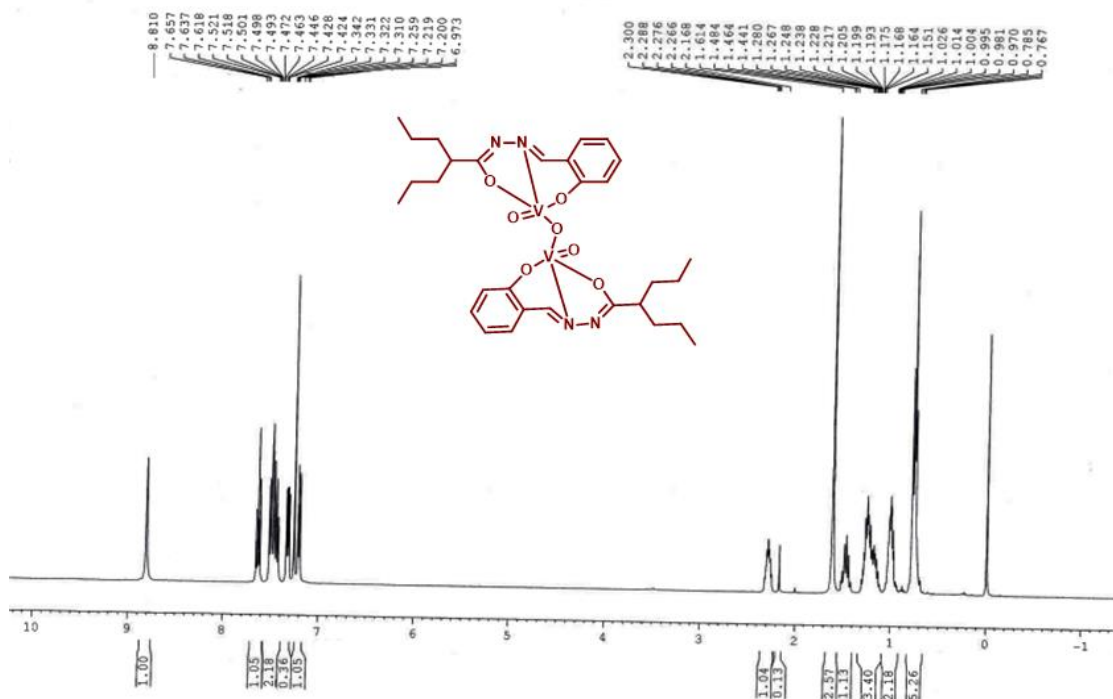


Figure IV.21. ^1H NMR spectra of complex 11 in CDCl_3

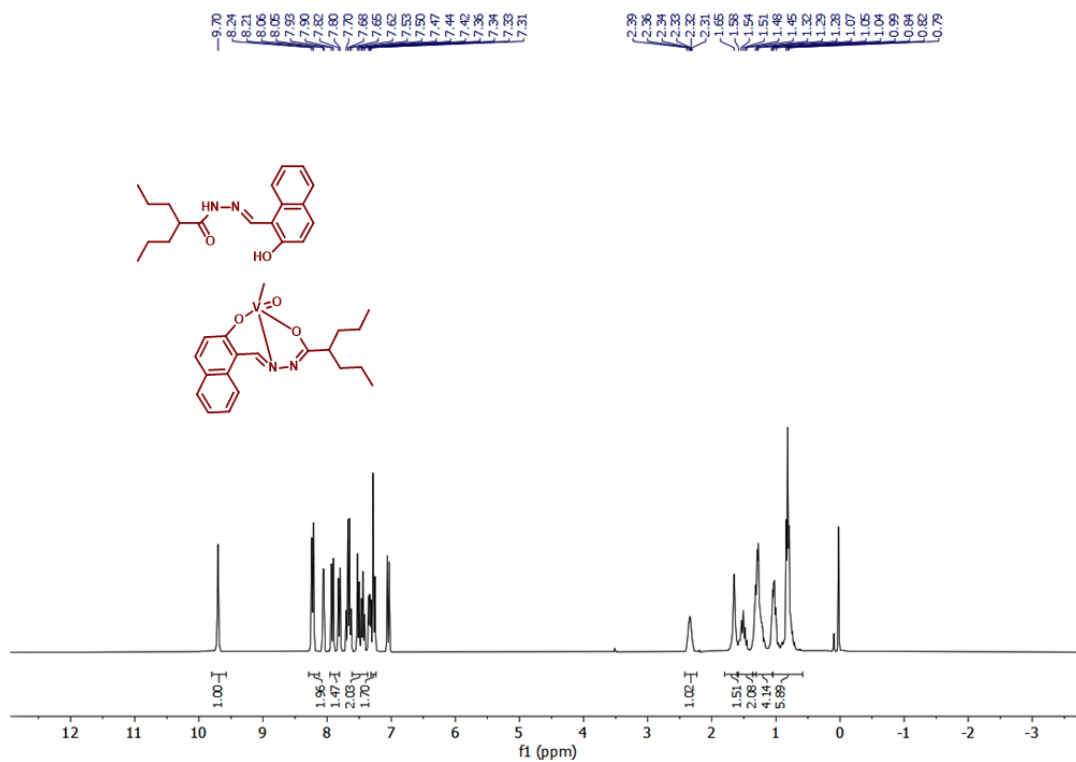


Figure IV.22. ^1H NMR spectra of complex 12 in CDCl_3

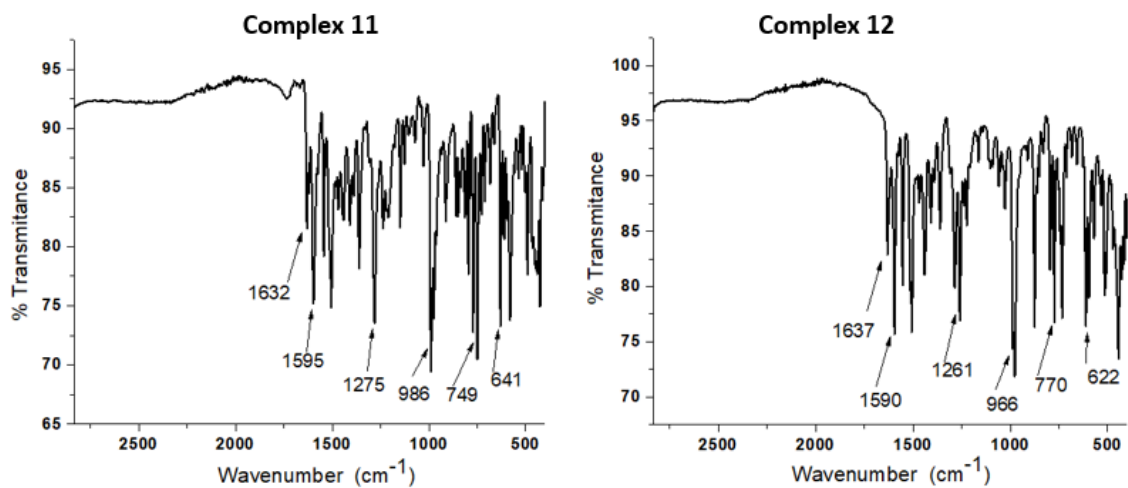


Figure IV.23. IR Spectra of Complex 11, 12

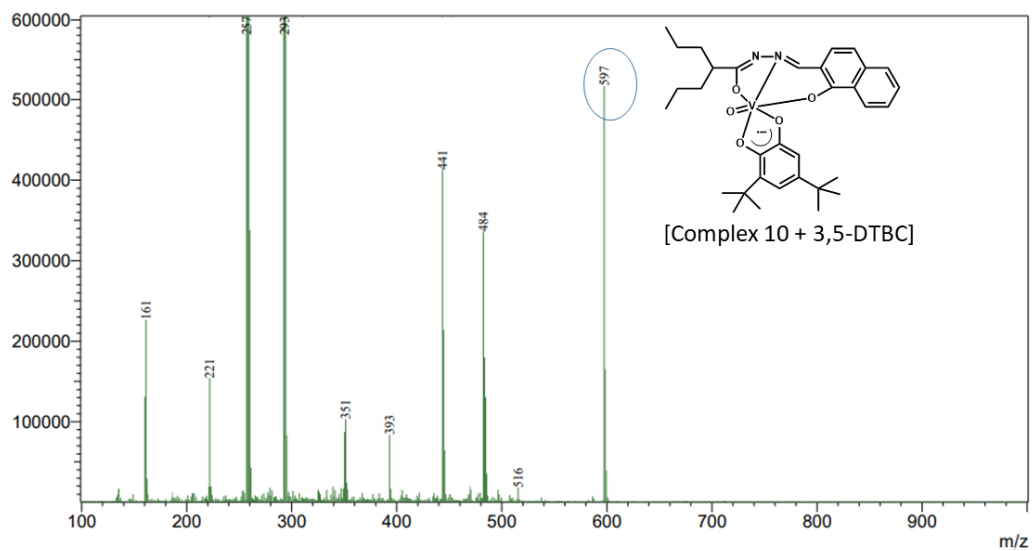


Figure IV.24. Mass Spectra of Complex 10 + Catechol Mixture

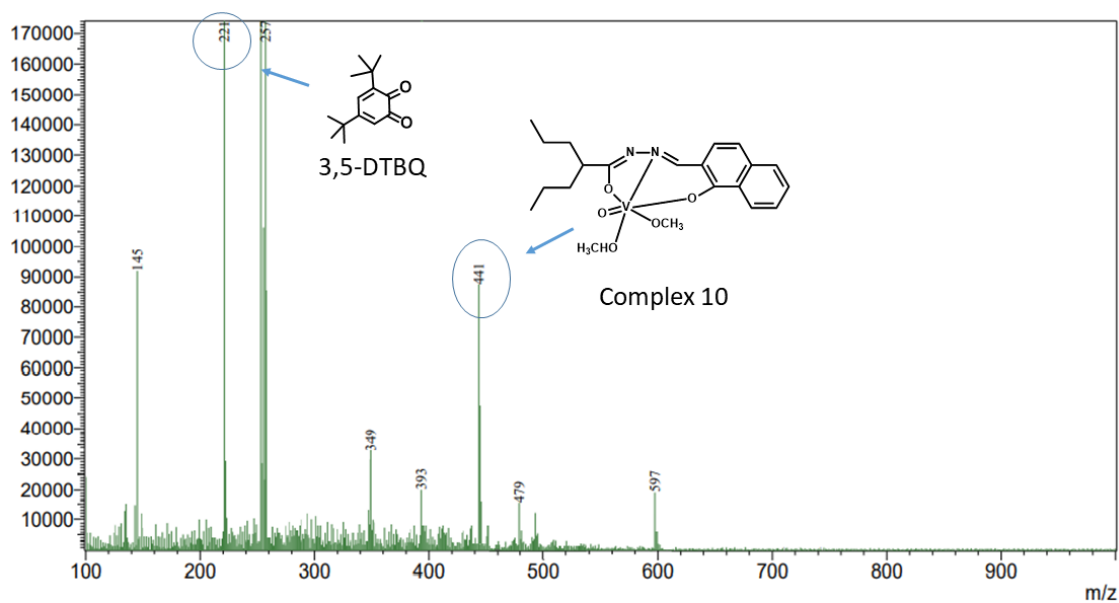


Figure IV.25. Mass Spectra of Complex 10 + Catechol at infinite time

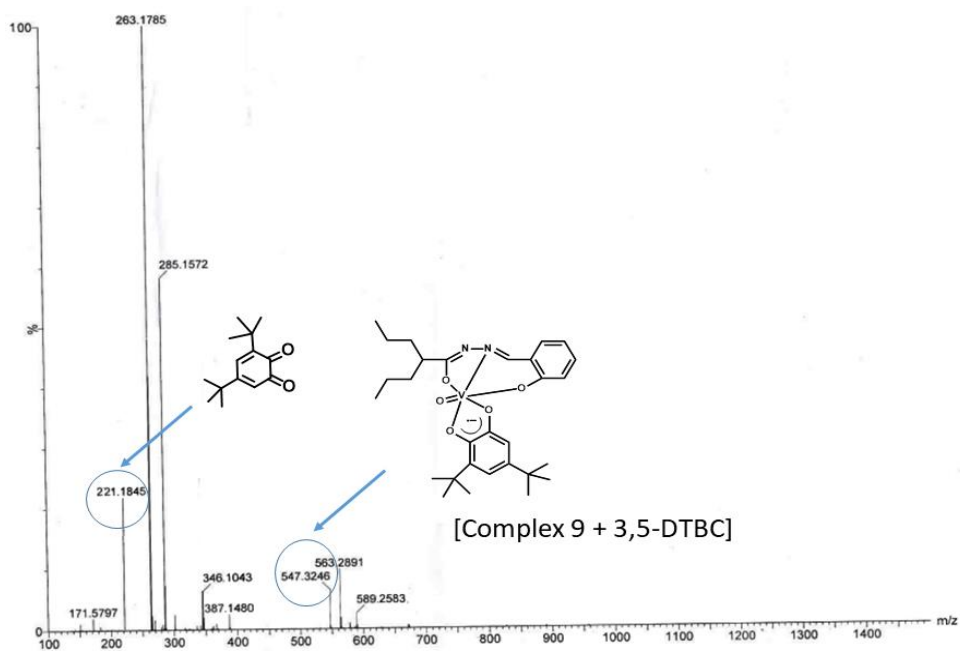


Figure IV.26. Mass Spectra of Complex 9 + Catechol

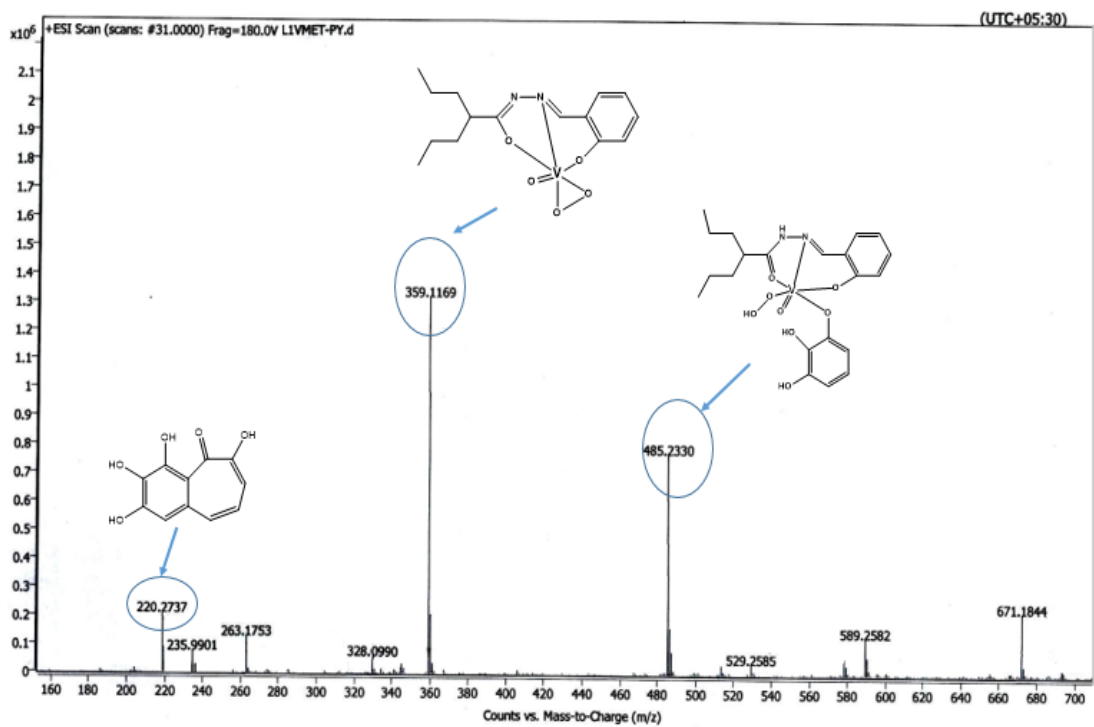


Figure IV.27. Mass spectrum of complex 9 and pyrogallol

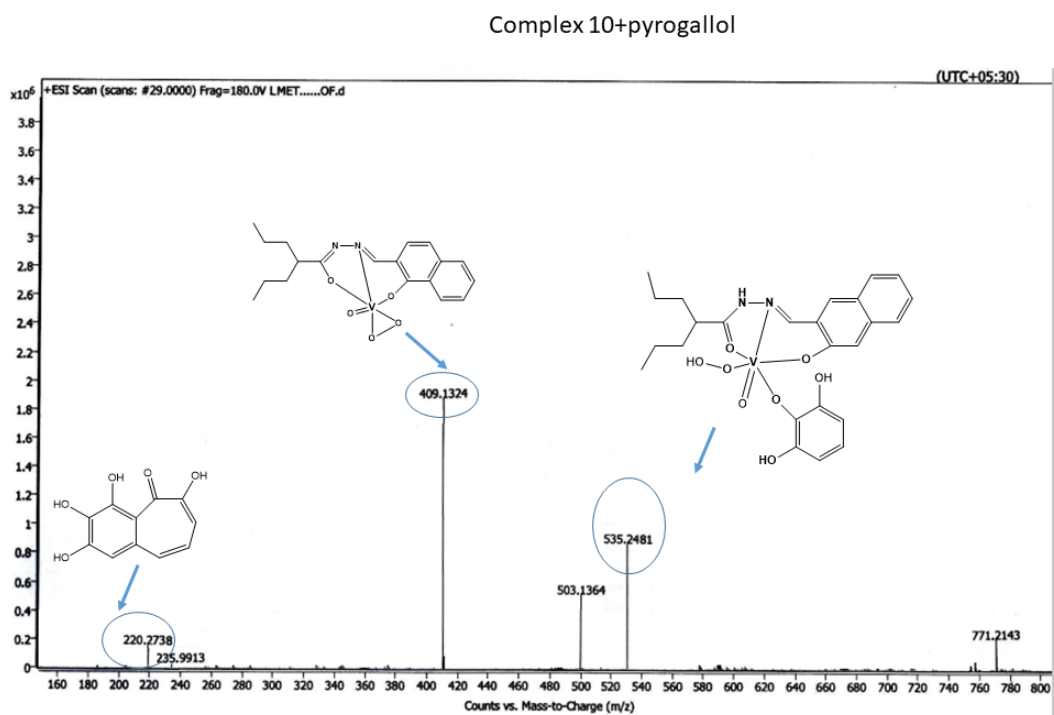


Figure IV.28. Mass spectrum of complex 10 and pyrogallol

C. X-RAY STRUCTURE DETERMINATION

The single crystal suitable for X-ray crystallographic analysis of complexes **9**, **12** were obtained by slow evaporation of methanolic solution at 25°C. Details of the X-ray work are given in tabular form in **Table IV.7.** (see also Chapter I). Atomic coordinates and isotropic thermal parameters are collected in **Table IV.8., Table III.9.**

D. PHYSICAL MEASUREMENTS AND COMPUTATIONAL STUDIES

All physical measurements that included elemental analyses, IR, ESI-MS studies, absorption spectra, ¹H NMR spectra, Cyclic Voltammetry studies, EPR Spectra, Constant Potential Electrolysis (CPE), Spectroelectrochemistry measurements and computational studies were performed as described in **Chapter I.**

Table IV.7 Crystallographic data for complexes

Crystal Data

	Complex 9	Complex 12
Chemical Formula	C ₁₇ H ₂₇ N ₂ O ₅ V	C ₃₈ H ₃₇ N ₄ O ₇ V ₂
Formula weight	390.34	763.59
Crystal system	Monoclinic	triclinic
Space group	P21/c	P - 1
<i>a</i> / Å	12.966(3)	8.6752(14)
<i>b</i> / Å	16.279(3)	13.712(2)
<i>c</i> / Å	10.330(2)	17.313(3)
α / °	90	75.983(5)
β / °	112.488(5)	89.588(5)
γ / °	90	75.312(5)
<i>V</i> / Å ³	2014.6(7)	1929.6(5)
<i>Z</i>	4	2
<i>D</i> _{calcd} / mg m ⁻³	1.082	1.314
μ / mm ⁻¹	0.519	0.079
θ / °	26.87	27.07
<i>T</i> / K	273.15	273.15

Data collection

	Complex 9	Complex 12
Total refl. collected	7359	20644
Unique refl. (<i>R</i> _{int})	4539	1673
Used refl.	2472	2499
<i>h k l</i> range	-16 ≤ <i>h</i> ≤ 16 -20 ≤ <i>k</i> ≤ 20 -13 ≤ <i>l</i> ≤ 13	-7 ≤ <i>h</i> ≤ 7 -11 ≤ <i>k</i> ≤ 11 -14 ≤ <i>l</i> ≤ 14

Structure Solution and Refinement

	Complex 9	Complex 12
Solution	Patterson	Patterson
Refinement	Full-matrix least-squares on F ²	Full-matrix least-squares on F ²
GOF on F ²	1.218	1.02
R1, ^a [I > 2σ(I)]	0.1740	0.0837
wR2 ^b [I > 2σ(I)]	0.3054	0.2157
R1 [all data]	0.2563	0.1250
wR2 [all data]	0.3439	0.2468

$${}^a R1 = \frac{\sum ||F_o| - |F_c||}{\sum |F_o|} \cdot {}^b wR2 = [\frac{\sum [w(F_o^2 - F_c^2)^2]}{\sum [w(F_o^2)^2]}]^{1/2}$$

Table IV.8 Fractional Atomic Coordinates ($\times 10^4$) and Equivalent Isotropic Displacement Parameters ($\text{\AA}^2 \times 10^3$) for **Complex 9**. U_{eq} is defined as 1/3 of the trace of the orthogonalized U_{ij} tensor.

Atom	<i>x</i>	<i>y</i>	<i>z</i>	U(eq)
V1	1806.4(11)	3908.1(8)	2195.7(12)	58.6(4)
O1	989(4)	3198(3)	776(5)	64.4(14)
O5	3292(4)	3329(3)	1730(5)	66.4(14)
O2	3085(5)	4168(3)	3901(5)	76.3(16)
O4	2024(4)	4729(3)	1211(5)	65.6(14)
O3	839(5)	4259(4)	2634(6)	81.3(16)
N1	2124(5)	2838(4)	3448(6)	60.4(16)
C1	458(6)	2495(5)	712(7)	60(2)
N2	2968(6)	2902(5)	4752(6)	79(2)
C3	1623(7)	2155(6)	3155(8)	70(2)
C2	740(7)	1947(5)	1839(8)	64(2)
C14	-381(7)	2281(6)	-567(9)	82(3)
C4	3420(7)	3621(7)	4874(8)	78(3)
C13	1519(9)	5515(5)	903(11)	97(3)
C15	-919(9)	1535(7)	-705(12)	108(4)
C17	173(8)	1198(6)	1662(11)	90(3)
C12	4194(8)	3807(6)	1700(10)	92(3)
C9	4061(13)	4253(9)	7247(14)	141(3)
(5	4412(9)	3828(10)	6235(12)	140(3)
C16	-634(9)	1002(7)	427(13)	107(3)
C7	5854(11)	3141(11)	5526(14)	140(3)
C11	3083(11)	5115(8)	8334(11)	141(3)
C10	3160(12)	4666(9)	7232(14)	141(3)
C6	5410(10)	3548(10)	6317(13)	140(3)
C8	6814(13)	2732(12)	5730(20)	227(10)

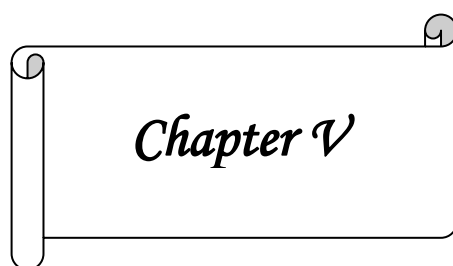
Table IV.9 Fractional Atomic Coordinates ($\times 10^4$) and Equivalent Isotropic Displacement Parameters ($\text{\AA}^2 \times 10^3$) for **Complex 12**. U_{eq} is defined as 1/3 of the trace of the orthogonalized U_{ij} tensor.

Atom	x	y	z	U(eq)
V1	1323(3)	8518.7(17)	7313.3(12)	57.2(10)
V2	2862(3)	6327.3(17)	6961.3(12)	58.7(11)
O2	3022(10)	7610(6)	8038(5)	62(3)
O4	2835(10)	5442(7)	7934(4)	61(3)
O7	-166(11)	8804(7)	7808(5)	68(3)
O1	1035(11)	9535(7)	6391(4)	67(3)
O5	3974(13)	7294(7)	6373(5)	70(3)
N1	2505(14)	9451(9)	7703(6)	56(3)
O6	2384(11)	5772(6)	6336(5)	70(3)
N3	5235(13)	5550(9)	7092(6)	60(3)
N4	6337(15)	6042(10)	6665(7)	77(4)
N2	3545(12)	8980(10)	8364(6)	61(3)
O3	1204(11)	7425(6)	6971(4)	65(2)
C2	1116(16)	11075(10)	6768(7)	49(3)
C6	4916(17)	3955(11)	7929(7)	64.6(16)
C29	-262(16)	12757(11)	5888(8)	53(4)
C5	3488(17)	4416(12)	8190(7)	64.6(16)
C1	656(17)	10585(11)	6248(8)	57(4)
C21	4590(17)	2254(11)	8684(7)	64.6(16)
C16	5539(17)	2812(11)	8176(7)	64.6(16)
C8	5470(20)	6964(14)	6282(9)	83(5)
C22	3194(16)	2780(11)	8955(7)	64.6(16)
C31	-246(18)	11161(11)	5547(7)	72(5)
C23	2624(16)	3821(10)	8728(6)	64.6(16)
C7	5834(17)	4592(11)	7445(7)	63(4)
C36	6177(18)	6509(11)	8981(8)	78(5)
C24	616(16)	12199(10)	6612(7)	47(3)
C17	6952(17)	2254(11)	7912(7)	64.6(16)
C4	3770(30)	7979(16)	8491(12)	110(3)
C27	-395(18)	14374(12)	6221(9)	73(4)
C28	-759(19)	13862(11)	5708(8)	72(5)
C18	7389(17)	1205(11)	8139(7)	64.6(16)
C33	3683(16)	6632(11)	9719(8)	71(5)
C32	4730(16)	7255(10)	9214(7)	60(4)
C3	2194(15)	10472(11)	7453(7)	49(3)
C15	6290(20)	9922(12)	6631(9)	110(3)
C10	5840(30)	7630(18)	4887(11)	169(6)
C11	6010(30)	6652(17)	4676(11)	169(6)
C14	6370(20)	8881(12)	6561(9)	110(3)
C12	5240(30)	6725(16)	3937(10)	169(6)
C13	6050(20)	8685(13)	5822(9)	110(3)
C20	5174(17)	1128(11)	8897(7)	64.6(16)
C25	955(16)	12773(11)	7115(8)	60(4)
C30	-680(20)	12207(12)	5371(8)	83(5)
C34	2199(17)	7283(12)	9978(8)	81(5)
C26	454(18)	13830(12)	6935(9)	72(4)
C9	6300(20)	7647(12)	5689(9)	101(5)
C19	6539(16)	648(11)	8625(7)	64.6(16)
C38A	8760(50)	6250(20)	8340(30)	84(13)
C37A	7370(40)	6990(20)	8570(20)	68(12)
C35	1247(19)	6631(13)	10509(9)	112(7)
C37	7710(60)	7190(30)	8850(30)	57(19)
C38	9180(60)	6340(30)	8680(40)	60(20)

References

1. Mishra, M. K.; Kukal, S.; Paul, P. R.; Bora, S.; Singh, A.; Kukreti, S.; Saso, L.; Muthusamy, K.; Hasija, Y.; Kukreti, R. *Molecules* **2022**, *27*, 104
2. Safdar, A.; Ismail, F. *Saudi Pharm. J.* **2022**, *31*, 265-278. Volume 31, Issue 2, February **2023**, Pages 265-278
3. Dong, L.; Fang, L.; Dai, X.; Zhang, J.; Wang, J.; Xu, P. *Drug Dev Res.* **2022**, *83*, 131-141.
4. El-Faham, A.; Farooq, M.; Khattab, S. N.; Elkayal, A. M.; Ibrahim, M. F.; Abutaha, N.; Wadaan, M. A.; Hamed, E. A. *Chem. Pharm. Bull.* **2014**, *62*, 591-599.
5. Su, X.; Aprahamian, I. *Chem. Soc. Rev.* **2014**, *43*, 1963-1981.
6. Popiołek, Ł.; Tuszyńska, K.; Biernasiuk, A. *Biomed. pharmacother.* **2022**, *153*, 113302
7. Szklarzewicz, J.; Jurowska, A.; Matoga, D.; Kruczała, K.; Kazek, G.; Mordyl, B.; Sapa, J.; Papież, M. *Polyhedron* **2020**, *185*, 114589.
8. Levina, A.; Pires Vieira, A.; Wijetunga, A.; Kaur, R.; Koehn, J. T.; Crans, D. C.; Lay, P. A. *Angew. Chem.* **2020**, *59*, 15834-15838.
9. (a) Mondal, A.; Sarkar S.; Chopra, D.; Guru Row, T. N.; Pramanik, K.; Rajak, K. K. *Inorg. Chem.* **2005**, *44*, 703–708. (b) Dinda, R.; Sengupta, P.; Sutradhar, M.; Mak, T. C. W.; Ghosh, S. *Inorg. Chem.* **2008**, *47(13)*, 5634–5640. (c) Mondal, S.; Ghosh, P.; Chakravorty, A. *Inorg. Chem.* **1997**, *36(1)*, 59–63.
10. Albino, A.; Benci, S.; Tesi, L.; Atzori, M.; Torre, R.; Sanvito, S., Sessoli, R.; Lunghi, A. *Inorg. Chem.* **2019**, *58(15)*, 10260–10268.
11. (a) Dutta, S. K.; Kumar, S. B.; Bhattacharyya, S.; Tiekink, E. R. T.; Chaudhury, M. Core. *Inorg. Chem.* **1997**, *36*, 4954-4960.
12. Dutta, S. K.; Samanta, S.; Kumar, S. B.; Han, O. H.; Burckel, P.; Pinkerton, A. A.; Chaudhury, M. *Inorg. Chem.* **1999**, *38*, 1982-1988.

13. (a) Patra, R.; Mondal, S.; Sinha, D.; Rajak, K. K. *ACS Omega* **2022**, *7*, 11710-11721. (b) Mahroof-Tahir, M.; Keramidas, A. D.; Goldfarb, R. B.; Anderson, O. P.; Miller, M. M.; Crans, D. C. *Inorg. Chem.* **1997**, *36*, 1657-1668.
14. (a) Salonen, P.; Peuronen, A.; Lehtonen, A. *Inorg. Chem. Commun.* **2017**, *86*, 165-167. (b) Banu, K. S.; Chattopadhyay, T.; Banerjee, A.; Bhattacharya, S.; Suresh, E.; Nethaji, M.; Zangrando, E., Das, D. *Inorg. Chem.* **2008**, *47*, 16, 7083-7093. (c) Dey, S. K.; Mukherjee A. *Coord. Chem. Rev.* **2016**, *310*, 80-115. (d) Rath, S. P.; Rajak, K. K.; Chakravorty, A. *Inorg. Chem.* **1999**, *38*, 4376-4377. (e) Salonen, P.; Savela, R.; Peuronen, A.; Lehtonen, A. *Dalton Trans.* **2021**, *50*, 6088.
15. Cornman, C. R.; Colpas, G. J.; Hoeschele, J. D.; Kampf, J.; Pecoraro, V. L. *J. Am. Chem. Soc.* **1992**, *114*(25), 9925-9933.
16. Maurya, M. R.; Sarkar, B.; Avecilla, F.; Correia, I. *Eur. J. Inorg. Chem.* **2016**, *2016*, 4028-4044.
17. Kurbah, S. D.; Syiemlieh, I.; Lal, R. A. *R. Soc. open sci.* **2018**, *5*, 171471.



Chapter V

Synthesis, crystal structure and redox studies of vanadium (V) complexes with Schiff base ligands derived from 3-amino-2-naphthol

*Synthesis, crystal structure and redox studies of vanadium(V) complexes with Schiff base ligands derived from 3-amino-2-naphthol**

Abstract

Four mononuclear vanadium (V) complexes (**13**– **16**) were synthesised by the stoichiometric reaction of VO(acac)₂ with four Schiff base ligands **H₂L⁵⁻⁸**. Complexes **13**, **14** have general formula VO(L⁵⁻⁶)(OMe)(MeOH) where the ligand systems were **H₂L⁵** = (E)-3-((2-hydroxybenzylidene)amino)naphthalen-2-ol, **H₂L⁶** = (E)-3-(((2-hydroxynaphthalen-1-yl)methylene)amino)naphthalen-2-ol. The other set of complexes i.e. complex **15**, **16** type of VO(L⁷⁻⁸)(OMe) where the ligand systems were **H₂L⁷** = (E)-3-((2-hydroxy-5-methylbenzylidene)amino)naphthalen-2-ol, **H₂L⁸** = (E)-3-((2-hydroxy-5-methoxybenzylidene)amino)naphthalen-2-ol. The X-ray analysis showed keto-amine tautomeric form of one of the ligand **H₂L⁸** and in case of complexes, octahedral geometry for **13**, **14** whereas penta-coordinated square-pyramidal geometry for **15**, **16** around the metal centre. The chemical identity of the complexes and their redox behaviour were unambiguously studied by cyclic voltammetry which confirms the presence of V^{VO}/V^{VO}, V^{VO}/V^{III}O, imine/imino radical and phenoxy/phenolato redox couple.

*This work is going to publish soon

Introduction

Ortho -hydroxyaryl Schiff bases exhibit tautomeric rearrangements as a result of intramolecular proton transfer between the oxygen and nitrogen atoms that can be adjusted using structural changes, solvent polarity, temperature, and UV - irradiation¹. Very small energy barrier between these two tautomeric forms leads to its utilisation as optic materials, molecular switches, and sensor probes.² The type of aldehyde utilised to make the appropriate Schiff bases has a significant impact on the dominant form's type³. Keto -amine tautomerism is prominent in naphthaldimine Schiff bases, but phenolimine is dominant in salicylaldimine Schiff bases, depending on the solvent polarity. However, in solid state, keto -amine tautomerism is determined in naphthaldimine Schiff bases, whereas phenol -imine in salicylaldimine Schiff bases⁴.

Metal complexes of Schiff base ligands, particularly those containing vanadium, have received a lot of interest due to their biological and catalytic applications⁵. The active participation of vanadium in the natural enzymes like nitrogenase and bromoperoxidase shows⁶ how important its redox characteristics are. The redox processes of vanadium have been examined in a number of model intricate structures. Depending on their oxidation state and coordination number, vanadium complexes, including organovanadium compounds, can be found in a number of different forms. Vanadium can exist in oxidation levels between -3 and +5, and it often changes states by one -electron redox reactions⁷. This adaptability enables the creation of a variety of organic reactions by manipulating the redox potential of the vanadium molecule⁸. Moreover, versatile electrochemical redox kinetics⁹ of vanadium has prompted researchers to focus on the development of electrochemical system for renewable energy storage, i.e., Vanadium redox flow battery¹⁰ (VRFB).

In this study, four ortho hydroxyl Schiff base ligands **H₂L⁵⁻⁸** and its V(V) complexes were synthesized. Molecular architectures, geometric characteristics have been determined using spectroscopic and analytical methods. In solid state,

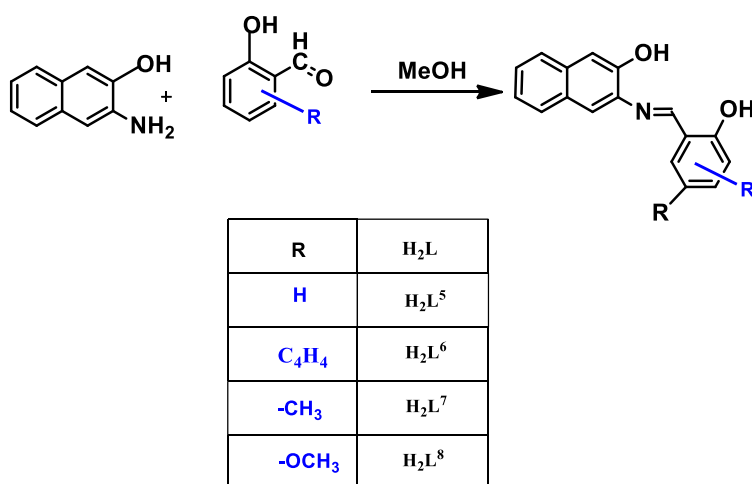
the ligand H_2L^8 exist in the keto -amine tautomeric forms (phenolimine, $\text{O}-\text{H}\dots\text{N} \rightleftharpoons$ keto -amine, $\text{O}\dots\text{H}-\text{N}$) forms as confirmed by single crystal X -ray data. Penta coordinated structure for complexes **13**, **14** and hexacoordinated structure for **15**, **16** were also elucidated by single crystal X -ray diffraction. Finally, cyclic voltametry were used to explore the presence of $\text{V}^{\text{VO}}/\text{V}^{\text{IVO}}$, $\text{V}^{\text{IVO}}/\text{V}^{\text{III O}}$, imine/imino radical and phenoxy/phenolato redox couple. The typical redox state of the complexes was further explained by EPR and theoretical spin density calculations.

V.1 RESULTS AND DISCUSSION

A. SYNTHESIS

i) Ligands

The hydrazone ligand H_2L^{5-8} has been used in the present work (Scheme V.1.) and it was synthesized by reacting aldehyde and aroyl hydrazine in a ratio of 1:1 in N,N -dimethyl formamide. Four tridentate Schiff base ligands (H_2L^{5-8}) were prepared by condensation of equimolar amount of 3 -amino -2 -naphthol with four different aldehydes, with salicylaldehyde (H_2L^5), naphthaldehyde (H_2L^6), 4 -methylsalicylaldehyde (H_2L^7) and with 4 -methoxysalicylaldehyde (H_2L^8) in methanol. (Scheme V.1). The details of synthetic procedures of the ligands are given in experimental section of this chapter.

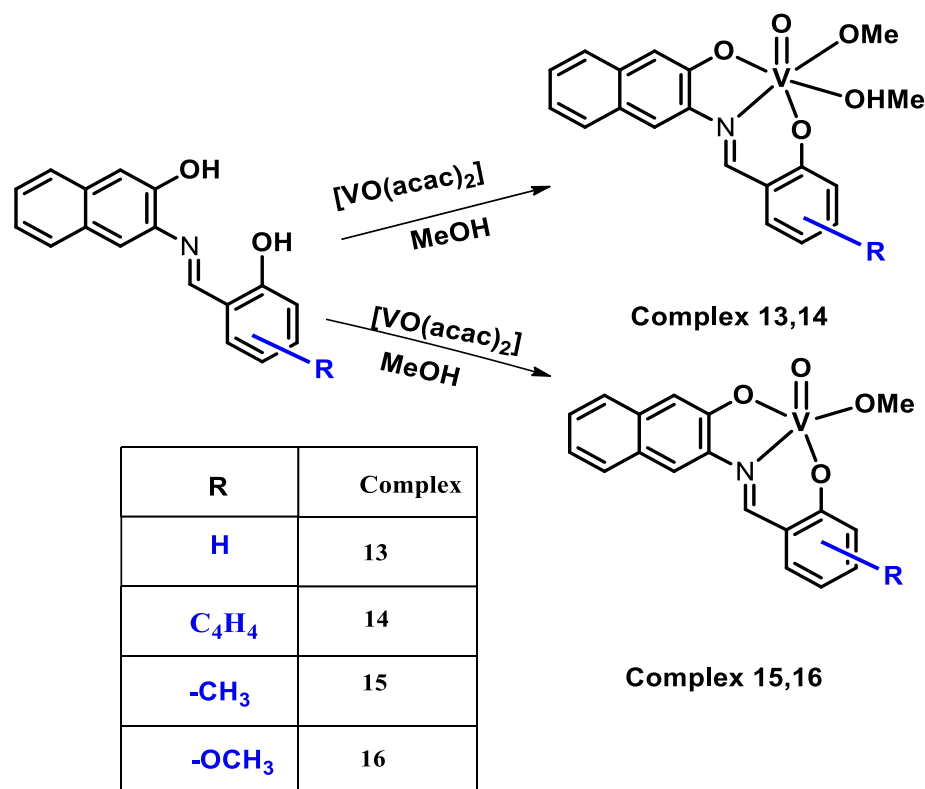


Scheme V.1. Schematic representation for the synthesis of the ligands.

ii) Complexes

The stoichiometric reaction of $\text{VO}(\text{acac})_2$ with methanolic solution of Schiff base ligand H_2L^5 and H_2L^6 yielded Complexes **13** and **14** respectively of general formula $\text{VO}(\text{L}^{5-6})(\text{OMe})(\text{MeOH})$. Reaction of $\text{VO}(\text{acac})_2$ with ligand H_2L^7 and H_2L^8 yielded Complexes **15** and **16** respectively general formula $\text{VO}(\text{L}^{7-8})(\text{OMe})$.

(Scheme V.2). The details of synthetic procedures of the complexes are given in experimental section of this chapter.



Scheme V.2. Schematic representation for the synthesis of the complexes.

B. CRYSTAL STRUCTURES

H₂L⁸: Solid state structures of the ligand was elucidated using single crystal X-ray diffraction technique. Selected bond lengths and angles of **H₂L⁸** are given in **Table V.1**. The phenolic OH from salicylaldehyde and imine nitrogen exist in O-H...N \rightleftharpoons keto -amine, O...H-N tautomeric form (**Figure V.1**).

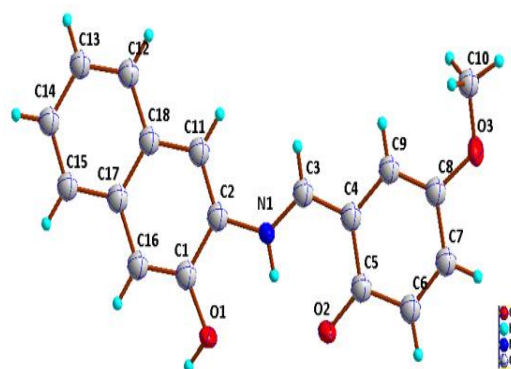


Figure V.1. Perspective view of **H₂L⁸**

The C5 -O2 (1.303 Å), the C1 -O1 (1.351 Å) suggest partial double bond character

in the C5 -O2 bond. The crystal structure of ligand revealed almost coplanar with dihedral angles of C2 -N1 -C3 -C4 (178.5 °), C3 -C4 -C5 -O2 (-0.3 °) and C9 -C4 -C5 -O2 (-178.3 °).

Table V.1. Selected Bond Lengths (Å) and Angles (°) for H₂L⁸

Bond Length (Å)		Bond Angle (°)	
O1-C1	1.351(4)	O2-C5-C4	121.3(2)
O2-C5	1.303(3)	O1-C1-C2	115.6(3)
O3-C8	1.374(4)	N1-C2-C1	114.9(2)
O3-C10	1.400(3)	N1-C3-C4	122.6(3)
N1-C2	1.407(4)	C2-N1-H1A	116.00
N1-C3	1.306(4)	C3-C4-C5-O2	0.3(4)
N1-H1A	0.8600	C9-C4-C5-O2	178.3(2)
		C3-N1-C2-C1	171.5(3)
		O1-C1-C2-N1	2.3(4)

Complex 13 and 14: Both the complexes crystallised in monoclinic system, complex **1** (**Figure V.2a**), with space group P21/n 1 and complex **2** (**Figure V.2b**), in with P -1 space group. Coordination geometry of the complexes can be described as distorted octahedral with the doubly bonded oxo group and very weakly bonded methanol in the axial position. The NOO donor from ligand and methoxide oxygen atom define the equatorial plane in the complexes. O3=V-O5(methanol) axis is almost linear with bond angle in the range of 174 °. Because of the *trans* effect of the oxo group, V-O(methanol) bond length is considerably elongated, making methanol weakly coordinated. For complex **1**, V1-O5(methanol) bond length is 2.458 Å while for complex **2**, it is 2.279 Å. The V=O bond, is in the range of 1.57-1.59 Å is the shortest. Other bond lengths, and the bond angles are in normal ranges. Intermolecular hydrogen bonding interactions, O-H...O established between the coordinated methanolic O-H with coordinated O atom from 3 -amino -2 -naphthol moiety further stabilised

the solid state structure. (Figure V.3). Selected bond lengths and angles of complexes are given in Table V.2 for 13 and Table V.3 for 14.

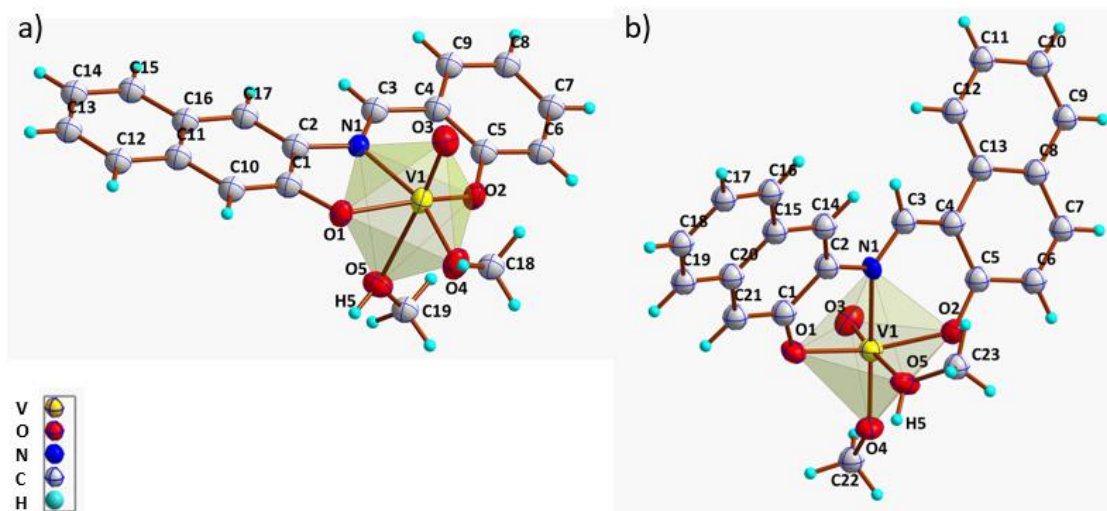


Figure V.2. Perspective view of (a) Complex 13, (b) Complex 14

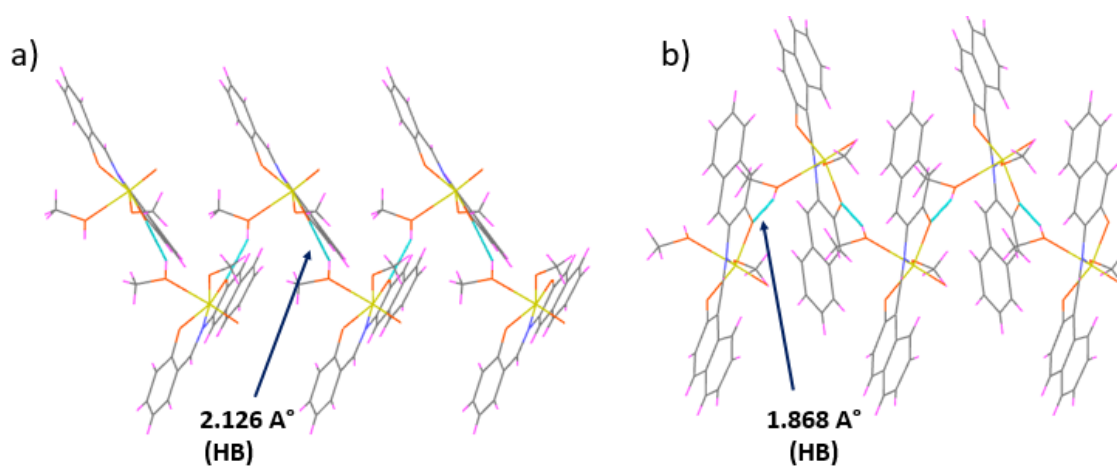


Figure V.3. Perspective view of a) Complex 13, b) Complex 14

Table V.2. Selected Bond Lengths (Å) and Angles (°) for **Complex 13**.

Bond Length (Å)		Bond Angle (°)	
V1-O1	1.940(3)	O1-V1-O2	152.85(15)
V1-O2	1.883(3)	O1-V1-O3	100.32(16)
V1-O3	1.598(4)	O1-V1-O4	92.32(15)
V1-O4	1.783(3)	O1-V1-N1	77.90(7)
V1-N1	2.180(4)	O2-V1-O3	99.96(7)
V1-O5	2.458(4)	O2-V1-O4	100.49(16)
O1-C1	1.360(5)	O2-V1-N1	83.79(14)
O2-C5	1.352(6)	O3-V1-O4	103.02(18)
		O3-V1-N1	96.46(17)
		O4-V1-N1	161.87(8)
		O3-V1-O5	174.123(17)

Table V.3. Selected Bond Lengths (Å) and Angles (°) for **Complex 14**

Bond Length (Å)		Bond Angle (°)	
V1-O1	1.949(18)	O1-V1-O2	155.2(2)
V1-O2	1.881(5)	O1-V1-O3	98.8(2)
V1-O3	1.578(5)	O1-V1-O4	93.7(2)
V1-O4	1.769(5)	O1-V1-O5	82.1(2)
V1-O5	2.279(5)	O2-V1-O3	96.5(2)
V1-N1	2.117(5)	O2-V1-O4	101.8(2)
O1-C1	1.338(8)	O2-V1-N1	82.0(2)
O2-C5	1.325(8)	O3-V1-O4	102.7(3)
		O3-V1-N1	95.7(2)
		O4 -V1-N1	82.4(2)
		O3 -V1-O5	174.7(2)

Complex 15 and 16: Both the complexes crystallised in monoclinic system with space group P21/n space group. In the complexes V atom is five –coordinated in a distorted square pyramidal geometry (**Figure V.4.a** for **15** and **Figure V.4.b** for **16**) in which the basal plane is defined by the two phenolateO, azomethine N and methoxy oxygen. The remaining apical position of the square pyramid is occupied by the oxo oxygen O3. The short V1=O3 bond distance in the range ~1.6 Å is comparable with other structurally characterized oxidovanadium complexes. The τ values of 0.50 (for **15**) and 0.48 (for **16**) suggest the geometries are very close to distorted square pyramid for both the complexes. The angles in the basal planes ranges from 78°–160° and that with the apical oxo –O atom and the basal donor atoms falls in the range 100°–107°. Selected bond lengths and angles of complexes are given in **Table V.4.** for **15** and **Table V.5.** for **16.**

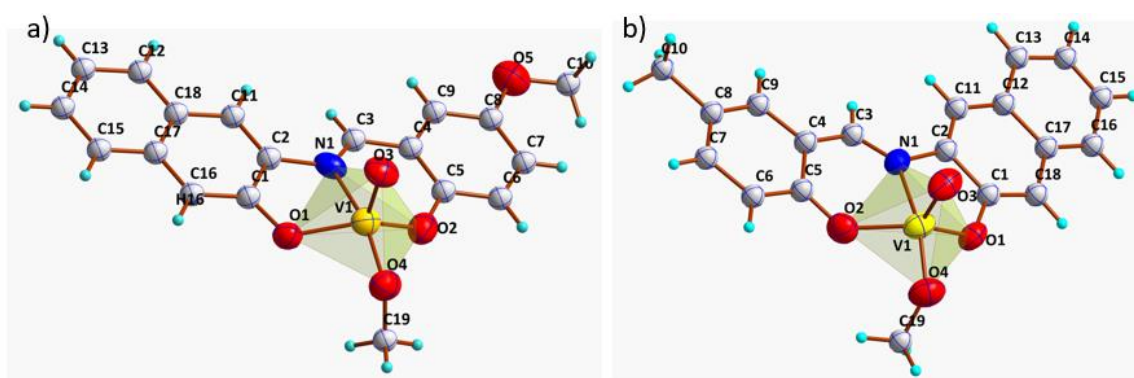


Figure V.4. Perspective view of a) Complex 15, b) Complex

Table V.4. Selected Bond Lengths (Å) and Angles (°) for Complex 15

Bond Length (Å)		Bond Angle (°)	
V1–O1	1.852(5)	O1–V1–O2	139.2(6)
V1–O2	1.857(6)	O1–V1–O3	107.5(3)
V1–O3	1.592(6)	O1–V1–O4	94.8(2)
V1–O4	1.759(6)	O1–V1–N1	79.51(18)
V1–N1	2.112(6)	O2–V1–O3	109.7(3)
O1–C1	1.342(9)	O2–V1–O4	91.6(3)
O2–C5	1.341(9)	O2–V1–N1	81.0(2)
		O3–V1–O4	104.7(3)
		O3–V1–N1	95.1(2)
		O4–V1–N1	160.2(3)

Table V.5. Selected Bond Lengths (Å) and Angles (°) for Complex 16

Bond Length (Å)		Bond Angle (°)	
V1-O1	1.862(5)	O1-V1-O2	138.8(2)
V1-O2	1.872(5)	O1-V1-O3	107.3(2)
V1-O3	1.587(5)	O1-V1-O4	93.4(2)
V1-O4	1.761(4)	O1-V1-N1	78.45(18)
V1-N1	2.133(6)	O2-V1-O3	109.7(2)
O1-C1	1.350(5)	O2-V1-O4	93.8(2)
O2-C5	1.381(7)	O2-V1-N1	81.2(2)
		O3-V1-O4	105.2(2)
		O3-V1-N1	94.6(2)
		O4-V1-N1	160.1(2)

C. ABSORPTION SPECTRA

UV -Vis spectrum of the ligands (**Figure V.5.**) and complexes (**Figure V.6.**) were performed in methanol at room temperature. The peaks observed around 333 nm and 272 nm are presumably assigned as $n-\pi^*$ and $\pi-\pi^*$ transitions. The spectral parameters with the experimental molar extinction coefficient (ϵ) values of all the compounds are listed in **Table V.6.** There are two well resolved peaks around 347 nm and ~ 270 nm for all and for the complexes. For **15** and **16** the peak observed around 420 nm and 440 nm are presumably assigned as O(alkoxide/phenoxide) \rightarrow V(V) LMCT excitation. Whereas the absorption in the range 270 nm and 347 nm are due to the ligand $\pi-\pi^*$ transition.

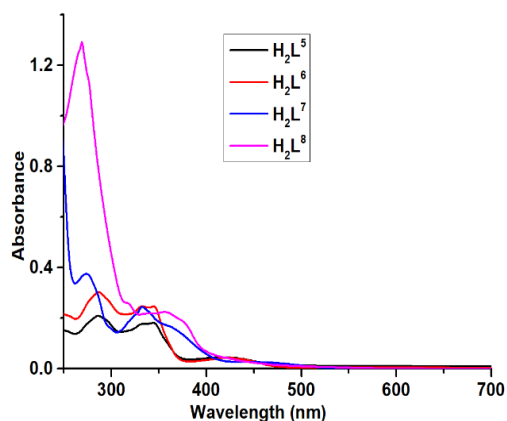


Figure V.5. Absorption Spectra of ligands in methanol, at room temperature.

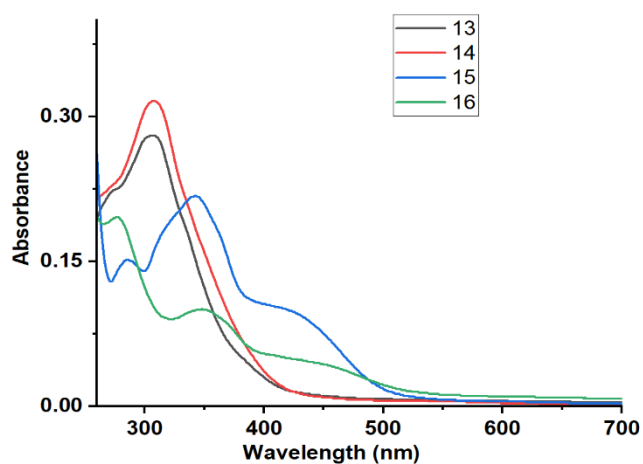


Figure V.6. Absorption Spectra of complexes in methanol, at room temperature.

Table V.6. Absorption spectral parameters of the ligands and complexes

Compound	$\lambda_{\max}(\text{nm})[\epsilon(\text{M}^{-1}\text{cm}^{-1})]$
H_2L^5	333(5350), 272(7900)
H_2L^6	288(7389), 344(8596)
H_2L^7	332(12250), 274(18750)
H_2L^8	269(64650), 355(11250)
13	347(11500), 273(21500), 397(7500)
14	344 (33650), 410 (17450)
15	341(10900), 284(7600), 423(5478)
16	278(15200), 348(9800), 446(4867)

D. REDOX PROPERTIES

The redox activities of **13** – **16** were investigated by cyclic voltammetry in CH_2Cl_2 using $[\text{N}(\text{n-Bu})_4]\text{PF}_6$ as supporting electrolyte at 298 K. The cyclic voltammograms with the redox potential data referenced to ferrocinium/ferrocene (Fc^+/Fc) redox couple is illustrated in **Figure V.7** and all the experiments were performed in the nitrogen atmosphere. The complexes **13** and **15** are quite similar and exhibits two successive cathodic waves whereas **16** gives three successive cathodic waves as shown in **Figures V.7 (a), V.7 (c) and V.7 (d)**. The first cathodic wave of **13** at -0.29 , **14** at -0.22 , **15** at -0.30 and **16** at -0.33 V are assigned to the reversible $\text{V}^{\text{VO}}/\text{V}^{\text{IVO}}$ redox couple¹² whereas the second cathodic waves for **13**, **15** and **16** at -0.72 , -0.77 and -0.77 V respectively are assigned to the $\text{V}^{\text{IVO}}/\text{V}^{\text{III O}}$ redox couple.¹³

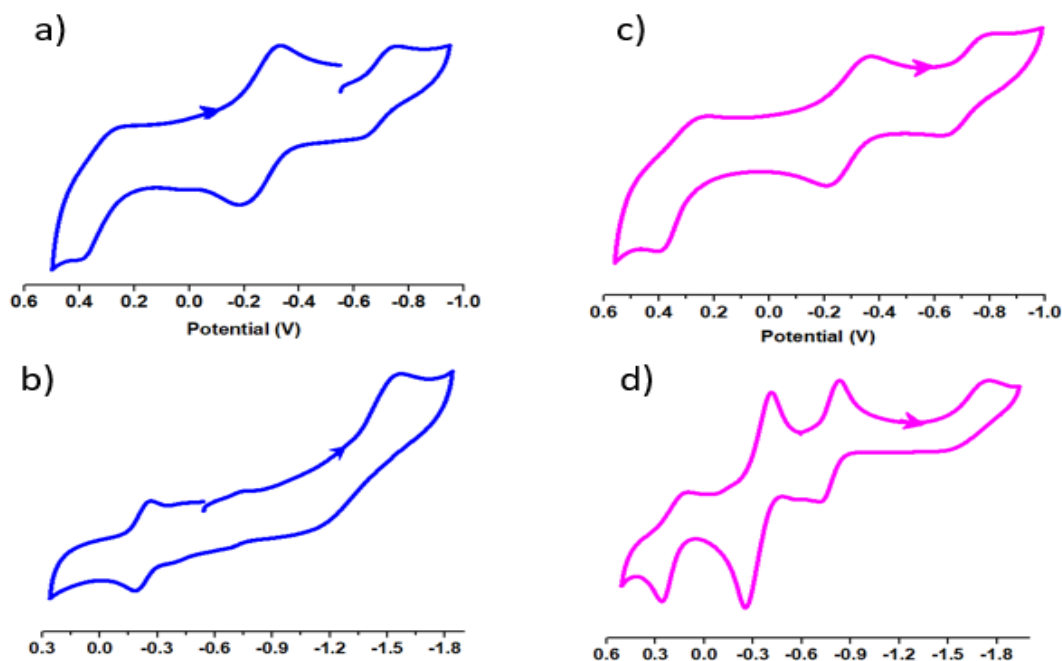


Figure V.7. Cyclic voltammograms of (a) **13**, (b) **14**, (c) **15**, (d) **16** in CH_2Cl_2 at 298 K. Conditions: scan rate, 100 mV s^{-1} ; $0.20 \text{ M } [\text{N}(\text{n-Bu})_4]\text{PF}_6$ supporting electrolyte; platinum working electrode.

Additionally, **16** also exhibits third reversible cathodic wave at 1.72 V due to imine/imino radical redox couple.¹⁴ Interestingly the complexes **13**, **15** and **16** display quasi-reversible anodic waves at 0.32 , 0.30 and 0.18 V respectively

which indicated that the ligand centered oxidation process for the phenoxy/phenolato redox couple.¹⁵ The redox activity of **14** is notably different from those of other complexes as shown **Figures V.7 (b)**. The cyclic voltammogram of **14** displays two cathodic waves at -0.23 V (reversible) and -1.69 V (quasi reversible) attributed to the V^{VO}/V^{IVO} redox couple and imine/imino-radical redox couple redox couple respectively.

E. EPR STUDY

All the four complexes were EPR silent hence diamagnetic in nature. Whereas, the electrochemically reduced and oxidized species were found to be paramagnetic. The EPR spectra of all the species were recorded in CH₂Cl₂ solution at ambient temperature. The EPR spectrum of all the electro-generated mononuclear anionic complexes exhibited characteristic eight-line spectrum due to presence of one extra unpaired electron spin ($S = \frac{1}{2}$) and hyperfine coupling of ⁵¹V ($I=7/2$) i.e., V(V) → V(IV) reversible electronic transition resulting in the reduction of the all the complexes **13** – **16**. The EPR spectra of the reduced complex **13** (**13⁻**) is given in **Figure V.8a**. as a representative case. The corresponding parameter is given in **Table. V.7**. This shifting of diamagnetic [V^{VO}]³⁺ to paramagnetic [V^{IVO}]²⁺ is also supported by spin density data from DFT calculations. On the other hand, electrochemically oxidized species of complex **16** exhibited characteristic spectra (**Figure V.8b**) indicating a ligand centre radical with some metal contribution having g value ~ 2.00037.

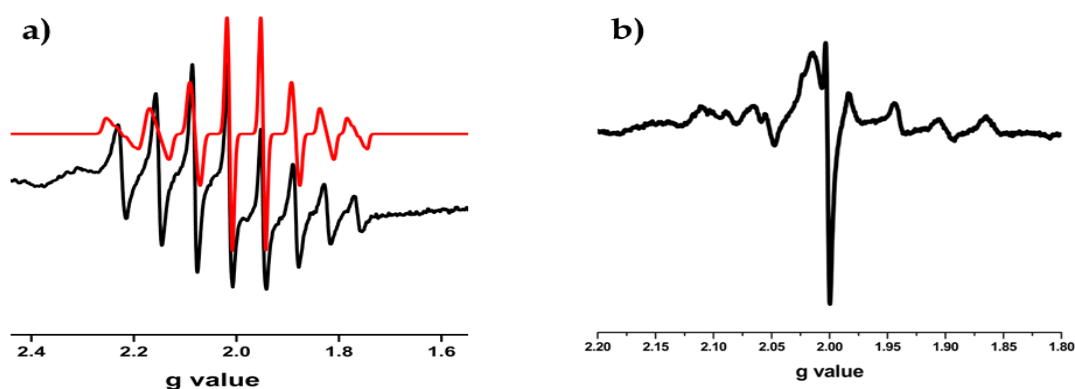


Figure V.8. X-band EPR spectra of (a) **13⁻**, (b) **16⁺** in frozen solution at RT (black-experimental; red-simulated)

Table V.7. X-band EPR Spectral parameter of the reduced complex **13** at RT

Complex	Matrix	g	A (G)	Iw (mT)
13	CH ₂ Cl ₂ ,	1.96355	310	1.7

F. DFT STUDY

DFT calculations were conducted to elucidate spectroscopic and redox properties of the complexes **13**, **14**, **15**, and **16**. In all the cases the HOMO is largely ligand centric mainly located on naphthyl group and oxygen atom from 3 -amino -2 -naphthol moiety. The LUMO is admixture of metal and ligand contribution from aldehyde moiety, where most of the electron density is on imine nitrogen in every cases. (**Figure V.9**). The reduction spin density distribution on vanadium centres are in accordance with the assignment of the V(IV) reduction. (**Figure V.10**.) The assignment of vanadium centre reduction followed by presence of V^{III}/ LO₂N^{•-} redox systems from cyclic voltamograms are accordance with the theoretical calculations. Again, for these monomeric complexes, Mulliken spin density distributions of the oxidized species are depicted in **Figure V.11**. which indicated electron distribution on the oxygen atom of naphthyl moiety from the amine part, which supports one electron oxidation of the ligand resulting formation of L_{NOO}^{•-} centre.

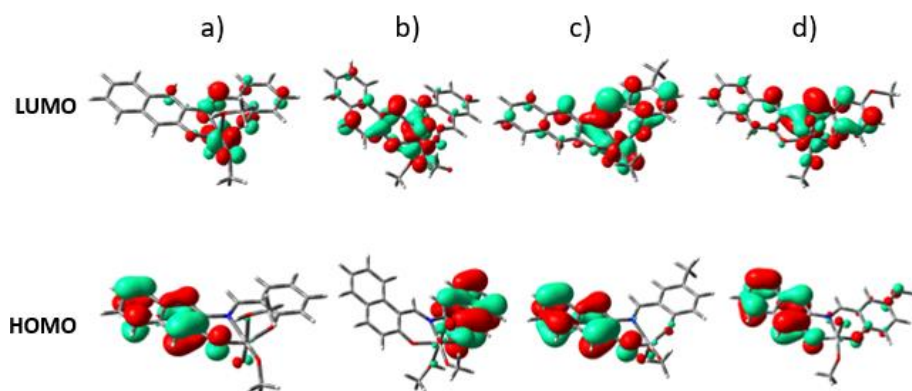


Figure V.9. Isodensity plot of selected frontier orbitals of the complexes a) **13**, b) **14**, c) **15**, d) **16**

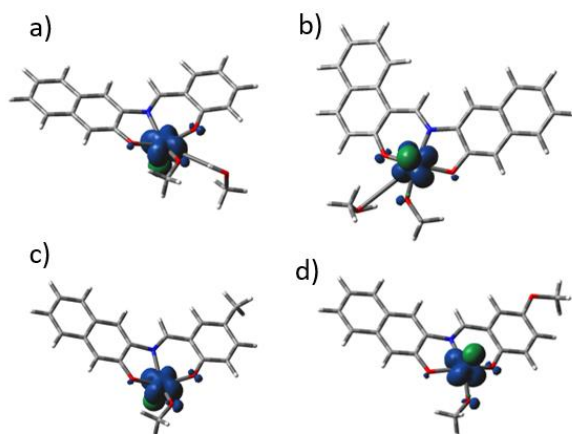


Figure V.10. Reduction Spin density plot of (a) 13^- , (b) 14^- , (c) 15^- , and (d) 16^-

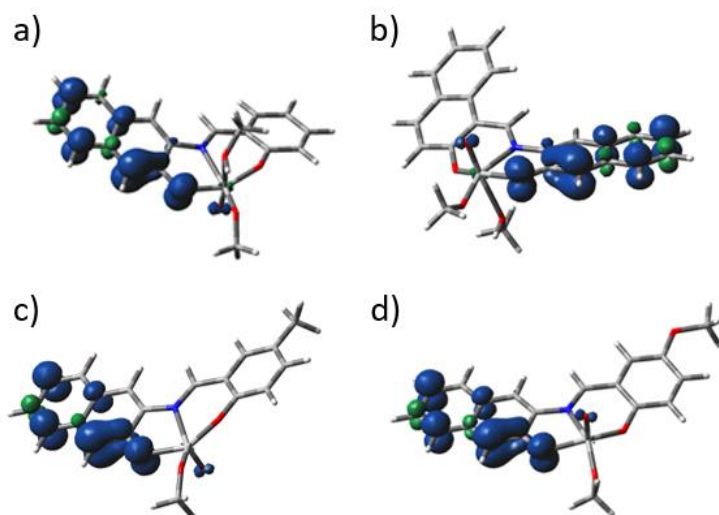


Figure V.11. Oxidation Spin density plot of (a) 13^+ , (b) 14^+ , (c) 15^+ , and (d) 16^+

V.2 CONCLUSION

In summary, we have synthesized a family of mononuclear tridentate *N*, *O*, *O* coordinating V(V) complexes bearing Schiff base derived from 3 -amino -2 -naphthol. The ligands and the complexes are characterized by different spectroscopic techniques, elemental analysis and X -ray structure determination.

The redox properties of the complexes were examined with the help of cyclic voltammetry studies. All the complexes have characteristic low potential V(V)/V(IV) reduction couple. Complex **13**, **15** and **16** have been found to show irreversible imine/imino radical couple whereas all these complexes (**13**, **15** and **16**) possess quasi reversible oxidation couple related to the formation of phenoxy radical. Complex **14** failed to exhibit these two redox nature due to the presence of naphthyl conjugation. EPR spectra of the reduced and oxidised species strongly supported this behaviour. The nature of the reduced and oxidized species further reinforced by Spin density difference map analysis.

V.3 EXPERIMENTAL SECTION

A. MATERIALS

[VO(acac)₂] used was prepared according to the literature.^{18a} are used throughout the study. All the reactions with metal salts are carried out under open air atmosphere. All analytically pure solvents were purchased from reputed commercial sources and used without further purification.

B. PREPARATION OF COMPOUNDS

Ligands

Four Schiff base ligands (**H₂L⁵⁻⁸**) were prepared by condensation of equimolar amount of 3-amino-2-naphthol (10 mmol) with different aldehydes namely with salicylaldehyde (**H₂L⁵**), naphthaldehyde (**H₂L⁶**), 4-methylsalicylaldehyde (**H₂L⁷**), 4-methoxysalicylaldehyde (**H₂L⁸**) in methanol.

H₂L⁵: Anal. Calc. for C₁₇H₁₃NO₂: C 77.55%; H 4.98%; N 5.32%. Found: C 77.46%; H, 4.83%; N, 5.26%. ¹H NMR {300 MHz, DMSO-D₆, δ (ppm)}: 10.11 (OH, s), 9.08 (-CH=N, s) 7.83-6.97 (10H, ArH). (ESI-MS (positive) in MeOH: The base peak was detected at *m/z* = 264.0618, corresponding to [M+H]⁺. IR (KBr, ν_{max} / cm⁻¹): 2909 (O-H); 1604 (C=N).

H₂L⁶: Anal. Calc. for C₂₁H₁₅NO₂: C 80.49%; H 4.82%; N 4.47%. Found: C 80.33%; H, 4.76%; N, 4.42%. ¹H NMR {300 MHz, DMSO-D₆, δ (ppm)}: 10.78 (OH, s), 9.64 (-CH=N, s) 8.48-6.77 (12H, ArH). (ESI-MS (positive) in MeOH: The base peak was

detected at $m/z = 314.1174$, corresponding to $[M+H]^+$. IR (KBr, ν_{\max} / cm^{-1}): 3061(O-H); 1608(C=N).

H₂L⁷: Anal. Calc. for C₁₈H₁₅NO₂: C 68.67%; H 8.45%; N 10.68%. Found: C 68.57%; H, 8.32%; N, 10.59%. ¹H NMR {300 MHz, DMSO-D₆, δ (ppm)}: 9.83 (OH, s), 9.09 (-CH=N, s) 7.83-6.36 (9H, ArH), 2.18 (CH₃, s). (ESI-MS (positive) in MeOH: The base peak was detected at $m/z = 278.1142$, corresponding to $[M+H]^+$. IR (KBr, ν_{\max} / cm^{-1}): 3371-3273(O-H); 1614(C=N).

H₂L⁸: Anal. Calc. for C₁₈H₁₅NO₃: C 73.71%; H 5.15%; N 4.78%. Found: C 73.65%; H, 5.07%; N, 4.70%. ¹H NMR {300 MHz, DMSO-D₆, δ (ppm)}: 10.05 (OH, s), 9.05 (-CH=N, s) 7.83-6.67 (9H, ArH), 3.78 (OCH₃, s). (ESI-MS (positive) in MeOH: The base peak was detected at $m/z = 294.1057$, corresponding to $[M+H]^+$. IR (KBr, ν_{\max} / cm^{-1}): 2940(O-H); 1605(C=N).

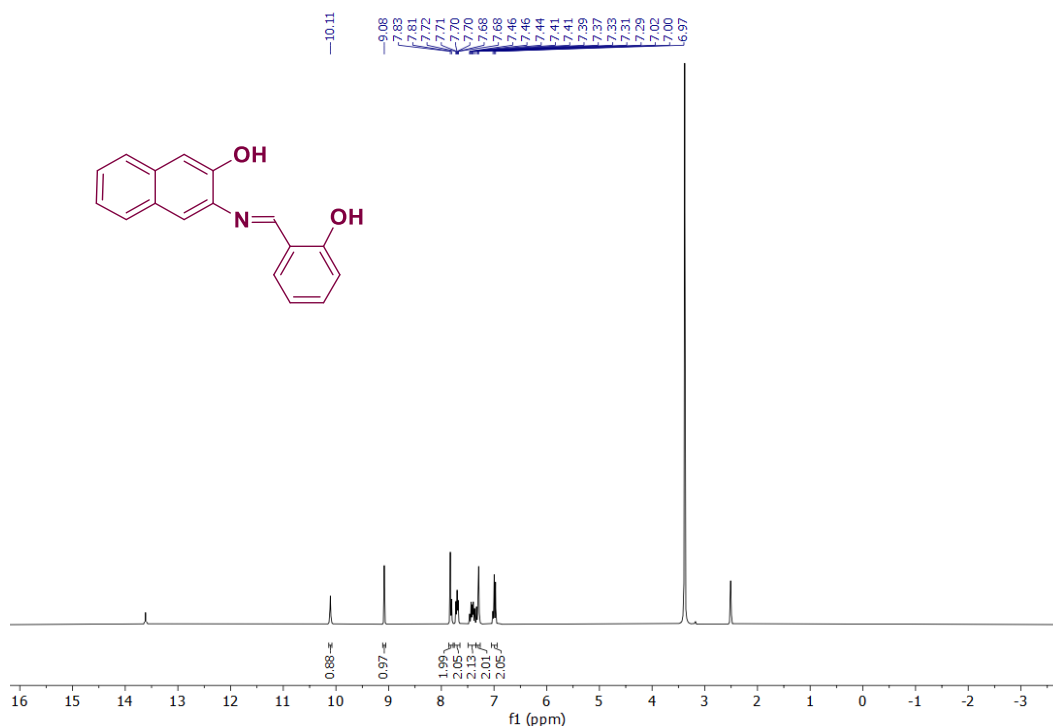


Figure V.12. ¹H NMR spectra of **H₂L⁵** in DMSO-D₆.

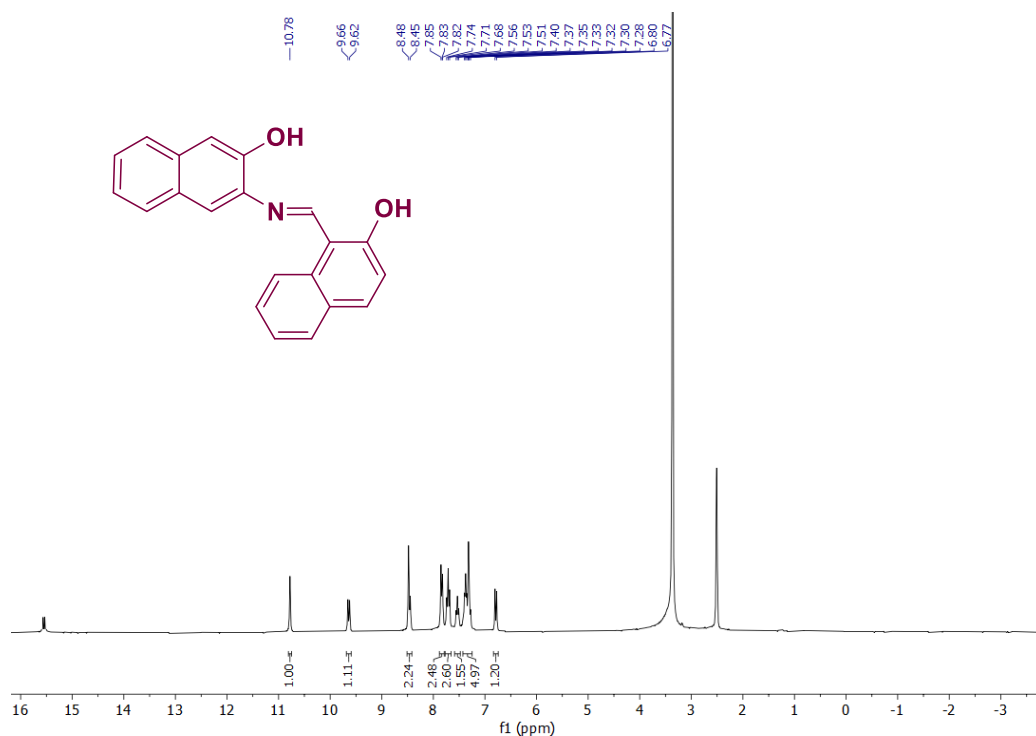


Figure V.13. 1H NMR spectra of H_2L^6 in $DMSO-D_6$.

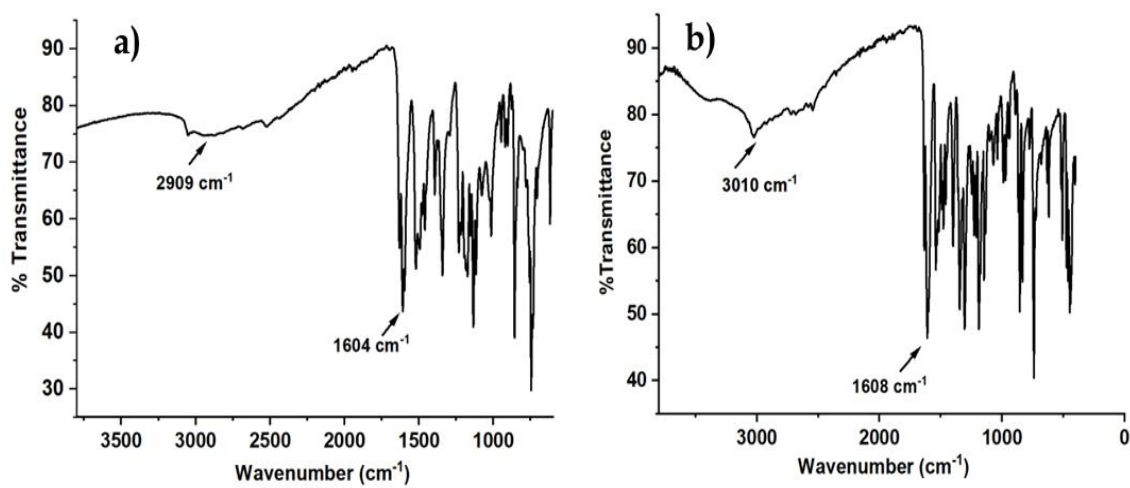


Figure V.14. IR spectra of ligands a) H_2L^5 , b) H_2L^6

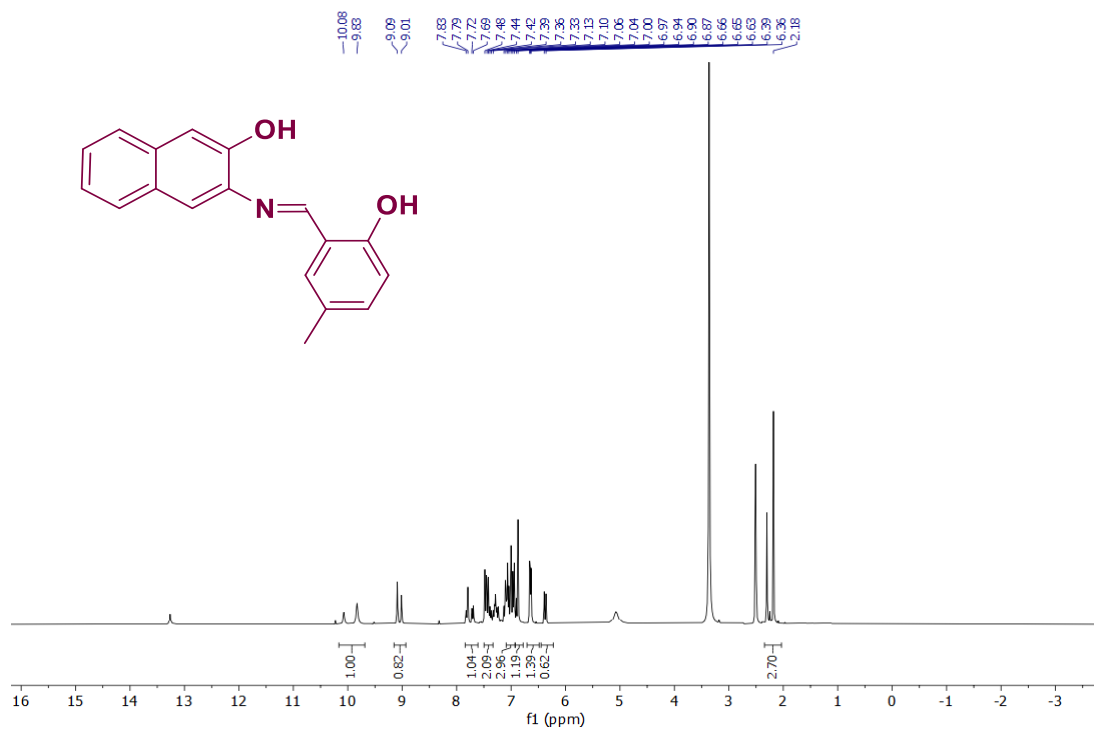


Figure V.15. 1H NMR spectra of H_2L^7 in $DMSO-D_6$.

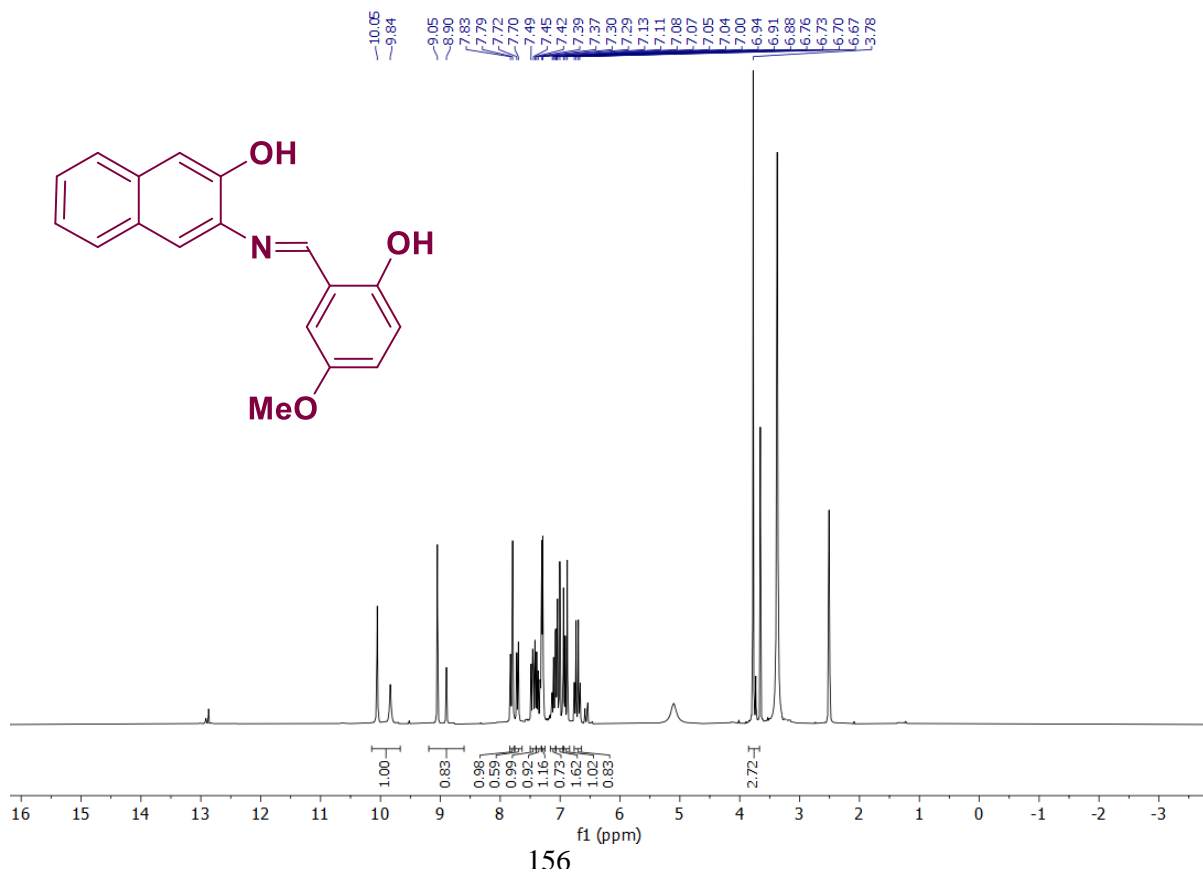


Figure V.16. 1H NMR spectra of H_2L^8 in $DMSO-D_6$.

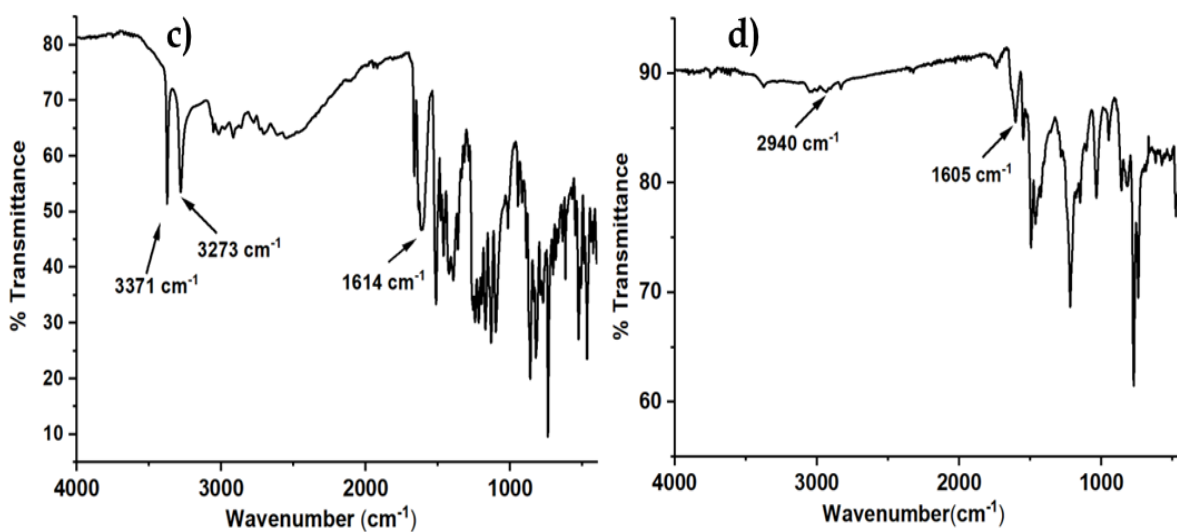


Figure V.17. IR spectra of ligands c) H_2L^7 , d) H_2L^8

Complexes

A 10 ml methanolic solution of $VO(acac)_2$ (5 mmol) was added to a methanolic solution of ligand (H_2L^5 or H_2L^6) (5 mmol) and the resultant reaction mixture was stirred at room temperature for four hour. The solution was then filtered. Brown coloured crystals resulted from the slow evaporation of methanolic solution of the complexes.

[VO(L⁵)(OMe)(MeOH)] (13): Yield: 76%. Anal.Calc. for $C_{19}H_{18}VNO_5$: C 58.32%; H 4.64 %; N 3.58%. Found: C 58.22%; H 4.56%; N 3.47%. 1H NMR {300 MHz, DMSO- D_6 , δ (ppm)} 9.51 (1H, s, $-N=CH$), 8.20-6.75 (10H, ArH), 3.18 (OCH₃, s). The base peak was detected at $m/z = 415.2746$, corresponding to $[M+Na]^+$. IR (KBr, ν_{max} / cm^{-1}): 1604 C=N), 1259 (C-O)_{enolic}; 984 (V=O); 763 (V-O).

[VO(L⁵)(OMe)(MeOH)] (14): Yield: 76%. Anal.Calc. for $C_{23}H_{20}VNO_5$: C 62.59%; H 4.57 %; N 3.17%. Found: C 62.51%; H 4.45%; N 3.09%. 1H NMR {300 MHz, DMSO- D_6 , δ (ppm)} 10.19 (1H, s, $-N=CH$), 8.76-6.96 (12H, ArH), 3.18 (OCH₃, s). The base peak was detected at $m/z = 411.2421$, corresponding to $[M-CH_3OH+H]^+$. IR (KBr, ν_{max} / cm^{-1}): 1612 C=N), 1263 (C-O)_{enolic}; 980 (V=O); 769 (V-O).

Synthesis of complexes $[\text{VO}(\text{L}^{7-8})(\text{OMe})]$, (15 and 16)

A 10 ml acetonitrile solution of $\text{VO}(\text{acac})_2$ (5 mmol) was added to a methanolic solution of ligand (H_2L^7 or H_2L^8) (5 mmol) and the resultant reaction mixture was stirred at room temperature for four hour. The solution was then filtered. Brown colored crystals resulted from the slow evaporation of the solution.

$[\text{VO}(\text{L}^7)(\text{OMe})]$ (15): Yield: 76%. Anal.Calc. for $\text{C}_{19}\text{H}_{16}\text{VNO}_4$: C 61.14%; H 4.32 %; N 3.75%. Found: C 61.08%; H 4.20%; N 3.63%. ^1H NMR {300 MHz, DMSO-D_6 , δ (ppm)} 9.08 (1H, s, $-\text{N}=\text{CH}$), 8.86-6.63 (9H, ArH), 2.18 (CH_3 , s). The base peak was detected at $m/z = 396.2357$, corresponding to $[\text{M}+\text{Na}]^+$. IR (KBr, ν_{max} / cm^{-1}): 1656 $\text{C}=\text{N}$), 1220 ($\text{C}-\text{O}$)_{enolic}; 989 ($\text{V}=\text{O}$); 768 ($\text{V}-\text{O}$).

$[\text{VO}(\text{L}^8)(\text{OMe})]$ (16): Yield: 76%. Anal.Calc. for $\text{C}_{19}\text{H}_{16}\text{VNO}_5$: C 58.62%; H 4.14 %; N 3.60%. Found: C 58.57%; H 4.05%; N 3.48%. ^1H NMR {300 MHz, DMSO-D_6 , δ (ppm)} 9.38 (1H, s, $-\text{N}=\text{CH}$), 8.21-6.61 (9H, ArH), 3.77 (OCH_3 , s), 3.23 (OCH_3 , s). The base peak was detected at $m/z = 411.9312$, corresponding to $[\text{M}+\text{Na}]^+$. IR (KBr, ν_{max} / cm^{-1}): 1622 $\text{C}=\text{N}$), 1217 ($\text{C}-\text{O}$)_{enolic}; 981 ($\text{V}=\text{O}$); 773 ($\text{V}-\text{O}$).

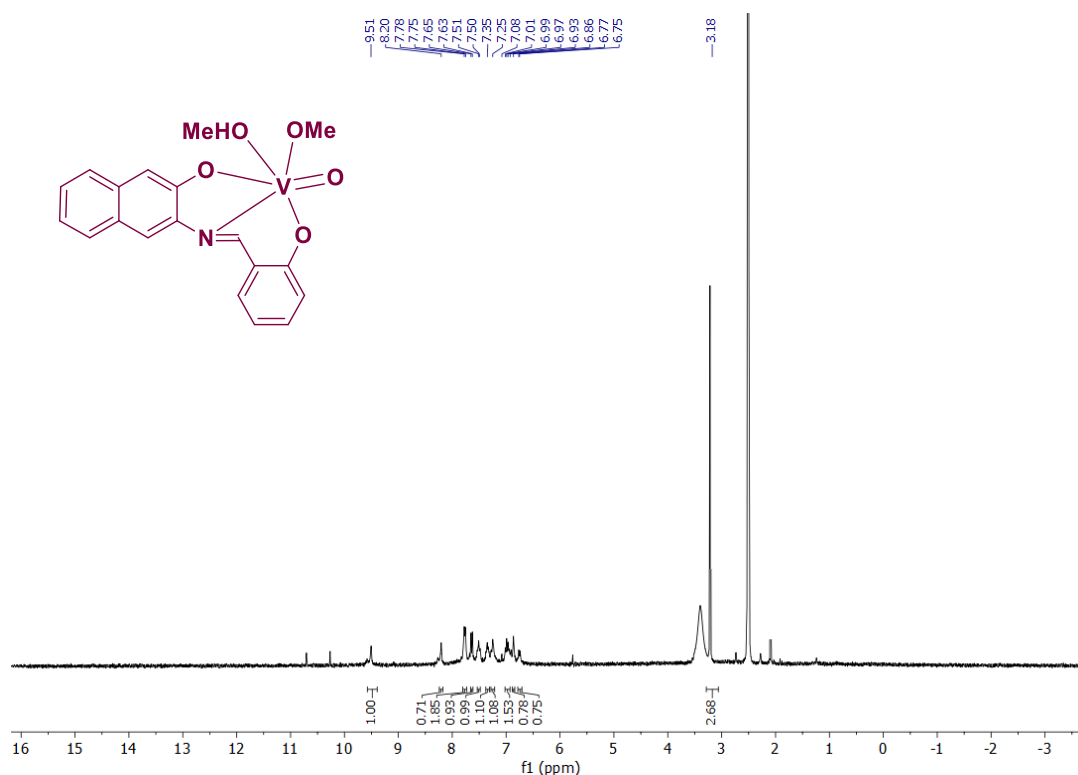


Figure V.18. ^1H NMR spectra of complex 13 in DMSO-D_6 .

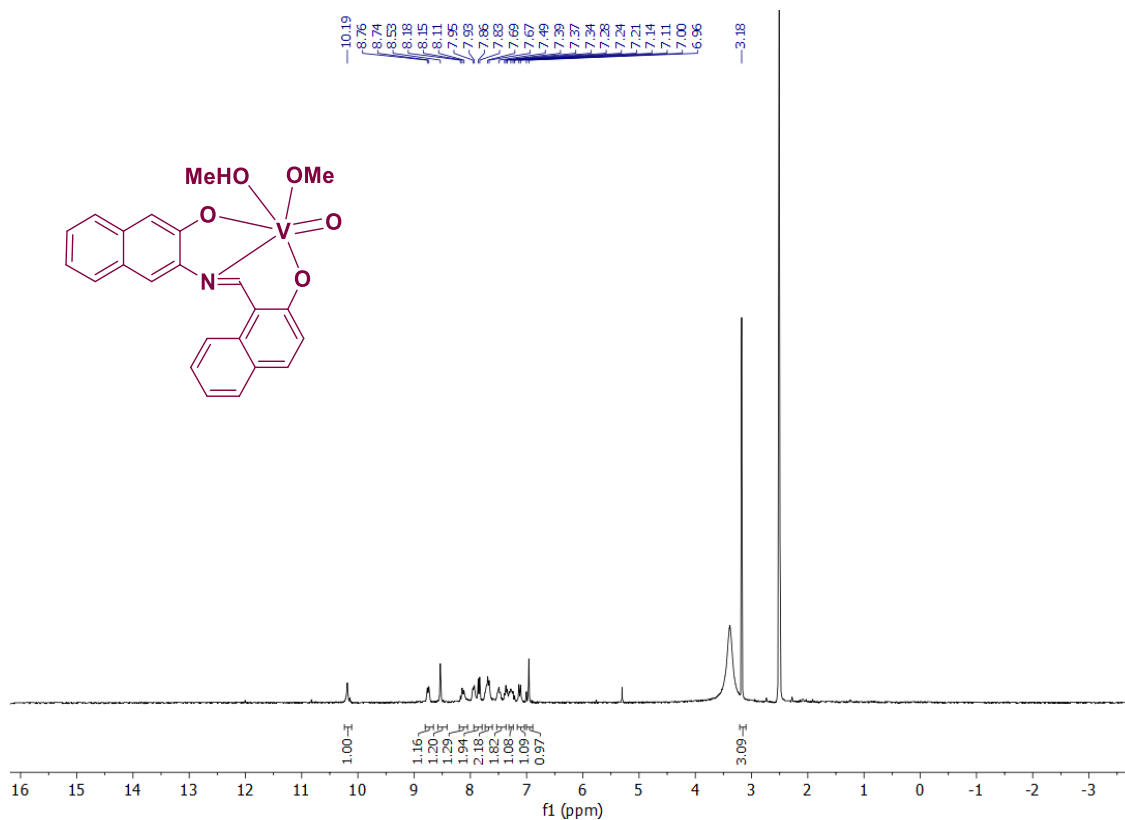


Figure V.19. ¹H NMR spectra of complex 14 in DMSO-*D*₆.

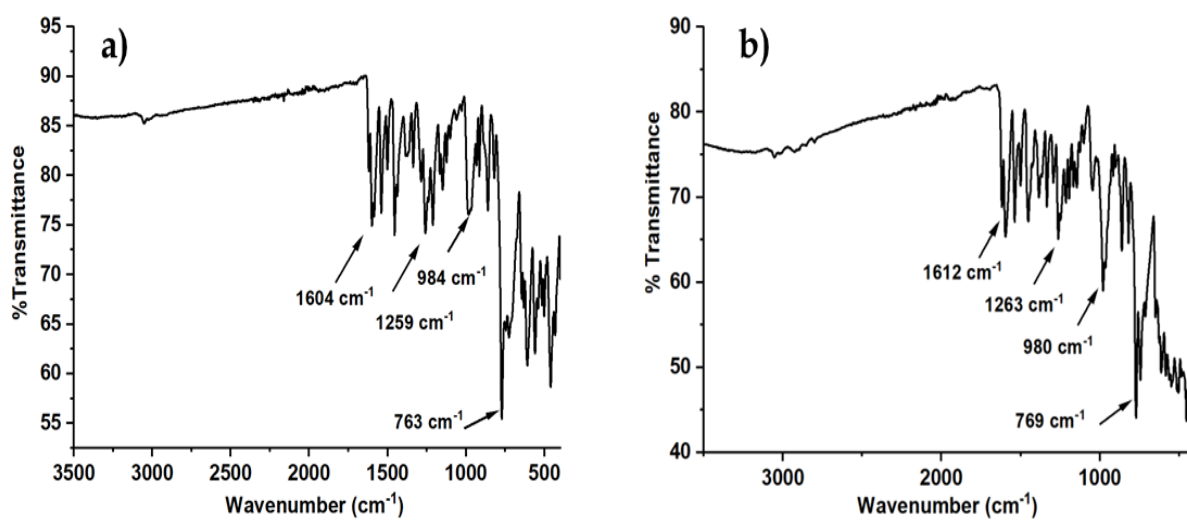


Figure V.20. IR spectra of the complexes a) 13, b) 14

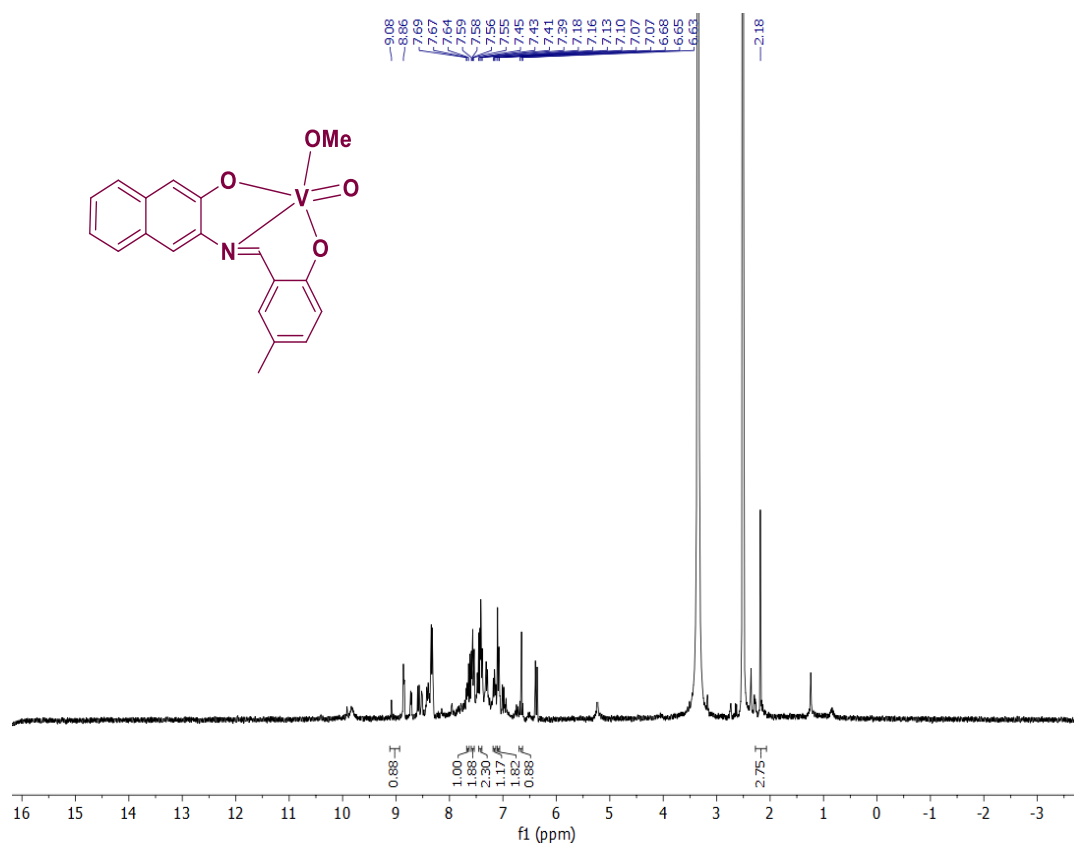


Figure V.21. ¹H NMR spectra of complex 15 in DMSO-D₆.

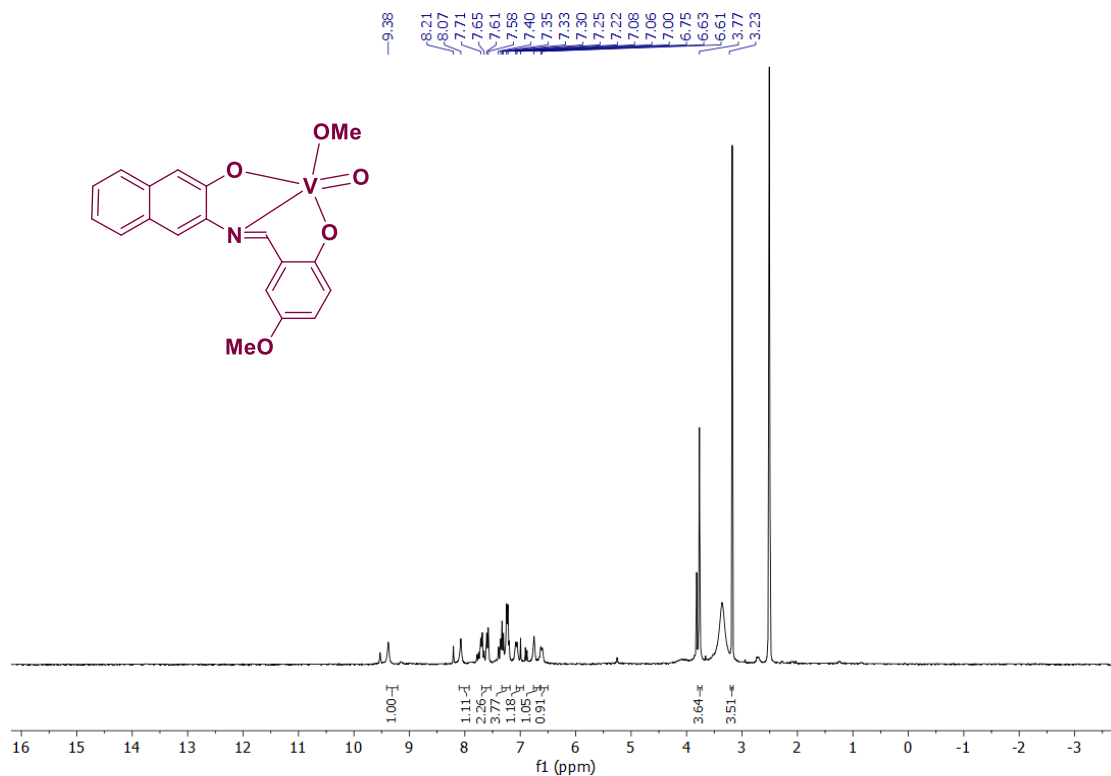


Figure V.22. ^1H NMR spectra of complex 16 in $\text{DMSO-}D_6$.

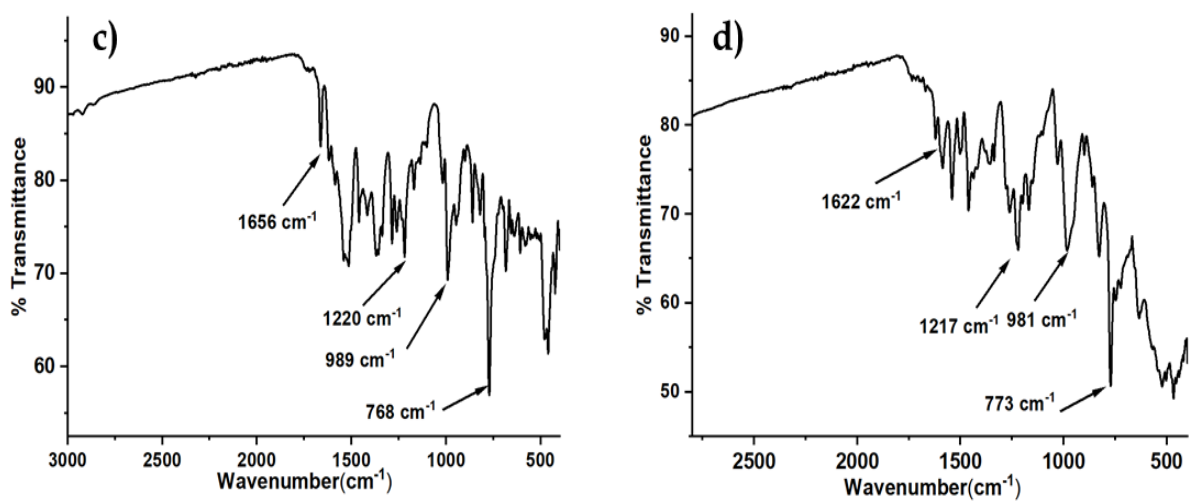


Figure V.23. IR spectra of the complexes c) 15, d) 16

C. X-RAY STRUCTURE DETERMINATION

The single crystal suitable for X-ray crystallographic analysis of the ligand and complexes were obtained by slow evaporation of methanol solution. Details of the X-ray work is given in tabular form in **Table V.8**. (See also Chapter I).

D. PHYSICAL MEASUREMENTS

All physical measurements including X-ray single crystal data analysis, elemental analyses, IR, NMR, absorption and emission spectra, ESI-MS studies and electrochemical studies were performed as described in **Chapter I**.

Table V.8. Crystallographic data for ligand and complexes**Crystal Data**

	H₂L⁸	13	14	15	16
Empirical	C ₁₈ H ₁₅ NO ₃ O ₂	C ₁₉ H ₁₈ NO ₅ V	C ₂₃ H ₂₀ NO ₅ V	C ₁₉ H ₁₆ NO ₄ V	C ₁₉ H ₁₆ NO ₅ V
Formula	293.31	391.28	441.34	373.27	389.27
Temperature/K	273	293	293	273	293
Crystal	Orthorhombic	Monoclinic	Monoclinic	Monoclinic	Monoclinic
Space group	P21 21 21	P21/n	P 21	P21/n	P21/n
a/Å	8.1059(2)	7.937(5)	10.3920(11)	8.4004(8)	8.330(3)
b/Å	8.8802(2)	21.438(14)	7.3927(9)	13.8337(13)	13.737(5)
c/Å	20.3290(5)	23.437(8)	14.4244(16)	14.7541(14)	15.221(5)
α/°	90	90	90	90	90
β/°	90	93.29(3)	110.474(11)	104.025(3)	102.664(10)
γ/°	90	90	90	90	90
Volume/Å ³	1463.32(6)	1855.5(34)	1038.2(2)	1663.4(3)	1699.0 (10)
Z	4	4	2	4	4
ρ _{calc} /cm ³	1.331	1.401	1.412	1.490	1.314
μ/mm ⁻¹	0.091	0.563	0.512	0.620	0.615
F(000)	616	1616.0	456	768	800
Radiation	MoKα	MoKα	MoKα	MoKα	MoKα
GOF	1.181	1.010	1.048	1.073	1.032
R ₁	0.0502	0.0743	0.0634	0.0913	0.0837
wR ₂	0.1155	0.2382	0.1591	0.2982	0.2946

Data collection

	H ₂ L ⁸	13	14	15	16
Total refl. collected	19665	46303	7828	53481	53180
Unique refl. (R _{int})	3242	7716	4122	3793	3457
Used refl.	2717	4211	2777	2317	1787
<i>h k l</i> range	-10 ≤ <i>h</i> ≤ 10	-9 ≤ <i>h</i> ≤ 9	-14 ≤ <i>h</i> ≤ 12	-10 ≤ <i>h</i> ≤ 10	-10 ≤ <i>h</i> ≤ 10
	-11 ≤ <i>k</i> ≤ 11	-26 ≤ <i>k</i> ≤ 24	-9 ≤ <i>k</i> ≤ 9	-17 ≤ <i>k</i> ≤ 17	-17 ≤ <i>k</i> ≤ 17
	-26 ≤ <i>l</i> ≤ 26	-32 ≤ <i>l</i> ≤ 29	-19 ≤ <i>l</i> ≤ 18	-19 ≤ <i>l</i> ≤ 19	-18 ≤ <i>l</i> ≤ 18

Structure Solution and Refinement

	H ₂ L ⁸	13	14	15	16
Solution	Patterson	Patterson	Patterson	Patterson	Patterson
Refinement	Full-matrix least-squares on F ²	Full-matrix least-squares on F ²	Full-matrix least-squares on F ²	Full-matrix least-squares on F ²	Full-matrix least-squares on F ²
GOF on F ²	1.181	1.010	1.048	1.073	1.032
R1, ^a [<i>I</i> > 2σ(<i>I</i>)]	0.0595	0.0743	0.0634	0.0884	0.0913
wR2 ^b [<i>I</i> > 2σ(<i>I</i>)]	0.1334	0.2099	0.1316	0.2472	0.2378
R1 [all data]	0.0761	0.1601	0.0979	0.1356	0.1676
wR2 [all data]	0.1487	0.2382	0.1591	0.2946	0.2982

$$^a R1 = \frac{\sum ||F_o| - |F_c||}{\sum |F_o|} \quad .^b wR2 = [\frac{\sum [w(F_o^2 - F_c^2)^2]}{\sum [w(F_o^2)]}]^{1/2}$$

Table V.9. Fractional Atomic Coordinates ($\times 10^4$) and Equivalent Isotropic Displacement Parameters ($\text{\AA}^2 \times 10^3$) for $\mathbf{H}_2\mathbf{L}^8$. \mathbf{U}_{eq} is defined as 1/3 of the trace of the orthogonalized U_{ij} tensor.

Atom	<i>x</i>	<i>y</i>	<i>z</i>	U(eq)
O3	-3692(3)	4765(3)	2050.7(12)	55.9(7)
O2	63(3)	2733(2)	4119.0(11)	44.2(6)
O1	3748(3)	3188(3)	4784.0(11)	51.0(7)
N1	2312(3)	4623(3)	3823.9(12)	34.9(6)
C9	-1108(4)	4909(4)	2658.2(15)	37.5(7)
C8	-2626(4)	4312(4)	2536.3(15)	38.2(7)
C1	4654(4)	4321(3)	4525.7(14)	34.4(7)
C16	6208(4)	4695(3)	4719.1(14)	37.3(7)
C2	3886(4)	5148(3)	4007.0(14)	32.5(7)
C5	-774(4)	3216(3)	3613.7(14)	34.0(7)
C6	-2350(4)	2615(3)	3460.9(16)	40.8(8)
C4	-151(4)	4373(3)	3195.9(14)	33.2(7)
C3	1397(4)	5028(3)	3326.9(15)	34.9(7)
C17	7064(4)	5909(3)	4425.3(14)	35.7(7)
C7	-3227(4)	3155(4)	2937.5(15)	41.4(8)
C18	6267(4)	6751(4)	3923.2(15)	39.2(7)
C15	8680(4)	6323(4)	4613.2(17)	45.4(8)
C11	4677(4)	6333(3)	3719.7(16)	38.7(7)
C14	9471(5)	7502(4)	4320.7(19)	55.6(10)
C12	7127(5)	7988(4)	3639.1(19)	56.3(10)
C13	8681(5)	8348(4)	3838(2)	60.9(11)
C10	-3083(5)	5731(5)	1567(2)	66.6(12)

Table V.10 Fractional Atomic Coordinates ($\times 10^4$) and Equivalent Isotropic Displacement Parameters ($\text{\AA}^2 \times 10^3$) for Complex 13. U_{eq} is defined as 1/3 of the trace of the orthogonalized U_{ij} tensor

Atom	<i>x</i>	<i>y</i>	<i>z</i>	U(eq)
V1	9077.4(11)	2735.4(4)	6407.7(3)	43.3(3)
O1	10105(4)	2203.0(14)	7012.0(13)	44.8(8)
O2	7243(5)	3250.6(15)	6075.6(14)	51.9(9)
O5	6367(5)	2195.1(16)	6714.5(17)	56.0(9)
N1	8621(5)	3269.8(16)	7177.7(15)	35.4(8)
O4	9067(5)	2118.9(17)	5897.1(14)	60.5(10)
O3	10823(5)	3131.7(17)	6264.2(15)	60.7(10)
C2	9323(6)	2971(2)	7688.4(19)	36.5(10)
C1	10154(6)	2382(2)	7569.1(19)	39.3(11)
C16	10098(6)	2845(2)	8701.1(19)	43.9(12)
C5	6757(7)	3849(2)	6166(2)	46.3(12)
C4	7105(6)	4148(2)	6698(2)	44.5(12)
C3	7923(6)	3828(2)	7195(2)	42.3(11)
C10	10961(6)	2043(2)	8009(2)	42.4(11)
C13	11773(8)	2151(3)	9598(2)	67.4(17)
C14	10899(9)	2730(3)	9726(2)	72.5(18)
C17	9302(6)	3190(2)	8240(2)	44.0(12)
C19	4552(7)	2314(3)	6517(3)	73.6(18)
C11	10970(6)	2267(2)	8589(2)	46.6(12)
C18	10343(9)	1938(3)	5485(3)	76.4(18)
C9	6514(7)	4767(2)	6770(2)	53.4(13)
C12	11769(7)	1926(3)	9055(2)	58.4(15)
C8	5605(8)	5085(3)	6320(3)	62.6(16)
C7	5233(8)	4786(3)	5812(3)	68.0(17)
C15	10087(8)	3057(3)	9281(2)	63.8(15)

Table V.11. Fractional Atomic Coordinates ($\times 10^4$) and Equivalent Isotropic Displacement Parameters ($\text{\AA}^2 \times 10^3$) for **Complex 14**. U_{eq} is defined as $1/3$ of the trace of the orthogonalized U_{ij} tensor.

Atom	<i>x</i>	<i>y</i>	<i>z</i>	U(eq)
V1	4898.1(10)	6277.0(16)	6612.4(7)	43.4(3)
O1	3950(4)	7228(7)	5288(3)	46.4(12)
O3	4996(5)	8079(7)	7220(3)	59.8(15)
O4	6512(4)	6194(9)	6457(3)	57.1(12)
O5	4586(5)	3606(7)	5774(4)	55.5(13)
O2	5168(5)	4679(8)	7679(3)	52.3(13)
N1	2809(5)	5758(7)	6393(3)	37.3(14)
C1	2630(6)	6799(9)	4819(4)	39.9(17)
C21	1952(6)	7160(10)	3846(4)	44.4(17)
C15	-95(6)	5610(9)	3949(4)	42.3(16)
C3	2340(6)	5568(9)	7120(4)	39.0(15)
C2	1946(6)	5926(9)	5396(4)	38.6(16)
C13	2612(7)	5310(10)	8898(4)	44.9(16)
C4	3188(6)	5274(9)	8119(4)	39.2(15)
C16	-1448(7)	4992(10)	3486(5)	50.7(18)
C14	621(6)	5315(10)	4981(4)	41.6(16)
C20	574(6)	6533(11)	3395(4)	42.9(16)
C8	3389(8)	4609(11)	9827(4)	50.8(18)
C6	5304(8)	4005(11)	9298(5)	54(2)
C7	4718(8)	3952(12)	10008(5)	55(2)
C12	1320(7)	6078(14)	8774(5)	60(2)
C19	-139(7)	6777(10)	2365(5)	53(2)
C5	4556(7)	4697(10)	8345(4)	44.4(16)
C9	2812(10)	4600(14)	10602(5)	70(2)
C18	-1455(8)	6124(13)	1931(5)	59.7(19)
C17	-2113(8)	5230(12)	2481(5)	63(2)
C10	1543(10)	5281(14)	10423(6)	82(3)
C11	780(9)	6069(17)	9506(5)	78(3)
C22	7622(8)	7410(16)	6730(7)	91(3)
C23	4208(12)	1951(13)	6044(7)	99(4)

Table V.12. Fractional Atomic Coordinates ($\times 10^4$) and Equivalent Isotropic Displacement Parameters ($\text{\AA}^2 \times 10^3$) for **Complex 15**. U_{eq} is defined as 1/3 of the trace of the orthogonalized U_{ij} tensor.

Atom	<i>x</i>	<i>y</i>	<i>z</i>	U(eq)
V1	2627.8(16)	7031.9(8)	5325.2(9)	73.9(5)
C19	330(13)	8445(9)	5587(8)	135(4)
N1	2965(6)	5519(4)	5415(3)	61.9(13)
O1	3588(6)	6897(3)	6588(3)	75.9(13)
O2	739(6)	6654(4)	4456(4)	85.7(15)
O3	4061(7)	7223(4)	4812(4)	92.3(16)
C12	6206(8)	4443(5)	7362(5)	69.0(17)
O4	1802(8)	8182(4)	5435(4)	96.3(17)
C2	4233(10)	5298(6)	6288(6)	81(2)
C11	5069(10)	4525(7)	6535(6)	89(2)
C13	7174(11)	3584(7)	7670(7)	100(3)
C14	8265(10)	3588(8)	8509(6)	99(3)
C15	8483(13)	4295(8)	9089(7)	115(3)
C16	7601(11)	5188(7)	8842(6)	102(2)
C17	6530(10)	5236(7)	8037(6)	90(2)
C18	5627(10)	6126(6)	7763(6)	84(2)
C1	4540(10)	6136(5)	6924(5)	74.3(19)
C3	2309(10)	4860(7)	4860(6)	90(2)
C4	1135(10)	4967(6)	4070(6)	85(2)
C5	360(10)	5890(5)	3885(6)	76.7(19)
C6	-844(11)	5957(6)	3076(7)	94(2)
C7	-1356(12)	5169(7)	2422(8)	110(3)
C8	-587(11)	4317(8)	2617(6)	105(3)
C10	-1070(12)	3450(7)	1899(6)	113(3)
C9	585(9)	4193(5)	3401(5)	76.5(19)

Table V.13. Fractional Atomic Coordinates ($\times 10^4$) and Equivalent Isotropic Displacement Parameters ($\text{\AA}^2 \times 10^3$) for **Complex 16**. U_{eq} is defined as 1/3 of the trace of the orthogonalized U_{ij} tensor.

Atom	<i>x</i>	<i>y</i>	<i>z</i>	U(eq)
V1	7342.4(13)	2932.4(7)	4690.3(7)	70.9(4)
O1	6405(5)	3044(3)	3466(3)	70.5(10)
O3	5885(6)	2772(3)	5194(3)	86.9(13)
O2	9231(5)	3344(4)	5515(3)	88.1(13)
N1	6984(6)	4467(4)	4550(3)	68.3(12)
O4	8129(6)	1760(3)	4576(3)	88.2(13)
O5	10651(8)	6579(4)	7792(4)	116.3(18)
C15	2357(4)	4773(3)	1239.7(18)	87.5(8)
C14	1509(4)	5633(3)	975(2)	87.5(8)
C13	1799(4)	6449(2)	1527(2)	87.5(8)
C12	2937(4)	6405(2)	2344(2)	87.5(8)
C18	3786(3)	5545.1(18)	2608.9(16)	87.5(8)
C17	3496(3)	4728.9(19)	2056.7(16)	87.5(8)
C16	4344(4)	3868.8(18)	2322(2)	77.8(16)
C1	5482(4)	3825(2)	3139(2)	65.8(13)
C2	5772(3)	4641(2)	3690.7(18)	69.4(14)
C11	4924(4)	5501(2)	3425.9(17)	79.1(17)
C5	9561(5)	4154(3)	6063(3)	74.8(16)
C4	8767(4)	5041(3)	5855(2)	78.9(17)
C9	9168(6)	5827(3)	6438(3)	85.7(18)
C8	10362(6)	5725(3)	7228(3)	98(2)
C7	11156(5)	4838(4)	7436(2)	89.1(19)
C6	10756(5)	4052(3)	6854(3)	81.8(17)
C3	7579(8)	5174(5)	5063(4)	77.9(16)
C10	11785(11)	6462(9)	8592(6)	132(4)
C19	9510(11)	1524(8)	4259(7)	131(3)

References

1. (a) Sıdır, Y. G.; Aslan, C.; Berber, H.; Sıdır, İ. *Struct. Chem.* **2019**, *30*, 835 – 851. (b) Minkin, V. I.; Tsukanov, A. V.; Dubonosov, A. D.; Bren, V. A. *J. Mol. Struct.* **2011**, *998*, 179 –191.
2. Köse, A.; Güngör, Ö.; Ballı, J. N.; Erkan, S. *J. Mol. Struct.* **2022**, *1268*, 133750
3. Filarowski, A.; Głowiaka, T.; Koll, J. *Mol. Struct.* **1999**, *484*, 75 –89.
4. Güngör, Ö. *Ö. Gazi Univ. J. Sci.* **2017**, *30*, 191 –214.
5. Bendia, S.; Benabid, W.; Bourzami, R.; Ouari, K. *J. Mol. Struct.* **2023**, *1281*, 135131
6. Rehder, D. *Inorganica Chim. Acta*, **2023**, *549*, 121387
7. Galloni, P.; Conte, V.; Floris, B. *Coord. Chem. Rev.* **2015**, *301*, 240 –299.
8. Hirao, T. *Chem. Rev.* **1997**, *97*, 2707 –2724.
9. Lee, J.; Muya, J. T.; Chung, H.; Chang, J. *ACS Appl. Mater. Interfaces* **2019**, *11*, 42066 –42077.
10. Lourenssen, K.; Williams, J.; Ahmadpour, F.; Clemmer, R; Tasnim, S. *J. Energy Storage* **2019**, *25*, 100844.
11. Blagus, A.; Cinčić, D.; Friščić, T.; Kaitner, B.; Stilinović, V. *Maced. J. Chem. Chem. Eng.* **2010**, *29*, 117 –138.
12. Patra, R.; Mondal, S.; Sinha, D.; Rajak, K. K. *ACS Omega* **2022**, *7*, 11710-11721.
13. Kundu, S.; Mondal, D.; Bhattacharya, K.; Endo, A.; Sanna, D.; Garribba, E.; Chaudhury, M. *Inorg. Chem.* **2015**, *54*, 6203–6215
14. Leitch, J. A.; Rossolini, T.; Rogova, T.; Maitland, J. A. P.; Dixon, D. J. *ACS Catalysis* **2020** *10* (3), 2009-2025.
15. Mondal, S.; Bera, S.; Maity, S.; Ghosh, P. *ACS Omega* **2018**, *3*, 10, 13323-13334



List of Publications

List of Publications

1. **Roumi Patra**, Sandip Mondal, Debopam Sinha, Kajal Krishna Rajak

Mono Versus Dinuclear Vanadium(V) Complexes: Solvent Dependent Structural Versatility and Electro Syntheses of Mixed-Valence Oxovanadium (IV/V) Entities in Solution.

ACS Omega **2022**, 7, 14, 11710–11721.
2. **Roumi Patra**, Kajal Krishna Rajak

Modulation of an Alpha-Beta Unsaturated *N*-Acylhydrazone as Phase Selective Dual Efficient Chemosensor for Zn (II) and Al (III)

ChemistrySelect **2020**, 5, 9477–9485.
3. **Roumi Patra**, Amit Maity, Kajal Krishna Rajak

Synthesis, crystal structure, DFT calculation and trans → cis isomerisation studies of bipyridyl ruthenium (II) complexes bearing 8-oxyquinolate azo ligands

J Chem Sci **2020**, 132, 140.